

Jet-Track Correlation Studies of the Quark Gluon Plasma

BY

HALLIE CAUSEY TRAUGER

M.Ed. University of Illinois at Chicago, 2015

M.S. University of Illinois at Chicago, 2014

B.A. University of Chicago, 2010

THESIS

Submitted in partial fulfilment of the requirements
for the degree of Doctor of Philosophy in Physics
in the Graduate College of the University of Illinois at Chicago, 2017

Chicago, IL

DEFENSE COMMITTEE:

Olga Evdokimov, Chair and Advisor

David Hofman

Zhenyu Ye

Mikhail Stephanov

Julia Velkovska, Vanderbilt University

For my students, with the hope that they, too, may enjoy the privilege of following their curiosity and passions wherever these may lead.

ACKNOWLEDGEMENTS

I owe the opportunity to earn a PhD almost entirely to my advisor Olga Evdokimov, who convinced me to pursue research and invested countless hours in teaching, coaching, and mentoring me. I am also indebted to all the professors and staff members at UIC who took chances on me, and provided me with the opportunities and support I needed to learn. In particular, I thank my Preliminary Examination and Dissertation committee members, Professors Evdokimov, Hofman, Ye, Stephanov, Cavanaugh, and Velkovska for their time, flexibility, and support. I also would like to thank my collaborators in CMS for their patience, availability, and invaluable thorough feedback. I thank my fellow graduate students and post-docs in UIC, especially Kolja Kauder and Pelin Kurt who, along with Professor Evdokimov, helped me get started with ROOT and in CMS, and the friends that made the first few years of graduate school fun and studying for qualifying exams tolerable. Finally, I would like to thank my parents Tom Trauger and Jana Belsky for teaching me from a young age the perserverence and problem-solving that prepared me to tackle this challenge, and my partner Eddie Vogel who provided the support, patience, and home-cooked meals that enabled me to persist and finish it.

HCT

CONTRIBUTION OF AUTHORS

The results reported here are the product of three jet-track correlation analyses which I carried out as a member of the CMS Collaboration, which have been either previously published in JHEP in Refs. [1, 2] (2.76 TeV results), or made public by the CMS Collaboration in Ref. [3] (5.02 TeV results). Following the CMS authorship policy, all members of the CMS Collaboration sign all papers from approximately six months after joining CMS until one year after leaving the collaboration. This policy reflects the fact that each CMS analysis relies heavily on an enormous amount of underlying work on detector and software design, calibration, and maintenance. The details of the CMS detector, track reconstruction, jet reconstruction, data selection and Monte Carlo simulation that are used in common by many CMS analyses are summarized in Sec. 5–8. I contributed to these as a member of the CMS heavy ion group, but the work summarized there is not primarily my own. Sections 9 and 10 report the analysis-specific work for which I, with support from my advisor and close collaborators, am primarily responsible; I also personally produced all figures appearing in these sections including those cited to Refs. [1, 2, 3]. In all cases, analysis was carried out in close collaboration with my advisor Olga Evdokimov, and with the support and helpful scrutiny of other members of CMS, particularly the high- p_T heavy ion analysis group and the Analysis Review Committees for each paper. In addition, Pelin Kurt contributed substantially to the early stages of the analysis documented in Ref. [1], and Kurt Jung, Dhanush Hangal, and Xiao Wang contributed to the analysis documented in Ref. [3].

CONTENTS

1	Introduction	1
2	The quark gluon plasma	3
2.1	Predictions and early evidence for the quark gluon plasma	3
2.2	Thermodynamics of the quark gluon plasma	5
2.3	Time-evolution of heavy ion collisions	7
2.4	Characterizing collision geometry and event centrality	8
2.5	Kinematic variables and coordinates	10
2.6	Collective behavior in the QGP	11
3	Jets as probes of the quark gluon plasma	14
3.1	Measuring suppression of high- p_T particles and jets	15
3.2	Jet fragmentation function and jet shape measurements	19
3.3	Dijet asymmetry and momentum balance studies	21
4	Models of jet energy loss in the quark gluon plasma	25
4.1	Survey of theoretical models of jet quenching mechanisms	25
4.2	Quenching model comparisons to high- p_T jet observables	28
4.3	Theoretical motivations for detailed jet-track correlation studies	39
5	The Large Hadron Collider and the CMS detector	42
5.1	The Large Hadron Collider	42
5.2	The CMS detector	43
5.3	Trackers in the CMS detector	43
5.4	Calorimeters in the CMS detector	45
5.5	The CMS trigger system	46
6	Track reconstruction and correction	48
6.1	Track reconstruction in pp collisions	48
6.2	Track reconstruction in PbPb collisions	49
6.3	High purity tracks	50
6.4	Tracking efficiency and fake rate evaluation and correction	51
7	Jet reconstruction and correction	53
7.1	Jet reconstruction with the anti- k_t algorithm	53
7.2	Underlying event subtraction in PbPb data	55
7.3	Jet energy corrections	56
8	Data and Monte Carlo samples	58
8.1	Data samples and event selection	58
8.2	Collision centrality determination and classes	59
8.3	Monte Carlo simulation	59
8.4	Jet selection and dijet asymmetry classes	64
8.5	Track selection and classes	64
8.6	Summary of analysis bins	66

9	Jet-track correlation measurements	67
9.1	Analysis procedure	67
9.2	Jet-track correlation pair-acceptance correction	68
9.3	Separation of correlations into long range and short-range components	68
9.4	Residual Jet Fragmentation Function correction	72
9.5	Background fluctuation bias correction	76
9.6	Evaluation of systematic uncertainties	83
10	Results	87
10.1	Inclusive jet particle density correlation results	87
10.2	Dijet correlation results at 2.76 TeV	98
10.3	Jet shapes at 2.76 TeV and 5.02 TeV	107
10.4	Decomposition of hemisphere momentum balance in dijet events at 2.76 TeV	111
10.5	Theory implications of these results	123
11	Conclusions	128
	References	130
	Appendices	136
A	Jet kinematics	136
B	Background fitting details	150
C	Pair acceptance and event decomposition systematic uncertainties	154
D	Correlation widths and related uncertainty	156
E	Open access statements for material adapted from previous publications	160
	Vita	161

LIST OF TABLES

I	Summary of data samples and number of selected events	58
II	Summary of Monte Carlo samples and generated events at 2.76 TeV	61
III	Summary of Monte Carlo samples and generated events at 5.02 TeV	63
IV	Summary of data selections and analysis bins	66
V	Systematic uncertainties for particle density correlation studies at 2.76 TeV	85
VI	Systematic uncertainties for particle density correlation studies at 5.02 TeV	85
VII	Systematic uncertainties for balanced and unbalanced dijets in transverse momentum distribution studies at 2.76 TeV	86

LIST OF FIGURES

1	QCD coupling constant α_s	4
2	QCD phase diagram	6
3	Glauber model illustration	9
4	Dihadron correlation in $\Delta\eta - \Delta\phi$	12
5	Fits to dihadron $\Delta\phi$ distributions to extract flow coefficients	13
6	Flow coefficients v_2 and v_3 by centrality and p_T	13
7	Illustration of QCD cross section factorization	15
8	Charged particle R_{AA} at 200 GeV and 2.76 TeV	17
9	Charged particle R_{AA} at 2.76 and 5.02 TeV	17
10	Jet R_{AA} at 2.76 TeV	18
11	Jet fragmentation function in 2.76 TeV PbPb and pp data	19
12	Jet shape measurement in 2.76 TeV PbPb and pp data	20
13	Illustration of dijet asymmetry	21
14	Dijet asymmetry and in 2.76 TeV PbPb and pp data	22
15	Hemisphere momentum balance in dijet events as a function of A_J	23
16	Radial distribution of hemisphere momentum balance as a function of Δr for unbalanced dijets	24
17	Temperature dependence of \hat{q} from different quenching models	26
18	Model comparisons to charged particle R_{AA} at 5.02 TeV	29
19	Simulated dependence of jet R_{AA} on R at 2.76 TeV from JEWEL	30
20	Simulated dependence of jet R_{AA} on R at 2.76 TeV with the coupled jet-fluid model	31
21	Predicted jet R_{AA} as a function of p_T at 2.76 TeV from SCET _G	31
22	Calculated jet R_{AA} as a function of p_T at 2.76 TeV from the hybrid model	32
23	Simulated jet shape ratio $\rho(\Delta r)_{\text{PbPb}}/\rho(\Delta r)_{\text{pp}}$ at 2.76 TeV from JEWEL	33
24	Calculated jet shapes in PbPb and pp and their ratio at 2.76 TeV from the coupled jet-fluid model	34
25	Calculated jet shapes in PbPb and pp at 2.76 TeV from the coupled jet-fluid model, extended to $\Delta r = 1$	34
26	Calculated jet shape ratio $\rho(\Delta r)_{\text{PbPb}}/\rho(\Delta r)_{\text{pp}}$ at 2.76 TeV with SCET _G	35
27	Calculated jet shape ratio $\rho(\Delta r)_{\text{PbPb}}/\rho(\Delta r)_{\text{pp}}$ at 2.76 TeV from the hybrid model for a range of values of broadening parameter K	36
28	Calculated jet shape ratio $\rho(\Delta r)_{\text{PbPb}}/\rho(\Delta r)_{\text{pp}}$ at 2.76 TeV from the hybrid model with and without the medium backreaction	36
29	Simulated JFF ratio PbPb/pp at 2.76 TeV from JEWEL	37
30	Calculated JFF ratio PbPb/pp at 2.76 TeV from the hybrid model	38
31	Simulated dijet asymmetry parameter A_J in pp and PbPb at 2.76 TeV from JEWEL	39
32	Missing- p_T as a function of A_J hybrid model	40
33	CMS detector perspective drawing	44
34	Diagram of CMS trackers	45
35	Diagram of the HCAL	46
36	Tracking efficiency correction example	52
37	Closure with and without JFF-JEC for quark and gluon jets.	57
38	Centrality distribution for PYTHIA+HYDJET reweighted to PbPb data.	61
39	Vertex z distribution for PYTHIA+HYDJET reweighted to PbPb data.	61
40	Vertex z distribution for PYTHIA reweighted to pp data.	62
41	Illustration of the pair-acceptance correction procedure	69

42	Illustration of the event decomposition procedure without $\Delta\phi$ fitting	70
43	Illustration of the event decomposition procedure with $\Delta\phi$ fitting	71
44	Jet fragmentation function bias corrections for particles with $1 < p_T^{\text{trk}} < 2$ GeV . . .	73
45	Jet fragmentation function bias corrections for particles with $2 < p_T^{\text{trk}} < 3$ GeV . . .	73
46	Jet fragmentation function bias corrections for particles with $3 < p_T^{\text{trk}} < 4$ GeV . . .	74
47	Jet fragmentation function bias corrections for particles with $4 < p_T^{\text{trk}} < 8$ GeV . . .	74
48	Integrated yield attributed to jet fragmentation function bias as a function of p_T^{trk} . .	75
49	Integrated yield attributed to jet fragmentation function bias as a function of centrality	75
50	Background fluctuation bias corrections for particles with $1 < p_T^{\text{trk}} < 2$ GeV	77
51	Background fluctuation bias corrections for particles with $2 < p_T^{\text{trk}} < 3$ GeV	77
52	Background fluctuation bias corrections for particles with $3 < p_T^{\text{trk}} < 4$ GeV	78
53	Background fluctuation bias corrections for particles with $4 < p_T^{\text{trk}} < 8$ GeV	78
54	Integrated yield attributed to background fluctuation bias as a function of p_T^{trk} . . .	79
55	Data-driven check of integrated yields attributed to background fluctuation bias . .	80
56	Data-driven check of correlated $\Delta\eta$ yields attributed to background fluctuation bias	81
57	Comparison of background selection bias effect for quark versus gluon jets	82
58	Inclusive jet $\Delta\eta$ correlations for tracks with $1 < p_T^{\text{trk}} < 2$ GeV at 2.76 TeV	88
59	Inclusive jet $\Delta\phi$ correlations for tracks with $1 < p_T^{\text{trk}} < 2$ GeV at 2.76 TeV	89
60	Inclusive jet $\Delta\eta$ correlations for tracks with $2 < p_T^{\text{trk}} < 3$ GeV at 2.76 TeV	90
61	Inclusive jet $\Delta\phi$ correlations for tracks with $2 < p_T^{\text{trk}} < 3$ GeV at 2.76 TeV	91
62	Inclusive jet $\Delta\eta$ correlations for tracks with $3 < p_T^{\text{trk}} < 4$ GeV at 2.76 TeV	92
63	Inclusive jet $\Delta\phi$ correlations for tracks with $3 < p_T^{\text{trk}} < 4$ GeV at 2.76 TeV	93
64	Inclusive jet $\Delta\eta$ correlations for tracks with $4 < p_T^{\text{trk}} < 8$ GeV at 2.76 TeV	94
65	Inclusive jet $\Delta\phi$ correlations for tracks with $4 < p_T^{\text{trk}} < 8$ GeV at 2.76 TeV	95
66	Inclusive jet $\Delta\eta$ correlations at 5.02 TeV	95
67	Inclusive jet $\Delta\phi$ correlations at 5.02 TeV	96
68	Inclusive jet distribution of charged particles as a function of Δr at 5.02 TeV	96
69	Integrated inclusive jet charged particle yields at 2.76 and 5.02 TeV	97
70	Dijet $\Delta\eta$ correlations for tracks with $1 < p_T^{\text{trk}} < 2$ GeV at 2.76 TeV	99
71	Dijet $\Delta\phi$ correlations for tracks with $1 < p_T^{\text{trk}} < 2$ GeV at 2.76 TeV	100
72	Integrated charged particle yields for inclusive, leading, and subleading jets	101
73	Leading jet $\Delta\eta$ correlation widths as a function of p_T^{trk} at 2.76 TeV	103
74	Leading jet $\Delta\phi$ correlation widths as a function of p_T^{trk} at 2.76 TeV	104
75	Subleading jet $\Delta\eta$ correlation widths as a function of p_T^{trk} at 2.76 TeV	105
76	Subleading jet $\Delta\phi$ correlation widths as a function of p_T^{trk} at 2.76 TeV	106
77	Inclusive jet shape at 5.02 TeV, shown differentially in p_T^{trk}	108
78	Leading jet shape at 2.76 TeV, shown differentially in p_T^{trk}	109
79	Subleading jet shape at 2.76 TeV, shown differentially in p_T^{trk}	110
80	Dijet subleading-to-leading hemisphere momentum balance for balanced dijets	113
81	Dijet subleading-to-leading hemisphere momentum balance for unbalanced dijets . .	114
82	Jet peak subleading-to-leading momentum balance for balanced dijets	115
83	Jet peak subleading-to-leading momentum balance for unbalanced dijets	116
84	long-range subleading-to-leading momentum balance for balanced dijets	118
85	long-range subleading-to-leading momentum balance for unbalanced dijets	119
86	Integrated transverse momentum in the long-range $\Delta\phi$ -correlated distribution as a function of track- p_T	120

87	Relative contributions from jet peaks and long-range asymmetry to the double difference PbPb–pp, subleading–leading in total hemisphere transverse momentum for central collisions	121
88	Relative contributions from jet peaks and long-range asymmetry to the double difference PbPb–pp, subleading–leading in total hemisphere transverse momentum for peripheral collisions	122
89	Comparison of leading and subleading jet shape measurements to the jet fluid model	124
90	Distribution of transverse momentum, pseudorapidity, and azimuthal distribution of all jet selections for Pythia data compared to PYTHIA simulation.	136
91	Transverse momentum distribution of all jet selections for PbPb data at 2.76 TeV compared to PYTHIA+HYDJET simulation.	137
92	Pseudorapidity distribution of all jet selections for PbPb data at 2.76 TeV compared to PYTHIA+HYDJET simulation.	138
93	Azimuthal angle distribution of all jet selections for PbPb data at 2.76 TeV compared to PYTHIA+HYDJET simulation for each collision centrality bin.	139
94	Distribution of pseudorapidity distribution of all jet selections for PbPb data compared to PYTHIA+HYDJET simulation for each collision centrality bin.	140
95	Transverse momentum distribution for PbPb data compared to PYTHIA+HYDJET simulation for each collision centrality bin.	140
96	Jet η distribution for PbPb data compared to PYTHIA+HYDJET simulation for each collision centrality bin.	140
97	Jet ϕ distribution for PbPb data compared to PYTHIA+HYDJET simulation for each collision centrality bin.	141
98	Jet p_T , η , and ϕ for all pp dijets and for pp dijets with A_J : $0 < A_J < 0.11$	142
99	Jet p_T , η , and ϕ for all pp dijets and for pp dijets with A_J : $0.11 < A_J < 0.22$	143
100	Jet p_T , η , and ϕ for all pp dijets and for pp dijets with A_J : $0.22 < A_J < 0.33$	144
101	Jet p_T , η , and ϕ for all pp dijets and for pp dijets with A_J : $A_J > 0.33$	145
102	Jet p_T , η , and ϕ for all PbPb dijets and for PbPb dijets with $0 < A_J < 0.11$	146
103	Jet p_T , η , and ϕ for all PbPb dijets and for PbPb dijets with $0.11 < A_J < 0.22$	147
104	Jet p_T , η , and ϕ for all PbPb dijets and for PbPb dijets with $0.22 < A_J < 0.33$	148
105	Jet p_T , η , and ϕ for all PbPb dijets and for PbPb dijets with $A_J > 0.33$	149
106	Dijet background fits (preliminary step)	150
107	Leading jet background fits	151
108	Subleading jet background fits	152
109	Inclusive jet background fits	153
110	Pair acceptance uncertainty determination	154
111	Background subtraction uncertainty determination	155
112	Width determination for PbPb leading jets	156
113	Width determination for pp leading jets	157
114	Width determination for PbPb subleading jets	158
115	Width determination for pp subleading jets	159

LIST OF ABBREVIATIONS

ADS/CFT	Anti-deSitter/Conformal Field Theory
AMY	Arnold-Moore-Yaffe
AMPT	A Multiphase Transport Model
ASW	Armesto-Salgado-Widemann
BDMPS-Z	Baier-Dokshitzer-Mueller-Peigné-Schiff-Zakharov
BNL	Brookhaven National Laboratory
CERN	Conseil Européen pour la Recherche Nucléaire
CMS	Compact Muon Solenoid
DGLAP	Dokshitzer-Gribov-Lipatov-Altarelli-Parisi
ECAL	Electromagnetic Calorimeter
E_T	Transverse Energy
GLV	Gyulassy-Lévai-Vitev
HCAL	Hadronic Calorimeter
HF	Hadronic Forward
HLT	High Level Trigger
HT-BW	Higher Twist Berkeley-Wuhan
HT-M	Higher Twist Majumder
JEC	Jet Energy Correction
JES	Jet Energy Scale
JFF	Jet Fragmentation Function
LBT	Linear Boltzman Transport
LHC	Large Hadron Collider
MC	Monte Carlo
PbPb	Lead-lead (collision data)
PDF	Parton Distribution Function
pPb	Proton-lead (collision data)
pp	Proton-proton (collision data)
pQCD	Perturbative Quantum Chromodynamics
p_T	Transverse Momentum
QCD	Quantum Chromodynamics
QGP	Quark Gluon Plasma
RHIC	Relativistic Heavy Ion Collider
SCET _G	Soft Collinear Effective Theory with Glauber Gluons
UE	Underlying Event
UrQMD	Ultrarelativistic Quantum Molecular Dynamics

SUMMARY

The quark gluon plasma (QGP), which is produced in heavy ion collisions, is a hot and dense medium consisting of quarks and gluons interacting via the strong force. In this analysis, the properties of the QGP are explored using correlations between jets with high transverse momentum (p_T) and charged hadrons in lead-lead (PbPb) and proton-proton (pp) collisions, using data collected with the CMS detector at collision energies $\sqrt{s_{NN}} = 2.76$ TeV and 5.02 TeV. High- p_T jets originate from partons produced in initial hard-scatterings in heavy ion collisions, and may be used as *in situ* probes as they subsequently pass through and interact with the QGP, losing energy in a phenomenon known as “jet quenching.” In this analysis two types of jet selections are considered: inclusive samples of jets with $p_T > 120$ GeV, and a sample of back-to-back dijets (with $p_{T,1} > 120$ GeV, $p_{T,2} > 50$ GeV, and $\Delta\phi_{1,2} > 5\pi/6$) that enable systematic studies of changes to dijet momentum balance in the presence of the medium. Correlations in relative pseudorapidity ($\Delta\eta$) and relative azimuth ($\Delta\phi$) are constructed between jets in each collision event and all charged tracks in the event, forming “jet-track correlations” in a number of different classes of associated-track p_T . These correlations are used to study jet properties, and to characterize changes to momentum distributions in dijet events.

Jet-track correlations are used to extract a number of different observables that can serve to constrain theoretical models of jet energy loss. These include the distributions of charged particles and of p_T in the event as a function of $\Delta\eta$, $\Delta\phi$, and radial distance from the jet axis $\Delta r = \sqrt{(\Delta\eta)^2 + (\Delta\phi)^2}$, as well as the jet transverse momentum profile (“jet shape”) $\rho(\Delta r)$. In order to evaluate these observables’ dependence on medium dynamics, results are studied differentially in event centrality, which parameterizes the degree of overlap between the two colliding nuclei. In these studies, an excess of low- p_T particles is observed in central (i.e. head-on) PbPb per-jet correlated hadron yields when compared to correlated yields in pp collisions, and this soft excess is found to remain correlated to the jet axis while extending to large relative angles $\Delta\eta = 1$ and $\Delta\phi = 1$. This observed redistribution from the mid- p_T (4-8 GeV) to low- p_T (1-3 GeV) sector and from small to larger angles from the jet axis may be theoretically interpreted via models of modified jet fragmentation in the medium and of possible hydrodynamic medium response to the propagating jet.

SUMMARY (CONTINUED)

In dijet studies, low- p_T excesses are observed for both leading and subleading jets (although larger for subleading jets), indicating that in the kinematic range studied here leading as well as subleading jets pass through and are quenched by the medium. Furthermore, in studies of the overall momentum balance in dijet events, the difference in transverse momentum contained in the gaussian-like jet peaks is found to only partially account for the total momentum redistribution in central PbPb events. Azimuthal asymmetry in the long-range correlated distribution of momentum under the jet peaks also contributes significantly to the overall modifications in subleading-to-leading momentum balance in PbPb compared to pp collisions, especially in asymmetric dijet events with relatively large differences in momenta between the leading and subleading jet p_T . In pp data, asymmetric dijets originate primarily from three-jet events, resulting in a substantial subleading-to-leading excess of mid- p_T tracks (with $p_T > 4$ GeV) in the long-range correlated distribution in the most central PbPb collisions. This subleading-to-leading mid- p_T excess is nearly absent in central PbPb events, indicating that the fraction of three-jet events in the sample of asymmetric dijets is significantly lower than in a selection of dijets from pp events with the same kinematics. In this long-range correlated distribution there is also a subleading-to-leading asymmetry in the low p_T tracks that can provide further input for the theory on the jet-medium coupling.

1 INTRODUCTION

The theory of quantum chromodynamics (QCD) describes the strong force interactions, mediated by gluons, that hold together quarks to form the protons, neutrons, and other hadrons that make up the everyday matter of the universe. Experimental particle physics probes the dynamics of the strong force using accelerators, including the Large Hadron Collider (LHC) at CERN, that collide hadrons at nearly the speed of light, producing hard-scatterings in which hadrons react violently to produce different particles. By colliding heavy ions (large nuclei such as lead-208 at the LHC) rather than individual hadrons in these accelerators, it is possible to induce sufficient density and temperature to produce a state of matter called the quark gluon plasma (QGP). These extreme conditions are rare; other than in modern accelerators, the only other known instance of the QGP occurred approximately one microsecond after the Big Bang, before the universe expanded and cooled to form hadrons. The QGP behaves as a near-perfect (i.e. low-viscosity) fluid composed of deconfined interacting quarks and gluons. Studying this novel state of matter offers opportunities to probe QCD in extreme conditions and thereby explore strong force dynamics and the QCD phase diagram.

The task of studying the quark gluon plasma is made challenging by the fact that it is produced only in high-energy colliders for lifetimes on the order of $10 \text{ fm}/c$ (10^{-22} seconds). One effective approach to this challenge is the use of *in situ* probes produced by hard-scatterings within the plasma: out-going partons from initial hadronic hard scatterings in heavy ion collisions pass through the medium before reaching the experimental detector, producing measurements that may be compared to the “vacuum-like” expectations derived from comparable proton-proton collisions. At the center-of-mass collision energies at the LHC, it is possible to focus these studies on partons that are distinguished by very large transverse momentum (momentum perpendicular to the beam direction, p_T) from most hadrons produced in the heavy ion event. Experimentally, we cannot directly measure these out-going partons, but only the particles they produce after undergoing hadronization. We may, however, reconstruct objects called “jets” formed by clustering energy deposited in the detector, that can approximate the parton energy. These reconstructed jets may serve as probes of the QGP by comparing jet measurements in PbPb and pp collisions.

One way in which the QGP may be probed with jets is via correlations between these jets and charged-hadron tracks, which offer the opportunities to characterize the event “from the perspective” of a parton propagating through the medium (in head-on PbPb collisions) compared to a parton propagating through the vacuum (in pp collisions). Through these correlations, we may probe the details of jet fragmentation (the process in which a parton radiates energy and hadronizes) and its modification in the presence of the QGP, and also study medium-induced changes to the transverse momentum profile of the jet. In addition to studying jet properties via correlations between jets and charged tracks, it is also possible to use back-to-back “dijet” events to characterize the overall distribution of momentum in the event with respect to the jet axes. The results reported here are obtained with jet-track correlation studies of PbPb and pp collisions, carried out with data collected at 2.76 TeV and 5.02 TeV by the CMS Collaboration. These studies provide experimental measurements that can distinguish between different models of jet energy loss in the medium as well as possible medium response to the propagating probe.

To motivate the studies reported here and provide a primer on the physics underlying these measurements, Sec. 2 discusses the properties of the quark gluon plasma, Sec. 3 provides an introduction to jet physics, and Sec. 4 summarizes a range of models of medium modifications to jets. The next several sections discuss the technicalities of measurements in CMS: Sec. 5 provides general information about the LHC and the CMS detector, and Secs. 6 and 7 discuss the processes of accurate reconstruction and correction of tracks and jets, respectively, that are crucial prerequisites for accurate jet-track correlation studies. Section 9 then discusses the details of how jet-track correlations are constructed, corrected, and analyzed. Finally, results and their implications for theoretical models are presented in Sec. 10.

2 THE QUARK GLUON PLASMA

2.1 Predictions and early evidence for the quark gluon plasma

The strength of the QCD interactions, described by the QCD coupling constant $\alpha_s(Q)$, decreases as distances between strongly interacting partons decreases and their exchanged momentum Q increases:

$$\alpha_s(Q) \propto \frac{1}{\ln(\frac{Q^2}{\Lambda_{QCD}^2})}, \quad (1)$$

where $\Lambda_{QCD} \approx 0.2$ GeV gives the QCD scale. Figure 1 shows the dependence of α_s on momentum scale Q . In the regime where separations between partons are relatively large (small Q), α_s is large, leading to the observed confinement of quarks and gluons in composite particles called hadrons, most commonly baryons (comprised of 3 quarks, including protons and neutrons) and mesons (comprised of 2 quarks). In the large Q regime, however—accessed via large baryon chemical potential μ_B or large temperature T —the strength of the coupling constant α_s decreases, in a phenomenon known as asymptotic freedom. Asymptotic freedom both permits the accurate approximation of high-energy hadron interactions using perturbation theory (pQCD), and implies the deconfinement of quarks and gluons. This phase of deconfined quarks and gluons, known as the quark gluon plasma (QGP), was originally conceived as a gas of color-charged quarks and gluons, analogous to the plasma of photons and electrons previously studied in quantum electrodynamics. In collider studies, this suggests the possibility of a phase transition anticipated between the hadron gas phase present under ordinary matter conditions, and the QGP phase present at sufficiently great μ_B or T [4, 5].

In the early 1980s, relativistic nuclear collisions were suggested as a means of producing sufficient temperatures and densities to induce a quark-gluon plasma and probe the transition between the QGP and ordinary matter. Efforts were also made to anticipate key experimental signatures of the short-lived possible QGP, relying in many cases on the anticipation that the QGP would behave according to a hydrodynamic description of a system in at least partial thermal equilibrium. Proposed signatures included enhancements of strange (heavy) quarks, unusual event structures, greater rates of direct dilepton and photon production [7]. The first heavy ion collisions began with fixed-target experiments at the Super Proton Synchrotron (SPS) at CERN in the mid-

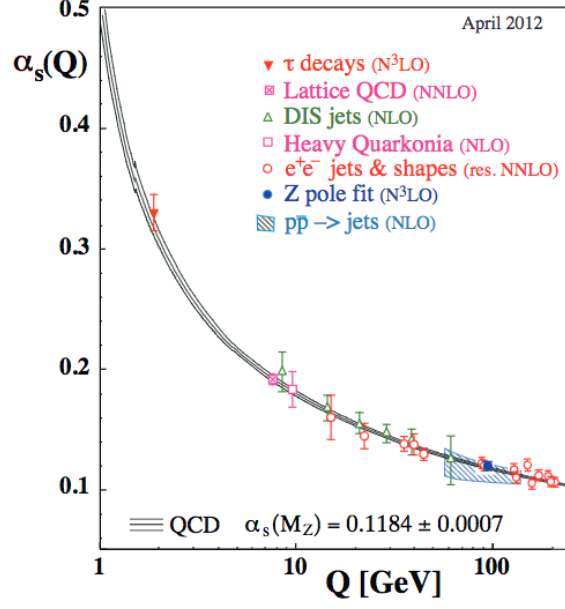


Figure 1. Momentum scale dependence of QCD coupling constant α_s , from Ref. [6].

1980s, colliding nuclei including gold and lead at energies from 40 GeV to 160 GeV through the 1990s. Analysis of the hadron yields in these collisions showed an apparent chemical equilibrium of quarks and gluons at about 170 MeV and enhancement (as anticipated) both of strangeness (via kaon/pion ratios, and J/ψ production rates). In the early 2000, a CERN press release cited these results in declaring that “a common assessment of the collected data leads us to believe that a new state of matter has indeed been created...[that] features many of the characteristics of the theoretically predicted quark-gluon plasma” [8].

Shortly after the SPS announcement, the first gold-gold collisions began at the Relativistic Heavy Ion Collider (RHIC) at Brookhaven National Laboratory, beginning an era of high-energy heavy ion collisions that would later be complimented by a parallel program at the Large Hadron Collider at CERN. Through data collection and analysis by experiments at each of these colliders over the ensuing nearly two decades, the field has gradually shifted from searches for signatures of QGP formation in heavy ion collisions, to detailed characterizations of its properties and evolution. In 2005, the four experimental collaborations at RHIC (BRAHMS, PHENIX, PHOBOS, and STAR) published coordinated white papers [9, 10, 11, 12] summarizing the assembled evidence that results from gold-gold collisions could not be explained by models of ordinary hadronic matter—

most notably in signatures of collective behavior (see Sec. 2.6) and in suppression of particles with relatively high transverse momentum (see Sec. 3). Beginning in 2010, heavy ion studies at the LHC by the ALICE, ATLAS, and CMS Collaborations (and more recently by the LHCb Collaboration) have complimented the RHIC access to a wide range of center-of-mass-energies in the 7.7 GeV to 200 GeV range with measurements at 2.76 TeV and 5.02 TeV.

2.2 Thermodynamics of the quark gluon plasma

The existence of a plasma phase of hadronic matter and a number of the properties of this phase can also be inferred directly from thermodynamic considerations of hadronic matter. In free space, the density of states of hadrons as a function of resonance mass m increases exponentially, following the Hagedorn spectrum

$$\rho(m) = m^{\frac{5}{2}} e^{\frac{m}{T_0}}, \quad (2)$$

where $T_0 \approx m_\pi \approx 140$ MeV. [13, 14]. When taking into account the finite size of hadrons (with radii on the order of 1 fm), this suggests an upper limit or critical temperature $T_c \approx 150 - 200$ MeV above which quark and gluon deconfinement occurs. The pressure and energy density of this plasma phase are both, to first order in the ideal gas, proportional to T^4 , with higher order corrections introduced by the non-zero effective (“thermal”) quark and gluon masses. Defining a color-dependent constant c and a “bag pressure” B (named after the MIT model of hadrons as “bags” of quarks and gluons) that takes into account the difference between quark and gluon ground states and the vacuum, pressure may be expressed to first order as:

$$P = cT^4 - B, \quad (3)$$

and energy density ϵ may be expressed to first order as:

$$\epsilon = 3cT^4 + B. \quad (4)$$

Interaction effects due differences between the ground state and the vacuum may be captured by “interaction measure” $\Delta = (\epsilon - 3P)/T^4$. Lattice QCD studies show a sharp rise in energy density

from the low-density hadronic state at the critical temperature T_c , saturating to constant values at larger T . These values are about 10% less than those expected for an ideal massless gas due to the higher order thermal mass corrections. The interaction measure remains non-zero above T_c , indicative of differences between the vacuum and the QCD ground state or possibly of color resonance states in the QGP. [14, 15]

Figure 2 gives a schematic illustration of the QCD phase diagram as a function of baryon chemical potential and temperature based on thermodynamic considerations and lattice QCD studies. While chiral symmetry is spontaneously broken for non-zero quark masses, asymptotic freedom implies chiral symmetry at sufficiently large temperatures and a phase transition between the two (hadronic and quark gluon plasma) phases, which is first-order at sufficiently large μ_B with singularities in thermodynamic functions. Below a certain critical point value of μ_B (and at critical temperature T_c), however, the transition is a cross-over without singular behavior, and lattice QCD simulations have demonstrated such cross-over behavior for the limit $\mu_B = 0$. This suggests the existence of a tricritical point on the phase boundary between confined and deconfined QCD phases. [14, 15, 16] The beam energy scan program at RHIC probes center-of-mass energies ranging from 7.2 to 200 GeV to probe temperatures around the predicted values for T_c ; at LHC energies 2.76 TeV and 5.5 TeV initial QGP temperatures are estimated in the 300 - 700 MeV range, well above the critical temperature. [17]

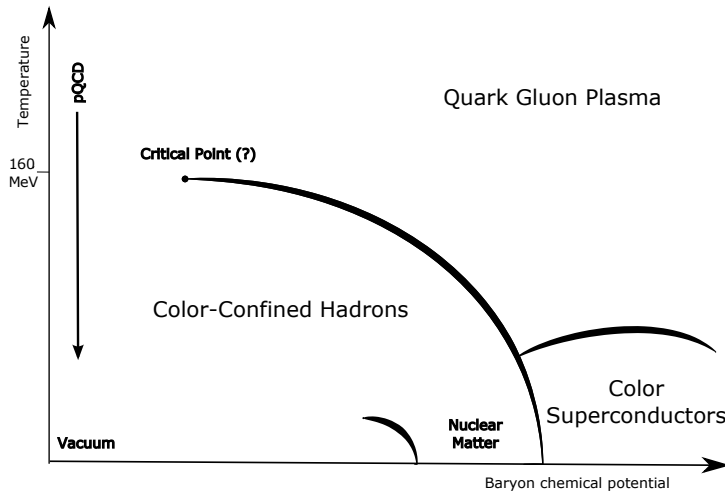


Figure 2. Schematic phase diagram of strongly interacting matter as a function of baryon chemical potential μ_B and temperature T .

2.3 Time-evolution of heavy ion collisions

Connecting predictions and simulations of QGP behavior to experimental results requires the description and analysis of several different sequential phases of heavy ion collisions [14, 18]:

1. **Initial state** – Nuclei A and B (lorentz-contracted into two flat discs) approach each other with impact parameter b and nucleon distributions $\rho A(r)$ and $\rho B(r)$, establishing a set of initial conditions with implications for the later evolution of the medium.
2. **Pre-equilibrium** – Initially after nuclei collide (before thermalization time τ_0), nucleons interact dynamically as the QGP begins to form. Various models – including IP-Glasma, A Multiphase Transport Model (AMPT), Ultrarelativistic Quantum Molecular Dynamics (UrQMD), and models based on the Anti-deSitter/Conformal Field Theory (ADS/CFT) correspondence – attempt to capture these dynamics.
3. **Hydrodynamic expansion** – After thermalization time τ_0 local thermodynamic equilibrium is achieved, producing an expanding medium whose properties can be described with ideal fluid dynamics with sheer viscosity to energy-density ratio $\eta/s \approx 1.6$ at RHIC and the LHC [19].
4. **Hadronization (“freeze-out”)** – Quarks and gluons recombine into hadrons in the phase transition back from deconfined to confined QCD matter. As the medium expands, it reaches sufficiently low densities and temperatures that thermal equilibrium is lost, and quark and gluon recombination stops. Chemical freeze-out occurs when particle number changing processes end; kinetic freeze-out occurs later, when the ratio of the expansion rate to the collision rate among particles drops to the point that collisions no longer occur.
5. **Free-streaming** – recombined hadrons move through the beam pipe vacuum and are measured by the detector. Experimental results can only directly access these final distributions of particles, from which inferences are made about the other collision stages.

Each stage of this QGP time evolution may be accessed via various experimental observables. Vacuum-like hadronization is well-modeled by parton shower simulations in Monte Carlo generators such as PYTHIA and HERWIG that capture proton-proton collision dynamics. Heavy ion colli-

sions, however, present the challenge of defining a freeze-out hypersurface at which hydrodynamic evolution terminates, and hadronization begins. This hypersurface occurs at the phase transition boundary, and may be experimentally accessed via the yields of hadron species in the final state (as particle numbers do not change during the free-streaming stage) [14]. Initial collision geometry may be described via Glauber Models and nuclear parton distribution functions (PDFs) of the incoming partons, as discussed in Sec. 2.4. Signatures of initial collision anisotropy and collective hydrodynamic evolution may be observed as “collective flow” via particle correlations (Sec. 2.6). Pre-equilibrium dynamics are particularly difficult to access, but probes including the medium modifications to high- p_T jets presented in this analysis provide possibilities for distinguishing between the different theoretical models.

2.4 Characterizing collision geometry and event centrality

In heavy ion events there is a wide range of possible collision geometries: at one extreme the nuclei may collide head-on (referred to as a “central” collision, with impact parameter $b = 0$), while at the other they may barely graze each other (referred to as a “peripheral” collision). The initial geometry, size, and evolution of the QGP formed in these events may vary considerably based on these initial collisions. At the most basic level, events may vary in both the number of participating nucleons (N_{part}), and in the number of binary nucleon-nucleon collisions (N_{coll}) occurring in the event. While it is not possible to directly measure b , N_{part} , or N_{coll} in a heavy ion experiment, it is possible to measure the total energy deposited in calorimeters at very forward rapidities along the beam line direction. The total energy deposited in these forward calorimeters is directly related to the number of “spectator” nucleons that do not collide in the event, and therefore inversely related to N_{part} . By dividing the total experimental event sample into “centrality classes” (ranging from 0% “most central” to 100% “most peripheral”) by total energy deposited at forward rapidity and mapping this classification to a simulated sample, it is possible to map events to Monte Carlo simulation and extract mean values for N_{part} and N_{coll} [20].

Glauber Models allow for the characterization of event parameters based on modeling of collision geometry. In the simplest “optical limit” of such models, it is assumed that individual nucleons accelerated to very high momenta move relatively independently and linearly, and deflection and shadowing effects are neglected. These assumptions reduce the problem to one of only

collision geometry, take the inelastic nucleon-nucleon cross-section $\sigma_{NN}^{\text{inel}}$ and the density of nucleons in each colliding nucleus $\rho A(r)$ and $\rho B(r)$ to calculate a “nuclear overlap function” T_{AB} , defined as:

$$T_{AB} = \int d^2\vec{s} \int dz_A \rho A(\vec{s}, z_A) \int dz_B \rho B(\vec{s} - \vec{b}, z_B), \quad (5)$$

where the integrals $\int dz_A \rho A(\vec{s}, z_A)$ and $\int dz_B \rho B(\vec{s} - \vec{b}, z_B)$ define the probability of finding a nucleon at locations (\vec{s}, z_A) and $(\vec{s} - \vec{b}, z_B)$, respectively with the geometry shown in Fig. 3.

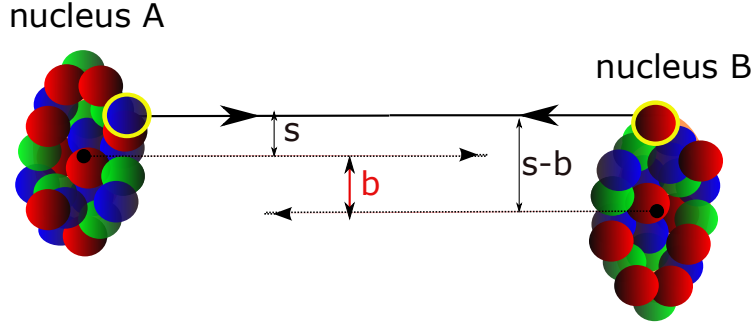


Figure 3. Schematic illustration of Glauber Model geometry for a nucleus-nucleus collision, showing impact parameter \vec{b} between the two nuclei and locations of two representative colliding nuclei.

The resulting total number of collisions is then given by:

$$N_{\text{coll}}(b) = \sigma_{NN}^{\text{inel}} T_{AB}(b). \quad (6)$$

For example for minimum bias collisions at LHC energy 2.76 TeV $\sigma_{NN} = 65$ mb, $\sigma_{\text{PbPb}} = 7660$ mb, $\langle T_{\text{PbPb}} \rangle = \int d^2b T_{\text{PbPb}} / \int d^2b = 5.65 \text{ mb}^{-1}$, and $\langle N_{\text{coll}}(b) \rangle = 367$ [20, 21]. The optical limit calculations described above are able to reasonably capture collision parameters, but are limited by their neglect of effects including nuclear shadowing and diffraction. Glauber Monte Carlo simulations are able to re-introduce some of these effects, thereby better capturing the nuclear cross section [20, 22].

2.5 Kinematic variables and coordinates

In high-energy colliders the z axis is defined parallel to the colliding beams, with x and y axes spanning a transverse plane perpendicular to the beam axis. Because the colliding nuclei are accelerated to nearly the speed of light, it is necessary to use relativistic coordinates starting from the energy-momentum relationship:

$$E^2 = p_x^2 c^2 + p_y^2 c^2 + p_z^2 c^2 + M^2 c^4 \quad (7)$$

for a particle with rest mass M . The azimuthal coordinate in the transverse plane is then simply given by:

$$\phi = \tan^{-1} \left(\frac{p_y}{p_x} \right) \quad (8)$$

With incoming particles colliding with very large p_z , the outgoing direction of collision products is characterized by their rapidity y , a generalization of velocity defined by:

$$y = \ln \sqrt{\frac{E + p_z c}{E - p_z c}}, \quad (9)$$

The rapidity is defined such that particles which emerge perpendicular to the beam axis (with $p_z = 0$) have $y = 0$, while $y \rightarrow \infty$ toward the beam line. In practice, however, the outgoing particle's rest mass M and energy E are generally unknown, while the total momentum \vec{p} can be measured in detectors. In ultrarelativistic collisions, where $\vec{p}^2 \gg M^2 c^2$, we instead measure the pseudorapidity η defined by:

$$\eta = \ln \left(\frac{|\vec{p}| + p_z}{|\vec{p}| - p_z} \right) \quad (10)$$

Pseudorapidity may also be calculated from the polar angle θ with respect to the beam pipe,

$$\eta = -\ln \left(\tan \left(\frac{\theta}{2} \right) \right) \quad (11)$$

As is clear from this representation, particles perpendicular to the beampipe with $\theta = \pi/2$ correspond to rapidity $\eta = 0$, while particles with $\theta = \pi/4$ correspond to $\eta \approx 0.88$.

In general throughout this document, energies and measurements are presented in natural units with $\hbar = c = 1$ (momenta, for example, are given in MeV or GeV rather than MeV/c or GeV/c). Azimuthal angle ϕ is measured in radians.

2.6 Collective behavior in the QGP

In any nucleus-nucleus collision, the initial collision region will exhibit some azimuthal anisotropy—both due to the elliptical overlap region for collisions with impact parameter $b > 0$, and due to local variations in the nuclear densities ρA and ρB . As the medium thermalizes and hydrodynamically expands, this spatial anisotropy translates into anisotropy in momentum space or “collective flow” of the expanding medium. This correlation is retained through the hadronization and free-streaming phases, and is ultimately detectable via modulation in the distribution of particles with respect to the reaction plane (ψ_{RP} , the plane spanned by the impact parameter \vec{b} and the beam direction). This may be expanded in a Fourier series,

$$\frac{dN}{d\phi} = \frac{N}{2\pi} \left(1 + 2\sum_n v_n \cos(n(\phi - \psi_{RP})) \right), \quad (12)$$

using Fourier coefficients v_1, v_2, v_3 , etc. (sometimes referred to as “harmonic flow coefficients”) to model the $\Delta\phi$ correlation between particles and the reaction plane. These coefficients may be interpreted as corresponding to different geometric anisotropies in the initial state: v_1 refers to “directed flow” which arises as colliding nucleons are repelled perpendicular to the beam direction in the reaction plane. Elliptic flow coefficient v_2 refers to the elliptical anisotropy arising from the overlap of two roughly circular nuclei, while v_3 (“triangular flow”) and higher coefficients refer to more complex initial geometries arising from fluctuations in the nucleon densities [23].

The azimuthal direction of the reaction plane ψ_{RP} cannot be directly experimentally measured, but may be estimated based on event-by-event particle distributions in the detector. Alternatively, flow may be measured by considering two-particle correlations measuring $\Delta\phi_{\text{trig,assoc}}$ between trigger and associated particles. In this case, the Fourier decomposition of the $\Delta\phi_{\text{trig,assoc}}$ distribution becomes

$$\frac{1}{N_{\text{trig}}} \frac{dN^{\text{pair}}}{d\Delta\phi_{\text{trig,assoc}}} = \frac{N_{\text{assoc}}}{2\pi} \left(1 + 2\sum_n V_n \cos(n(\Delta\phi_{\text{trig,assoc}})) \right), \quad (13)$$

Here the combined flow coefficients V_n are found to be factorizable into coefficients for the trigger and associated hadrons, i.e. $V_n = v_{n,\text{trig}} \times v_{n,\text{assoc}}$ [24, 25]. To measure collective flow through this two-particle method, two dimensional correlations in $\Delta\eta - \Delta\phi$ are constructed between trigger and associated hadrons, as shown in Fig. 4 from CMS study [25]. These distributions are projected over the large $\Delta\eta$ region (in this case $|\Delta\eta| < 2$ to capture long range correlations, and are fit in $\Delta\phi$ with the Fourier function shown above to extract flow coefficients V_1 , V_2 , and V_3 , from which v_1 , v_2 , and v_3 may be calculated. These studies find centrality- and p_T -dependent flow coefficients through v_3 , with v_3 present substantially smaller than v_2 . As expected from simple geometrical considerations, values of v_2 and v_3 are greatest for mid-central collisions in which collision anisotropy is greatest, and peak as a function of p_T in the 2-3 GeV range, as shown in Fig. 6.

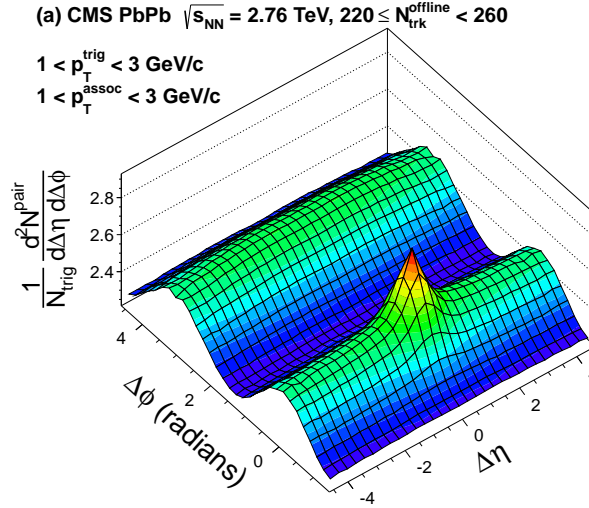


Figure 4. Illustration of dihadron correlation in $\Delta\eta - \Delta\phi$ for $1 < p_T^{\text{trig}} < 3$ GeV and $1 < p_T^{\text{assoc}} < 3$ GeV in central PbPb collisions at 2.76 TeV from Ref. [25]

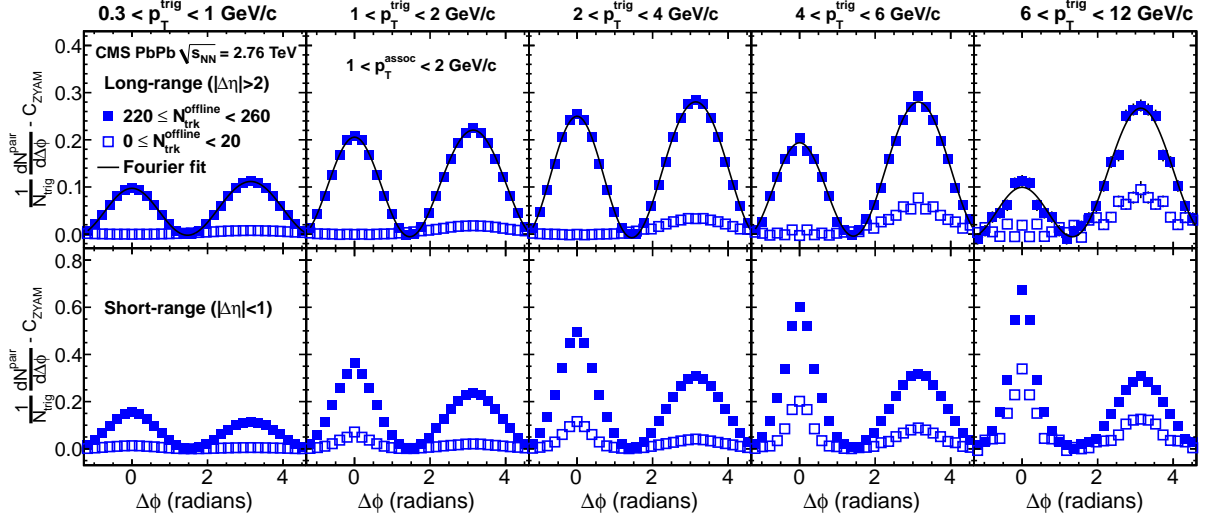


Figure 5. Fourier fits to dihadron $\Delta\phi$ distributions for $1 < p_T^{\text{assoc}} < 2$ GeV as a function of p_T^{trig} in central PbPb collisions at 2.76 TeV from Ref. [25]

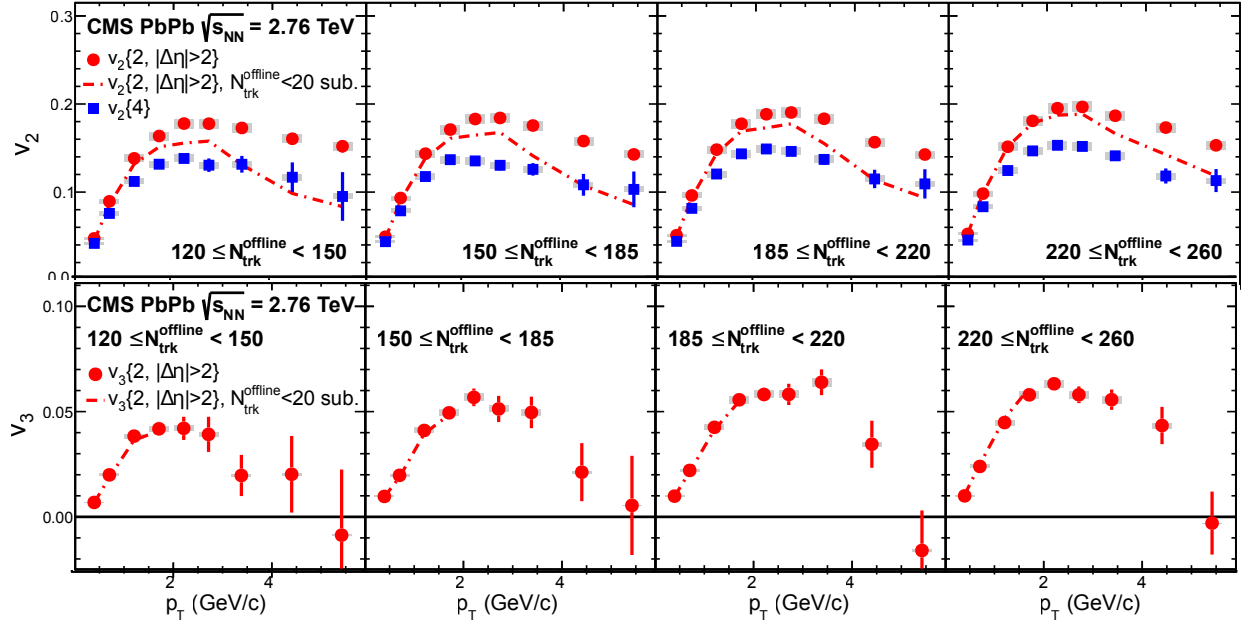


Figure 6. Flow coefficients v_2 and v_3 by centrality and p_T at 2.76 TeV from Ref. [25]

3 JETS AS PROBES OF THE QUARK GLUON PLASMA

Hard scatterings in heavy ion collisions can provide powerful probes of the quark gluon plasma. Because of asymptotic freedom, high-energy parton-parton processes can be accurately characterized via pQCD, and have been thoroughly studied experimentally in hadron-hadron collisions. In heavy ion collisions, the initial parton-parton interaction should by causality behave the same as a parton-parton interaction in hadron-hadron collisions. After the collision, however, outgoing partons traverse the quark gluon plasma, providing the opportunity to study medium properties by comparing heavy ion results to expectations inferred from hadron-hadron “vacuum” reference data. These studies are facilitated by the “factorization theorem” in pQCD, which states that the cross section $\sigma_{AB \rightarrow h}^{\text{hard}}$ of hadron h produced in the hard process $A + B \rightarrow h$ can be decomposed into contributions from:

- The perturbative cross section of the parton hard scattering $\sigma_{ab \rightarrow c}^{\text{hard}}$
- The initial parton distribution functions (PDFs) of partons in the colliding nuclei A and B ($f_{a/A}$ and $f_{b/B}$ for partons of flavor a and b)
- The fragmentation function $\mathcal{D}_{c \rightarrow h}$ describing the probability that parton c fragments into hadron h with momentum fraction $z = p_h/p_c$

The total cross section may be represented, schematically, as:

$$d\sigma_{AB \rightarrow h}^{\text{hard}} = f_{a/A}(x_a, Q^2) f_{b/B}(x_b, Q^2) \times d\sigma_{ab \rightarrow c}^{\text{hard}}(x_a, x_b, Q^2) \times \mathcal{D}_{c \rightarrow h}(z, Q^2), \quad (14)$$

Each contribution to $d\sigma_{AB \rightarrow h}$ can be experimentally determined, and in hadron-hadron collisions $\sigma_{ab \rightarrow c}^{\text{hard}}$, fragmentation functions, and PDFs should each be universal. Figure 7 illustrates this factorization for hard-scattering interaction $A + B \rightarrow h$. The final state parton branching is given by the Dokshitzer-Gribov-Lipatov-Altarelli-Parisi (DGLAP) equations that encode the QCD radiation probabilities for a parton propagating in the vacuum.

The partonic cross section $\sigma_{ab \rightarrow c}^{\text{hard}}$ furthermore should not, by causality, depend on the presence or absence of the QGP. Medium modifications may enter at two phases in this process: first, via energy loss by parton c passing through the medium, and second via possible medium-induced

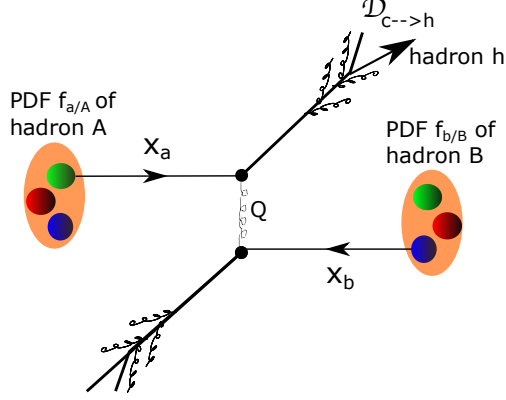


Figure 7. Illustration of the QCD hard-scattering $A + B \rightarrow h$.

changes to fragmentation functions $\mathcal{D}_{c \rightarrow h}$. Parton energy loss is attributed to two primary mechanisms: collisional energy loss from scatterings with partons in the medium, and medium induced radiation roughly analogous to electromagnetic ionization in a medium [26, 27]. This medium-induced parton energy loss implies an observable reduction of medium properties can also be further probed by comparing measurements of jet substructure in heavy ion collisions compared to pp reference data (Sec. 3.2), and by studying modifications to p_T balance in back-to-back dijet events (Sec. 3.3).

3.1 Measuring suppression of high- p_T particles and jets

One observable to probe parton energy loss in the medium is to compare yields of both particles with relatively high transverse momentum (p_T), and of reconstructed jets (collections of particles clustered in an effort to reconstruct the original parton energy – see Sec. 7). This reduction in jet yields compared to expectations from “vacuum” reference or scaled binary collisions can be studied as both a signature of the presence of the QGP, and an observable to distinguish between models of interactions within the QGP (see Sec. 3.1).

Since by pQCD factorization the partonic cross-section $\sigma_{ab \rightarrow c}$ should be independent, in the absence of the quark gluon plasma, the nuclear inclusive cross section would be expected to scale with the number of participating nucleons, i.e.

$$d\sigma_{AB \rightarrow h}^{\text{hard}}(b) = \langle T_{AB}(b) \rangle \sigma_{pp}^{\text{hard}} \quad (15)$$

where $T_{AB}(b)$ parameterizes the probability of nucleon-nucleon interactions for a given impact parameter for nuclei A and B colliding with impact parameter b as discussed in Sec. 2.4. A comparison of actual hadron (or jet) yields compared to this expectation can therefore give information about parton interactions with the medium, as characterized by the nuclear modification factor R_{AA} defined as the ratio of the observed yield in heavy ion data to the expectation from binary scaled pp data:

$$R_{AA}(p_T, \eta) = \frac{d^2\sigma_{AA}/dp_T d\eta}{\langle T_{AB}(b) \rangle d^2\sigma_{pp}/dp_T d\eta} \quad (16)$$

Consistent with quenching expectations, RHIC measurements of R_{AA} in gold-gold collisions showed substantial suppression of a factor of 70-80% for $p_T > 4$ GeV [9, 10, 11, 12]. Comparisons of RHIC measurements to early LHC results showed similar qualitative features, but greater suppression at low- p_T at the LHC, despite the more slowly falling pp spectrum at the LHC, as shown in Fig. 8. Measurements at the LHC have also found that R_{AA} rises with p_T for charged particles with $p_T > 7$ GeV, and have shown no significant center-of-mass energy differences when comparing R_{AA} at 2.76 TeV and 5.02 TeV, as shown in Fig. 9. The p_T dependence of R_{AA} is generally driven by three factors: the kinematic constraints on jet energy loss (model-specific details will be discussed in Sec. 4), the fact that R_{AA} takes the ratio of two steeply falling spectra the scattered partons, one shifted by energy loss and one un-shifted, and the effects of nuclear shadowing and anti-shadowing in the nuclear PDFs [27, 28].

Studies of high- p_T tracks make use of the fact that such tracks are likely to originate from outgoing partons in hard-scattering interactions, providing an indirect look at energy loss by the parton used as a probe of the QGP. To more directly reconstruct parton energy, we may instead consider reconstructed jets, defined as the collection of (spatially grouped) particles resulting from the fragmentation of a high- p_T quark or gluon. Jet reconstruction, described in detail in Sec. 7, groups detector deposits to reconstruct a jet energy, and uses Monte Carlo simulation to reconstruct a “true” jet energy of the original parton. Quenching studies with reconstructed jets therefore can offer a more direct look at energy loss in the medium by comparing measured energy in jets in heavy ion collisions to those in proton-proton collisions. Measurements of jet R_{AA} at the LHC

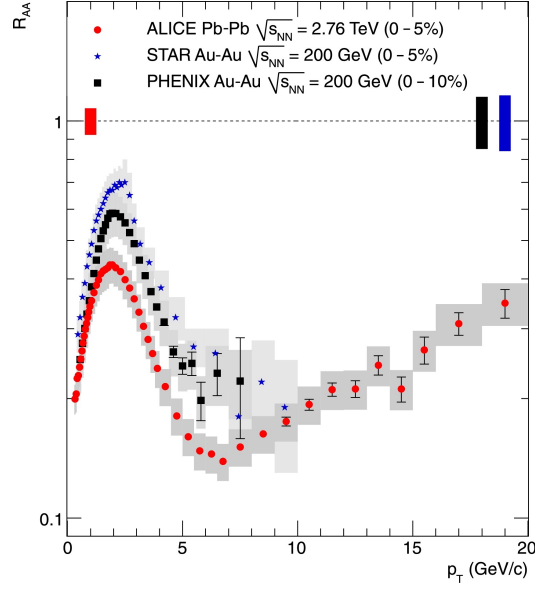


Figure 8. Measurements of charged particle R_{AA} from the STAR and PHENIX Collaborations at 200 GeV at RHIC, compared to ALICE results from the LHC at 2.76 TeV from Ref. [29].

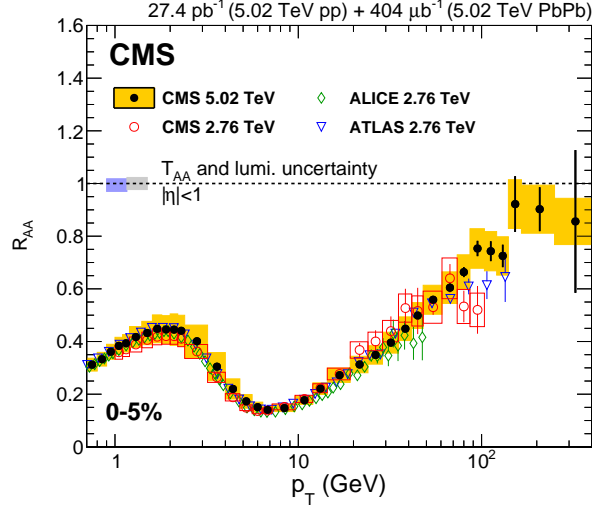


Figure 9. Measurements of charged particle R_{AA} at LHC energies 2.76 TeV and 5.02 TeV from Ref. [30].

reported in Refs. [31, 32] show suppression by a factor of approximately 40-60% in most central PbPb collisions, with weak dependence on jet p_T as shown in Fig. 10.

Jet R_{AA} measurements capture parton energy loss by measuring the reduction in yields in the presence of the QGP. To connect jet R_{AA} to charged particle R_{AA} measurements, it is necessary

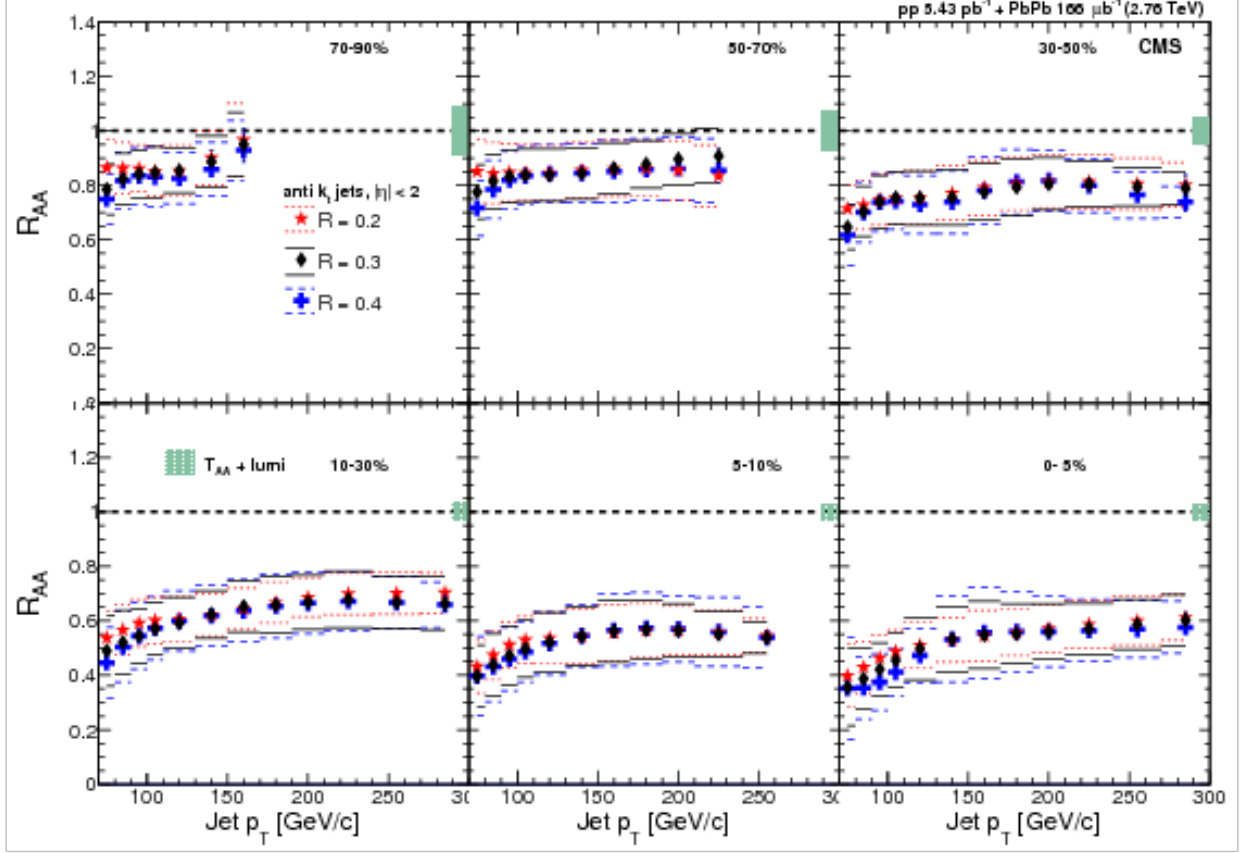


Figure 10. Jet R_{AA} at 2.76 TeV from Ref. [32].

to also consider trends in jet fragmentation patterns with jet- p_T . High- p_T jets are more likely to originate from quarks than from gluons, and therefore exhibit “harder” fragmentation patterns—i.e. higher- p_T jets fragment into relatively fewer particles each with more p_T compared to jets at lower- p_T . Jets with softer fragmentation are also expected to exhibit greater modification in the QGP, as low- p_T fragmentation products rescatter in the medium. The highest- p_T tracks, for which R_{AA} is the smallest, are associated with those jets that have not only the highest- p_T , but also the hardest fragmentation. The high- p_T sector of jet R_{AA} measurements at LHC energies, however, still includes significant contributions from jets reconstructed from softer particles that exhibit significant suppression.

3.2 Jet fragmentation function and jet shape measurements

Measurements of jet R_{AA} quantify the overall reduction in numbers of high- p_T jets passing a certain momentum threshold, providing an indication of the magnitude of jet energy loss in different p_T regions. As discussed above, this measurement can constrain the possible mechanisms of jet energy loss. To further constrain models of jet energy loss, additional observables aim to capture the details of jet fragmentation and its modification in the quark gluon plasma. One such measurement is the jet fragmentation function, which captures the p_T distribution of tracks carrying jet momentum, parameterized via the variables z and ζ :

$$z = \frac{p_{||}^{\text{track}}}{p_{||}^{\text{jet}}}, \zeta = \frac{1}{\ln(z)}, \quad (17)$$

where $p_{||}^{\text{track}}$ refers to the component of the track p_T along the jet axis. Jet fragmentation function measurements from CMS shown in Fig. 11 show a centrality-dependent modification to fragmentation function in PbPb relative to pp data, with a depletion in the mid- ζ range, balanced by an enhancement at large ζ , in the region corresponding to low- p_T tracks. This shows a redistribution of energy within the jet cone toward softer particle production in the presence of the medium, consistent with predictions of parton energy loss corresponding to a suppression of high- p_T particles (model details will be discussed in Sec. 4).

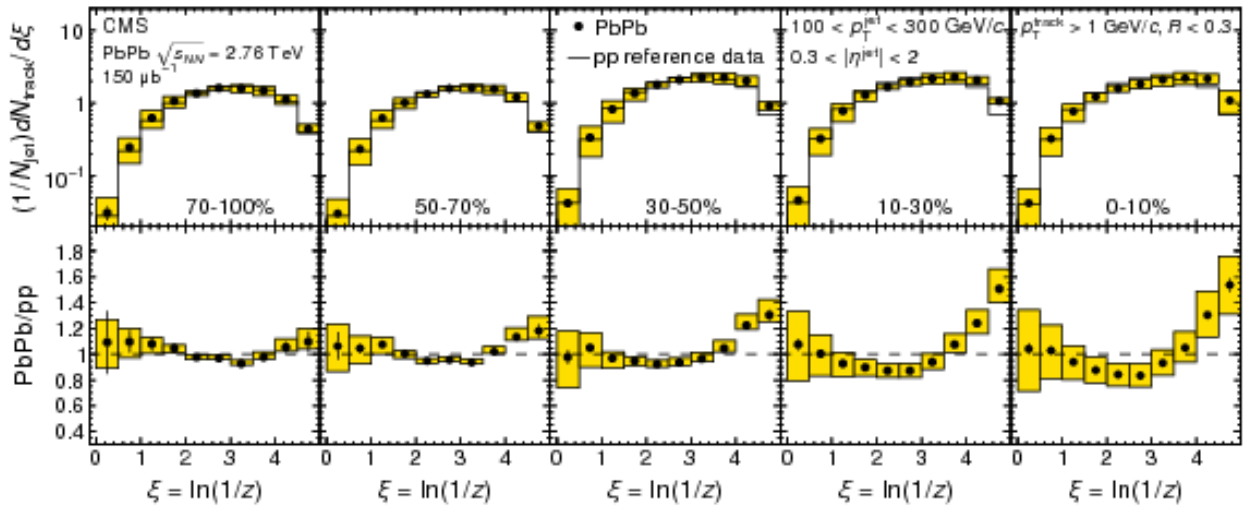


Figure 11. Jet fragmentation function for jets with $100 < p_T < 300$ GeV in 2.76 TeV PbPb and pp data from Ref. [33].

In addition to characterizing the p_T spectrum of jet constituents, the distribution of p_T with respect to the jet axis can also help to constrain fragmentation scenarios. This distribution, known as the jet shape, is defined within the jet cone as:

$$\rho(\Delta r) = \frac{1}{\delta r} \frac{1}{N^{\text{jet}}} \sum_{\text{jets}} \frac{\sum_{\text{tracks} \in [r_a, r_b]} p_T^{\text{track}}}{p_T^{\text{jet}}}, \quad (18)$$

where r_a and r_b correspond to the inner and outer radii, respectively, of an annulus of width $\delta r = 0.5$ around the jet axis. The first jet shape measurement from CMS, shown in Fig. 12 (measured with particles with $p_T > 1$ GeV), shows a spatial redistribution of energy from small radii ($\Delta r \approx 0.1$) to larger radii ($\Delta r > 0.2$) from the jet axis. This is qualitatively consistent with predictions of energy redistribution into particles that are both relatively soft ($p_T < 3$ GeV, as observed in jet fragmentation function measurements), and recovered at relatively large angles from the jet axis. In this way, the study of jet shape modifications *within* the jet cone motivate extension of these measurements to larger angles from the jet axis to quantify the distribution and p_T composition of particles at angles larger than $\Delta r = 0.3$.

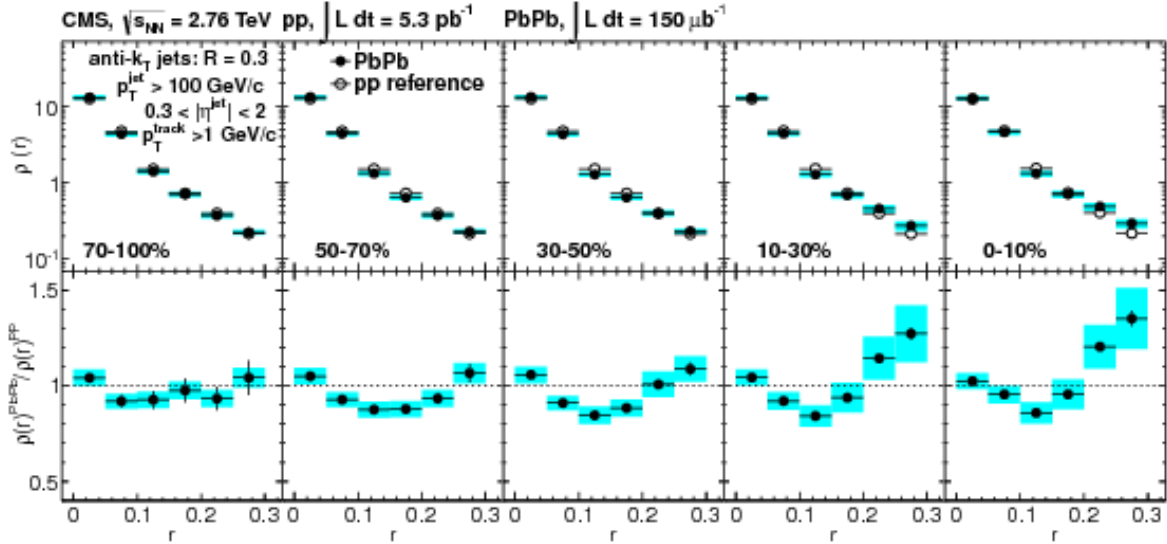


Figure 12. Jet shape measurement in 2.76 TeV PbPb and pp data from Ref. [34].

3.3 Dijet asymmetry and momentum balance studies

Additional possibilities for exploration of medium properties follow from the consideration of “dijets,” jets that are back-to-back in azimuthal angle ($\Delta\phi_{\text{jets}} \approx \pi$). As the incoming collision participants each begin with $p_T \approx 0$ GeV, the total p_T of outgoing partons immediately after the collision must also be 0. If both partons experience either no energy loss (as in the vacuum) or approximately equal energy loss (i.e. by experiencing roughly equal path-lengths through the medium), the measured p_T of each jet in the dijet pair would be approximately equal. If, however, the hard-scattering occurs toward the surface of the QGP, the jet with a longer path-length through the medium might be expected to experience substantially more energy loss, leading to a p_T asymmetry in the dijet pair as illustrated in Fig. 13. This expectation was probed via studies of di-hadron correlations with high- p_T particle triggers ($4 < p_T < 6$ GeV by STAR at RHIC, $8 < p_T < 15$ GeV by ALICE at the LHC) showed results consistent with the expectation. These studies showed the substantial suppression (even disappearance, in the STAR studies) of yields of particles with $p_T > 2$ GeV in the region opposite the trigger hadron in azimuth [35, 36], consistent with path-length dependent jet quenching and a surface bias in trigger particles.

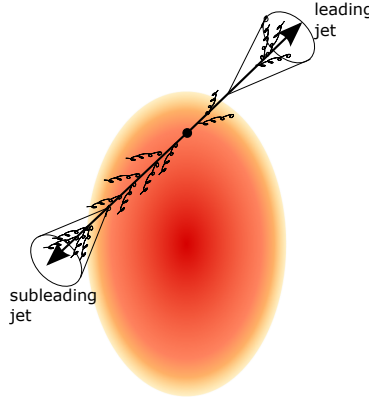


Figure 13. A “back-to-back” pair of dijets separated by $\Delta\phi = \pi$, with a highest- p_T leading jet experiencing less quenching in the medium, and a more-quenched subleading jet with a longer path length through the medium.

The large kinematic reach of hard probes at the LHC allows for dijet studies at much higher p_T . The first of these studies measured the “dijet imbalance” between the highest- p_T (“leading

jet,” with $p_{T,1}$) and second-highest- p_T jets (“subleading jet,” with $p_{T,2}$ in the event, parameterized as:

$$A_J = \frac{p_{T,1} - p_{T,2}}{p_{T,1} + p_{T,2}} \quad (19)$$

These studies, by the ATLAS and CMS Collaborations [37, 38] showed a centrality-dependent shift in the A_J in PbPb collisions, with greater dijet asymmetry in central PbPb data than in pp or in peripheral PbPb collisions. In pp and peripheral PbPb collisions, asymmetric dijet events are those in which some p_T is carried by a third jet, and the A_J distribution is steeply falling. In central PbPb collisions, however, there are expected to be two contributions to the sample of asymmetric dijet events: not only three-jet events, but also dijet events in which the subleading jet is substantially quenched. As shown Fig. 14, this effect is evident in the shift toward larger values of A_J in central PbPb collisions.

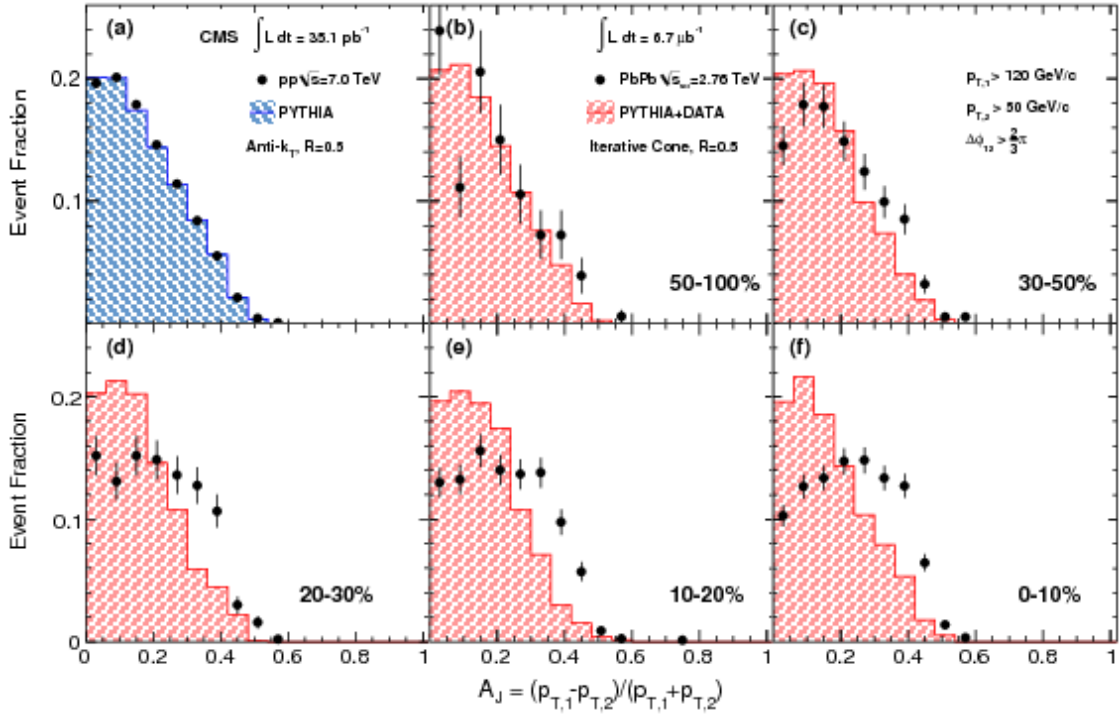


Figure 14. Dijet asymmetry in 2.76 TeV PbPb and pp data for jet selection $p_{T,1} > 120$ GeV, $p_{T,2} > 50$ GeV, and $\Delta\phi_{1,2} > 2\pi/3$ from Ref. [38].

The transverse momentum difference between the leading and subleading jets may be conceptualized as “missing- p_T ” from the subleading jet, which must by momentum conservation be

recovered somewhere in the hemisphere of the event surrounding the subleading jet axis. One way to capture this momentum balance is by comparing the total p_T carried by tracks in different p_T classes in the subleading relative to the leading hemisphere. This balance is shown in the top row of Fig. 15, for $\langle p_T^\parallel \rangle$ defined as the projection of each track's p_T projected in ϕ onto the dijet axis (i.e. the average of the leading and subleading jet axes) [39]. In pp and peripheral PbPb data, this balance shows the depletion of tracks with $p_T > 8$ GeV in the subleading relative to the leading hemisphere balanced primarily by tracks with $2 < p_T < 8$ GeV, consistent with the localization of these tracks in additional jets for unbalanced dijets in this scenario. The magnitude of the “missing- p_T ” balancing distribution increases with growing A_J by construction. Comparing PbPb to pp distributions (differences shown in the bottom row of Fig. 15), the balancing distribution in unbalanced (large A_J) events in central PbPb data shows larger contributions from soft particles with $p_T < 2$ GeV and smaller contributions from particles with $p_T > 4$ GeV, indicating that the more of the balancing p_T distribution in the subleading side is carried by soft quenching products rather than additional jets.

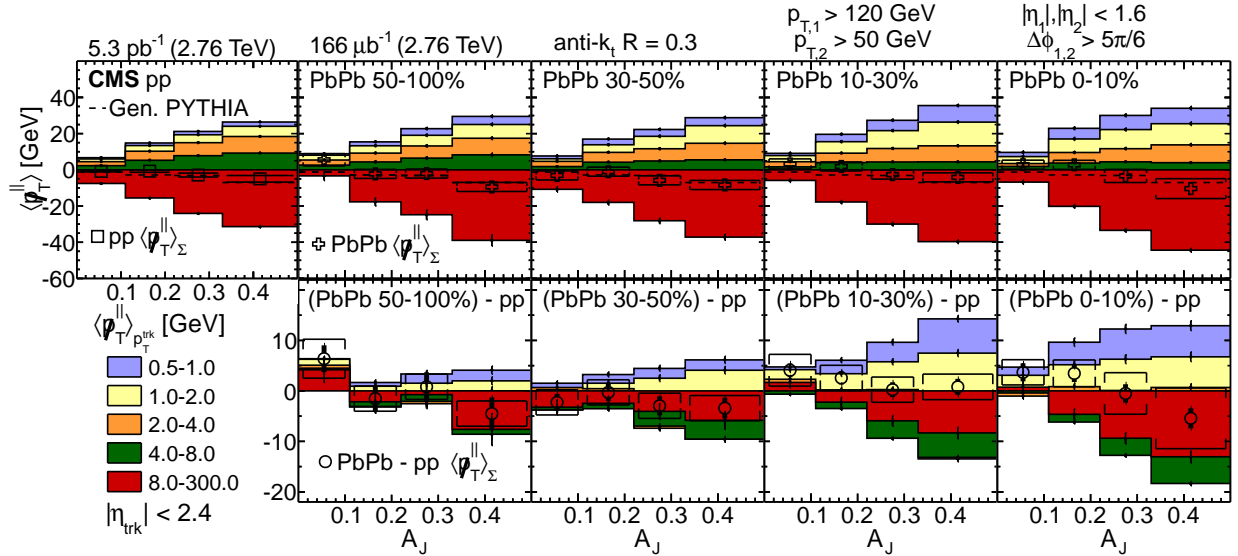


Figure 15. Top row: hemisphere p_T momentum balance in dijet events as a function of A_J , taking the total difference $\langle p_T^\parallel \rangle$ in the subleading hemisphere minus that in the leading hemisphere from Ref. [39] in pp and PbPb data. Bottom row: Differences PbPb - pp.

Dijet momentum balance studies therefore show evidence of redistribution of jet energy from harder to softer particles via jet quenching, and greater quenching of the subleading than

leading jets. As discussed above, the angular distribution of quenching products relative to the jet axis is also highly relevant for constraining models of interactions between the jet and the medium. This measurement is shown in Fig. 16 for unbalanced dijets with $A_J > 0.22$. Comparing the radial distribution with respect to the dijet axis shows that in this unbalanced dijet sample in central PbPb events, more p_T is recovered in lower- p_T particles extending to large angles from the jet axis. It is important to note that this measurement shows overall hemisphere differences in the radial p_T distribution, combining the effects of quenching to the subleading jet, quenching to the leading jet, and also any azimuthal asymmetry in the underlying event (as would arise if the direction of the dijet axis coupled to odd underlying event flow terms such as v_3). Isolating and further studying each of these contributions will be a major goal of this analysis, as discussed in Sec. 4.3.

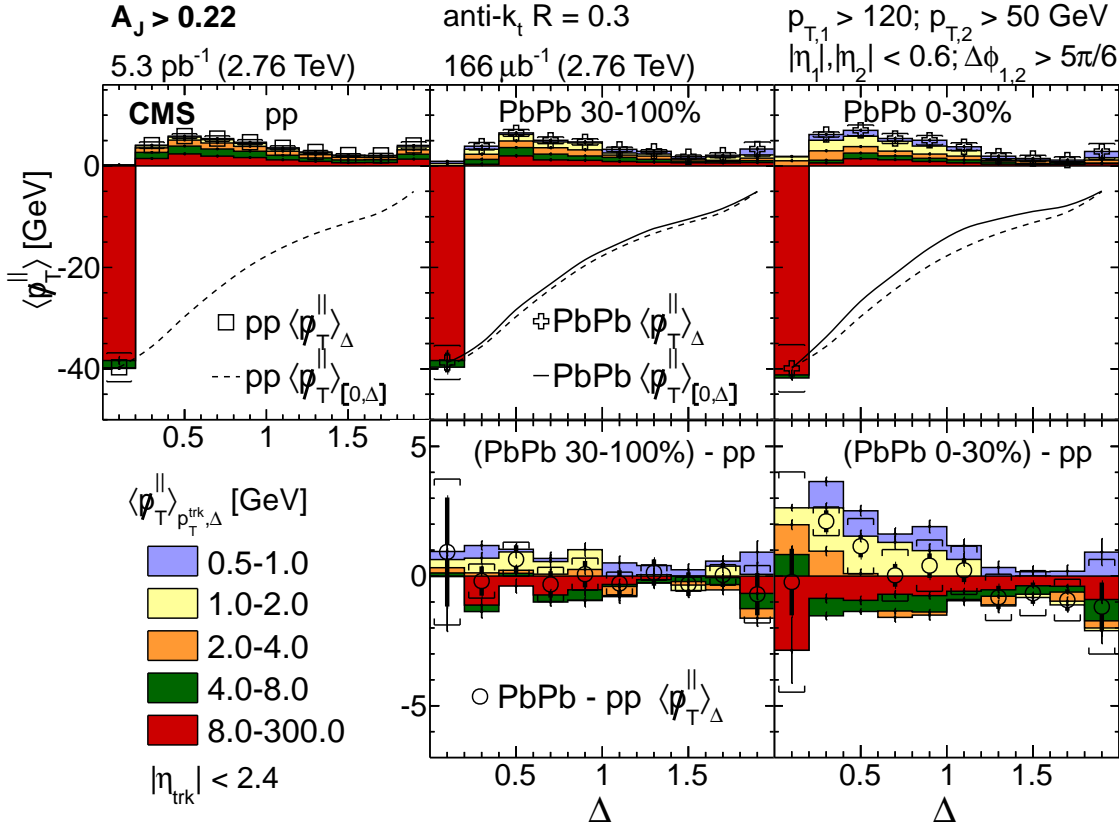


Figure 16. Top row: hemisphere p_T momentum balance in dijet events with $A_J > 0.22$ as a function of Δr , taking the total difference p_T^\parallel in the subleading hemisphere minus that in the leading hemisphere from Ref. [39] in pp and PbPb data. Bottom row: Differences PbPb - pp.

4 MODELS OF JET ENERGY LOSS IN THE QUARK GLUON PLASMA

A range of theoretical models of jet quenching have been developed to specifically account for the energy loss of a propagating probe through the quark gluon plasma. In general, models characterize collisional energy loss mechanisms (i.e. jet energy loss via elastic interactions with the medium), radiative energy loss by the propagating parton, and in some cases a medium response in the form of a “plasma wave” or back reaction. Some prominent examples of specific quenching models are surveyed briefly in Sec. 4.1. Some relevant comparisons to data are shown in Sec. 4.2, and then Sec. 4.3 summarizes goals of the present analysis in the context of the current state of jet quenching models.

4.1 Survey of theoretical models of jet quenching mechanisms

Jet quenching models consider a range of different conceptual pictures and mathematical formalisms to account for parton energy loss in the QGP and to predict experimental observables such as R_{AA} , jet substructure, and dijet momentum balance. In all cases, one or more controlling parameters are fit or varied to experimental data (in many cases based on R_{AA}), and other observables are then extracted. One example of such a parameter (used directly in the Higher Twist approach and calculable in other approaches) is the jet transport parameter \hat{q} that measures the average squared transverse momentum per unit path length λ transferred to the medium from the parton via collisional and/or elastic energy loss:

$$\hat{q} = \frac{\langle p_T^2 \rangle_{\text{med}}}{\lambda}. \quad (20)$$

Several models, discussed briefly and qualitatively below, have shown notable convergence in values of \hat{q} obtained via different approaches, as illustrated in Fig. 17 [40] from the JET Collaboration. These correspond to approximate values for temperature-scaled \hat{q} of 4.6 ± 1.2 at RHIC and 3.7 ± 1.4 at the LHC. The brief summaries of these models included below are adapted from the more detailed descriptions in Refs. [22, 40, 41].

- **Higher Twist** – The “Higher Twist” approach treats medium modification to jets as an extension of pQCD factorization, suppressed by powers of the hard scattering momentum scale

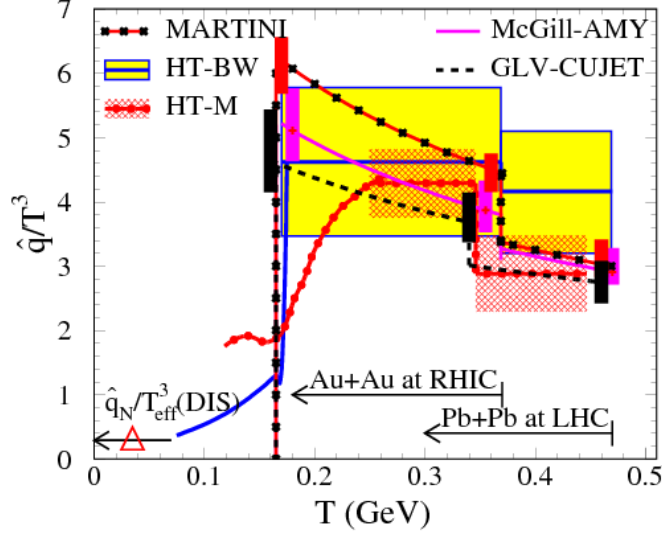


Figure 17. Temperature dependence of \hat{q}/T^3 for a 10 GeV jet from different quenching models, analyzed by the JET Collaboration in Ref. [40].

Q^2 . These modifications involve “higher-twist” processes in which multiple partons interact coherently, in medium-induced splitting functions depend on medium properties via transport parameter \hat{q} . The Higher Twist Majumder (HT-M) approach extends the Higher Twist Berkeley Wuhan (HT-BW) model to include multiple gluon scatterings via modifications to the DGLAP vacuum evolution equations.

- **Arnold-Moore-Yaffe (AMY)** – The AMY approach treats the quark gluon plasma with a finite temperature field theory, with equilibrated particles with thermal mass gT and jet virtuality comparable to this thermal mass scale. With this approach, there is no hard scale for the jet, and vacuum-like jet fragmentation is not directly handled. Predictions are carried out by solving thermal QCD rate equations for parton distribution functions, either with collinearized interaction equations in the McGill implementation, or via full Monte Carlo simulation based on PYTHIA 8 in the MARTINI implementation.

- **Gyulassy-Lévai-Vitev (GLV)** – The GLV approach (expanded to include thermal mass and heavy quark effects as DGLV and implemented in the CUJET Monte Carlo framework) treats the medium as a collection of partially screened scattering centers. GLV starts from the hard radiation spectrum and also includes multiple soft gluon emissions. Scatterings in this model are governed by the ratio of the jet path length through the medium to the scattering length L/λ . Calculations are carried out as expansions in powers of L/λ , with the leading order corresponding to low opacity (or “thin medium”) and higher orders corresponding to additional scatterings in a denser or thicker QGP.
- **Baier-Dokshitzer-Mueller-Peigné-Schiff-Zakharov (BDMPS-Z) and Armesto-Salgado-Widemann (ASW)** – The BDMPS-Z and ASW approaches compute energy loss via multiple soft scatterings in the medium. Similar to GLV, these approaches model the QGP as a collection of scattering centers with which an outgoing parton interacts. These interactions are encoded via quenching weights (modeled with Poisson distributions) that capture the probability that a parton loses a fraction of energy ϵ due to n gluon emissions. JEWEL and YAJEM are both full Monte Carlo implementations of this approach.
- **Linear Boltzman Transport (LBT)** – The LBT approach handles inelastic scattering in the medium via the Boltzmann equation, and also incorporates medium-induced gluon radiation with a spectrum taken from the Higher-Twist formalism. In this approach, collision kernels are taken from pQCD, while medium evolution is modeled with hydrodynamic simulation. Explicit calculation of \hat{q}/T^3 yields results consistent with those shown in Fig. 17 [42, 43].

In addition to the family of models with consistent jet transport coefficients summarized above, other diverse models have shown some success in capturing observables of jet suppression and structure modification in the medium, as will be discussed in Sec. 4.2.

- **Soft Collinear Effective Theory with Glauber Gluons (SCET_G)** – The development of SCET in proton-proton physics was motivated by the inability of pQCD (due to infrared divergences) to handle interactions between propagating partons and low-energy particles traveling in the same direction as the parton. SCET is able to handle multiple soft energy scales via power-counting formalism at a range of energy scales. To apply SCET to studies

of QGP interactions, it is extended to include interactions in the medium with Glauber gluons, which are gluons with transverse momentum that is much larger than their momentum collinear with the parton. In SCET_G medium interactions via Glauber gluons are modeled as background color fields that mediate interactions between the propagating parton and the QGP [44, 45, 46].

- **Strong/Weak Hybrid Model from AdS/CFT** – The strong/weak hybrid model assumes that the initial jet fragmentation occurs as in the vacuum (considering, as in HT, jets with virtuality scales much larger than the medium), so that interactions occur via modifications to the energy loss of partons within the jet. Predictions about this parton energy loss are derived from gauge-string duality modeling QCD as a $\mathcal{N} = 4$ supersymmetric Yang-Mills theory. Here the propagating parton is treated as dual to a string falling into a black hole, and its rate of energy loss is computed via holography as a function of its initial energy and stopping distance in a medium of temperature T . [47, 48, 49]. Recent developments to this model have incorporated a “back reaction” in the hydrodynamic medium response to the jet taking the form of both a wake in the plasma and a Mach cone carrying energy through the plasma in the direction of the jet at large angles [50].
- **Coupled Jet-Fluid Model** – In this model, the full jet parton shower is coupled to the hydrodynamic flow of the medium. Modeled jet modifications include longitudinal energy loss, transverse momentum broadening, and medium-induced partonic splittings. In addition, the energy deposited in the medium by the parton shower of the jet is treated as a source terms for jet-induced changes to the evolution of the medium. In simulation, this results in a Mach cone shock wave induced by a jet propagating faster than the speed of sound in the medium. [51].

4.2 Quenching model comparisons to high- p_T jet observables

Comparisons to various experimental observables can help to validate or challenge these diverse models of jet quenching, and the models outlined above have each shown some successes in this regard. A wide range of models have captured the p_T dependence of charged particle suppression factor R_{AA} (illustrated in Fig. 18, particularly in the high- p_T sector where radiative

energy loss is likely to dominate. Recently, however, there have been increasing efforts to accurately capture quenching dynamics via reconstructed jets, including capturing jet R_{AA} (discussed in Sec. 4.2.1), jet fragmentation functions (Sec. 4.2.3), jet shapes (Sec. 4.2.2), and dijet momentum balance (Sec. 4.2.4). To summarize the state of the theoretical field in capturing these observables, the discussion below will focus on four diverse models that represent very different approaches to jet quenching and that each offer recent predictions for several different observables: BDMPS as implemented in JEWEL, SCET_G, the Hybrid model, and the Coupled Jet-Fluid model.

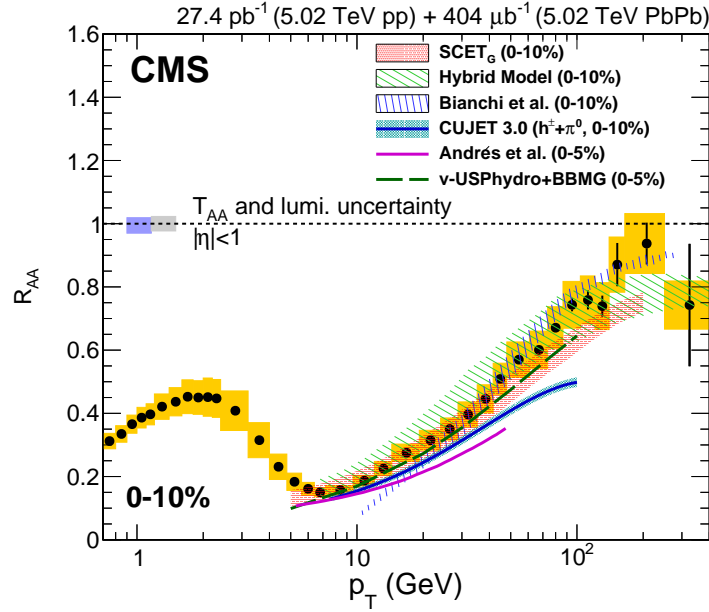


Figure 18. Model comparisons to charged particle R_{AA} in 0-10% central PbPb data at 5.02 TeV from Ref. [30].

4.2.1 Quenching model comparisons: jet R_{AA}

In JEWEL the background is treated as ensemble of partons, and interactions between a propagating jet and this medium may be handled in several ways; in the predictions considered here, thermal partons produced in jet-medium interactions will be retained in the jet and hadronized with other jet partons. In considering the JEWEL predictions with this method, it is important to note that this is a limiting case, in which these partons then do not interact further with the medium. This approach can accurately capture the nearly flat p_T dependence of jet R_{AA} observed by the ATLAS and CMS Collaborations. As shown in Fig. 19, it also exhibits a dependence in

R_{AA} on jet cone radius parameter R , as larger cone sizes capture additional jet-related particles redistributed to larger angles from the jet axis (in PbPb relative to pp) via interactions with the medium [52].

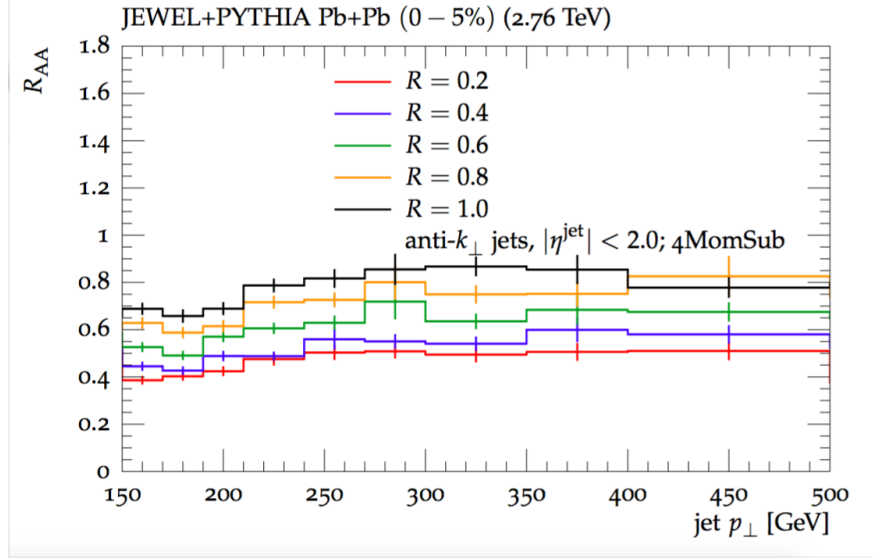


Figure 19. Simulated dependence of jet R_{AA} on jet reconstruction parameter R at 2.76 TeV from JEWEL in Ref. [52].

Similar to the JEWEL simulation, the calculations of R_{AA} from the coupled jet-fluid model, shown in Fig. 20 suggests greater dependence on jet reconstruction parameter R than is evident in the CMS measurement (although calculations are consistent within the large uncertainties on the measurement). In this calculation, about 10% of the suppression obtained with parton shower modifications alone is recovered when hydrodynamic response is also included, bringing calculated R_{AA} closer to the experimentally measured p_T dependence when this coupled fluid evolution is taken into account.

Calculations of jet R_{AA} with SCET_G explicitly parameterize the effects of initial state energy loss, also known as “cold nuclear matter” (CNM) effects, with parameter μ_{CNM} . Varying this parameter changes the calculated values of R_{AA} substantially with larger values better capturing ATLAS and CMS measurements as shown in Fig. 21, suggesting the relevance of initial state effects in overall jet suppression. It is important to note that in these calculations radiative but not collisional energy loss is taken into account. Like JEWEL and the coupled jet-fluid model, SCET_G

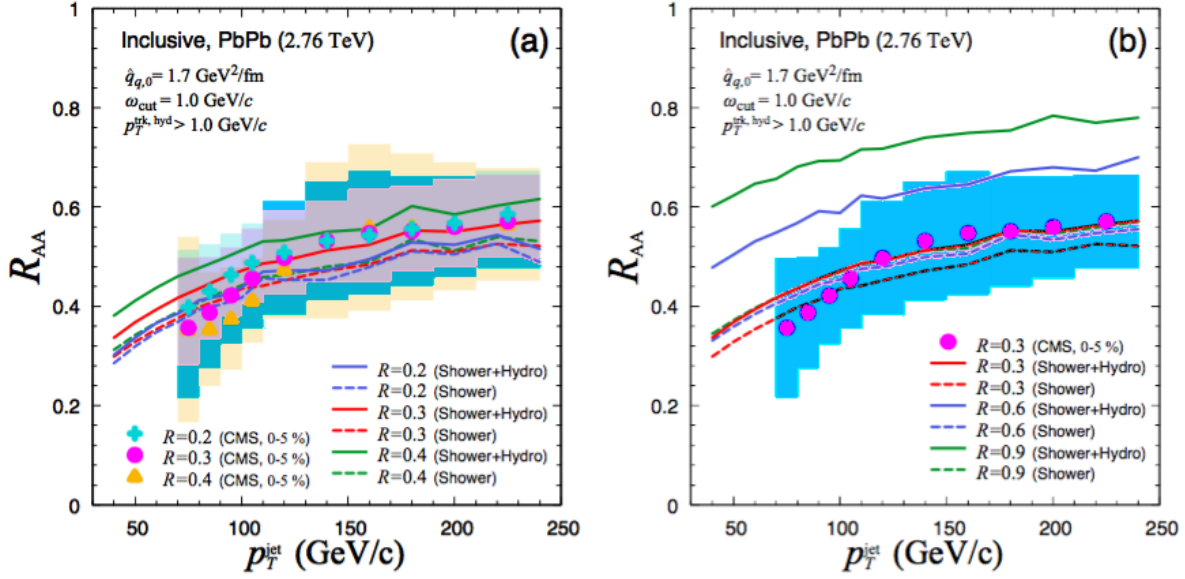


Figure 20. Simulated dependence of jet R_{AA} on jet reconstruction parameter R at 2.76 TeV from the coupled jet-fluid model, compared to CMS data at $R = 0.2, 0.3, 0.4$ in Ref. [51].

also suggests significant R_{AA} dependence on jet reconstruction parameter R , with less suppression for larger values of R as “lost” energy is recovered at relatively large angles [45].

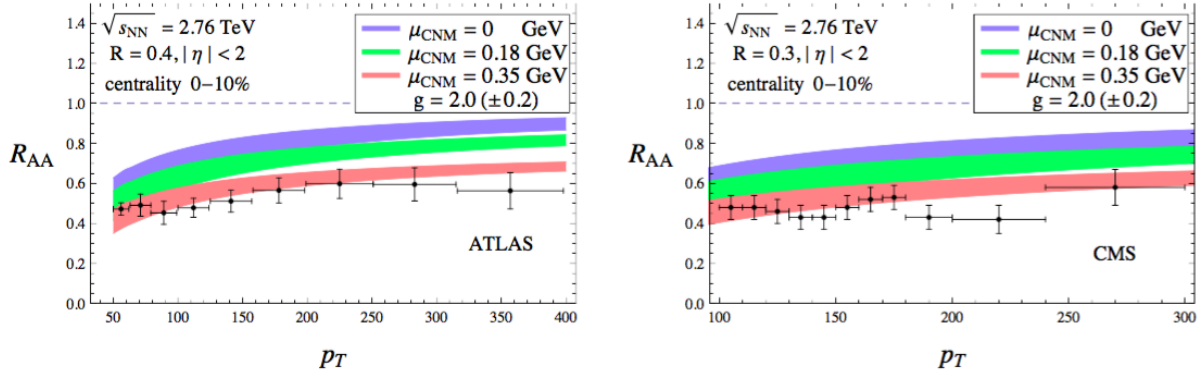


Figure 21. Predicted jet R_{AA} as a function of p_T at 2.76 TeV from SCET_G, shown for several values of initial state energy loss parameter μ_{CNM} in Ref. [45].

In the strong/weak hybrid model derived from the AdS/CFT correspondence, the theory-dependent constant $K = \hat{q}/T^3$ is defined to capture jet broadening in the medium. Comparisons of this model to data aim to constrain possible values of K , which are expected to be between

5 and 20 (although a much wider range of possible is considered in calculations). However, as Fig. 22 demonstrates in comparing model predictions, at several different jet radii R , for the rather extreme cases $K = 0$ and $K = 40$, observables including R_{AA} are in fact rather insensitive to the value of K . This is likely due to the fact that broad jets are more quenched than narrow jets by the plasma, so that the PbPb jet sample ends up dominated by jets with hard fragmentation. For these jets made up of few (or only one) parton the transverse momentum “kicks” from the medium used to introduce broadening in this model end up only changing the jet axis direction rather than broadening the jet. The hybrid model predicts only weak dependence on jet reconstruction radius parameter R similar to the CMS measurement, although in this case the model uncertainties and experimental uncertainties are both large [50].

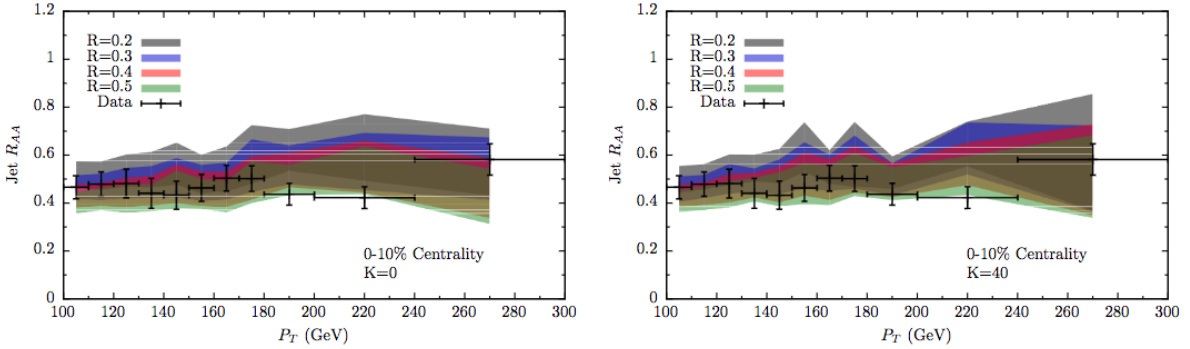


Figure 22. Calculated jet R_{AA} as a function of p_T at 2.76 TeV from the strong/weak hybrid model for broadening parameters $K = 0$ (left, corresponding to no broadening) and $K = 40$ (right, corresponding to extreme broadening) and a range of values of radius parameter R in Ref. [50].

4.2.2 Quenching model comparisons: jet shapes

The JEWEL simulation of the jet shape observables accurately captures the redistribution of p_T from small to larger angles only with the inclusion of recoil effects from the medium as shown in Fig. 23. This larger-angle enhancement is driven by the soft ($p_T < 3$ GeV) particles, and is completely absent in simulation without recoil effects, suggesting that these soft recoil particles drive the energy redistribution to larger angles from the jet axis. Taken with the jet radius dependence of R_{AA} also found by JEWEL to much larger radii than the $R = 0.3$ measurement and simulation

shown in Fig. 23, this interpretation motivates the extension of p_T -differential measurements of jet shape to larger angles from the jet axis.

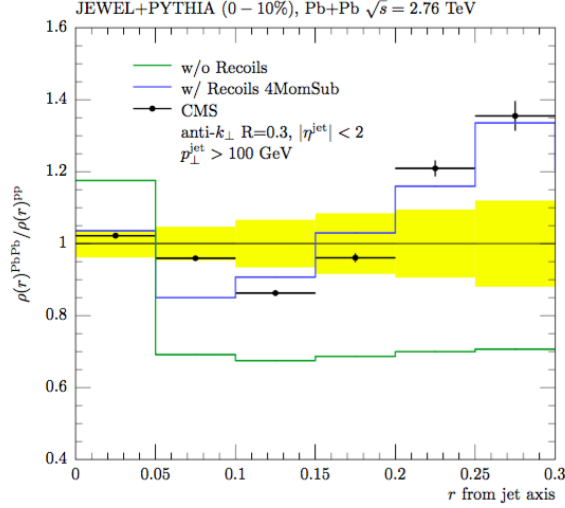


Figure 23. Simulated jet shape ratio $\rho(\Delta r)_{\text{PbPb}}/\rho(\Delta r)_{\text{pp}}$ at 2.76 TeV from JEWEL in Ref. [52].

In the coupled jet-fluid model, accounting for modifications to the parton shower only captures the jet modifications to jet shape $\rho(\Delta r)$ fairly well at small angles from the jet axis, but as the angle grows the relevance of the hydrodynamic response becomes increasingly evident, as shown in Fig 24. This is consistent with the qualitative idea that medium modifications may make the inner cone of the jet more narrowly collimated, while hydrodynamic response and medium transport results in broadening evident in a long and soft “tail” to the jet extending to large angles in Δr from the jet axis. The expectation in considering excitations that evolve with the medium is that these should in fact extend to significantly larger angles than the previously measured Δr , as shown in Fig 25.

Considerations of jet shape ratio $\rho(\Delta r)_{\text{PbPb}}/\rho(\Delta r)_{\text{pp}}$ with SCET_G separately consider CNM effects, effects arising from cross section suppression R_{AA} (with no direct modification to shape), and modifications to the parton shower in the medium. As Fig. 26 shows, CNM effects alone show little deviation from 1, implying that CNM effects do not change the relative fraction of quark jets to gluon jets much (as quark and gluon jets have significantly different shapes, so changes in the quark jet to gluon jet ratio would be evident in the jet shape ratio). Accounting for the overall cross section suppression shown in R_{AA} calculations above but assuming no changes to

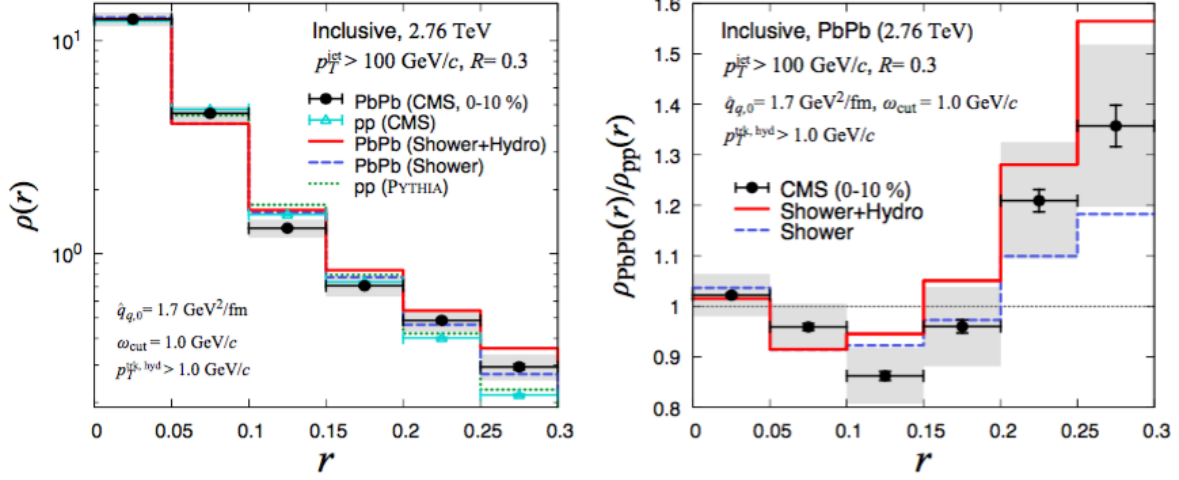


Figure 24. Calculated jet shapes in PbPb and and their ratio at 2.76 TeV from the coupled jet-fluid model from Ref. [51].

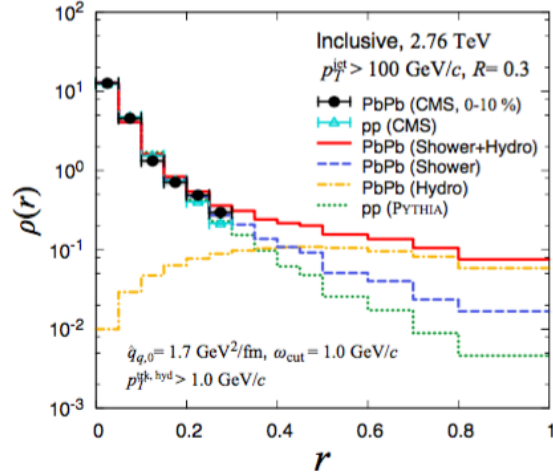


Figure 25. Calculated jet shapes in PbPb and pp at 2.76 TeV, extended to $\Delta r = 1$ from the coupled jet-fluid model from Ref. [51].

individual jet shapes in PbPb versus pp collisions results in narrowing of the jet cone, as shown in red in Fig. 26, due to the fact that broader gluon jets experience greater suppression, leaving a larger relative contribution from narrower quark jets. Adding in the jet-by-jet modifications to the parton shower captures the enhancement at relatively large Δr observed in CMS measurements. In this case, broadening is captured by modifications to radiative energy loss via glauher gluon interactions, without directly accounting for collisional energy loss effects [45].

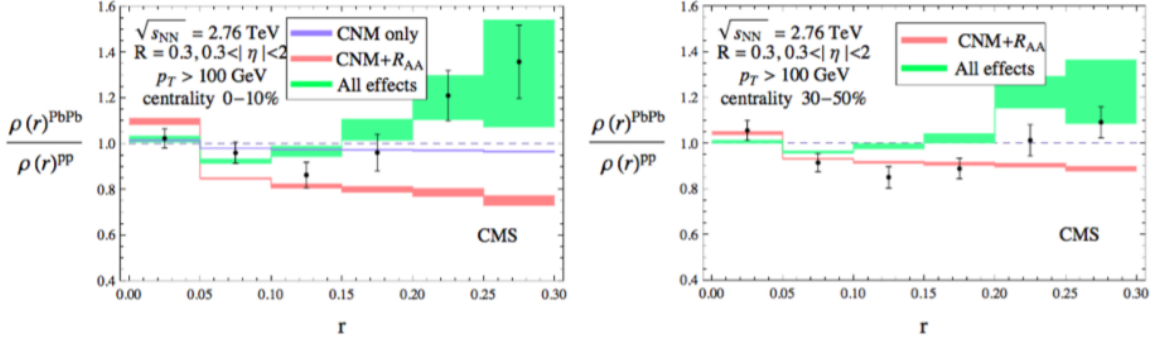


Figure 26. Calculated jet shape ratio $\rho(\Delta r)_{\text{PbPb}}/\rho(\Delta r)_{\text{pp}}$ at 2.76 TeV with SCET_G, showing contributions from cold nuclear matter, from jet suppression R_{AA} , and from medium modifications to the parton shower, in Ref. [45].

When hybrid model calculations of jet shape are carried out with a variety of broadening parameters K but without taking into account a back-reaction in the medium, all exhibit a narrowing within the jet cone as shown in Fig. 27. As discussed above with the hybrid model calculations of R_{AA} , this is likely due to the fact that broader jets are more likely to be quenched, leaving behind a narrower jet sample. Again as with the R_{AA} calculation, little dependence on broadening parameter K is evident, since for these jets with hard fragmentation the transverse momentum kicks in the medium only change the jet direction and the jet shape is constructed with respect to the reconstructed jet axis rather than the original parton direction. For any choice of K , including unrealistically large values corresponding to extreme broadening, the model in this form does not capture the soft enhancement at large Δr from the jet axis [50].

In order to begin to account for this feature, the hybrid model must incorporate a “back-reaction” in the medium in the form of a plasma wake and/or a Mach cone carrying momentum through the medium in the same direction as the jet. This is implemented in the model as perturbations in the medium dependent on the kinematics of the jet and the momentum it loses as it passes through the medium. Figure 28 compares hybrid model jet shape calculations with and without this backreaction to CMS data. With the backreaction implemented, the model exhibits a slight reversal in the narrowing trend at large Δr in central PbPb data relative to pp data that comes closer to experimental results, although even with this backreaction it is still far from capturing the large Δr enhancement in PbPb relative to pp observed by CMS and captured by other

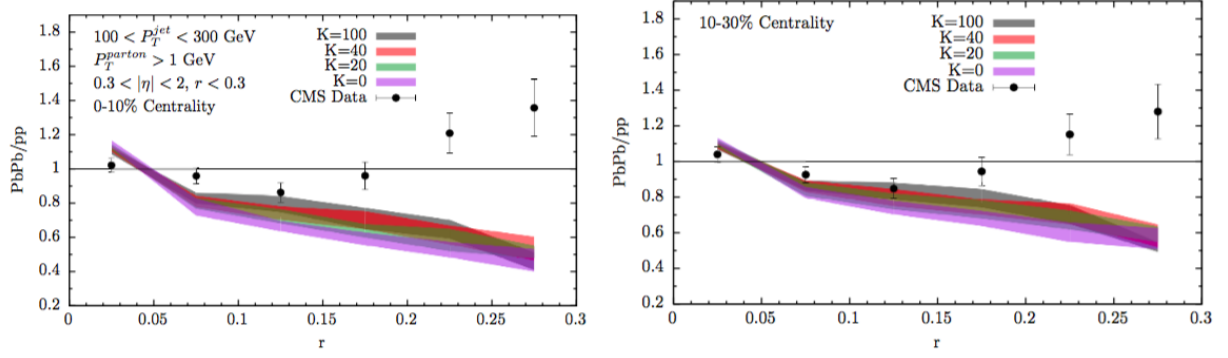


Figure 27. Calculated jet shape ratio $\rho(\Delta r)_{\text{PbPb}}/\rho(\Delta r)_{\text{pp}}$ at 2.76 TeV from the strong/weak hybrid model for a range of values of broadening parameter K in Ref. [50].

models. This suggests the relevance of including a medium response in the jet shape calculation, but that the current implementation of this response substantially underestimates the effect, which the authors speculate may be due to under-estimation of the momentum deposited in the medium by the jet, over-thermalization of this deposited energy, or greater removal of backreaction effects via background subtraction than is applied to data [50].

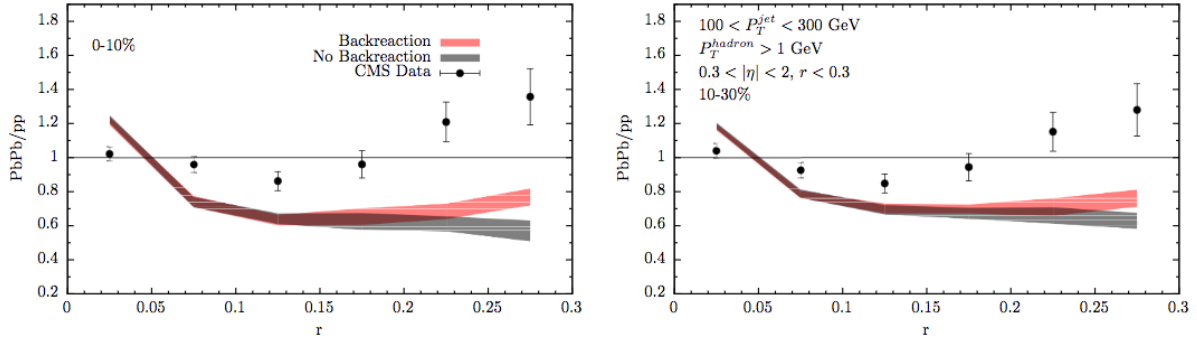


Figure 28. Calculated jet shape ratio $\rho(\Delta r)_{\text{PbPb}}/\rho(\Delta r)_{\text{pp}}$ at 2.76 TeV from the strong/weak hybrid model, comparing calculations with and without the plasma backreaction from Ref. [50].

4.2.3 Quenching model comparisons: jet fragmentation functions

Fragmentation function measurements capture the p_T distribution of constituent hadrons (or tracks) in a jet defined by a particular radius R . In JEWEL, track-by-track background subtraction is not possible, so while jet p_T is background-subtracted the fragmentation function measure-

ment is carried out with all tracks. Figure 29 shows ATLAS and CMS JFF measurements compared to JEWEL with and without medium recoil. As expected due to the lack of background subtraction, the simulation with recoil included overshoots the low- p_T (high- ζ) enhancement observed in PbPb relative to pp. Without recoil, however, JEWEL shows suppression rather than enhancement in this region, supporting the interpretation of this soft enhancement as due to medium response to the propagating jet [52].

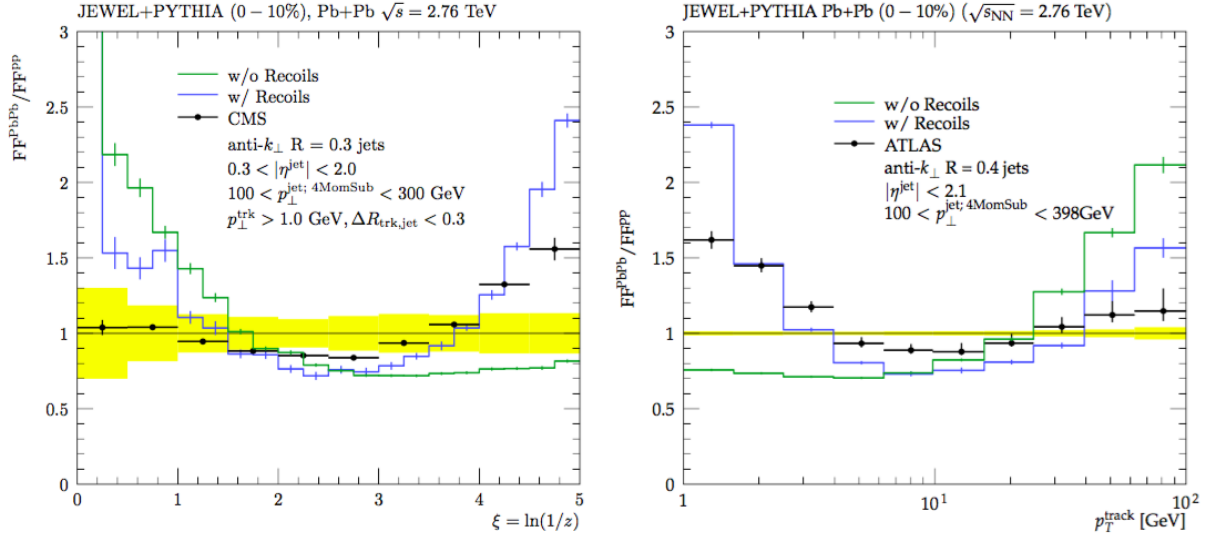


Figure 29. Simulated jet fragmentation function ratio PbPb/pp at 2.76 TeV from JEWEL in Ref. [52].

In the hybrid model before the implementation of the backreaction, energy lost by the jet is assumed to thermalize completely so that it loses all correlation to the jet axis. The calculated jet fragmentation function modification PbPb/pp in this scenario (for $K = 0$) is shown in the gray band in Fig 30. Like the JEWEL simulation without recoil, the hybrid model in this scenario misses the enhancement of low- p_T particles (corresponding to large $\zeta = 1/\ln(z)$) in the fragmentation function measurement. When the backreaction is included in the calculation, the model comes qualitatively closer to the shape of the ζ -dependence of the fragmentation function, capturing the rising trend toward large ζ that corresponds to low- p_T enhancement. As with the jet shapes calculation, however, while the inclusion of the backreaction improves the qualitative correspondence between the shape of the trend from the model calculation and the shape of the data, even with the backreaction quantitative agreement is not achieved [50].

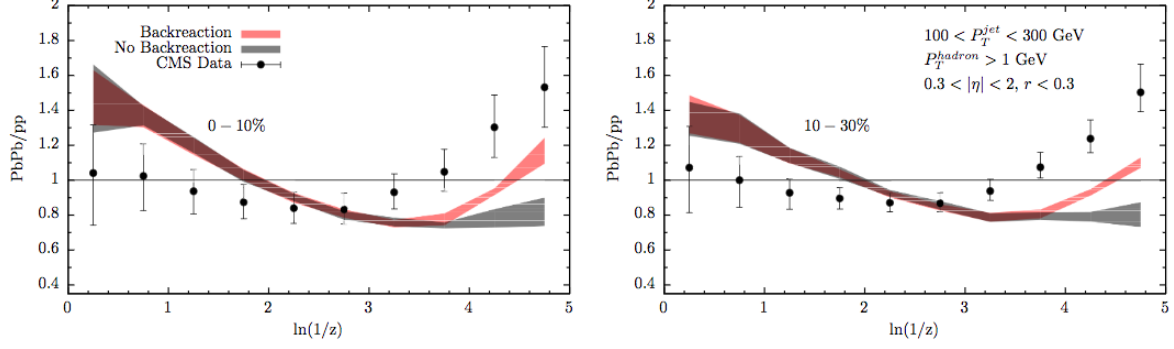


Figure 30. Calculated jet fragmentation function ratio PbPb/pp at 2.76 TeV from the strong/weak hybrid model comparing calculations with and without the plasma backreaction from Ref. [50].

4.2.4 Quenching model comparisons: dijet asymmetry

Dijet asymmetry studies include both measurements of the distribution of asymmetry parameter A_J , and studies to capture the balancing distribution of p_T “missing” from the subleading jet. In JEWEL simulations of the A_J distribution, shown in Fig. 31, little effect is shown from adding medium response (“recoils”), and this serves to slightly reduce the A_J modifications observed with medium-induced fragmentation but without the inclusion of recoil partons into medium-modified jets [52].

The hybrid model compares simulation to CMS measurements of the “balancing” distribution of track- p_T in the subleading (plotted positive) versus the leading (plotted negative) hemisphere. Experimental results (discussed in Sec. 3.3) are shown again in the bottom panel of Fig. 32 for reference. Without the backreaction (shown in the top panel of Fig. 32), the hybrid model captures the energy loss by the subleading jet, as evident in the large high- p_T depletions, but none of the soft enhancements in unbalanced dijets evident in PbPb data. With the backreaction implemented, the hybrid model qualitatively captures the soft enhancement, but yields fewer particles with $2 < p_T < 4$ GeV and somewhat more particles with $p_T < 2$ GeV than the data. Comparisons between the hybrid model and CMS data for the Δr distribution of the balancing transverse momentum in the subleading jet hemisphere shows this same behavior: without the backreaction none of the balancing excesses of soft particles in the subleading jet hemisphere relative to the leading jet

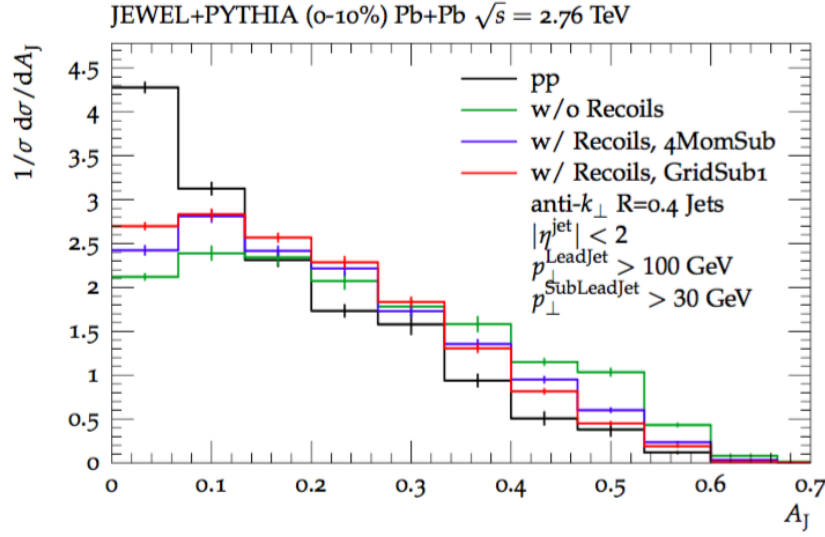


Figure 31. Simulated dijet asymmetry parameter A_J in pp and PbPb at 2.76 TeV from JEWEL in Ref. [52].

hemisphere are recovered, while adding the backreaction captures the general momentum balancing distribution while missing some particles in the $2 < p_T < 4$ GeV range [50].

4.3 Theoretical motivations for detailed jet-track correlation studies

Recent theory developments have included increasingly robust treatment of soft physics, and increasingly detailed treatment of jet substructure and predictions of medium reactions to propagating jets including at large angles from the jet axis. These approaches are accompanied by increasing interest in observables that are sensitive to the details of jet-medium interaction, and in particular to the angular distributions of jet fragmentation particles and to a possible Mach cone or other medium response at potentially large angles from the jet axis. In both JEWEL simulation and the strong/weak hybrid model, a “back reaction” or recoil in the medium is needed to properly capture both the enhancement of low- p_T particles in jet fragmentation functions, and the large angle enhancement in the PbPb jet shape. The SCET_G model, on the other hand, captures jet shape modifications via glauher gluon interactions but without an explicit recoil effect, while coupled jet-fluid model is able to capture jet shape coupled parton shower modification and hydrodynamic evolution. Measurements in pp and a range of PbPb centralities that are both differential in track-

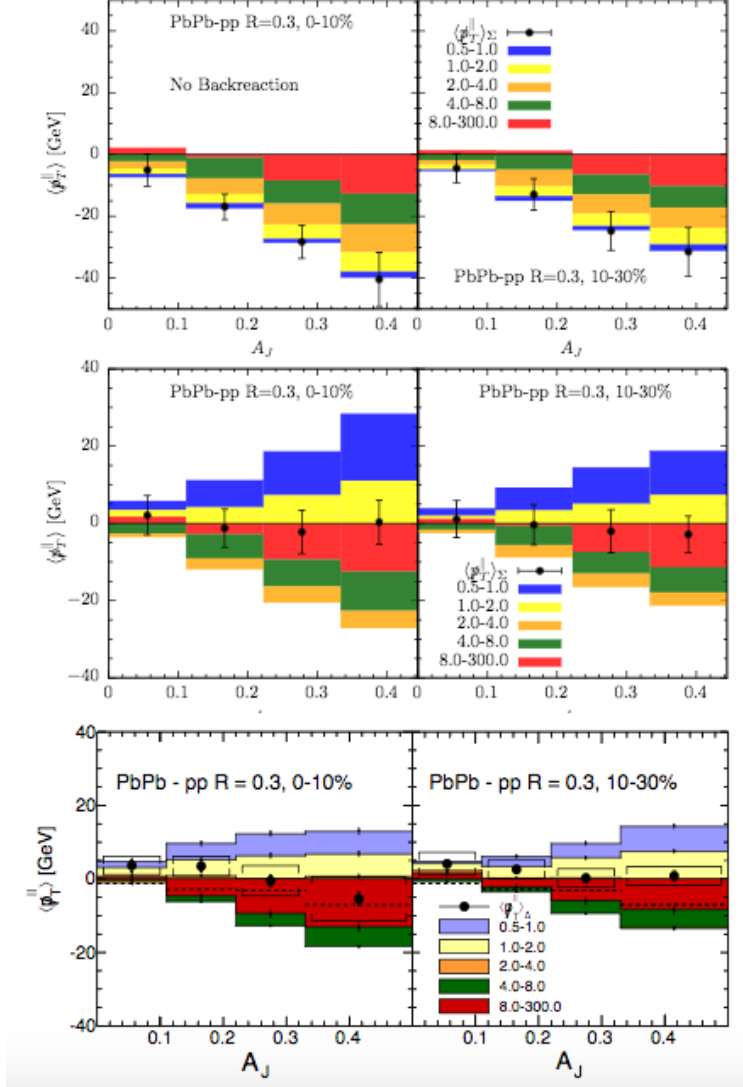


Figure 32. Calculated jet shape ratio $\rho(\Delta r)_{\text{PbPb}}/\rho(\Delta r)_{\text{pp}}$ at 2.76 TeV from the strong/weak hybrid model in Ref. [50].

p_T and extend to large angles from the jet axis can offer the potential to help distinguish between these quite different pictures of jet-medium interactions.

Toward that end, the results from the CMS Collaboration discussed in this analysis use correlations between jets and charged particles to extend jet shape measurements to large angles from the jet axis and provide detailed characterization of jet peak in separate dimensions $\Delta\eta$ and $\Delta\phi$. In addition to measurements for an inclusive selection of high- p_T jets, dijet correlation studies are carried out for leading and subleading jets as a function of A_J . These studies can help to connect measurements of dijet asymmetry and event-wide momentum balance to studies of jet

modifications at small angles, clarifying the interpretation of transverse momentum distributions in heavy ion events compared to a “vacuum” reference of pp dijet data.

5 THE LARGE HADRON COLLIDER AND THE CMS DETECTOR

5.1 The Large Hadron Collider

The Large Hadron Collider (LHC), located at CERN near Geneva, is the largest and highest-energy particle accelerator in the world. It consists of two counter-rotating particle beam lines in a tunnel 26.7 km in circumference, located between 45 m and 170 m underground [53]. During standard operation, the LHC collides beams of protons accelerated and focused using a series of superconducting magnets, cooled to below 2 K using supercritical helium. Particle beams are brought together for collisions at four experimental detectors at four points in the accelerator ring: the ATLAS, CMS, ALICE, and LHCb detectors. In addition to the proton-proton (pp) data collected at center-of-mass energies $\sqrt{s_{\text{NN}}} = 7$ TeV, 8 TeV, and 13 TeV, the LHC has also been operated for heavy ion physics by colliding with fully-stripped lead nuclei ($^{182}\text{Pb}^{82+}$) in lead-lead (PbPb) and proton-lead (pPb) collisions. Heavy ion runs at the LHC have included PbPb data and pp “reference” runs at $\sqrt{s_{\text{NN}}} = 2.76$ TeV (2011 and 2013, respectively) and 5.02 TeV (2015) and pPb data at $\sqrt{s_{\text{NN}}} = 5.02$ TeV (2013 and 2016) and 8.16 TeV (2016). This analysis relies on PbPb data at 2.76 TeV and 5.02 TeV, and corresponding pp reference data at the same center-of-mass energies.

In peak proton-proton operation, the LHC collides 2,808 bunches each containing approximately 10^{11} protons with a minimum bunch spacing of 25 ns, for a maximum luminosity of $10^{34}\text{cm}^{-2}\text{s}^{-1}$ delivered to the high-luminosity detectors (ATLAS and CMS). The lead-lead performance target of $10^{27}\text{cm}^{-2}\text{s}^{-1}$ delivered via 592 bunches of 10^7 lead ions was slightly exceeded during the 2015 PbPb run. At this high-intensity frontier, it is common during nominal pp data collection and possible in PbPb data collection that multiple distinct proton-proton collisions may occur within a recorded event in a phenomenon known as “pile-up.” However, pile-up is relatively rare in PbPb collisions due to the lower luminosities, and in the present analysis only one primary vertex will be considered (with products of any other possible interactions removed via background subtraction procedures).

5.2 The CMS detector

The CMS detector is named for the Compact Muon Solenoid at its heart: a superconducting magnet with magnetic field of 3.8 T, length of 13 m, diameter of 6 m, and weight 14,000 tons. Inside of this solenoid, the detector includes silicon pixel and strip detectors for particle tracking (see Sec. 5.3 for a detailed explanation), and electromagnetic and hadronic calorimeters (see Sec. 5.4). Calorimeters within the solenoid volume are complemented by additional calorimetry outside of the solenoid that provides coverage in the very forward direction close to the beam line, including the hadronic forward (HF) calorimeter in the region $3.0 < |\eta| < 5.2$ used in this analysis for centrality determination, and the Zero Degree and CASTOR calorimeters in the even more forward region. The CMS detector also includes an extensive muon system outside of the solenoid volume, consisting of aluminum drift tubes in the barrel region, cathode strip chambers in the forward region, and a complementary system of resistive plate chambers (not discussed in detail here as muons are not of primary relevance to this analysis). Full details about the CMS detector may be found in Ref. [54], and a perspective drawing of the CMS detector from this report is shown in Fig. 33.

In the CMS detector, the $+z$ axis is defined to be horizontal, pointing to the West along the beam line direction. The x axis is horizontal, pointing to the South toward the center of the LHC. The $+y$ axis is vertical, pointing upward. The azimuthal angle $\phi = \tan^{-1}(\frac{y}{x})$ is defined in the x - y plane such that $\phi = 0$ is the $+x$ axis. Pseudorapidity $\eta = -\ln(\tan(\frac{\theta}{2}))$ is defined to have the same sign as the $+z$ axis. Pseudorapidity coverage in the CMS detector ranges from $\eta = 0$ at the y -axis, to $|\eta| > 8.3$ in Zero Degree Calorimeter approaching the $+/-z$ axis.

5.3 Trackers in the CMS detector

The CMS tracking system consists of a small silicon pixel detector for precise measurement near the interaction point (with three layers with radii 4.4 cm to 10.2 cm), surrounded by a large silicon strip detector with layers to a radius of 110 cm. In both detectors, a cylindrical tracker “barrel” is complemented by “endcap” disks that together provide full azimuthal coverage and pseudorapidity coverage in the range $|\eta| < 2.5$. The pixel detector consists of 66 million pixels in 1440 modules. It provides three-dimensional measurements of “hits,” or interactions of particles with tracker materials, with a transverse resolution $10\mu\text{m}$ and longitudinal resolution $20 - 40\mu\text{m}$

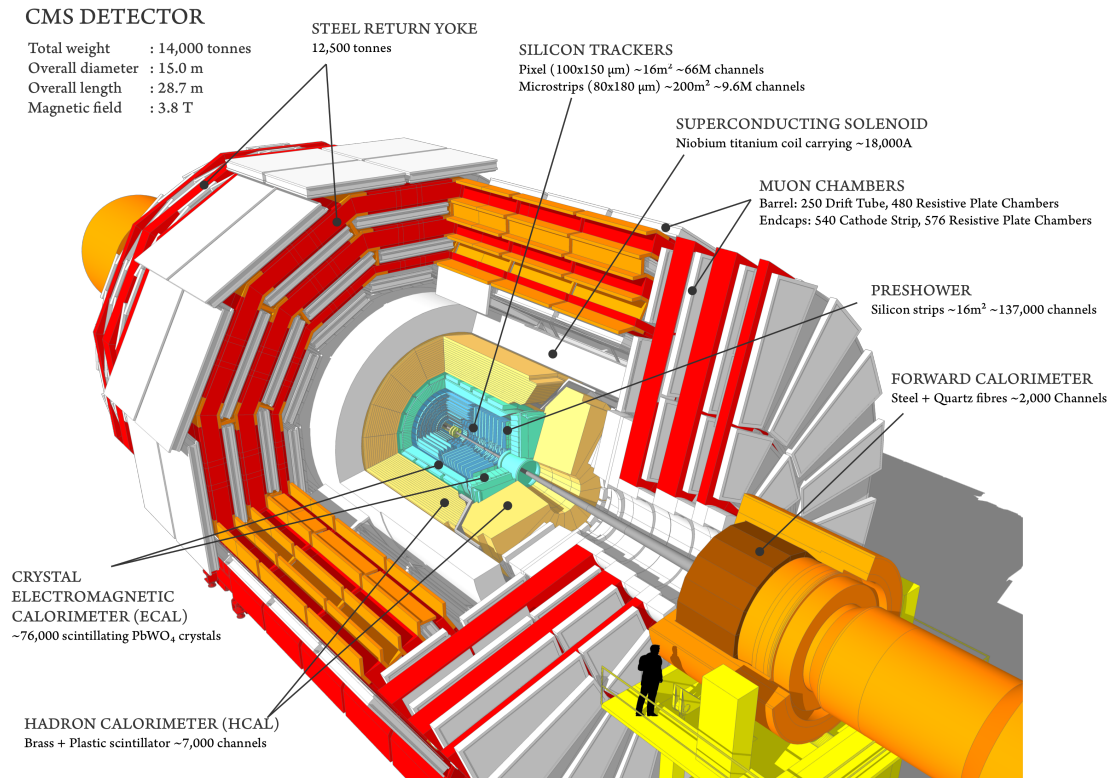


Figure 33. Perspective rendering of the CMS detector, showing component sub-detectors with a human included for scale perspective [55].

(and a third coordinate provided by the pixel plane). The silicon strip detector consists of 9.3 million strips in 15,148 modules, organized in four components: Tracker Inner Barrel (TIB) and Disks (TID), Tracker Outer Barrel (TOB, covering the region $r > 55$ cm), and Tracker End Caps (TEC, covering the region $124 < |z| < 282$ cm). Figure 34 shows a diagram of the pixel and strip detectors, which have total length 5.8 m and diameter 2.5 m [56]. Track reconstruction and tracking efficiency will be discussed in detail in Sec. 6.

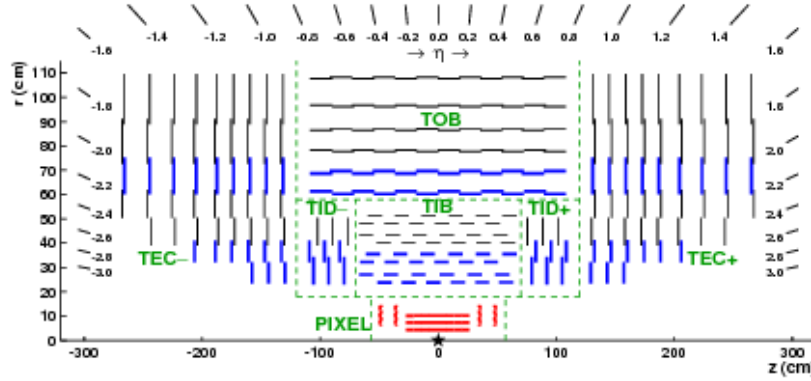


Figure 34. Diagram of CMS pixel and silicon strip detectors in the $r - z$ plane [56].

5.4 Calorimeters in the CMS detector

This analysis relies on electromagnetic and hadronic calorimeters for the energy measurements used as inputs for the reconstruction of high- p_T jets. The ECAL, which measures the energy of charged particles, consists of 75 848 lead tungstate (PbWO_4) crystal scintillators, organized in 5 arrays, covering $|\eta| < 1.48$ in a barrel region and $1.48 < |\eta| < 3.0$ in the endcap region. Light from the scintillators is captured with avalanche photodiodes in the barrel region, and vacuum phototriodes in the endcap region. A preshower detector system in front of the ECAL is used to assist in the identification of neutral pions and electrons [54]. ECAL energy resolution ranges from about 1-2.5% (depending $|\eta|$ and photon conversion) in the barrel region, and from 2.5-4% in the endcap region. [57].

Hadrons pass through the ECAL and are stopped by the HCAL, a hermetic detector which records their energy using a system of scintillator tiles embedded with wavelength-shifting fibers.

The HCAL has three regions, as shown in Fig. 35: barrel (HB), endcap (HE), and an outer region (HO) outside of the solenoid, necessitated by the fact that the HB is volume-limited by the solenoid diameter. In the barrel region $|\eta| < 1.74$, the HCAL cells have widths of 0.087 in pseudorapidity and 0.087 in ϕ , while for $|\eta| > 1.74$ the coverage of the towers increases progressively to a maximum of 0.174 in $\Delta\eta$ and $\Delta\phi$. HCAL towers are mapped onto ECAL towers within the barrel region, and their summed energies are used to determine the location, energy, and axis of jets, as described below in Sec. 7. The HCAL is complimented in the forward region by the HF calorimeters, which each consist quartz fibers in the $\pm z$ directions organized in 432 readout towers in the region $3.0 < |\eta| < 5.2$ [54]. In this analysis, only jets from the barrel region of the calorimeters will be included, while the HF detector is used for the determination of PbPb event centrality as described in Sec. 8.2.

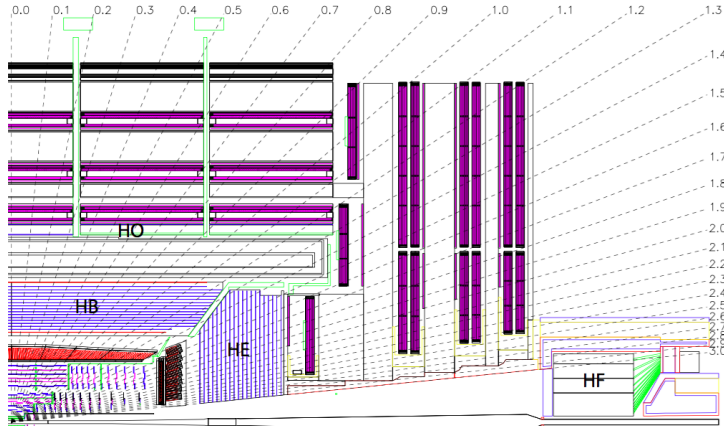


Figure 35. Diagram of the HCAL [54].

5.5 The CMS trigger system

The collision rate at in the LHC is so high that it is impossible to store and process every event that occurs in the CMS detector. A two-level online trigger system is therefore used to select events of interest. Furthermore, data selected with loose trigger requirements (for example “zero bias” data with no selection criteria and “minimum bias” criteria consisting of minimal requirements to demonstrate the presence of a collision event) may also need to be further “prescaled” to limit the rate of recorded events by a specified factor. The trigger system consists of a first (L1) trigger consisting of programmable electronics that use information from the calorimeter and muon systems

of the detector to select events to record. The L1 trigger operates with an interval of approximately $4\mu\text{ s}$, with a maximum rate of 100 kHz. The next trigger level, the High Level Trigger (HLT), consists of a processor farm that allows for more sophisticated event selection based on the reconstruction of physics objects. Reconstruction is performed in a series of steps, or a “HLT path,” chosen to apply selection in order of increasing reconstruction complexity, so as to minimize processing time [58]. This analysis will rely primarily on two kinds of triggers: minimum bias data, and jet-triggered data samples selected by requiring the presence of an online reconstructed jet with $p_{\text{T}} > 80\text{ GeV}$ ($p_{\text{T}} > 100\text{ GeV}$ for 5.02 TeV PbPb data). No prescale is applied for the jet-triggered data samples used in this analysis.

6 TRACK RECONSTRUCTION AND CORRECTION

6.1 Track reconstruction in pp collisions

Standard track reconstruction in CMS occurs in the following steps, summarized here and described in detail in Ref. [56]:

- **Hit reconstruction** – In the pixel tracker, zero-suppression is performed by setting an adjustable threshold, equivalent charge to 3200 for each pixel. Pixel hits are reconstructed as clusters of adjacent pixels, requiring a minimum charge equivalent of 4000 electrons (compared to at least 21,000 electrons deposited by a typical ionizing particle). In the strip detector, zero-suppression is performed by subtracting the baseline pedestal and noise from the signal, and clusters are seeded with channels which contain charge at least three times that of the pedestal. Adjacent strips are added to the cluster if their charge is more than twice that of the pedestal, and the cluster is kept if its total charge is at least five times larger than the combined strip noise. Cluster position in the strip detector is determined from the charge-weighted average of strip positions, corrected for Lorentz drift. The average efficiency for hit reconstruction in both the pixel and strip detectors (excluding 2.4% of pixel modules and 2.3% of strip modules known to be defective) is $> 99\%$.
- **Track seed generation** – Track reconstruction begins by first running a fast track and vertex reconstruction using the pixel tracker only to reconstruct the beamspot position and the location of primary vertices in the event. After this, track reconstruction is carried out in six iterations, each of which begins with “seeds” that define the trajectories and uncertainties of potential tracks. The first set of seeds are pixel triplets, produced from corresponding sets of three pixel hits (on a helical track trajectory) with weak constraints on compatibility with the beam spot to require that the tracks correspond to promptly produced particles. In later iterations, additional information from vertex reconstruction and the silicon strip detector is incorporated in seed generation.
- **Track finding** – The seeds generated in the step above are used as starting points for track-finding based on the Kalman filter method, implemented in four steps for each tracker layer. First, track parameters at the starting level are extrapolated, assuming a perfectly

helical track trajectory (neglecting multiple scatterings, energy loss, and non-uniformity in the magnetic field), to determine the locations of interception in other pixel layers. The second step is a search for tracker modules consistent with the interception locations determined in the previous step. In the third step, hits from mutually exclusive module groups (i.e. groups of modules for which it is not possible that one track could pass through more than one of the grouped modules) are used to update and refine hit locations (including the possibility of adding “ghost” hits where a particle failed to produce a hit due to module inefficiency) and to calculate the Lorentz drift in the silicon bulk. Finally, in the fourth and last step, new track candidates are formed by adding one compatible hit from each of the module groupings, and trajectories are updated combining this added hit with the original track path extrapolation. All track candidates at a given level are then extrapolated to the next compatible layer and the procedure repeated through five iterations.

- **Track fitting** – Finally, the track trajectory is refitted to reduce possible biases (due, for example, to the beam spot constraint introduced in initial seed finding), and to remove outlying hits falsely associated to a track.

After tracks are reconstructed according to this procedure, the track sample both includes a contribution from “fake” tracks (that do not correspond to the trajectory of an ionizing particle), which is reduced by requiring certain selection criteria as discussed in Sec. 6.3. The collection also suffers from detector and reconstruction inefficiencies, which are corrected in this analysis according to the procedure described in Sec. 6.4.

6.2 Track reconstruction in PbPb collisions

In PbPb collision data, dedicated track reconstruction is necessary due to the dramatically greater multiplicity in PbPb compared to pp collisions. This heavy ion tracking occurs in the following steps, and is detailed in Refs. [59] and [60]:

- **Hit reconstruction** – Tracker hits are reconstructed following the same basic procedure applied in pp collisions.
- **Track seed generation** – First, primary vertex positions are reconstructed using only a collection of pixel hits, extrapolated to the region near the beam spot. In PbPb data pileup

is negligible, so there is generally only one primary vertex reconstructed in each event. Initial track seeds are then constructed from pixel triplets only. To reduce combinatorial backgrounds, seeds are restricted to those pointing to a region within 2 mm of the primary vertex, and further selections are applied on track p_T , goodness-of-fit (χ^2), and compatibility between the seed trajectory and the primary vertex.

- **Track finding** – Track trajectories are propagated through the tracker following a procedure similar to that outlined above for pp data. The track seeding and finding procedure is repeated through three iterations. In the second and third iterations, hits belonging unambiguously to a previously identified tracks are first removed, and then reconstruction is repeated using pixel triplet and pixel pair seeds (in the 2nd and 3rd iterations, respectively). Tracks identified in these later iterations are merged into first-iteration tracks, with duplicates removed based on hit matching.

6.3 High purity tracks

The track reconstruction procedures described above for pp and PbPb collision data give track collections with significant “fake rates,” or fraction of reconstructed tracks that cannot be associated with a particle. This fake rate is reduced with a series of quality selections, defined in three levels: “loose” criteria define the minimum to keep tracks in track collections, “tight” criteria are somewhat more stringent (sacrificing some lost efficiency for a lower fake rate), and finally “high purity” criteria are most strict and are those applied for most CMS analyses, including those reported here. Track quality in each case is set with flags for each track, and criteria in each case are applied separately at each iterative tracking step. The precise criteria for high purity tracks at each iterative pass are defined in Refs. [56, 59, 60], and include the following types of selections, imposed as a function of p_T and η :

- Requirements on the number of hits on the track trajectory (N_{hit})
- Requirements on the minimum layers in which the track has an associated hit (N_{layers} , and on the maximum intercepted layers in which the track has no assigned hits
- A minimum imposed on the goodness-of-fit of the track ($\chi^2/\text{Ndof}/N_{\text{layers}}$ or χ^2/N_{hit})

- A maximum on relative track- p_T uncertainty
- Maxima on longitudinal and transverse impact parameters (d_z and d_{xy}) with respect to the primary vertex position and beam spot

In pp data, criteria are optimized by the quality metric $Q(\rho) = s/\sqrt{s + \rho b}$, where s = selected (“real”) tracks, b = selected fake tracks, and parameter $\rho \approx 10$ weights the metric toward minimizing the fake rate. In PbPb data from Run 2, optimization is performed via the output of a multivariate analysis tool (MVA), as detailed in Ref. [60].

6.4 Tracking efficiency and fake rate evaluation and correction

Tracking efficiency is 80-90% in pp collisions, with efficiency lowest at $p_T = 0.5$ GeV and increasing for larger p_T . In the high-multiplicity heavy-ion environment, tracking efficiency is approximately 30% at 0.5 GeV, and increases to 70% for tracks with $p_T > 10$ GeV. Tracking efficiencies are evaluated using PYTHIA and PYTHIA+HYDJET Monte Carlo simulation, by comparing track distributions as generated to those after MC samples are passed through GEANT detector simulation and reconstructed with the algorithms used to reconstruct data. Corrections are derived as a function of centrality, p_T , η , ϕ , and local charged particle density. Tracking efficiency closure and systematic uncertainty is evaluated in pythia and pythia+hydjet, comparing generated track p_T , η , and ϕ distributions to reconstructed distributions before and after correction. For illustration, examples of these closure checks for 5.02 TeV PYTHIA simulation are shown in Fig. 36. Additional 5% residual systematic uncertainty is conservatively assigned for possible differences between MC and data that might affect tracking performance.

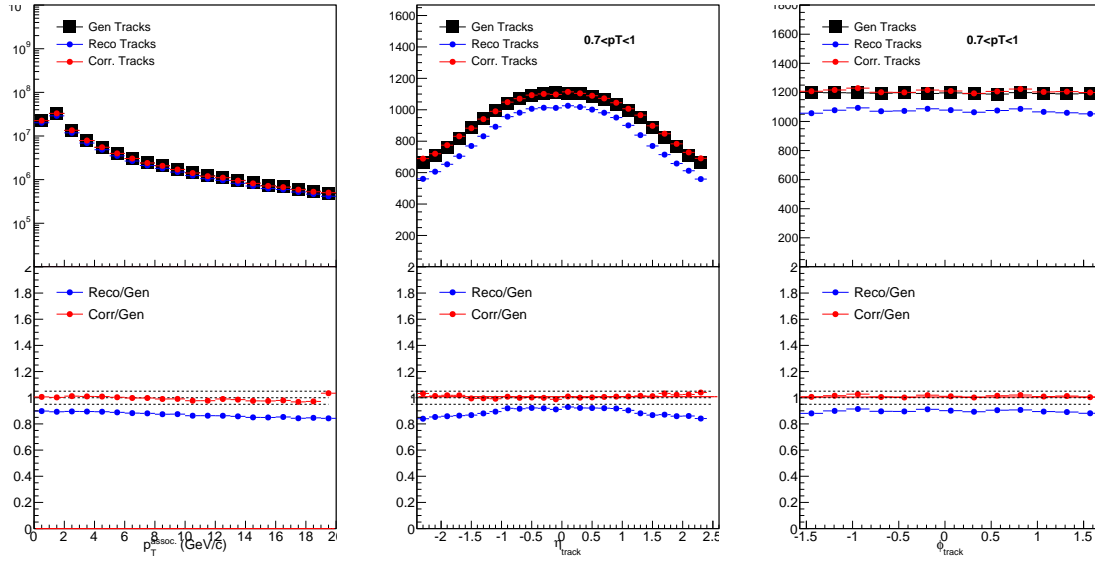


Figure 36. Tracking efficiency correction closure for PYTHIA simulation at 5.02 TeV, comparing tracking generated tracks to uncorrected and corrected reconstructed tracks, as a function of track p_T and of pseudorapidity, and azimuth for the lowest p_T^{trk} bin.

7 JET RECONSTRUCTION AND CORRECTION

7.1 Jet reconstruction with the anti- k_t algorithm

The goal in jet reconstruction is to identify clusters of hadrons originating from a fragmenting high-energy parton. In high- p_T jet studies in pp collisions, the general locations of jets in an event may be qualitatively obvious via large energy deposits in calorimeters; however, there is no clear single standard of how jet boundaries should be drawn. In practice, jets are defined by the algorithms used to find and determine their direction. These algorithms fall in two primary categories: “cone algorithms,” which define jets within specific conical regions (based on the fact that hadronization has little effect total momentum flow), and “sequential recombination algorithms,” which iteratively identify and cluster pairs of closest particles to form jets that are not necessarily conical. [61, 62, 63]. Several properties are desirable, from theoretical and experimental perspectives, in jet finding:

- Straightforward implementation for both theoretical calculations and jet-finding and reconstruction in experimental measurements
- Cross-sections that are finite in perturbation theory
- Infrared and collinear (IRC) safety – the property that a soft collinear emission in a parton splitting should not modify the overall collection of hard (high- p_T) jets in the event, in particular avoiding the possibility of non-cancelling divergences in perturbation calculations
- Soft resilience – clustering jets that are reasonably regular and not overly sensitive to soft particles, a property motivated by the finite resolution of experimental detectors.

Heavy ion jet studies in CMS use the anti- k_t algorithm, a soft-resilient, IRC safe, and straightforward sequential recombination algorithm [62], implemented in the FastJet framework [63]. The anti- k_t algorithm clusters entities (calorimeter towers, particles, or partially clustered pseudo-jets) i and j based on the distance measures d_{ij} between the two particles and d_{iB} between the particle and beam, with the measures defined as:

$$d_{ij} = \min(k_{ti}^{-2}, k_{tj}^{-2}) \frac{(\Delta R_{ij})^2}{R^2}, \quad (21)$$

$$d_{iB} = k_{ti}^{-2}, \quad (22)$$

where k_{ti} refers to the transverse momentum of particle i , ΔR_{ij} refers to the spatial distance (in rapidity and azimuth) between the two particles, and radius parameter R is a reconstruction parameter. The name anti- k_t derives from the negative exponent for k_t (in contrast to other sequential recombination algorithms), which enables IRC safety and soft resilience by making jet shape sensitivity to a particle inversely correlated to the particle's transverse momentum. With this low sensitivity to soft particles, the anti- k_t algorithm results in a collection of mostly circular jets (except in the case of jets separated by less than $2R$, in which each jet has a radius of πR^2). The choice of parameter R is a trade-off between capturing more fragmentation products (as can extend as far as $\Delta R_{ij} = 0.8$ in pp collisions), and limiting the influence of background particles in jet reconstruction. In heavy ion experimental studies, where background levels are very high, typical choices of R range from 0.2 to 0.5.

With the CMS detector, jets may be clustered from ECAL and HCAL information only (“calorimeter jets”) or from information from the full detector, using the particle flow (PF) algorithm. The PF algorithm improves jet energy resolution (JER) substantially at low- p_T (at 10 GeV JER is 15% for PF jets versus 40% for calorimeter jets) with improvements decreasing for higher- p_T jets (at 100 GeV PF jet JER is 8% versus 12% for calorimeter jets, falling to a difference of 4% versus 5% at 1 TeV). For jet-track correlation studies, however, the resolution improvements that the particle flow algorithm offers come at the cost of enhancing sensitivity to tracking biases in the jet-track correlation signal, since low- p_T tracks are included in jet reconstruction. In this analysis, calorimeter jets are used to avoid these auto-correlation effects, and because we will consider jets with $p_T > 120$ GeV for which calorimeter jet energy resolution is adequate. Jets are reconstructed with anti- k_t radius $R = 0.3$ for 2.76 TeV data (“ak3Calo” jets), and with radius $R = 0.4$ for 5.02 TeV data (“ak4Calo” jets). In pp data at 2.76 TeV and 5.02 TeV the contribution to the jet energy from the underlying event (UE) is negligible (less than 1 GeV), so no underlying event subtraction is employed.

7.2 Underlying event subtraction in PbPb data

In PbPb collisions it is necessary to subtract contributions from the large underlying event in order to recover the true jet energy. There are a variety of methods used for underlying event subtraction, of which the following two are relevant for this analysis.

7.2.1 Noise/pedestal subtraction

In most CMS high- p_T jet analyses, including 5.02 TeV PbPb data studies here, underlying event subtraction is performed using a variant of an iterative noise/pedestal subtraction technique [64]. This algorithm occurs in the following steps:

- First, the mean “pedestal” energy in calorimeter cells as a function of energy η ($P(\eta)$) is calculated along with its dispersion.
- The pedestal function $P(\eta)$ is subtracted from all cells.
- Cells with non-physical negative energy entries are then set to zero.
- $\langle E_{\text{cell}} \rangle + \langle \sigma(E_{\text{cell}}) \rangle$ is subtracted from each cell to compensate for the elimination of negative energy cells.
- Jets are clustered from the pedestal-subtracted cells using the anti- k_t algorithm.
- The pedestal function $P(\eta)$ is then re-derived using only cells that are not a part of clustered jets, and the algorithm is repeated.

After this underlying event subtraction is applied, the anti- k_t algorithm with radius parameter $R = 0.4$ is then employed for jet reconstruction (“akPu4Calo jets”).

7.2.2 HF/Voronoi subtraction

For 2.76 TeV PbPb data a different algorithm, designed to eliminate the threshold and possible resulting bias from the noise/pedestal technique, is employed [59]. This algorithm uses information from the HF detector to model and subtract the underlying event using Voronoi decomposition (“HF/Voronoi” algorithm) in the following steps:

- The distribution of underlying E_T as a function of η and ϕ is modeled using singular value decomposition (SVD) training ($dp_T/d\eta/\phi$ with Voronoi parameters $v_1\dots v_4$) to extrapolate the UE distribution from the HF calorimeter at large η to the central analysis region ($|\eta| < 1.6$).
- The modeled UE distribution is subtracted from all calorimeter cells.
- Each calorimeter cell is associated with its nearest neighbors, and energy is redistributed between neighboring in an “equalization” procedure used to eliminate non-physical negative E_T entries (optimized to minimize energy transfers).

After Voronoi subtraction and equalization, the anti- k_t algorithm is employed with radius parameter $R = 0.3$ to cluster (“akVs3Calo”) jets.

7.3 Jet energy corrections

Jet reconstruction as described above gives spatial coordinates and p_T for each jet as measured by the detector. Our goal in jet studies, however, is to reconstruct the true total parton or particle energy. This is achieved through jet energy corrections (JEC) that establish a mapping between measured energy (which does not, for example, include neutrinos produced in jet fragmentation) and “true” jet energies. This mapping is complicated by nonlinearity in detector response. Initial corrections are derived as a function of p_T and η using dijet QCD samples of PYTHIA and PYTHIA+HYDJET Monte Carlo, spatially matching reconstructed jets to generated particles, and comparing generated versus reconstructed jet energy for these matched jets. These “MC truth” corrections are applied to measured jet energies to return a collection of jets that, on average, capture the kinematic distribution of the partons before fragmentation.

These corrections do not, however, fully account for the non-linearity of calorimeter response. In particular, in an effect particularly relevant for jet-track correlation studies, the jet energy scale depends on jet fragmentation. Given two jets with identical parton energy, the jet with softer fragmentation (i.e. jets with a higher fraction low- p_T particles) will be on average reconstructed with lower energy than the jet with harder fragmentation. When combined with a jet selection threshold, this non-linearity results in a bias that systematically underestimates the jets with soft fragmentation in the analysis sample. An additional fragmentation-function dependent jet energy correction (JFF-JEC) is therefore applied after initial jet energy corrections in order to

reduce this bias (detailed in Ref. [59]). These JFF-JEC are derived using the number of particle flow candidates (N_{PF}) in the jet with $p_T > 2$ GeV, with this threshold chosen to reduce the influence of soft fluctuations in the underlying event. Correction tables are derived as a function of N_{PF} , jet p_T , and PbPb event centrality in PYTHIA and PYTHIA+HYDJET simulation, and are applied to jets after the JECs described above. Finally, iterative residual corrections are applied as a function of jet p_T . The application of JFF-JECs reduces the overall quark/gluon non-closure, as illustrated for PbPb data in Fig. 37, and slightly improves jet energy resolution overall.

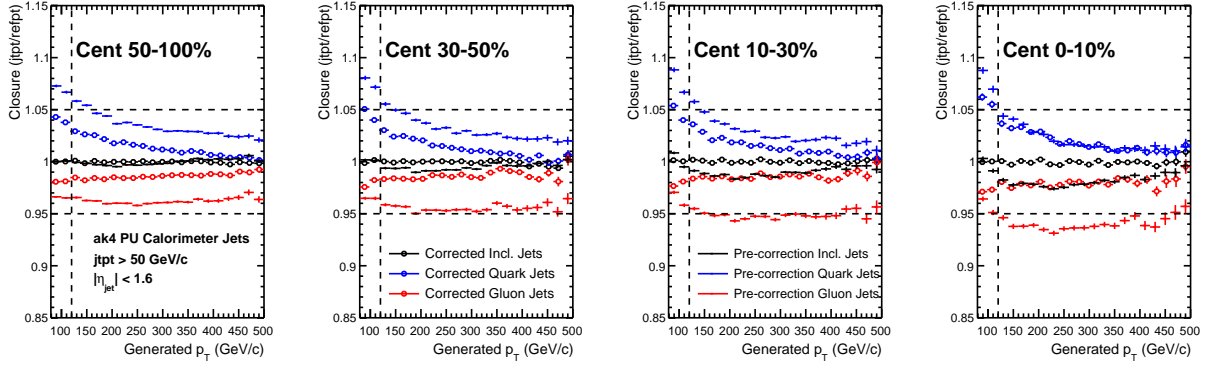


Figure 37. Closure with and without JFF-JEC for quark and gluon jets.

8 DATA AND MONTE CARLO SAMPLES

8.1 Data samples and event selection

This analysis is based on PbPb and pp data collected with the CMS detector at 2.76 TeV and 5.02 TeV during Run 1 and Run 2 of the CERN LHC. Studies at 2.76 TeV use $166 \mu\text{b}^{-1}$ of PbPb data collected in 2011, and 5.3 pb^{-1} of pp data collected in 2013. Studies at 5.02 TeV use $404 \mu\text{b}^{-1}$ of PbPb data and 25 pb^{-1} of pp data, both collected in 2015. Online collision selection was performed using the CMS HLT described in Sec. 5.5 to obtain a minimum bias sample of PbPb collision events, and to obtain samples of PbPb and pp data with the requirement that events contain at least one high- p_{T} jet (with $p_{\text{T}} > 80 \text{ GeV}$ for pp data and 2.76 TeV PbPb data, $p_{\text{T}} > 100 \text{ GeV}$ for 5.02 TeV PbPb data). These jet triggers are fully efficient for offline-reconstructed jets with $p_{\text{T}} > 120 \text{ GeV}$. Total numbers of selected events are summarized in Table I.

TABLE I. Summary of data samples and number of selected events

Dataset	Number of selected events
2.76 TeV PbPb MinimumBias	1.01 M
2.76 TeV PbPb Jet-triggered ($p_{\text{T}} > 80 \text{ GeV}$)	1.25 M
2.76 TeV pp Jet-triggered ($p_{\text{T}} > 80 \text{ GeV}$)	1.27 M
5.02 TeV PbPb MinimumBias	764 k
5.02 TeV PbPb Jet-triggered ($p_{\text{T}} > 100 \text{ GeV}$)	3.35 M
5.02 TeV pp Jet-triggered ($p_{\text{T}} > 80 \text{ GeV}$)	2.66 M

A number of quality cuts are applied, as is standard for CMS analyses to remove detector noise backgrounds, ultra-peripheral collisions, beam gas events, and events with exceptionally large pixel occupancy. These selection criteria have shown to have negligible impact on dijet analyses [65, 66], and are as follows in PbPb and pp collisions:

- Vertex-z position within 15 cm of the center of the detector ($|v_z| < 15$)
- Primary vertex filter – a requirement that events include a reconstructed primary vertex filter with at least two tracks, requiring the presence of inelastic hadronic scattering and removing beam-gas events and ultra-peripheral collisions

- Beam-scraping filter – a requirement of pixel clusters compatible with the primary vertex. In pp, this requires that if there are more than 10 tracks, at least 25% of tracks must be highPurity (see Sec. 6)
- HB/HE noise filter – a filter to exclude events exhibiting uncharacteristic calorimeter noise [67]
- PbPb data only: HF coincidence filter – at least 3 GeV recorded in at least each of at least three hadronic forward calorimeter towers on each side of the interaction point

These cleaning cuts are applied to both minimum bias and jet-triggered data samples. Additional event selection will later be applied to obtain samples of high- p_T jets and dijet events, as discussed in Sec. 8.4 below.

8.2 Collision centrality determination and classes

The variable centrality is used to parameterize the degree of overlap of the colliding nuclei. In CMS, centrality is determined using total transverse energy (E_T) in the HF calorimeter towers, in the region $4.0 < |\eta| < 5.2$. The distribution of total E_T in all events is used to divide the total minimum bias event sample into centrality bins, each containing 0.5% of the total events. The resulting centrality distribution is flat in minimum bias data by construction. In jet-triggered data, however, requiring the presence of a high- p_T jet results in a larger fraction of more central collisions (in which hard-scatterings are more likely). The collisions defined as “most central” (centrality = 0%) are those with the greatest E_T , corresponding to collisions in which the nuclei collided head-on. In contrast, the collisions defined as “least central” or “most peripheral” (centrality = 100%) are those in which the nuclei barely overlapped at all. To observe how jet modifications evolve with changing centrality, this analysis considers four centrality classes: 0-10% (most central), 10-30%, 30-50%, and 50-100%.

8.3 Monte Carlo simulation

Monte Carlo (MC) simulation is used in this analysis to evaluate and correct for jet reconstruction performance and tracking efficiency for both pp and PbPb data. Simulation of pp data and of the hard processes in PbPb data are performed using the PYTHIA (version 6, tune Z2 [68]) event generator. In order to have reasonable event samples in all jet p_T ranges, different samples

are produced with various cut-off values of \hat{p}_T , which are then combined using their respective cross-sections as weights. To simulate CMS detector output for MC events, GEANT4 detector simulation is used [69]. Jet and track reconstruction performance and efficiency for pp data is evaluated by comparing observables in PYTHIA samples as generated to the same observables after they have been passed through the detector simulation and the same reconstruction procedures applied to pp data. For the relevant jet kinematics observables relevant to this analysis, PYTHIA reasonably reproduces pp data.

For PbPb data, the underlying event is simulated using HYDJET (Drum5 tune) [70], which combines hydrodynamics with “mini-jets” produced with quenched PYTHIA input. Hard processes are generated using PYTHIA, and are directly embedded in this HYDJET sample (referred to as PYTHIA+HYDJET simulation), with no medium quenching effects applied to the embedded jets. This PYTHIA+HYDJET sample is used to evaluate the reconstruction effects of the presence of the heavy ion collision environment, *other* than the jet-medium interactions that are our objects of study. As for PYTHIA simulation of pp data, comparing PYTHIA+HYDJET samples that have been passed through the detector and reconstructed chain to the generated Monte Carlo allows for the evaluation of jet and track reconstruction performance.

8.3.1 Monte Carlo centrality and vertex-z reweighting

Simulated PYTHIA+HYDJET samples are generated minimum bias, and therefore must be reweighted to match the bias toward more central events induced by requiring the presence of a high- p_T jets discussed in Sec. 8.2. Reweighting factors are calculated for each 0.5%-wide centrality bin, and applied to the PYTHIA+HYDJET sample overall to match the PbPb centrality distribution. Similarly, another reweighting procedure is performed to match the distributions of the position of the primary interaction along the beam direction in MC and data for both pp and PbPb collisions. Figures 38-40 illustrate the necessity and effects of these reweighting procedures.

8.3.2 Monte Carlo samples at 2.76 TeV

Tables II and III summarize the PYTHIA and PYTHIA+HYDJET samples used in this analysis by \hat{p}_T , with respective numbers of generated events and cross-sections used for combining samples.

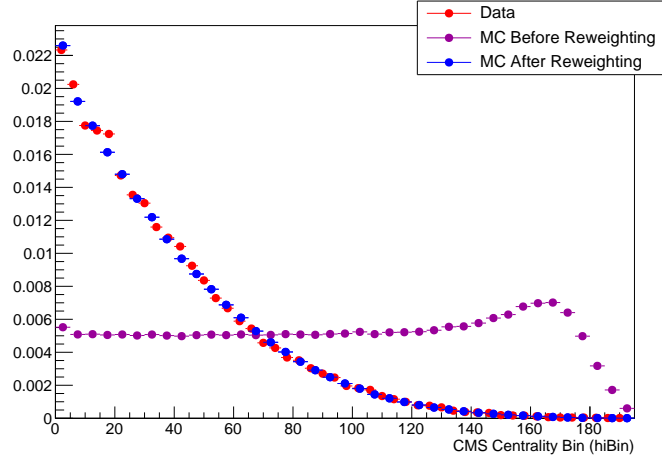


Figure 38. Centrality distribution for PYTHIA+HYDJET reweighted to PbPb data.

TABLE II. Summary of Monte Carlo samples and generated events at 2.76 TeV

Generator	Process	Cross section (mb)	Number of events
PYTHIA+HYDJET	$\hat{p}_T > 50$ GeV	1.025×10^{-3}	395k
PYTHIA+HYDJET	$\hat{p}_T > 80$ GeV	9.865×10^{-5}	368k
PYTHIA+HYDJET	$\hat{p}_T > 120$ GeV	1.129×10^{-5}	367k
PYTHIA+HYDJET	$\hat{p}_T > 170$ GeV	1.465×10^{-6}	392k
PYTHIA+HYDJET	$\hat{p}_T > 220$ GeV	2.837×10^{-7}	181k
PYTHIA+HYDJET	$\hat{p}_T > 280$ GeV	2.837×10^{-7}	50k
PYTHIA	$\hat{p}_T > 80$ GeV	9.865×10^{-5}	104k
PYTHIA	$\hat{p}_T > 120$ GeV	1.129×10^{-5}	975k
PYTHIA	$\hat{p}_T > 170$ GeV	1.465×10^{-6}	69k

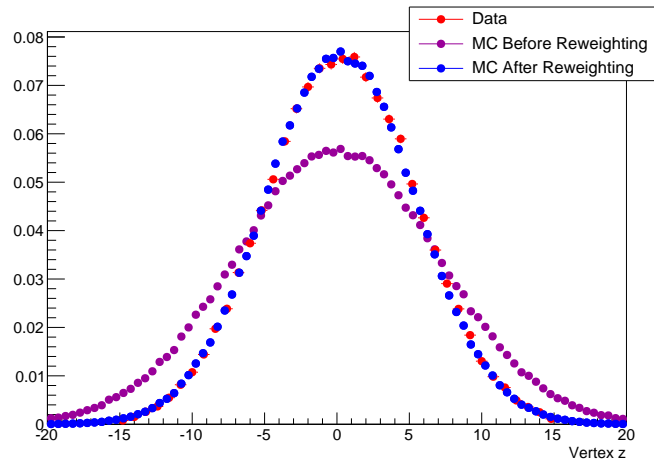


Figure 39. Vertex z distribution for PYTHIA+HYDJET reweighted to PbPb data.

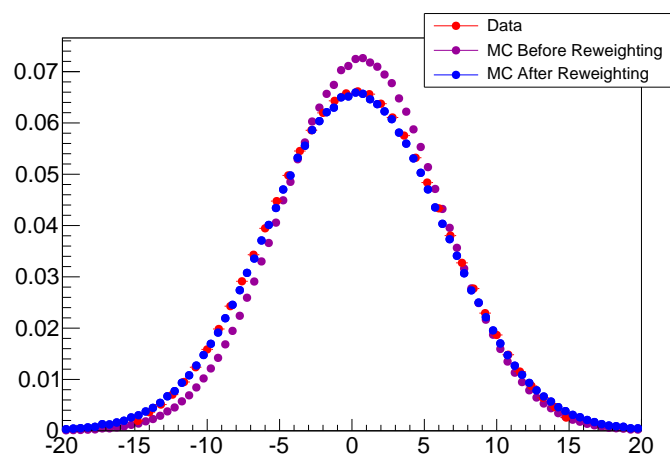


Figure 40. Vertex z distribution for PYTHIA reweighted to pp data.

8.3.3 Summary of Monte Carlo samples at 5.02 TeV

TABLE III. Summary of Monte Carlo samples and generated events at 5.02 TeV

Generator	Process	Cross section (mb)	Number of events
PYTHIA+HYDJET	$\hat{p}_T > 80 \text{ GeV}/c$	4.412×10^{-4}	499k
PYTHIA+HYDJET	$\hat{p}_T > 120 \text{ GeV}/c$	6.147×10^{-5}	496k
PYTHIA+HYDJET	$\hat{p}_T > 170 \text{ GeV}/c$	1.018×10^{-5}	498k
PYTHIA+HYDJET	$\hat{p}_T > 220 \text{ GeV}/c$	2.477×10^{-6}	200k
PYTHIA+HYDJET	$\hat{p}_T > 280 \text{ GeV}/c$	6.160×10^{-7}	200k
PYTHIA	$\hat{p}_T > 80 \text{ GeV}/c$	4.412×10^{-4}	500k
PYTHIA	$\hat{p}_T > 120 \text{ GeV}/c$	6.147×10^{-5}	500k
PYTHIA	$\hat{p}_T > 170 \text{ GeV}/c$	1.018×10^{-5}	499k
PYTHIA	$\hat{p}_T > 220 \text{ GeV}/c$	2.477×10^{-6}	200k
PYTHIA	$\hat{p}_T > 280 \text{ GeV}/c$	6.160×10^{-7}	200k

8.4 Jet selection and dijet asymmetry classes

Jet selection in this analysis is restricted to the pseudorapidity region $|\eta_{\text{jet}}| < 1.6$ to ensure stable reconstruction performance in the calorimeter barrel region. A requirement is also imposed that the highest- p_T track contains no less than 1% and no more than 98% of the total jet p_T . In the jet selection referred to as “inclusive jets” for analysis at both 2.76 TeV and 5.02 TeV, all jets with $p_{T,\text{jet}} > 120$ GeV are considered. In this selection, it is possible to select more than one jet from the same event, provided that each jet satisfies the inclusive selection criteria.

In addition to the inclusive jet selection, a “dijet” selection of events containing two back-to-back high- p_T jets is also analyzed for the 2.76 TeV data sample. Events are included in this sample based on the criteria that they contain highest- p_T “leading” jet with $p_{T,1} > 120$ GeV and a second-highest- p_T “subleading” jet with $p_{T,2} > 50$ GeV with relative azimuthal separation between the two jets $\Delta\phi_{1,2} > \frac{5\pi}{6}$. This dijet sample is subdivided into a sample of relatively “balanced” dijets, with similar $p_{T,1}$ and $p_{T,2}$ and a sample of relatively “unbalanced” dijets in which the leading jet has a much larger p_T than the subleading jet based on asymmetry parameter A_J . The balanced selection is defined as those events for which $A_J < 0.22$, while the unbalanced selection as defined as those events for which $A_J > 0.22$. The dividing value $A_J = 0.22$ is chosen for consistency with previous CMS analyses [38, 39]. In this analysis, 52% of central PbPb events are balanced, while 67% of pp events are balanced. Jet kinematics for all jet samples (broken down by asymmetry for 2.76 TeV dijet data) are shown in Appendix A.1 for 2.76 TeV data and in Appendix A.2 for 5.02 TeV data.

8.5 Track selection and classes

Tracks, reconstructed as described in Sec. 6 are required to satisfy the following criteria:

- $|\eta_{\text{trk}}| < 2.4$ – restricts to the barrel region of the tracker
- $0.5 < p_T^{\text{trk}} < 300$ GeV – excludes very low- p_T tracks where reconstruction performance is not stable
- High Purity criteria – see Sec. 6.3

- Distance of closest approach (DCA) in x-y plane and in z less than 3 times the DCA error – reduces fraction of tracks not associated with a primary vertex
- Relative p_T^{trk} error less than 30% (10% for 5.02 TeV PbPb data) – removes tracks with very poor resolution (has a negligible effect on efficiency as CMS resolution is generally good)

For 5.02 TeV PbPb data, the following additional criteria are also applied to reduce the contribution from misidentified tracks [60]:

- Exclude tracks with fewer than 11 tracker hits
- Require that for each track the chi-squared over number of degrees of freedom (χ^2/Ndof) of the track fit, also divided by the number of tracker layers (nLayer) hit as the track passed through the detector, is less than 0.15, i.e. $\chi^2/\text{Ndof}/\text{nLayer} < 0.15$.
- For tracks with $p_T > 20$ GeV (the kinematic region in which misreconstruction is difficult to access with Monte Carlo), calorimeter matching is applied: since high- p_T tracks eventually deposit their energy in a calorimeter after passing through the tracker, tracks are required to be associated with calorimeter transverse energy $E_T = (E_{\text{ECAL}} + E_{\text{HCAL}})/\cosh(\eta_{\text{trk}})$, such that $E_T > 0.5p_T^{\text{trk}}$

After these selection criteria are applied, tracking efficiency corrections are applied as described in Sec. 6.4. Tracks in this analysis are considered in the following classes: 0.5–1 GeV, 1–2 GeV, 2–3 GeV, 3–4 GeV, 4–8 GeV, 8–12 GeV, 12–16 GeV, 16–20 GeV, and above 20 GeV. Not all bins are considered in every analysis, and for 5.02 TeV studies the lowest- p_T^{trk} bin is 0.7–1 GeV.

8.6 Summary of analysis bins

Table IV summarizes the key kinematic selections and bins for the three components to this analysis. In all cases, identical selection is applied to PbPb and pp data. Event, jet, and track quality cuts are not included in this table.

TABLE IV. Summary of data selections and analysis bins

Variable	2.76 TeV Inclusive	5.02 TeV Inclusive	2.76 TeV Dijets
PbPb Centrality	0-10%, 10-30%, 30-50%, 50-100%	0-10%, 10-30%, 30-50%, 50-100%	0-10%, 10-30%, 30-50%, 50-100%
Jet Selection	$ \eta_{\text{jet}} < 1.6$ $p_{\text{T}} > 120 \text{ GeV}$	$ \eta_{\text{jet}} < 1.6$ $p_{\text{T}} > 120 \text{ GeV}$	$ \eta_{\text{jet}} < 1.6$ $p_{\text{T},1} > 120 \text{ GeV}$ $p_{\text{T},2} > 50 \text{ GeV}$ $\Delta\phi_{1,2} > \frac{5\pi}{6}$
A_{J} Bins	–	–	$A_{\text{J}} < 0.22$, $A_{\text{J}} > 0.22$
Track η	$ \eta_{\text{trk}} < 2.4$	$ \eta_{\text{trk}} < 2.4$	$ \eta_{\text{trk}} < 2.4$
$p_{\text{T}}^{\text{trk}}$ Bins	1-2 GeV, 2-3 GeV, 3- 4 GeV, 4-8 GeV	0.7-1 GeV, 1-2 GeV, 2-3 GeV, 3-4 GeV, 4- 8 GeV	0.5-1 GeV, 1-2 GeV, 2-3 GeV, 3-4 GeV, 4- 8 GeV, 8-300 GeV

9 JET-TRACK CORRELATION MEASUREMENTS

Portions of the material in this chapter, which is my own work, were published in Refs. [1, 2, 3].

9.1 Analysis procedure

Measurements in this analysis are carried out by considering correlations between high- p_T jets and tracks in PbPb and pp collisions. Jets are selected within $\eta < 1.6$ and p_T above a particular threshold. For each jet, the relative separation in pseudorapidity ($\Delta\eta = \eta_{\text{track}} - \eta_{\text{jet}}$) and azimuth ($\Delta\phi = \phi_{\text{track}} - \phi_{\text{jet}}$) is measured between the jet and all charged-hadron tracks within $\eta < 2.4$. For each jet-track pair, these measurements are recorded in a two-dimensional $\Delta\eta - \Delta\phi$ correlation in a particular track transverse momentum (p_T^{trk}) and centrality class. Each correlation is normalized by dividing by the number of jets in the sample (N_{jets}), resulting in a signal pair distribution, $S(\Delta\eta, \Delta\phi)$, that gives the per-jet yield of tracks and their relative distance from the jet:

$$S(\Delta\eta, \Delta\phi) = \frac{1}{N_{\text{jets}}} \frac{d^2 N^{\text{same}}}{d\Delta\eta d\Delta\phi}. \quad (23)$$

This procedure results in a two dimensional measurement of the distribution of charged tracks with respect to the jet axis. The same procedure may also be repeated, weighting each track by its p_T^{trk} , in order to obtain a distribution of transverse momentum with respect to the jet axis. These particle density and p_T^{trk} correlations form the basis for all results discussed in this analysis. From this point, several additional corrections and other steps are necessary to isolate jet-related effects from long range and uncorrelated backgrounds. These additional steps are as follows:

- A correction for jet-track pair acceptance effects;
- Separation of correlations into short-range jet peaks and long range components;
- Monte Carlo-based corrections for biases related to jet reconstruction.

After these steps, a range of different observables may be extracted to characterize the multiplicity and distribution of tracks and p_T^{trk} at both small and large angles from the jet axis.

9.2 Jet-track correlation pair-acceptance correction

This analysis considers $\Delta\eta$ jet-track separations as large as $\Delta\eta = 2.5$. With finite η acceptance for both jets and tracks ($|\eta_{\text{jet}}| < 1.6$ and $|\eta_{\text{track}}| < 2.4$, tracks that fall within $\Delta\eta = 2.5$ of a jet may be outside the tracking acceptance. This pair acceptance effect results in trapezoidal correlations that fall with rising $|\Delta\eta|$ as tracks are “lost” outside of the acceptance. This effect is purely geometric, and may be corrected by reproducing this pair acceptance geometry. This is done by creating a “mixed event” correlation in which jets in the sample are correlated to tracks within $|\eta| < 2.4$ from randomly selected events in a minimum bias PbPb sample, matched in vertex- z position (within 0.5 cm) and centrality (within 2.5%). This reproduces the pair acceptance geometry from the signal correlations:

$$ME(\Delta\eta, \Delta\phi) = \frac{1}{N_{\text{jets}}} \frac{d^2 N^{\text{mix}}}{d\Delta\eta d\Delta\phi}, \quad (24)$$

is constructed to account for pair-acceptance effects, with N^{mix} denoting the number of mixed-event jet-track pairs. The mixed event correction is normalized to unity at $\Delta\eta=0$, where the jet and track are colinear in η and therefore have perfect pair acceptance, with the normalization factor $ME(0, 0)$. Dividing the signal correlation $S(\Delta\eta, \Delta\phi)$, defined in Equation 23, by this normalized mixed event correlation $ME(\Delta\eta, \Delta\phi)/ME(0, 0)$ yields the corrected per-jet correlated yield distribution, as illustrated in Figure 41:

$$\frac{1}{N_{\text{jets}}} \frac{d^2 N}{d\Delta\eta d\Delta\phi} = \frac{ME(0, 0)}{ME(\Delta\eta, \Delta\phi)} \times S(\Delta\eta, \Delta\phi). \quad (25)$$

9.3 Separation of correlations into long range and short-range components

After correlations are corrected for pair-acceptance effects, in each correlation we are left with a well-defined jet peak sitting at $\Delta\eta = 0$, $\Delta\phi = 0$ on top of a large combinatoric and long range correlated background. For most measurements, it is necessary to isolate this jet peak in order to distinguish jet-related effects from eventwise correlations. In order to achieve this, we note that the long range correlation is independent of $\Delta\eta$ at distances larger than $\Delta\eta = 1.5$ from the jet. This “sideband” region ($1.5 < |\Delta\eta| < 3.0$) is used to model the underlying event, capturing both

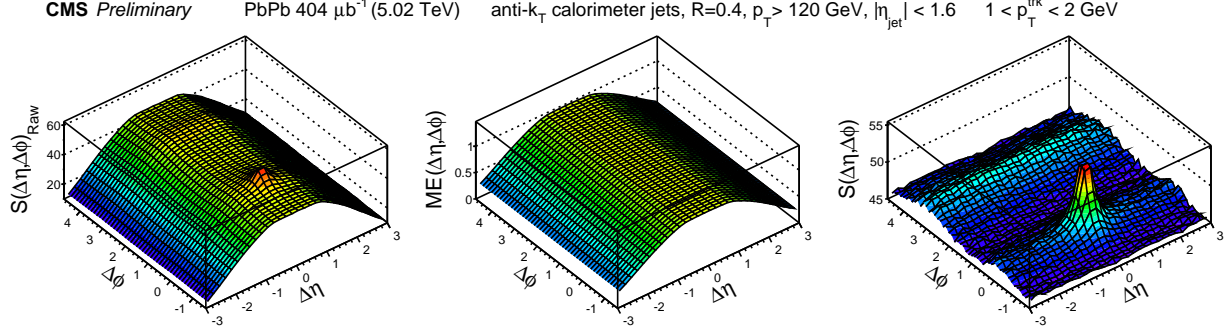


Figure 41. Illustration of the pair-acceptance correction procedure: left panel shows signal correlation $S(\Delta\eta, \Delta\phi)$, and center panel shows mixed event correlation $ME(\Delta\eta, \Delta\phi)$. Dividing the signal correlation by the normalized mixed event correlation yields the corrected per-jet correlated yield distribution shown in the right panel.

the level of the combinatoric background in the event, and also the long range “flow” correlations in the event. The assumption of rapidity–independence of the flow harmonics is based on the CMS study [71], which shows no appreciable variation of the elliptic flow for charged particles above 1 GeV in the pseudorapidity interval of $\Delta\eta < 3.0$ relevant for this study. As long range correlations depend only on $\Delta\phi$, the sideband region is projected into $\Delta\phi$ to obtain a one-dimensional model of the underlying event. To subtract this long range correlation in 2D, this distribution may be either directly re-propagated into $\Delta\phi$ (as shown in Figure 42), or may be fit in $\Delta\phi$ before repropagation in a smoothing procedure as shown in Fig. 43. When aiming to simply remove the long range correlated background, we fit long range correlations function modeling harmonic flow plus a term to capture the (Gaussian or sharper) “away-side” peak opposite the jet in relative azimuth:

$$B(\Delta\phi) = B_0(1 + 2V_1 \cos(\Delta\phi) + 2V_2 \cos(2\Delta\phi) + 2V_3 \cos(3\Delta\phi)) + A_{\text{AS}} \exp\left(-\left(\frac{|\Delta\phi - \pi|}{\alpha}\right)^\beta\right), \quad (26)$$

In this case, the fit is performed only as a smoothing procedure to model the background under the near-side jet peak.; as only the jet peak within $|\Delta\phi| < \frac{\pi}{2}$ is studied, the fit to the away-side peak is not relevant to the analysis. Furthermore, no physics conclusions can be extracted from the V_n terms in this fit, which are used only to establish a reasonable functional form for smooth modeling of the background distributions.

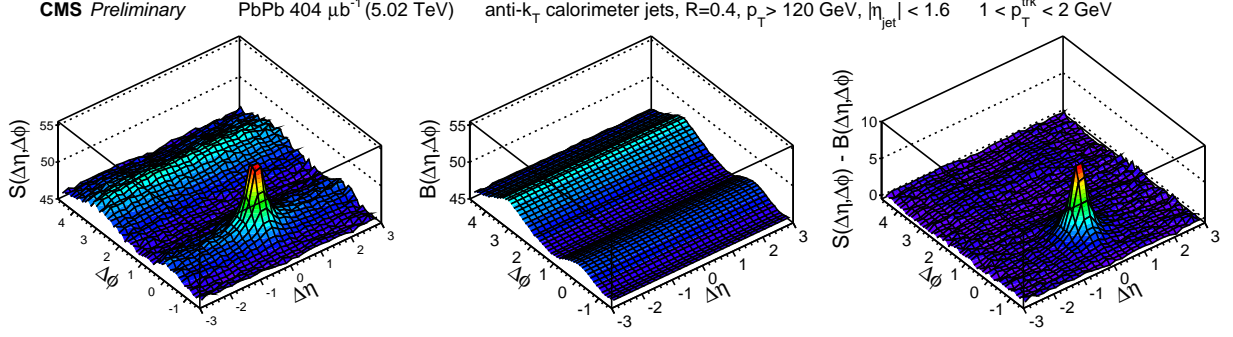


Figure 42. Illustration of the event decomposition procedure without $\Delta\phi$ fitting: left panel shows the acceptance-corrected correlation, middle panel shows the projected and re-propagated long range distribution, and right panel shows the background-subtracted jet peak.

The long range correlations in the underlying event are in themselves interesting objects of study, however, as they contain information about the collective behavior of particles in the event as a whole, and the extent to which the distribution of high- p_T jets in the event couple to this collective flow. To further study the long range correlations, we may apply the well-established harmonic flow decomposition method used to study two-particle correlations [72] to correlations between jets and tracks. In dijet studies, more accurate information about long range flow correlations can furthermore be obtained by making use of the fact that for our dijet selection and a given value of $\Delta\eta$ the region $-\frac{\pi}{2} < \Delta\phi < \frac{\pi}{2}$ of the leading correlation is by definition equivalent to the region $\frac{\pi}{2} < \Delta\phi < 3\frac{\pi}{2}$ of the subleading correlation. This provides a full 2π distribution of the long range correlated underlying event under both the leading and subleading jet peaks. We can then perform a single fit to the combined background. Here we fit with harmonic flow terms only:

$$B(\Delta\phi)^{\text{Dijet}} = B_0(1 + 2V_1 \cos(\Delta\phi) + 2V_2 \cos(2\Delta\phi) + 2V_3 \cos(3\Delta\phi)), \quad (27)$$

In this fit, we find that terms through V_3 are necessary to describe the low- p_T , central background, while at higher- p_T only V_1 , V_2 . From this combined fit, we extract parameters V_1 , V_2 , and V_3 . Then, to better constrain the background under the signal and minimize the effects of random background fluctuations, we apply the factorization relation of overall Fourier harmonic $V_2 = v_2^{\text{jet}} \times v_2^{\text{trk}}$ [73, 24]. The values of v_2^{trk} for charged particles are determined in Ref. [72], while the fit parameter v_2 is expected to be independent of p_T^{trk} ranges for a given centrality class. The

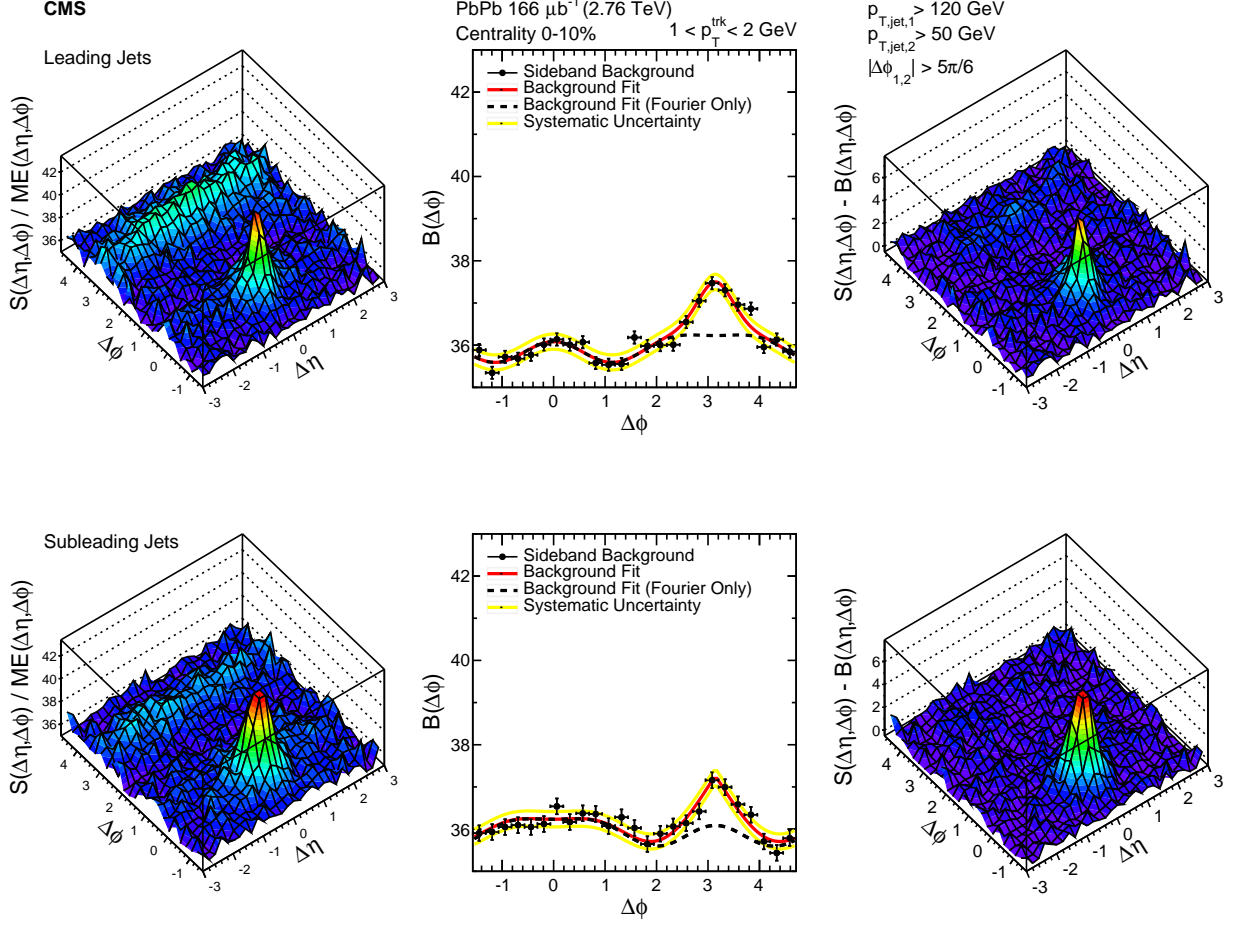


Figure 43. Illustration of the event decomposition procedure with $\Delta\phi$ fitting: left panel shows the acceptance-corrected correlation, middle panel shows the projected and fit long range distribution, and right panel shows the background-subtracted jet peak.

average value of v_2^{jet} from each p_T^{trk} range is calculated, and used to fix the V_2 parameter on the second iteration of the fit. Both the combined dijet fit with $B(\Delta\phi)^{\text{Dijet}}$ and the final $B(\Delta\phi)$ fits are shown in Appendix B. Through this process, we characterize the underlying event and note that the distribution of jets as well as tracks couples to the flow modulation of the underlying event. This has immediate consequences for studies of momentum balance between leading and subleading hemispheres of the event: as there are non-zero contributions from odd harmonics to the long-range correlated backgrounds, we cannot expect flow cancellation when directly subtracting hemisphere p_T^{trk} distributions.

For jet peak studies the underlying event is a background to subtracted to isolate jet peaks. After this is done, either by direct subtraction or by subtracting the fit and re-propagated background, we are left with isolated 2D jet peaks. Before extracting observables, we must carefully consider and correct for reconstruction biases affecting these correlated yields. Before correlations are constructed, both tracks and jets are corrected for detector efficiencies and other reconstruction effects, as discussed in detail in Sec. 6 and Sec. 7, respectively. There are two additional effects, however, in which jet biases are coupled to the multiplicity of low- p_T tracks: a bias against reconstructing jets with soft fragmentation that arises from nonlinearity in calorimeter response (reduced but not eliminated by the JFF-JEC described in Sec. 7.3), and a bias toward selecting jets that sit on upward (soft) fluctuations in the background resulting in excess low- p_T yields around the jet axis. Both effects are studied and corrections obtained by carrying out the full analysis in Monte Carlo simulation, and corrections are applied to the data correlations after background subtraction.

9.4 Residual Jet Fragmentation Function correction

Jets with harder fragmentation are more likely to be successfully reconstructed than jets with softer fragmentation, resulting in a bias toward the selection of jets with fewer associated tracks in both pp and PbPb data for all track- p_T selections studied. This bias is partially resolved by the jet fragmentation function-dependent jet energy corrections described in Sec. 7. Following the method used in [39], corrections are derived for this bias and for the related possible effect of "jet swapping" between leading, subleading, and additional jets by comparing correlated per-trigger particle yields for all reconstructed jets versus all generated jets. This correction is derived for each jet selection in PYTHIA-only simulation, and also in PYTHIA embedded and reconstructed in a HYDJET underlying event, excluding HYDJET tracks from the correction determination. For illustration, the derivation and magnitude of these corrections for inclusive jets at 2.76 TeV are shown in Figs. 44–47.

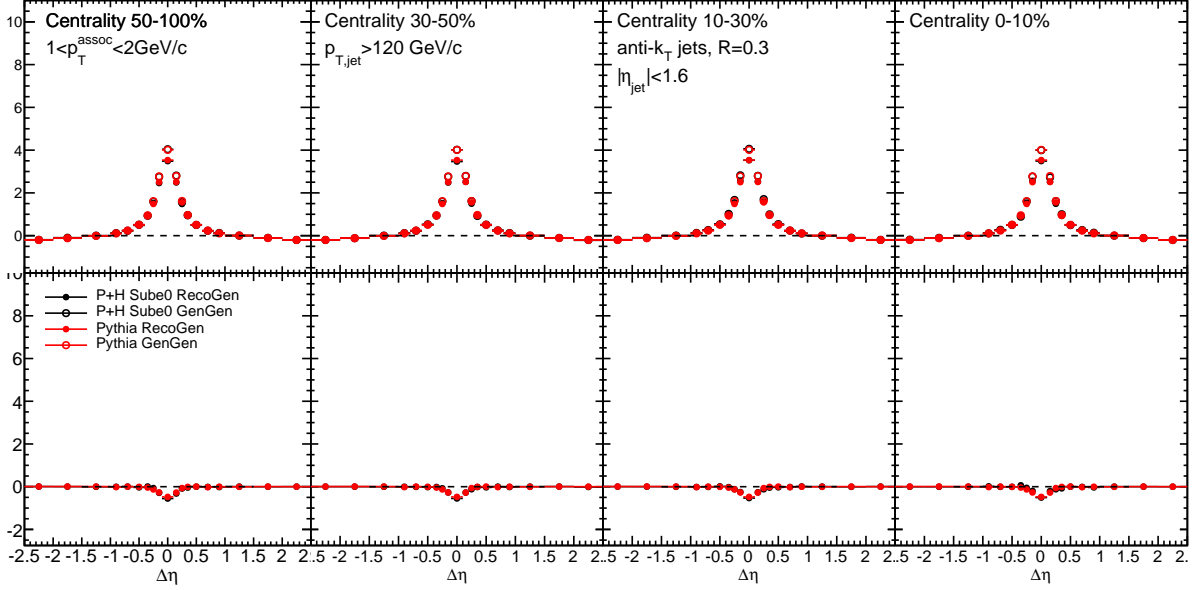


Figure 44. $\Delta\eta$ jet fragmentation function bias corrections derived by comparing correlations between reconstructed vs. generated jets and generated PYTHIA events, with and without embedding into the HYDJET heavy ion environment, for particles $1 < p_T^{\text{trk}} < 2$ GeV.

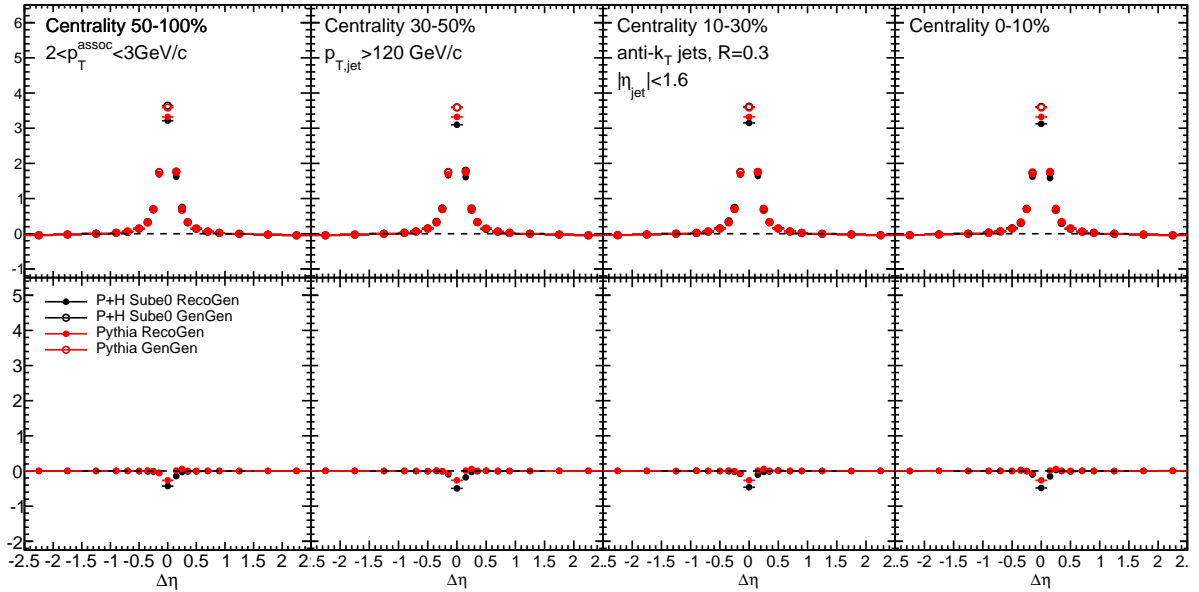


Figure 45. $\Delta\eta$ jet fragmentation function bias corrections derived by comparing correlations between reconstructed vs. generated jets and generated PYTHIA events, with and without embedding into the HYDJET heavy ion environment, for particles $2 < p_T^{\text{trk}} < 3$ GeV.

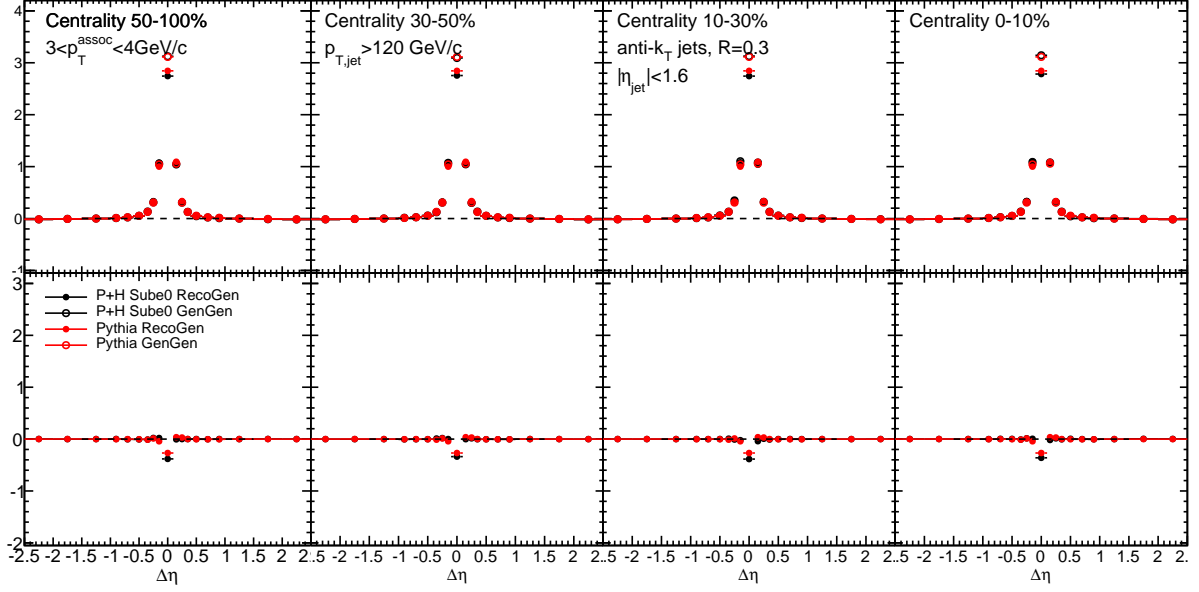


Figure 46. $\Delta\eta$ jet fragmentation function bias corrections derived by comparing correlations between reconstructed vs. generated jets and generated PYTHIA events, with and without embedding into the HYDJET heavy ion environment, for particles $3 < p_T^{\text{trk}} < 4$ GeV.

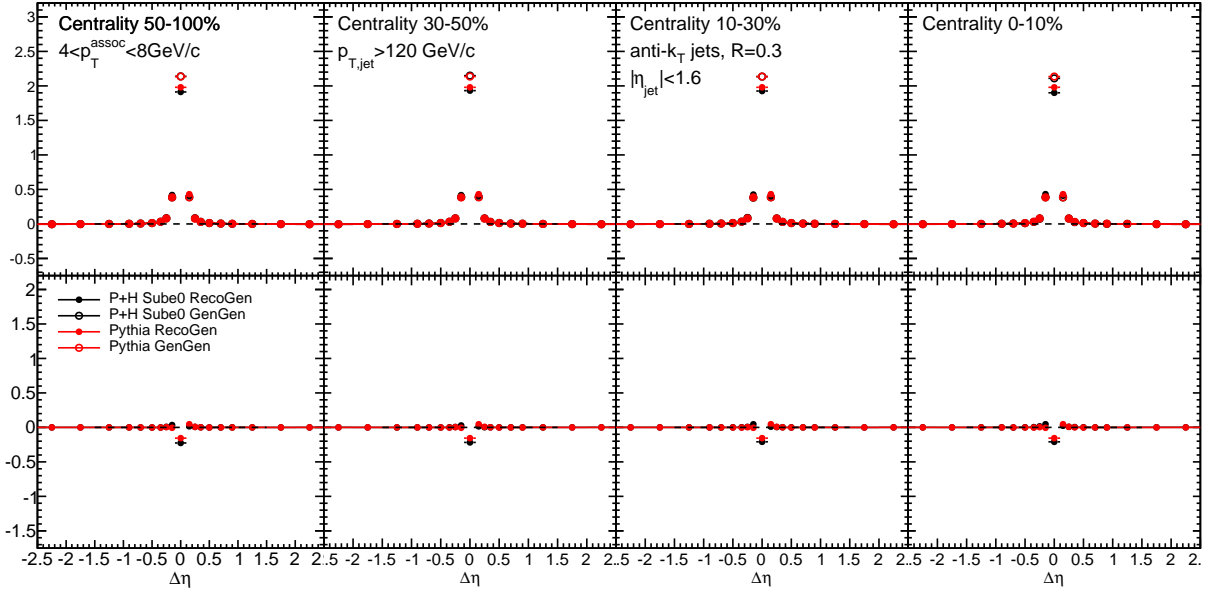


Figure 47. $\Delta\eta$ jet fragmentation function bias corrections derived by comparing correlations between reconstructed vs. generated jets and generated PYTHIA events, with and without embedding into the HYDJET heavy ion environment, for particles $4 < p_T^{\text{trk}} < 8$ GeV.

To assess the overall effect of these corrections, the integrated yield of these corrections is shown as a function of transverse momentum and centrality in shown for inclusive, leading, and subleading jets as a function of p_T^{trk} in Fig. 48 and as a function of PbPb centrality in Fig. 49. The correction magnitude shows little centrality dependence, and is very similar for pure PYTHIA simulation and PYTHIA embedded into HYDJET.

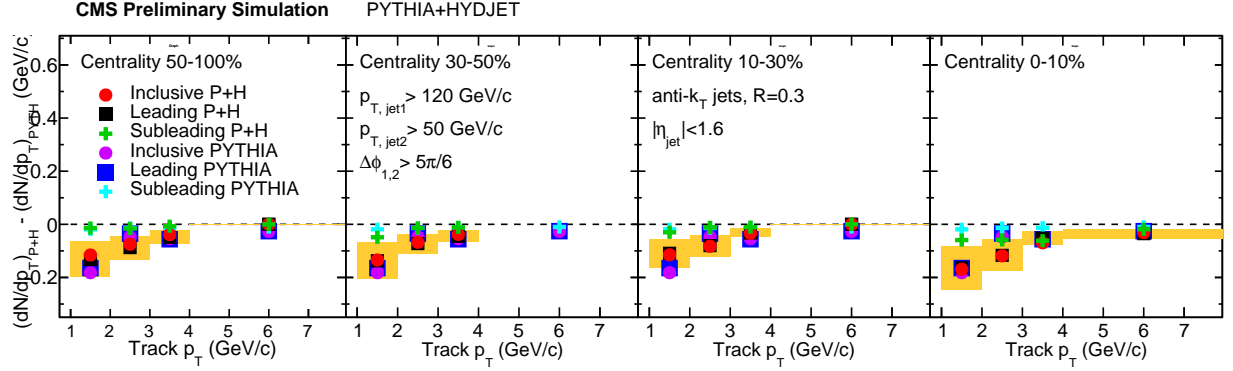


Figure 48. Integrated yield attributed to jet fragmentation function bias in jet reconstruction for PYTHIA alone and embedded into HYDJET, shown as a function of p_T^{trk} for each centrality class.

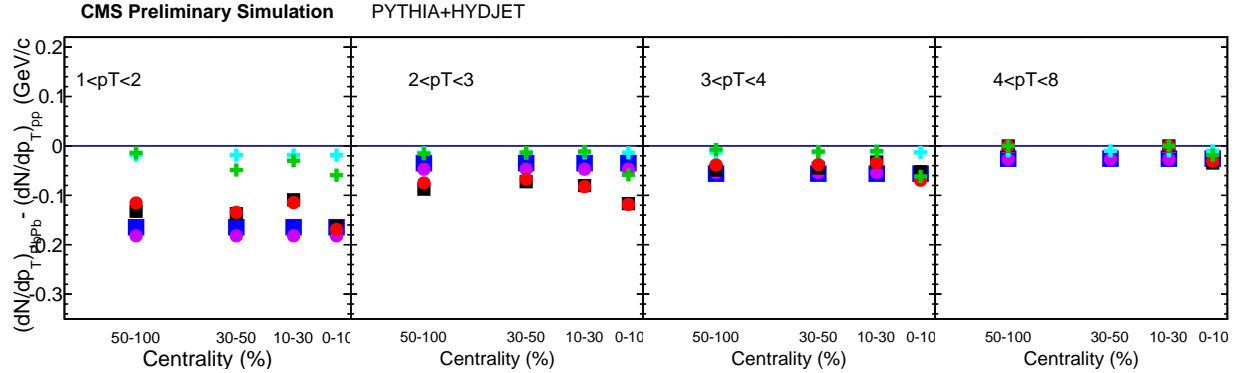


Figure 49. Integrated yield attributed to jet fragmentation function bias in jet reconstruction for PYTHIA alone and embedded into HYDJET, shown as a function of centrality for each associate track p_T range.

9.5 Background fluctuation bias correction

In central PbPb collisions background levels are very high, and naturally fluctuate throughout the event. As discussed in Section 7, the process of jet reconstruction in PbPb collisions includes background subtraction that accounts for the general distribution of energy in the event. However, small, local variations in background levels remain (on the order of 5 GeV within a radius of $R = 0.3$). These are reconstructed into the jet, raising or lowering the measured jet energy depending on whether the jet sits on an upward or a downward fluctuation in the background. As a result, jets with “true” p_T slightly below the 120 GeV selection threshold that sit on upward background fluctuations will be included in the sample, while jets sit on downward will be excluded. Because the jet spectrum is steeply falling, it is much more common for a lower- p_T jet (on an upward fluctuation) to be included in the sample than for a higher- p_T jet to be excluded. This results in the systematic inclusion of tracks from background fluctuations in the peak of tracks observed about the jet axis, resulting in a contribution to the initially measured jet peak that must be accurately quantified and subtracted.

To estimate and subtract the contribution to the excess yield due to background fluctuation bias in jet reconstruction to the measured excess yield, we perform simulations in PYTHIA+HYDJET samples with reconstructed jets (but generated tracks, as the tracking efficiency uncertainty is analyzed separately), and construct correlations excluding particles generated with the embedded PYTHIA hard-scattering process. As the PYTHIA+HYDJET simulation does not include interactions between the PYTHIA hard process and the medium, this procedure by construction isolates the contribution to the jet peak that is attributable to the background fluctuation bias. The resulting corrections are illustrated in Fig. 50 - Fig. 53 for inclusive jets at 2.76 TeV. These correlations show a diminishing effect with increasing particle transverse momentum. We subtract the gaussian fit to these correlations bin-by-bin from the data results, and also assign the half its magnitude as systematic uncertainty to the final measurements. To assess the overall effect of these corrections, the integrated yield of these corrections is shown in Fig. 54 as a function of transverse momentum and centrality is shown for inclusive, leading, and subleading jets at 2.76 TeV.

Considering that the background fluctuation bias effect in many ways mimics the jet peak signal, it is particularly important to validate this correction and confirm both that its origin

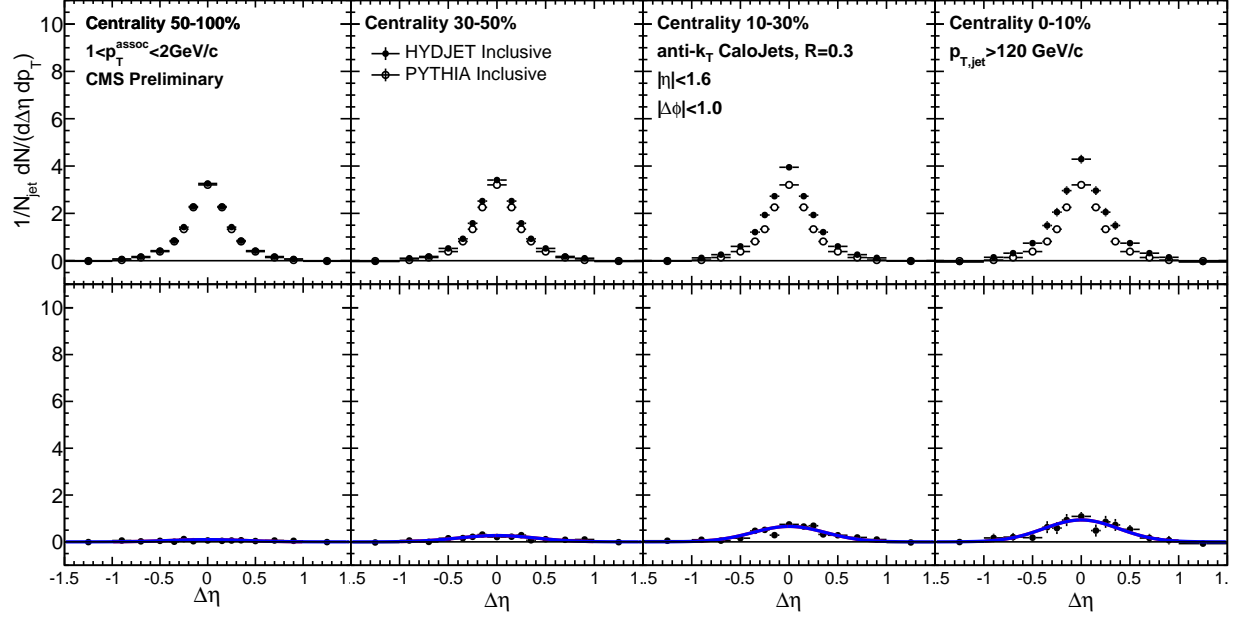


Figure 50. $\Delta\eta$ background fluctuation bias correction for inclusive jets derived by constructing correlations in PYTHIA+HYDJET between reconstructed jets and only those tracks simulated as part of the heavy ion underlying event rather than the embedded PYTHIA hard process, for particles $1 < p_T^{\text{trk}} < 2$ GeV

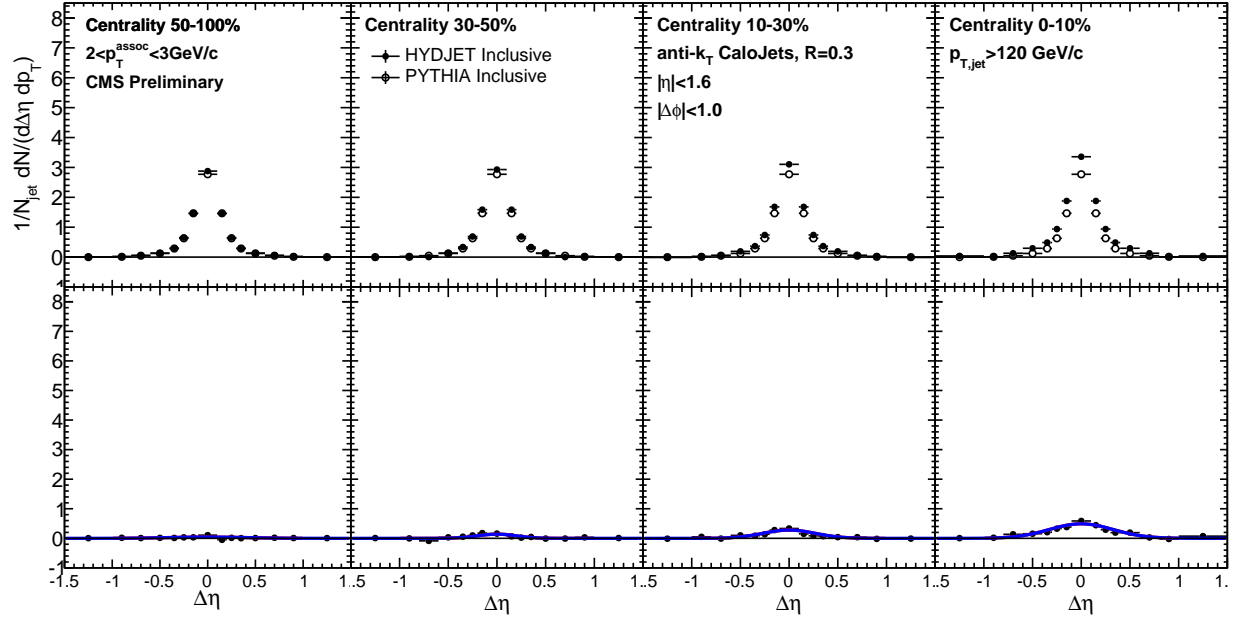


Figure 51. $\Delta\eta$ background fluctuation bias correction for inclusive jets derived by constructing correlations in PYTHIA+HYDJET between reconstructed jets and only those tracks simulated as part of the heavy ion underlying event rather than the embedded PYTHIA hard process, for particles $2 < p_T^{\text{trk}} < 3$ GeV

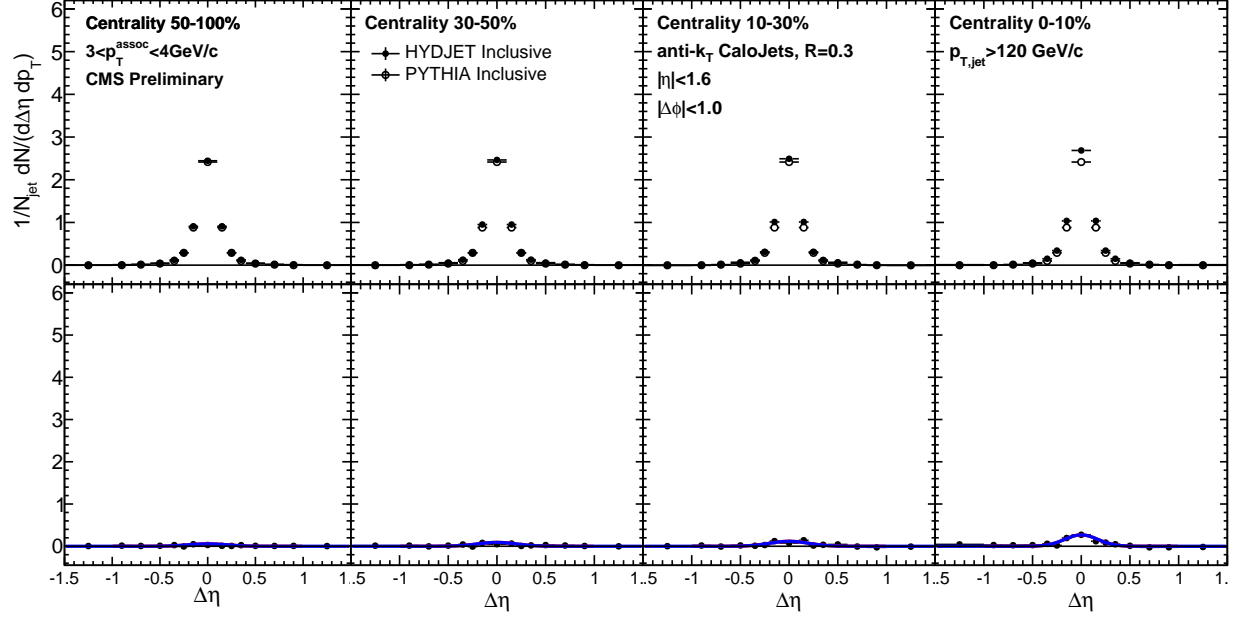


Figure 52. $\Delta\eta$ background fluctuation bias correction for inclusive jets derived by constructing correlations in PYTHIA+HYDJET between reconstructed jets and only those tracks simulated as part of the heavy ion underlying event rather than the embedded PYTHIA hard process, for particles $3 < p_T^{\text{trk}} < 4$ GeV

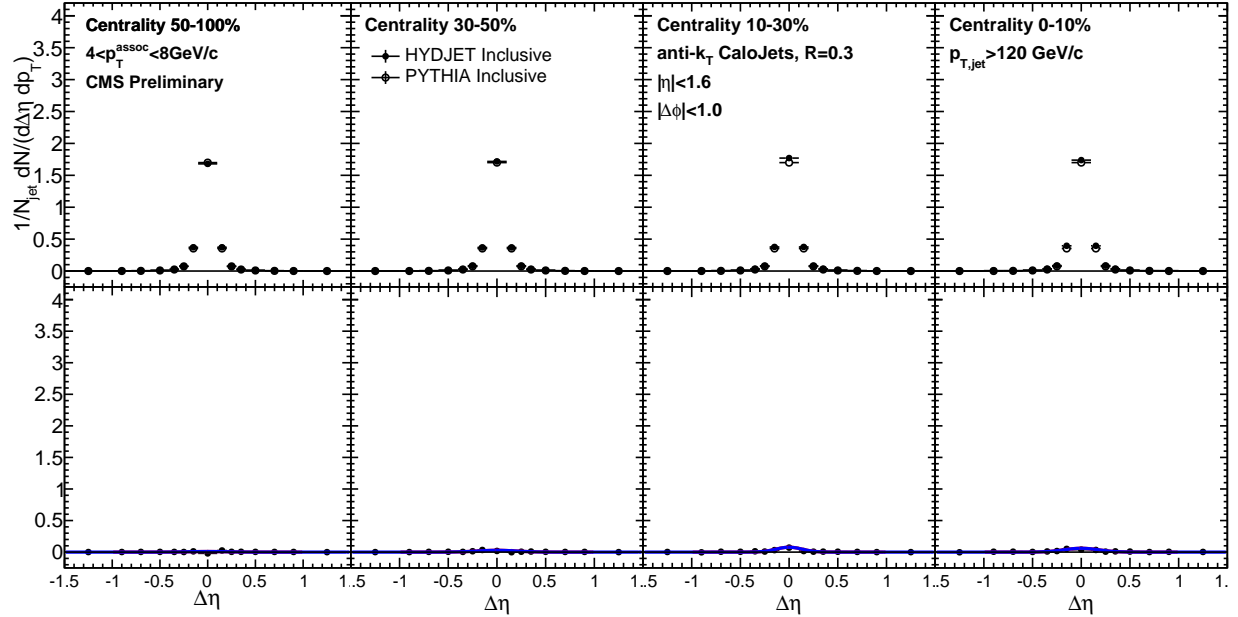


Figure 53. $\Delta\eta$ background fluctuation bias correction for inclusive jets derived by constructing correlations in PYTHIA+HYDJET between reconstructed jets and only those tracks simulated as part of the heavy ion underlying event rather than the embedded PYTHIA hard process, for particles $4 < p_T^{\text{trk}} < 8$ GeV

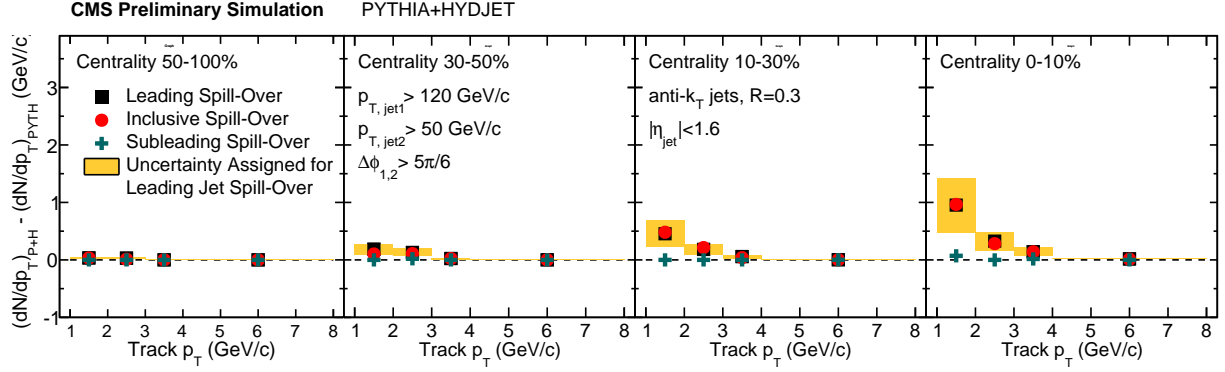


Figure 54. Integrated yield attributed to background fluctuation bias in the selection of inclusive and leading jets, shown as a function of associate track p_T for each centrality class.

is well-understood and that the HYDJET simulation used to derive it reproduces the background fluctuations in data closely enough to accurately obtain corrections. To check this, we extract a direct estimate of the effect from data using a “pseudo-embedding” of pp jets into a minimum bias PbPb data sample. The goal of this study is to verify that we recover a similar magnitude of excess yield as we attribute based on our more detailed PYTHIA+HYDJET simulations. Here we approximate the effect by adding the total transverse momentum in a circle of radius $R = 0.3$ around all jets with $p_T > 90$ GeV, and considering the total deviation up or down of this $(\Sigma p_T)_{\text{cone}}$ from the average total transverse momentum $\langle (\Sigma p_T)_{\text{cone}} \rangle$. First, we may directly compare the average p_T and fluctuations in p_T in these random cones between data and Monte Carlo. We find that our Monte Carlo approximately reproduces the data: in data $\langle (\Sigma p_T)_{\text{cone,data}} \rangle = 10.0$ GeV, with $\sigma((\Sigma p_T)_{\text{cone,data}}) = 4.9$ GeV, while in Monte Carlo $\langle (\Sigma p_T)_{\text{cone,MC}} \rangle = 11.9$ GeV, with $\sigma((\Sigma p_T)_{\text{cone,data}}) = 5.6$ GeV.

We then use these random cones to adjust jet energy and re-select jets: we add the deviation up or down of this $(\Sigma p_T)_{\text{cone}}$ to each embedded pp jets with this adjusted p_T . We then fill $\Delta\eta - \Delta\phi$ correlations to all jets that pass our nominal $p_T > 120$ GeV jet selection cut. We apply this technique to both our PYTHIA+HYDJET sample and a minimum-bias PbPb data sample to measure the charged particle yield associated with the embedded jet axis as a result of the jet fluctuation bias. As Fig. 55–56 show, this data pseudo-embedding recovers the same magnitude of excess yield due to background fluctuation bias as our nominal Monte Carlo studies, but artificially confines this

effect to a $R = 0.3$ cone by construction, due to the artificially simple jet reconstruction procedure. This gives confidence that the origin and magnitude of the effect are well-understood.

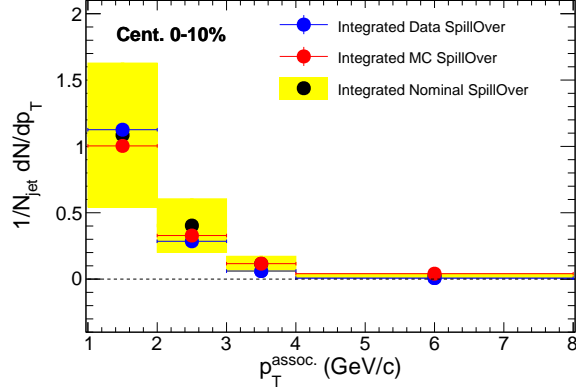


Figure 55. Total integrated magnitude of background fluctuation bias as simulated with pp jets embedded in Minimum Bias events (blue points) compared to the effect as simulated with PYTHIA jets into minimum bias HYDJET and to nominal corrections obtained with full PYTHIA+HYDJET simulation. Nominal systematic errors of $\pm 50\%$ as assigned in this analysis are shown as yellow systematic error bars on nominal (full MC simulation) points.

The background fluctuation bias could also be sensitive to the same calorimeter nonlinearity bias that necessitates fragmentation-jet energy corrections. To study this question and validate the uncertainty associated with this correction, we separately study the effect for quark jets and gluon jets, as shown in Figure 57. This study is limited by statistics, but deviations (or fluctuations) in the bias for quark versus gluon jets are within the 50% systematic uncertainty assigned.

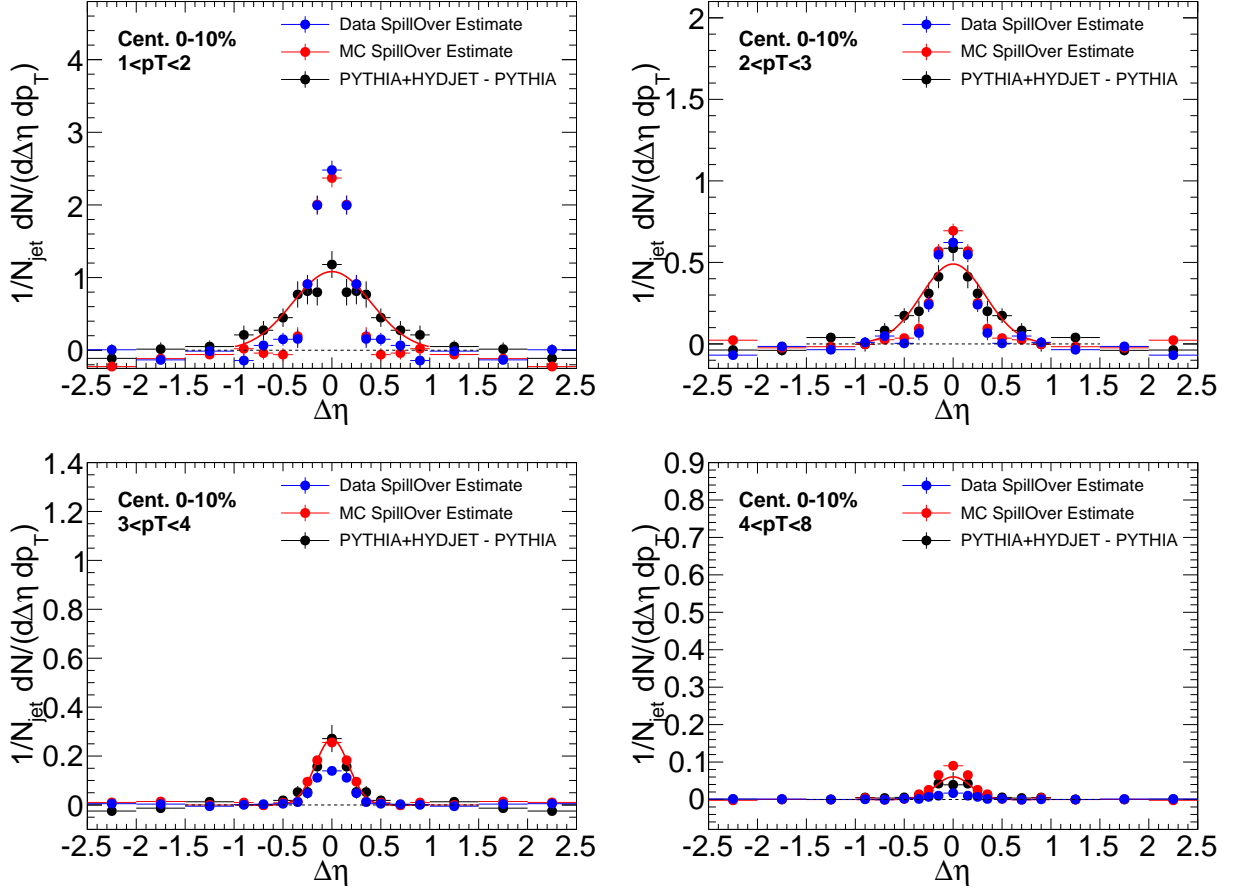


Figure 56. Correlated yield $\Delta\eta$ due to background fluctuation bias as simulated with pp jets embedded in Minimum Bias events (blue points) compared to the effect applying the same technique with PYTHIA jets in HYDJET minimum bias events, as well as in full PYTHIA+HYDJET simulation (black points with red fit line).

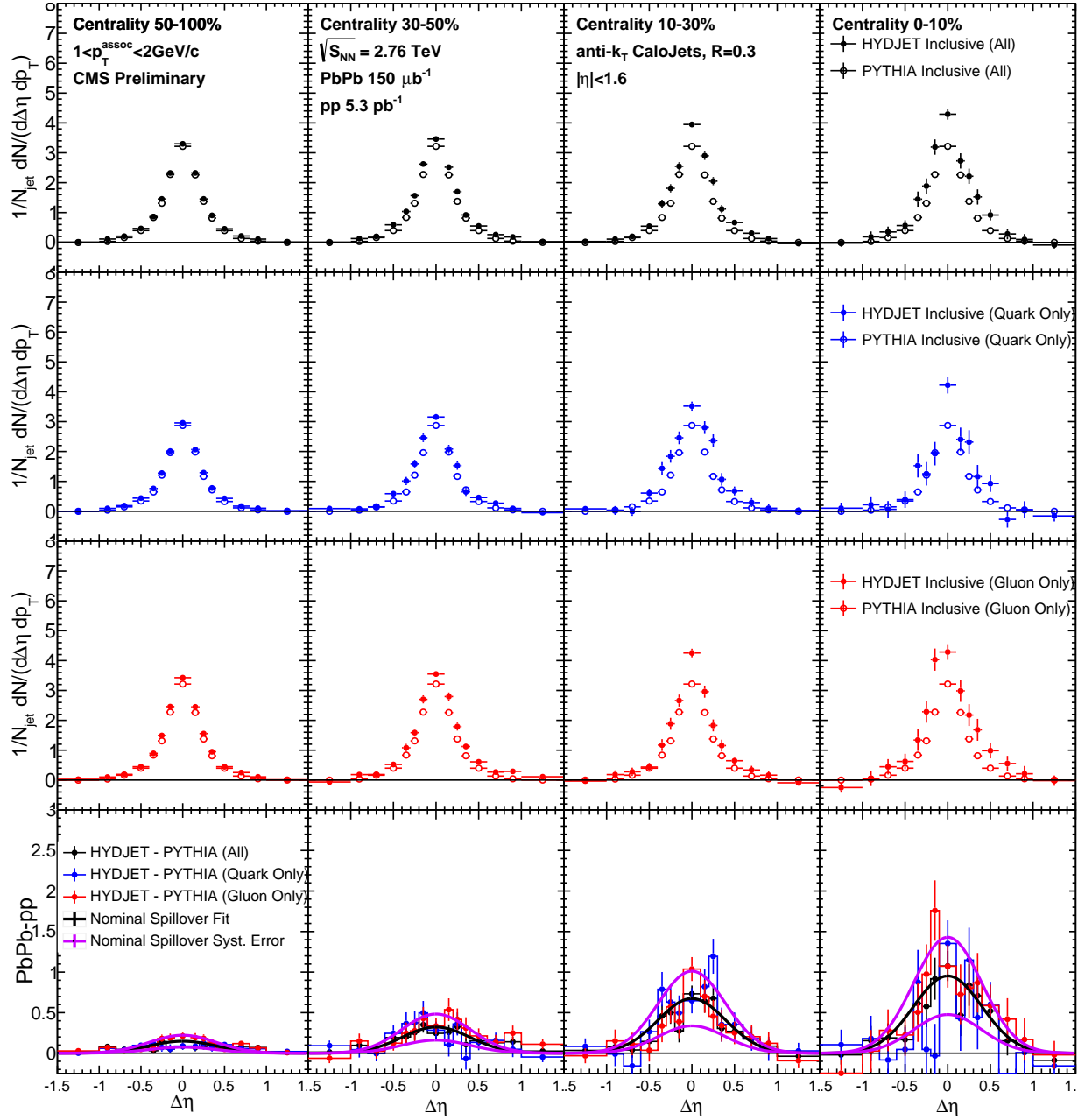


Figure 57. Comparison of magnitude of background selection bias effect for quark and gluon jets versus our nominal sample. Jet selection is inclusive in all cases.

9.6 Evaluation of systematic uncertainties

A number of sources of systematic uncertainty have been discussed in presenting jet and track reconstruction and the jet-track correlation analysis procedure. To estimate the total systematic uncertainty in these measurements, these contributions are added in quadrature. A brief summary of all systematic uncertainty contributions, together with the procedure used to estimate their magnitude follows. The contributions from each source (relative to jet peak signal) are summarized in Tables V–VII.

9.6.1 Systematic uncertainties related to jet reconstruction

Jet reconstruction-related sources of systematic uncertainty in this analysis include the two reconstruction biases as discussed above, as well uncertainty associated with the jet energy scale (JES) evaluation. We consider three sources of uncertainty on the JES: (1) differences in calorimeter response for quark versus gluon jets, meaning that medium-induced changes in jet flavor could result in either over-correction or under-correction of jet energy and a resulting bias in jet selection (evaluated via Monte Carlo non-closure for quark and gluon jets); (2) possible differences between data and simulation; (3) uncertainty due to quenching effects not included in our HYDJET simulation. To evaluate how each of these sources of JES uncertainty affects final correlations, we vary jet selection threshold by the combined uncertainty, and then quantify the resulting differences in the final correlations as a measure of the combined residual JES uncertainty. Since all the measured correlations are studied per-reconstructed jets, the jet reconstruction efficiency does not contribute to the systematic uncertainty of this measurement.

9.6.2 Systematic uncertainties related to tracking and tracking efficiency corrections

The tracking efficiency correction uncertainty is estimated from the ratio of corrected reconstructed yields and generated yields by using generator level charged particles as a “truth” reference. To account for the possible track reconstruction differences in data and simulation, a residual uncertainty in track reconstruction efficiency and fake rate corrections is also estimated.

9.6.3 Systematic uncertainty associated with pair acceptance correction and event decomposition

Uncertainty arising from pair-acceptance effects is estimated by considering the sideband asymmetry after dividing by the mixed-event background. Each sideband region of the final $\Delta\eta$ distribution ($-2.5 < \Delta\eta < -1.5$ and $1.5 < \Delta\eta < 2.5$) is separately fit with a horizontal line after background subtraction. The greater of these two deviations from zero is assigned as systematic error. Uncertainties resulting from the background subtraction are determined by considering the average point-to-point deviation in two parts of the sideband region ($1.5 < |\Delta\eta| < 2.0$ and $2.0 < |\Delta\eta| < 2.5$) after background subtraction. The derivations of both of these sources of uncertainty are illustrated in Appendix C. In PbPb data this background subtraction uncertainty is greatest for the most central events (0–10%) and the lowest track p_T bin where the background is most significant compared to the signal level, and decreases for less central collisions and for higher p_T tracks ($p_T^{\text{trk}} > 2$ GeV).

9.6.4 Summary of systematic uncertainties

The contributions to total systematic uncertainty from each of the sources described above are given in Tables V–VII. Table V gives uncertainty evaluations for correlation studies at 2.76 TeV, while Table VI gives the same for studies at 5.02 TeV. Finally, Table VII gives uncertainty evaluations for balanced ($A_J < 0.22$) and unbalanced ($A_J > 0.22$) dijet events in momentum balance studies at 2.76 TeV.

TABLE V. Systematic uncertainties in the measurement of the jet-track correlations in PbPb and pp collisions at 2.76 TeV, as percentage of the total measured correlated yield. The numbers presented in this table summarize the range of values of systematic uncertainty (as a function of p_T^{trk}) for different centrality bins.

Source	0–10%	10–30%	30–50%	50–100%	pp
Background fluctuation bias	3–12%	2–7%	1–5%	0–1%	–
Jet fragmentation function bias	0–2%	0–2%	0–2%	0–2%	0–2%
Residual jet energy scale	3%	3%	3%	3%	3%
Tracking efficiency uncertainty	4%	4%	4%	4%	3 %
Residual track efficiency corr.	5%	5%	5%	5%	5%
Pair acceptance corrections	5–9%	5–9%	4–8%	2–6%	2–3%
Background subtraction	2–5%	2–5%	2–5%	2–5%	1–2%
Total	9–17%	9–14%	8–13%	8–10%	7–8%

TABLE VI. Systematic uncertainties in the measurement of the jet track correlations in PbPb and pp collisions at 5.02 TeV. The numbers presented in this table summarize typical range of systematic uncertainty as a function of collision centrality. The upper limits of the cited values correspond to uncertainties at lowest p_T^{trk} , and uncertainties decrease with rising p_T^{trk} .

Source	0–10%	10–30%	30–50%	50–100%	ppRef
Background fluctuation bias	0–10%	0–5%	0–2%	0–1%	–
Background fluctuation bias residual	0–2%	0–3%	0–1%	0–1%	–
JFF bias	3–5%	3–4%	3–4%	3–4%	3%
Residual JES	4%	4%	4%	4%	4%
Tracking efficiency uncertainty	1%	1%	1%	1%	1%
Residual tracking efficiency	5%	5%	5%	5%	5%
Pair-acceptance corrections	1–5%	1–4%	1–4%	1–4%	1–2%
Event decomposition	1–9%	0–4%	0–4%	0–3%	0–3%
Total	7–16%	7–11%	7–9%	7–9%	7–8%

TABLE VII. This table summarizes the systematic uncertainties in the measurement of the p_T^{trk} correlations in PbPb and pp collisions at 2.76 TeV. Upper and lower limits are shown as a function of collision centrality. Upper values correspond to the uncertainties at lowest p_T^{trk} .

Source	0–30%	30–50%	50–100%	pp
Balanced jet selection ($A_J < 0.22$):				
Background fluctuations	1–8%	1–3%	0–1%	–
JFF bias and jet swapping	0–2%	0–2%	0–2%	0–2%
Residual JES	3%	3%	3%	3%
Tracking efficiency	4%	4%	4%	3 %
Residual track efficiency corr.	5%	5%	5%	5%
Pair acceptance corrections	5–9%	4–8%	2–6%	2–3%
Event decomposition	2–5%	2–5%	2–5%	1–2%
Total	9–15%	8–13%	8–10%	7–8%
Unbalanced jet selection ($A_J > 0.22$):				
Background fluctuations	1–10%	1–5%	0–2%	–
JFF bias and jet swapping	0–2%	0–2%	0–2%	0–2%
Residual JES	3%	3%	3%	3%
Tracking efficiency	4%	4%	4%	3 %
Residual track efficiency corr.	5%	5%	5%	5%
Pair acceptance corrections	5–9%	4–8%	2–6%	2–3%
Event decomposition	2–5%	2–5%	2–5%	1–2%
Total	9–16%	8–13%	8–10%	7–8%

10 RESULTS

Portions of the material in this chapter, which is my own work, were published in Refs. [1, 2, 3].

Jet-track correlation studies can produce measurements of the density of particles (in each p_T^{trk} class) with respect to the jet axis and can also, by creating correlations weighted per-track by its p_T^{trk} , produce measurements of the distribution of p_T^{trk} in the event as a whole. Both types of measurements are presented here, for inclusive selections of jets with $p_T > 120$ GeV at 2.76 TeV and 5.02 TeV, and for high- p_T dijet events at 2.76 TeV. First, particle density correlation results are presented in Secs. 10.1- 10.2. Next, p_T^{trk} distributions are used to extract measurements of jet shapes (the transverse momentum profiles of jets) in Sec. 10.3. Finally, in Sec. 10.4, p_T^{trk} distributions are used to decompose and analyze the hemisphere momentum balance in dijet events.

10.1 Inclusive jet particle density correlation results

Particle density correlation studies allow for the detailed characterization of jet fragmentation, and of medium-induced modifications to jet fragmentation in PbPb data (as a function of collision centrality) compared to pp data. The analysis procedure described in Sec. 9 results in fully-corrected 2D jet peaks in $\Delta\eta - \Delta\phi$, which may then be projected to obtain the distribution of particles in each p_T^{trk} class as a function of $\Delta\eta$ or $\Delta\phi$. The top panels of Figs. 58-65 show these $\Delta\eta$ and $\Delta\phi$ distributions (projected over $|\Delta\phi| < 1$ and $|\Delta\eta| < 1$, respectively) for 2.76 TeV pp data and PbPb data in each p_T^{trk} range from 1–2 GeV (Fig. 58-59) up to 4–8 GeV (Fig. 64-65). The bottom panels of these figures show the differences PbPb–pp for illustration of medium modifications to jet fragmentation patterns. In both the $\Delta\eta$ and $\Delta\phi$ dimensions, centrality-dependent excesses of soft (low- p_T^{trk}) particles are evident. These exhibit the greatest modifications in the most central PbPb collisions, decreasing with centrality until the most peripheral collisions show little modification when compared to pp data. These excesses decrease with increasing p_T^{trk} , until in the 4-8 GeV range the enhancements evident at lowest- p_T^{trk} reverse to possible slight depletion. In both $\Delta\eta$ and $\Delta\phi$ dimensions, the soft excesses exhibit a gaussian-like distribution around the jet axis, while also extending to large angles $\Delta\eta = 1$ and $\Delta\phi = 1$ at lowest p_T^{trk} .

Figures 66 and 67 show the corresponding $\Delta\eta$ and $\Delta\phi$ distributions at 5.02 TeV. Here, the distribution of particles in each p_T^{trk} class are stacked (with lowest- p_T^{trk} particles on top), and

pp data shown separately at left. Again the differences PbPb–pp are shown in bottom panels to illustrate the medium modifications, and exhibit similar qualitative trends to those described above for 2.76 TeV results. Results may also be presented as a function of radial distance from the jet axis $\Delta r = \sqrt{\Delta\eta^2 + \Delta\phi^2}$. Figure 68 presents charged particle yields, differentially in p_T^{trk} , as a function of Δr . For comparison, the bottom row of each plot shows the difference, PbPb minus pp. This shows the particles contributing to a jet fragmentation function measurement within a given radius from a jet, and illustrates the radial dependence of modifications extending to at least $\Delta r = 1$.

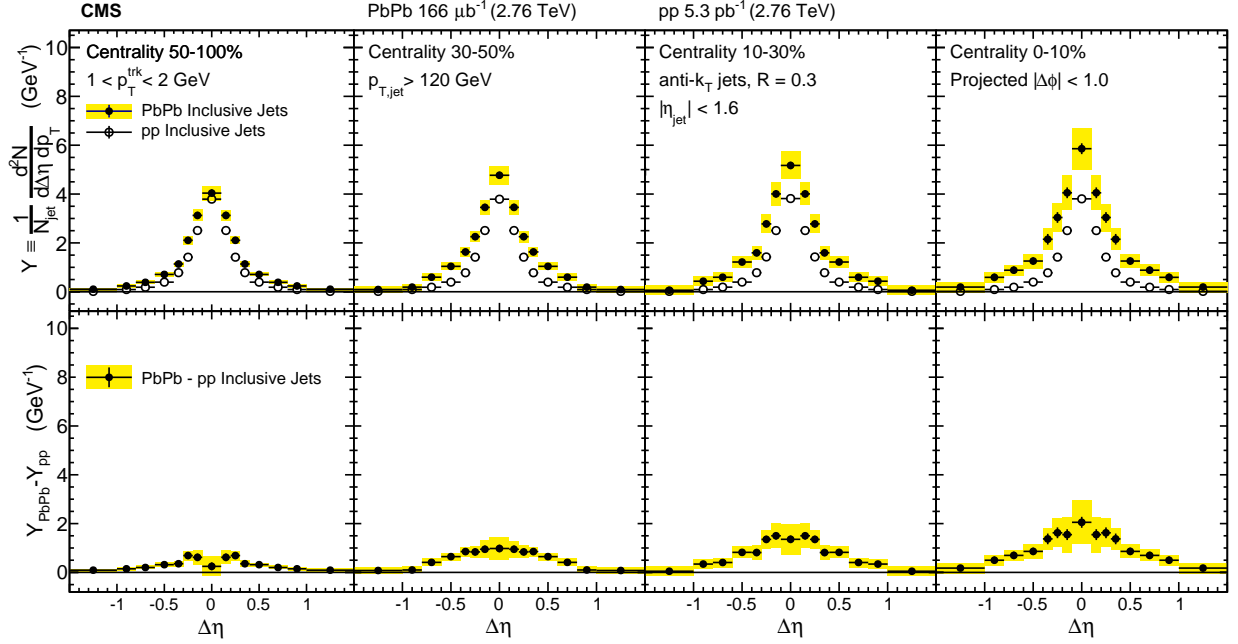


Figure 58. Symmetrized $\Delta\eta$ distributions (projected over $|\Delta\phi| < 1$) of background-subtracted particle yields correlated to PbPb and pp inclusive jets with $p_T > 120$ GeV are shown in the top panels for tracks with $1 < p_T^{\text{trk}} < 2$ GeV. The difference in PbPb and pp per-jet yields is shown in the bottom panels. The total systematic uncertainties are shown as shaded boxes, and statistical uncertainties are shown as vertical bars (often smaller than the symbol size).

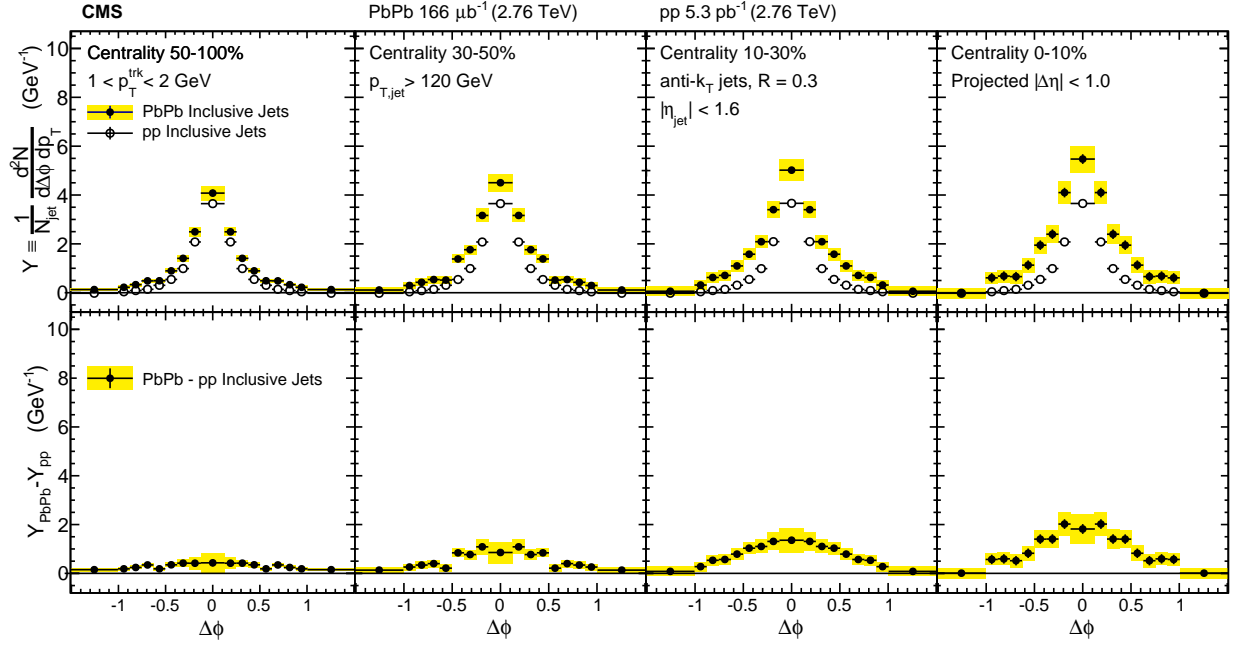


Figure 59. Symmetrized $\Delta\phi$ distributions (projected over $|\Delta\eta| < 1$) of background-subtracted particle yields correlated to PbPb and pp inclusive jets with $p_T > 120$ GeV are shown in the top panels for tracks with $1 < p_T^{\text{trk}} < 2$ GeV. The difference in PbPb and pp per-jet yields is shown in the bottom panels. The total systematic uncertainties are shown as shaded boxes, and statistical uncertainties are shown as vertical bars (often smaller than the symbol size).

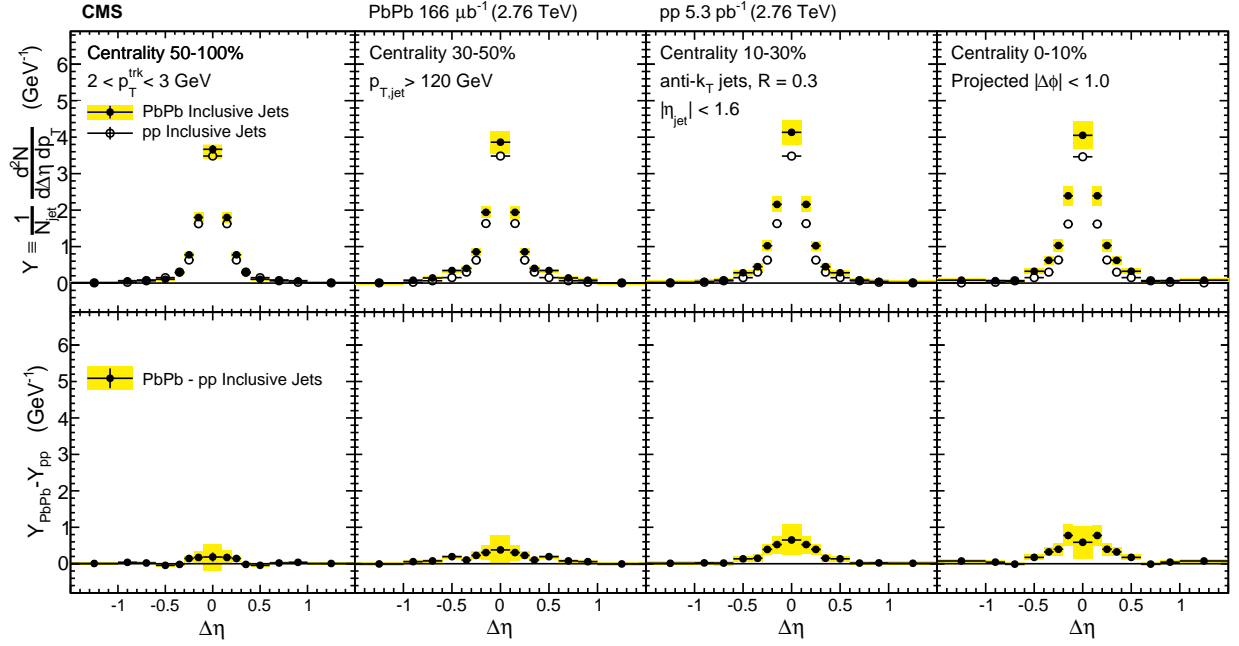


Figure 60. Symmetrized $\Delta\eta$ distributions (projected over $|\Delta\phi| < 1$) of background-subtracted particle yields correlated to PbPb and pp inclusive jets with $p_T > 120$ GeV are shown in the top panels for tracks with $2 < p_T^{\text{trk}} < 3$ GeV. The difference in PbPb and pp per-jet yields is shown in the bottom panels. The total systematic uncertainties are shown as shaded boxes, and statistical uncertainties are shown as vertical bars (often smaller than the symbol size).

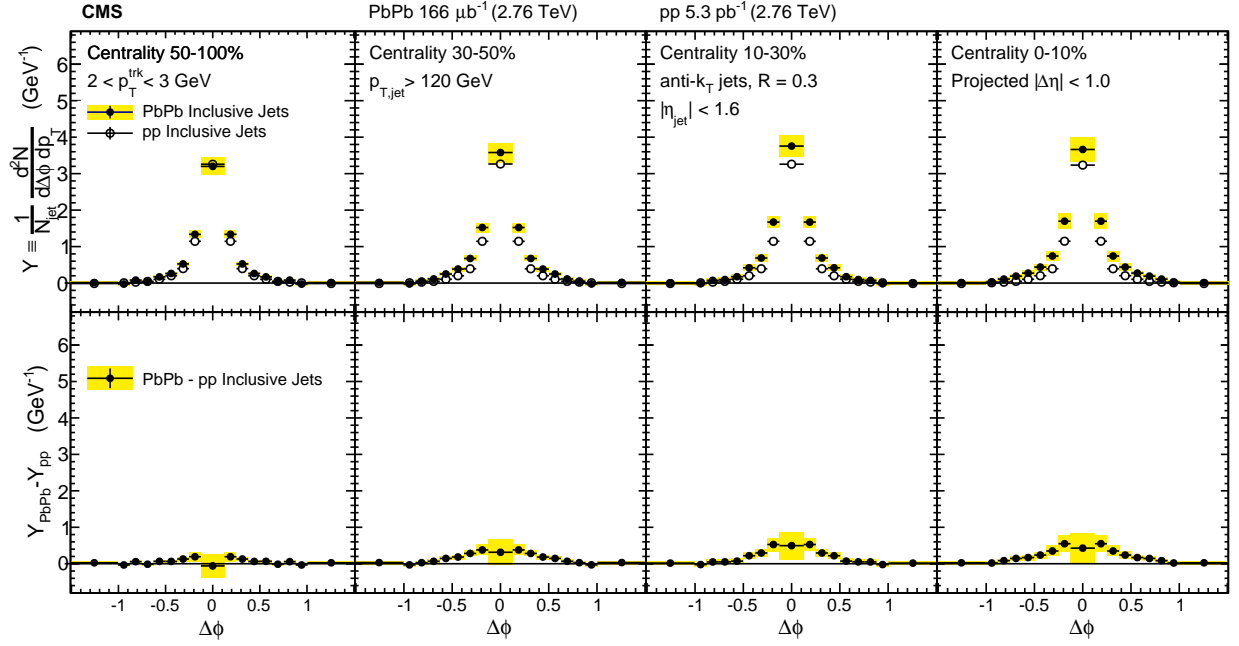


Figure 61. Symmetrized $\Delta\phi$ distributions (projected over $|\Delta\eta| < 1$) of background-subtracted particle yields correlated to PbPb and pp inclusive jets with $p_T > 120 \text{ GeV}$ are shown in the top panels for tracks with $2 < p_T^{\text{trk}} < 3 \text{ GeV}$. The difference in PbPb and pp per-jet yields is shown in the bottom panels. The total systematic uncertainties are shown as shaded boxes, and statistical uncertainties are shown as vertical bars (often smaller than the symbol size).

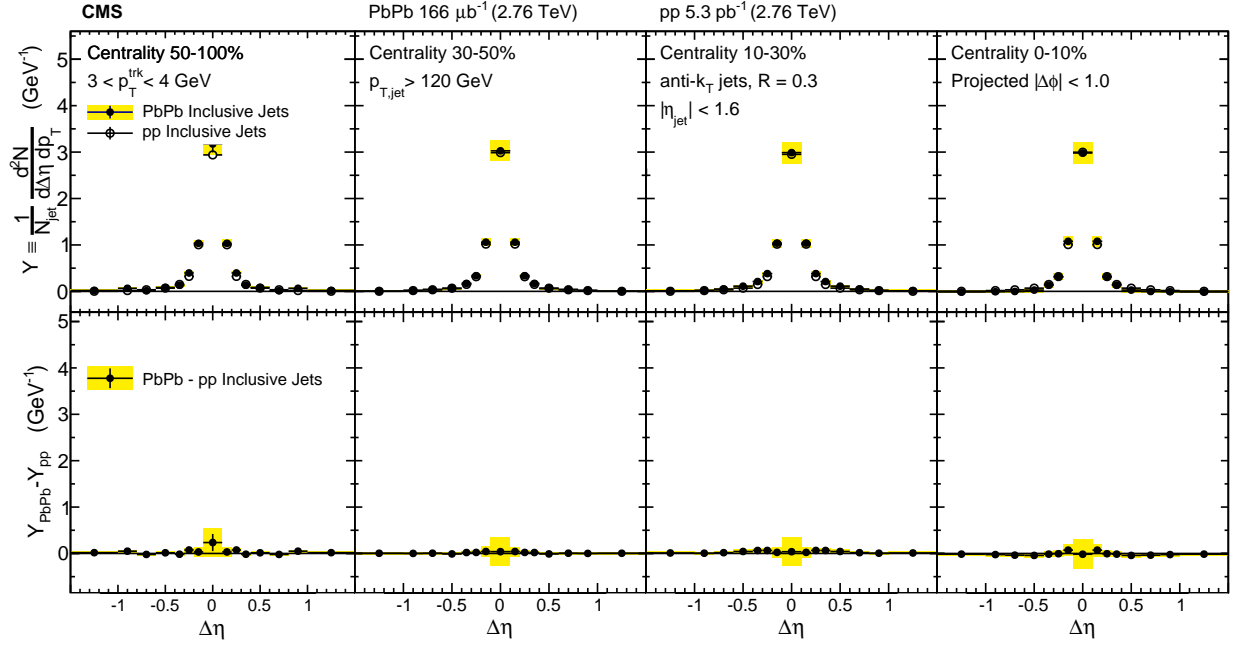


Figure 62. Symmetrized $\Delta\eta$ distributions (projected over $|\Delta\phi| < 1$) of background-subtracted particle yields correlated to PbPb and pp inclusive jets with $p_T > 120$ GeV are shown in the top panels for tracks with $3 < p_T^{\text{trk}} < 4$ GeV. The difference in PbPb and pp per-jet yields is shown in the bottom panels. The total systematic uncertainties are shown as shaded boxes, and statistical uncertainties are shown as vertical bars (often smaller than the symbol size).

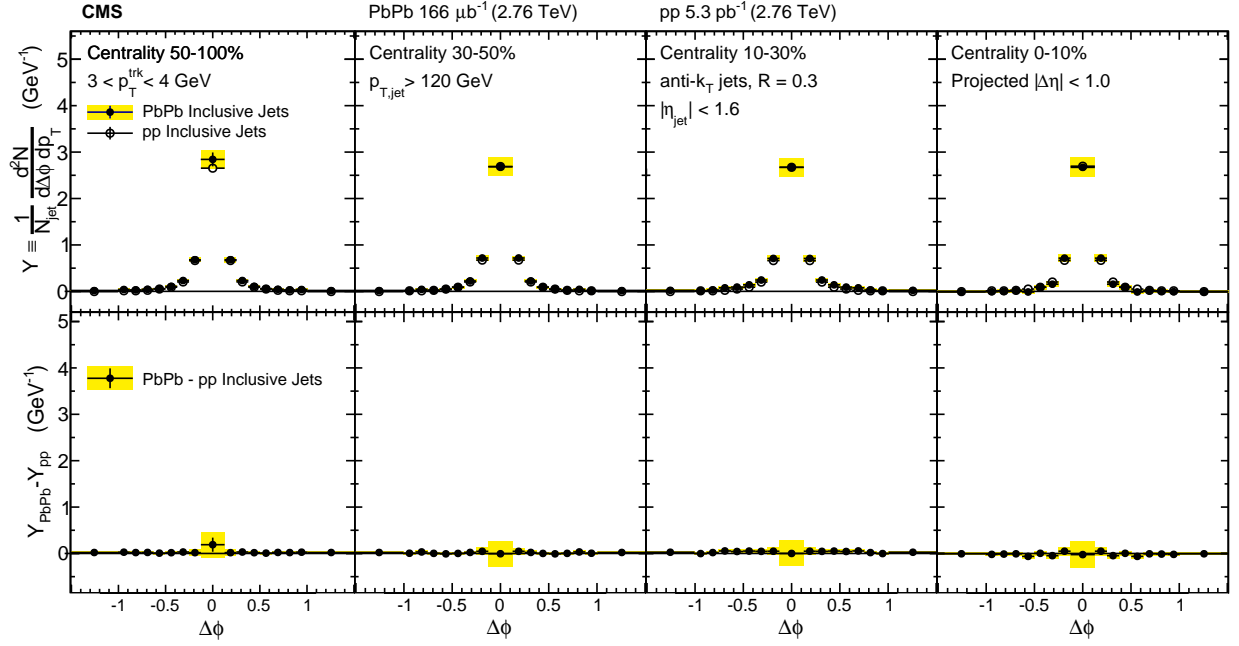


Figure 63. Symmetrized $\Delta\phi$ distributions (projected over $|\Delta\eta| < 1$) of background-subtracted particle yields correlated to PbPb and pp inclusive jets with $p_T > 120$ GeV are shown in the top panels for tracks with $3 < p_T^{\text{trk}} < 4$ GeV. The difference in PbPb and pp per-jet yields is shown in the bottom panels. The total systematic uncertainties are shown as shaded boxes, and statistical uncertainties are shown as vertical bars (often smaller than the symbol size).

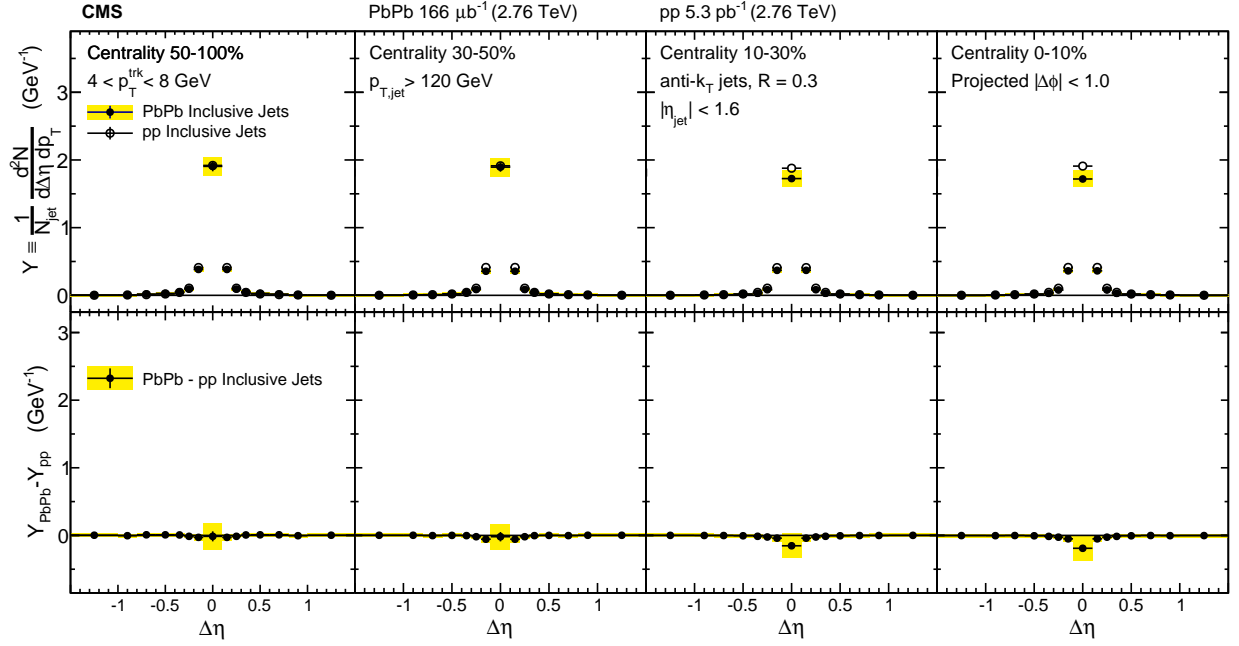


Figure 64. Symmetrized $\Delta\eta$ distributions (projected over $|\Delta\phi| < 1$) of background-subtracted particle yields correlated to PbPb and pp inclusive jets with $p_T > 120$ GeV are shown in the top panels for tracks with $4 < p_T^{\text{trk}} < 8$ GeV. The difference in PbPb and pp per-jet yields is shown in the bottom panels. The total systematic uncertainties are shown as shaded boxes, and statistical uncertainties are shown as vertical bars (often smaller than the symbol size).

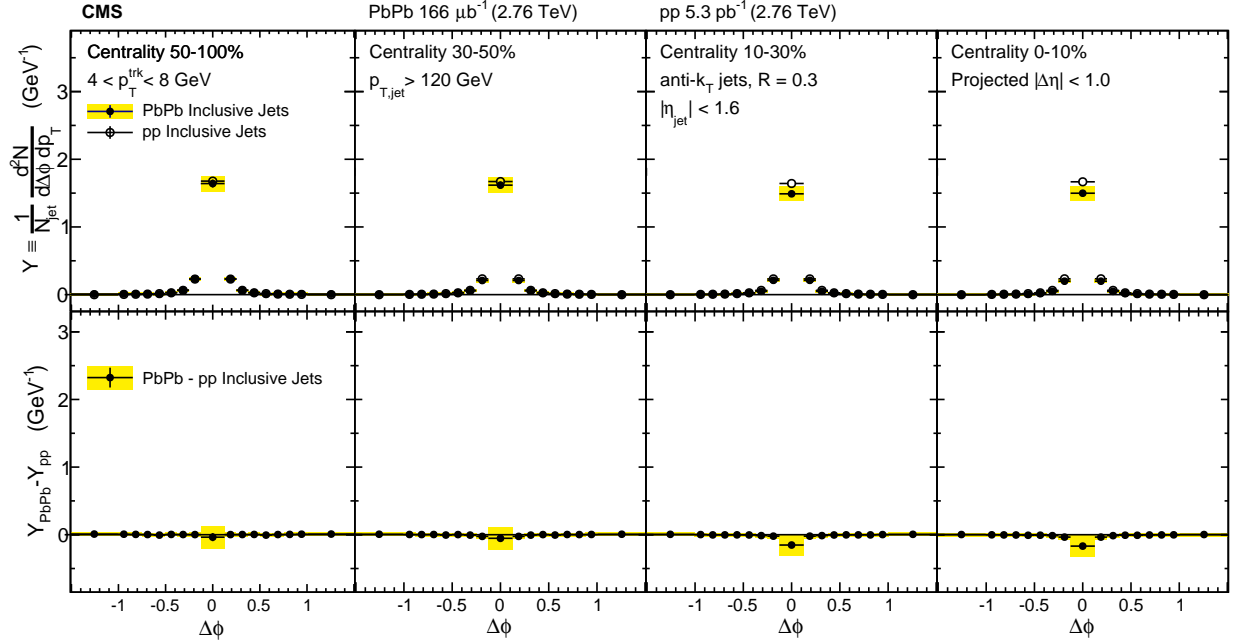


Figure 65. Symmetrized $\Delta\phi$ distributions (projected over $|\Delta\eta| < 1$) of background-subtracted particle yields correlated to PbPb and pp inclusive jets with $p_T > 120$ GeV are shown in the top panels for tracks with $4 < p_T^{\text{trk}} < 8$ GeV. The difference in PbPb and pp per-jet yields is shown in the bottom panels. The total systematic uncertainties are shown as shaded boxes, and statistical uncertainties are shown as vertical bars (often smaller than the symbol size).

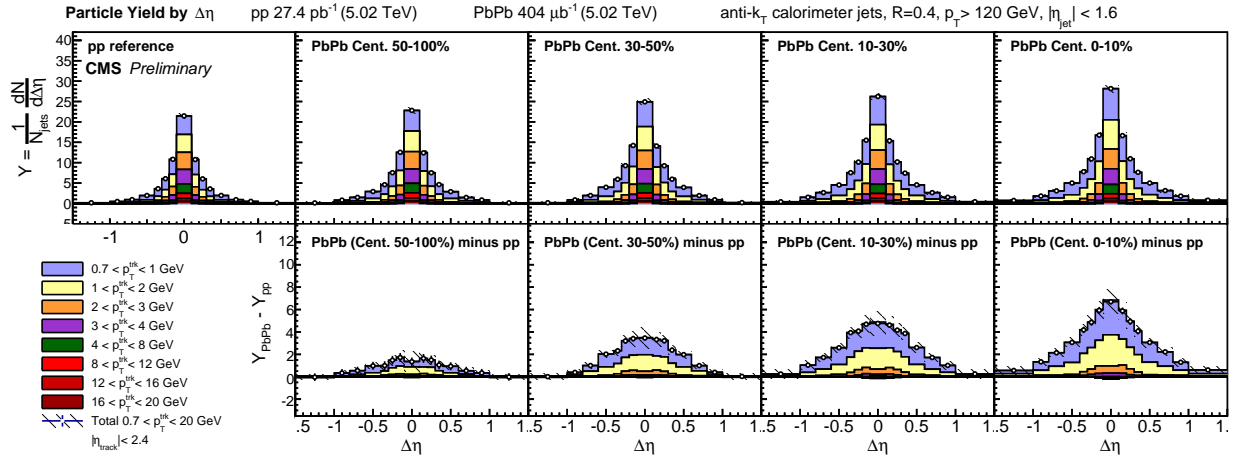


Figure 66. Top row: distributions of charged particle yields correlated to jets with $p_T > 120$ GeV as a function of $\Delta\eta$ (projected over $|\Delta\phi| < 1$), shown differentially for all p_T^{trk} bins for pp, peripheral PbPb, and central PbPb data. Bottom row: PbPb minus pp difference in these distributions. Hatched lines on p_T^{trk} -inclusive points show total systematic uncertainties.

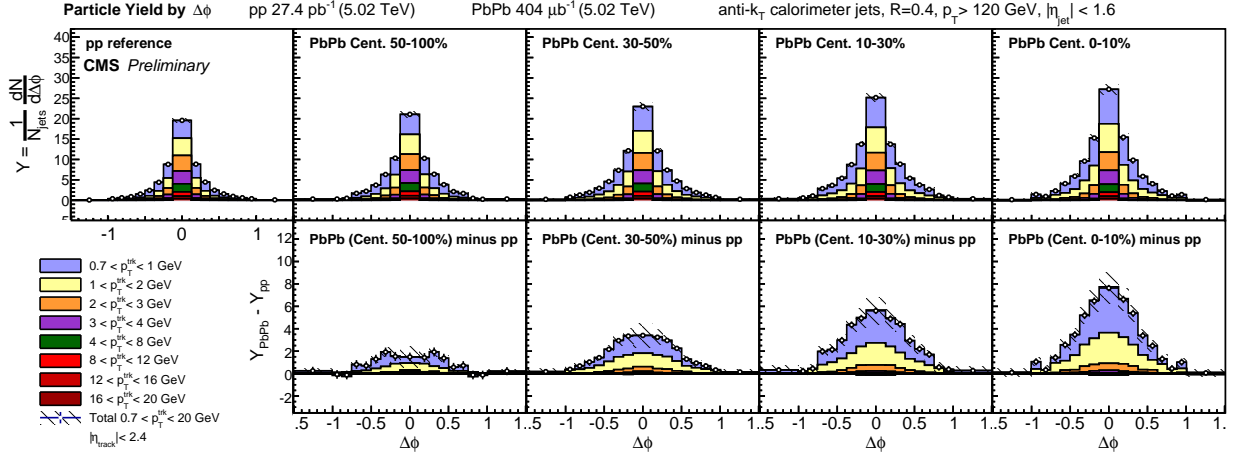


Figure 67. Top row: distributions of charged particle yields correlated to jets with $p_T > 120$ GeV as a function of $\Delta\phi$ (projected over $|\Delta\eta| < 1$), shown differentially for all p_T^{trk} bins for pp, peripheral PbPb, and central PbPb data. Bottom row: PbPb minus pp difference in these distributions. Hatched lines on p_T^{trk} -inclusive points show total systematic uncertainties.

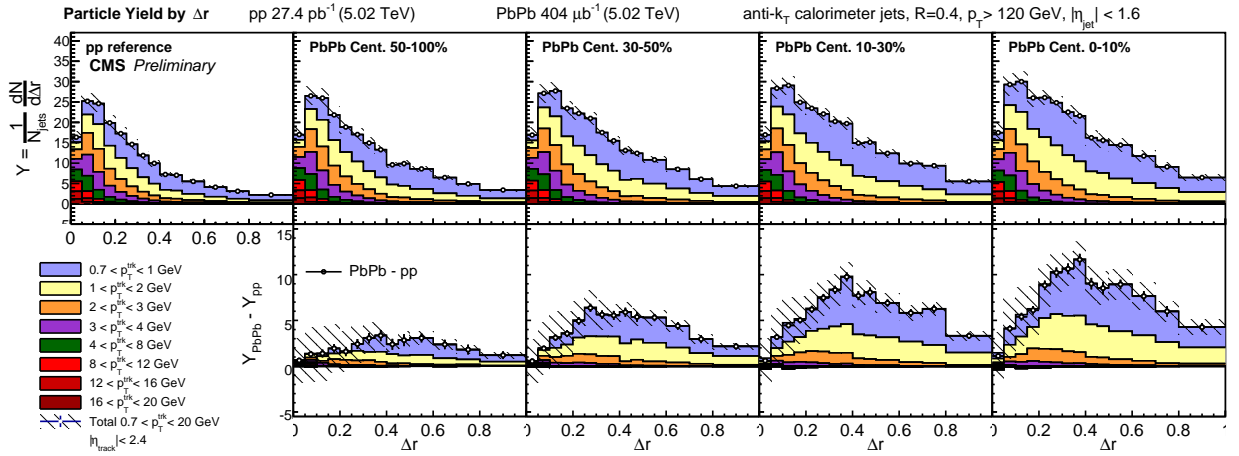


Figure 68. Top row: distributions of charged particle yields correlated to jets with $p_T > 120$ GeV as a function of Δr , shown differentially for all p_T^{trk} bins. Bottom row: PbPb minus pp difference in these distributions. Hatched lines on p_T^{trk} -inclusive points show total systematic uncertainties.

To summarize the magnitude of the modifications to particle yields in PbPb relative to pp collisions, integrated yields as a function of p_T^{trk} are presented in the top panel of Fig. 69. The bottom panel of Fig. 69 shows differences PbPb–pp in total integrated particle yields in each p_T^{trk} class for results at 5.02 TeV compared to 2.76 TeV results. This quantifies the low- p_T excess in central PbPb collisions to as many as 4 additional particles (in central PbPb relative to pp reference) per unit of p_T^{trk} in the lowest p_T^{trk} bin. This excess decreases smoothly with p_T^{trk} in each centrality bin, until the 4–8 GeV central PbPb bin is consistent with or slightly depleted relative to pp reference. For tracks with $p_T^{\text{trk}} > 8$ GeV, there is no evident modification in PbPb compared to pp. Excess yields do not exhibit significant dependence on collision energies; particle yields at low- p_T^{trk} are consistently larger at 5.02 TeV than at 2.76 TeV, but within the systematic uncertainties of the two measurements.

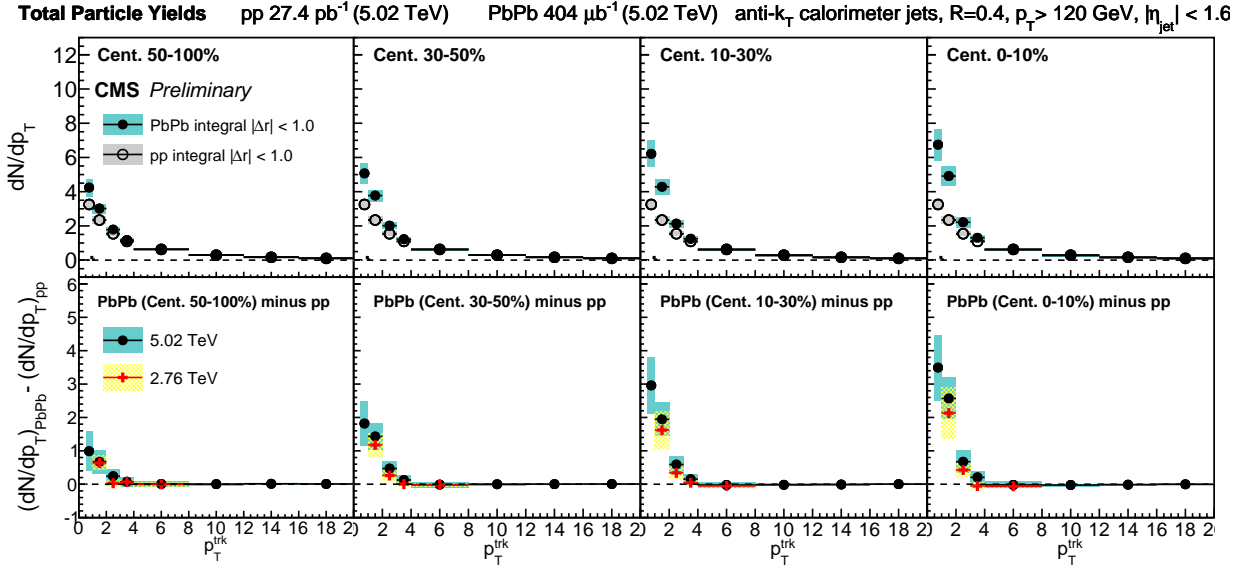


Figure 69. Top row: integrated yields of charged particle yields correlated to jets with $p_T > 120$ GeV as a function of p_T^{trk} bins for PbPb data, compared to pp reference. Bottom row: integrated excess yield, PbPb minus pp. New measurements of excess yields at 5.02 TeV are compared to those measured at 2.76 TeV.

10.2 Dijet correlation results at 2.76 TeV

In the studies of charged-particle yields correlated to an inclusive sample of jets with $p_T > 120$ GeV presented above, jet quenching is evident in the redistribution of p_T^{trk} from harder to softer particles, and particularly in the observed centrality-dependent excess of low- p_T^{trk} particle yields. Jet quenching effects may be further probed by considering charged-particle yields correlated to each jet axis in dijet events. Requiring events with two back-to-back jets (leading jet $p_{T,1} > 120$ GeV, subleading jet $p_{T,2} > 50$ GeV, $\Delta\phi_{1,2} > \frac{5\pi}{6}$), we construct separate correlations to the leading and the subleading jet axes. In pp data, most dijets are balanced while in central PbPb a greater fraction of dijet pairs are unbalanced (as discussed in Sec. 8.4), suggesting that central PbPb data contains a significant fraction of dijet pairs in which the highest- and second-highest- p_T hard-scattering products had similar transverse momenta, but in which one jet experienced a greater path-length through the medium and correspondingly greater quenching. This is expected to correspond to a “surface-bias” toward leading jets with very short path-lengths through the medium, that might be expected to cause minimal quenching in the leading jet sample. It is therefore interesting to separately compare charged-particle distributions with respect to the leading and subleading jet axes in PbPb and pp data to look for evidence of path-length dependence in jet quenching.

Figures 70 and 71 show these correlation patterns in $\Delta\eta$ and $\Delta\phi$, respectively, for the $1 < p_T^{\text{trk}}$ GeV range in which the greatest quenching was evident in the 2.76 TeV inclusive jet studies. As expected, quenching effects are greater for subleading than leading jets, as evident in larger excesses of soft particles in subleading jet correlations (while retaining the same centrality trends and gaussian-like distributions observed for the inclusive jet sample). However, leading jets exhibit evidence of quenching as well, showing similar soft-particle excesses to those observed in the inclusive sample. To quantitatively compare subleading and leading jet modifications to those in the inclusive jet sample, Fig. 72 shows integrated particle yields for all three jet samples at 2.76 TeV. Here it is clear that leading jets show similar PbPb–pp modifications to those observed in the inclusive sample, with approximately 2 excess particles in PbPb compared to pp data at lowest- p_T^{trk} , while the subleading jet sample shows as many as 4 excess particles in PbPb compared to pp data at lowest- p_T^{trk} .

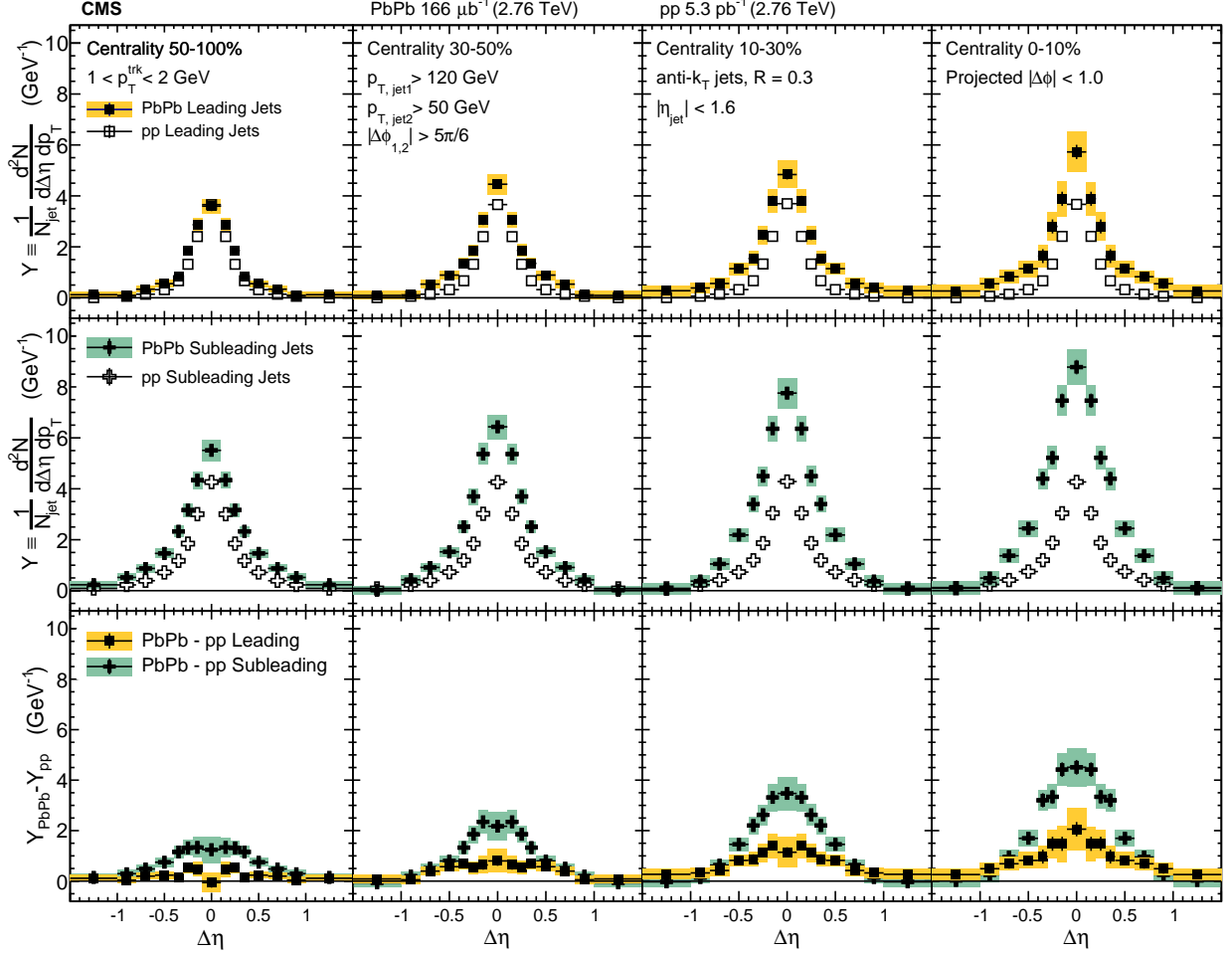


Figure 70. The top panels show the $\Delta\eta$ distributions (projected over $|\Delta\phi| < 1$) of charged-particle background-subtracted yields correlated to PbPb and pp leading jets with $p_{T,\text{jet1}} > 120$ GeV. The middle panels show the same distributions for subleading jets with $p_{T,\text{jet2}} > 50$ GeV, and the bottom panels show the difference PbPb minus pp for both leading and subleading jets. The total systematic uncertainties are shown as shaded boxes, and statistical uncertainties are shown as vertical bars (often smaller than the symbol size).

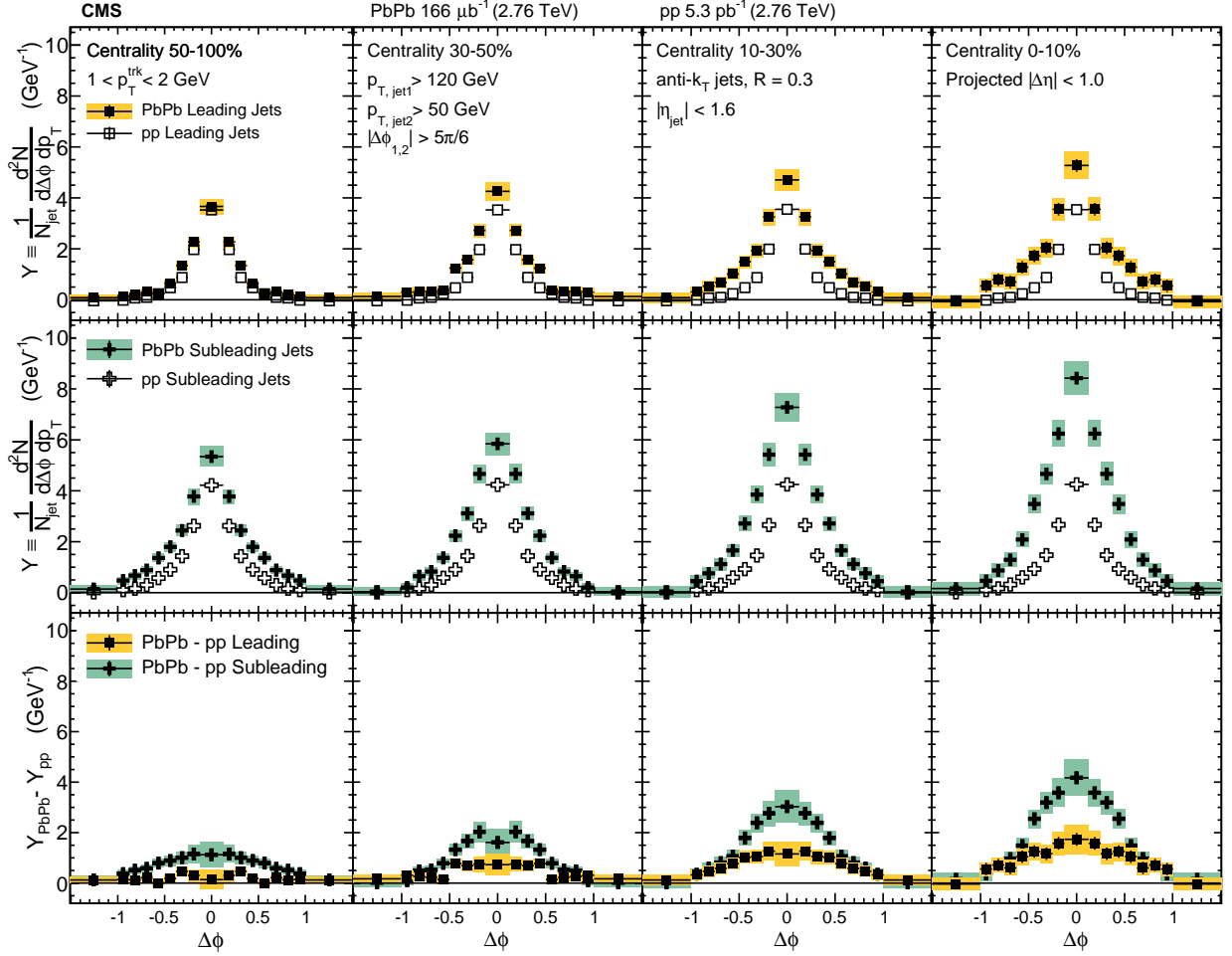


Figure 71. The top panels show the $\Delta\phi$ distributions (projected over $|\Delta\eta| < 1$) of charged-particle background-subtracted yields correlated to PbPb and pp leading jets with $p_{T,jet1} > 120$ GeV. The middle panels show the same distributions for subleading jets with $p_{T,jet2} > 50$ GeV, and the bottom panels show the difference PbPb minus pp for both leading and subleading jets. The total systematic uncertainties are shown as shaded boxes, and statistical uncertainties are shown as vertical bars (often smaller than the symbol size).

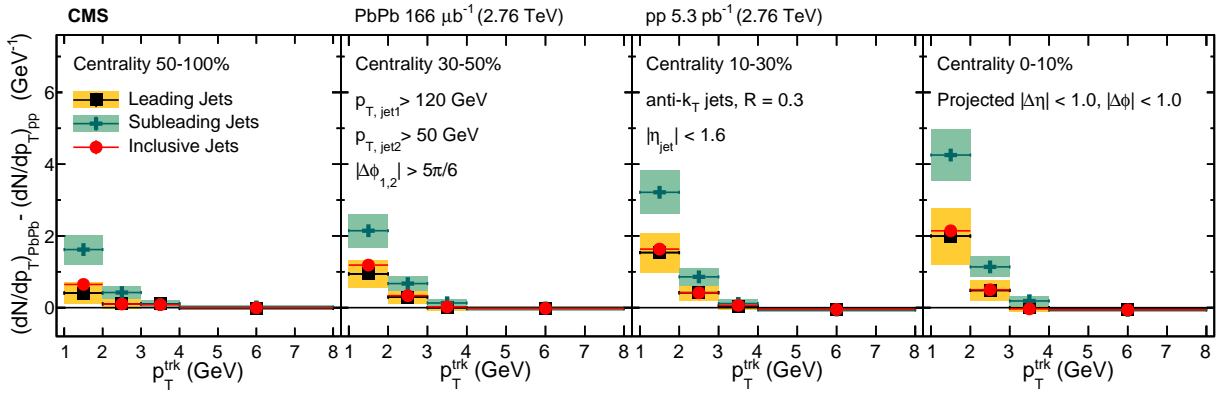


Figure 72. Total excess correlated yield observed in the PbPb data with respect to the reference measured in pp collisions, shown as a function of track p_T in four different centrality intervals (0–10%, 10–30%, 30–50%, 50–100%) for both leading jets with $p_{T,\text{jet1}} > 120$ GeV and subleading jets with $p_{T,\text{jet2}} > 50$ GeV. The total systematic uncertainties are shown as shaded boxes, and statistical uncertainties are shown as vertical bars (often smaller than the symbol size).

In addition to characterizing the magnitude of jet quenching products (via the centrality-dependent excess of low- p_T^{trk} tracks greatest in correlations to subleading jets but also present in leading jet correlations), modifications to charged-particle correlated yields may also be characterized by their widths. These studies are relevant to look for the presence and extent of jet peak broadening due to medium interactions, and can be used to distinguish between different models for jet-medium interaction and medium-modified jet radiation. In order to characterize correlation widths, correlations are fit to double-gaussian functions (all $\Delta\eta$ fits are shown in Appendix D for illustration), and the width (σ) of these fits is obtained as the range in $|\Delta\eta|$ or $|\Delta\phi|$ containing 67% of the total yield under the fit curve. To obtain systematic uncertainties on these fits, points are varied up and down by their systematic uncertainties, and widths are re-calculated from these varied distributions.

Figures 73 and 74 show correlation widths in $\Delta\eta$ and $\Delta\phi$ for leading jets in PbPb and pp data at 2.76 TeV. At low- p_T^{trk} there is a significant broadening evident in central PbPb data when compared to pp data, with this broadening decreasing in more peripheral collisions and with increasing p_T^{trk} (with similar trends to those exhibited by correlated yield magnitudes). Widths and width modifications are similar in $\Delta\eta$ and $\Delta\phi$, but slightly broader in $\Delta\phi$ for PbPb data. These leading jet correlation widths and width modifications may also be compared to subleading jet correlation widths and width modifications, shown in Figs. 75 and 76. In peripheral PbPb data subleading and leading correlation widths are similar, but subleading jet PbPb correlation widths exhibiting less centrality dependence than leading jet correlation widths so that leading jet correlations in central PbPb data are slightly broader than than subleading jet correlations (but not significantly so, when taking into account the systematic uncertainties on both measurements). Subleading jet peaks in pp data are, however, significantly broader than leading jet peaks in pp data—as is to be expected since the kinematic selection defining subleading jet as that with lower- p_T , also implies that subleading jets will on average have softer fragmentation than leading jets. Since subleading pp jets are broader than leading pp jets while subleading and leading jets have similar widths in PbPb, the jet peak broadening quantified as the PbPb–pp difference in widths is greater for leading jets than for subleading jets.

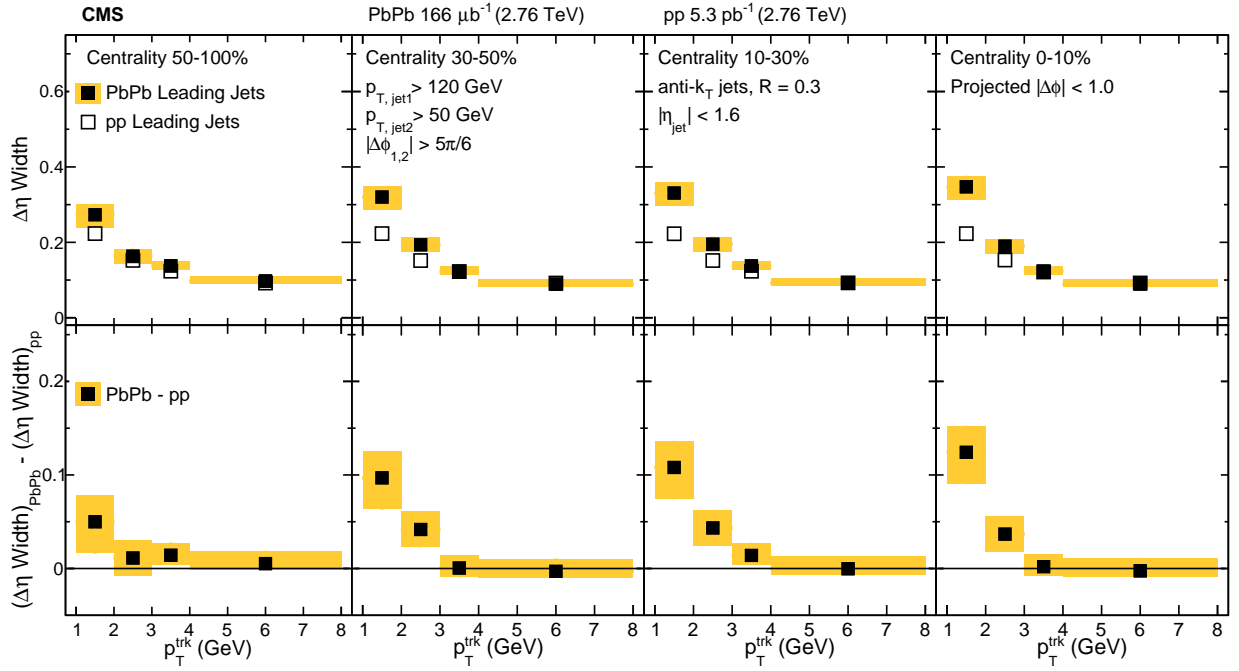


Figure 73. Comparison of the widths in PbPb and pp of the $\Delta\eta$ charged-particle distributions correlated to leading jets with $p_{T,jet1} > 120$ GeV, as a function of p_T^{trk} . The bottom row shows the difference of the widths in PbPb and pp data. The shaded band corresponds to systematic uncertainty, and statistical uncertainties are smaller than symbol size.

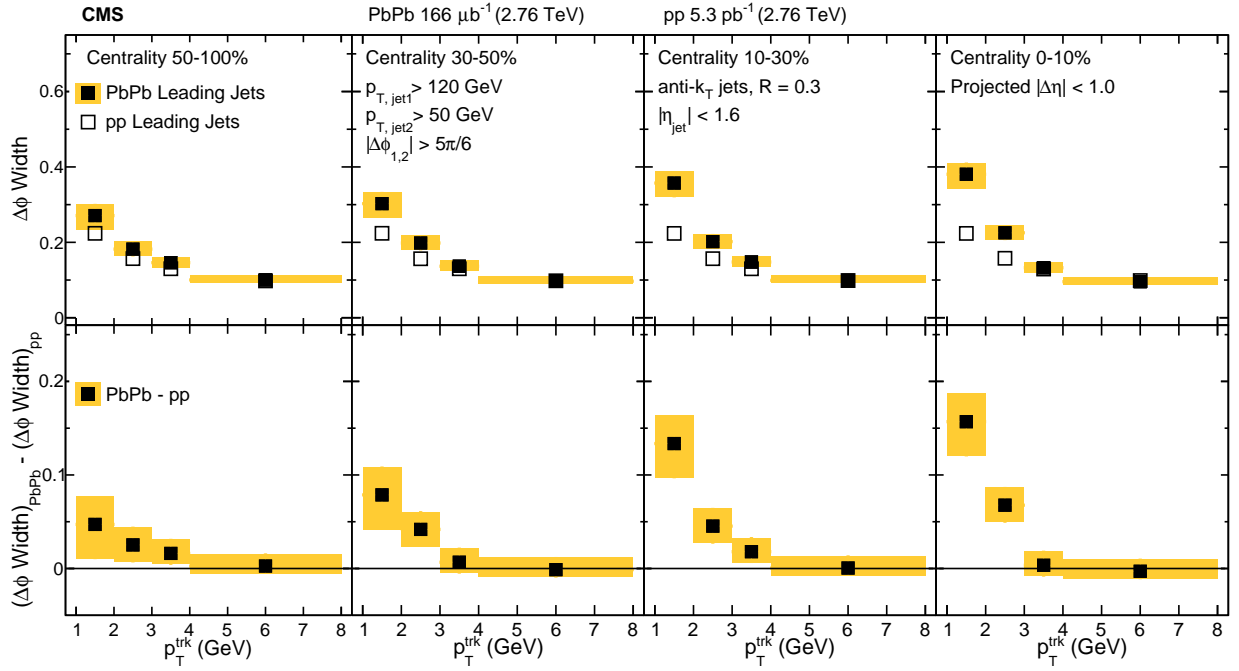


Figure 74. Comparison of the widths in PbPb and pp of the $\Delta\phi$ charged-particle distributions correlated to leading jets with $p_{T,jet1} > 120$ GeV, as a function of p_T^{trk} . The bottom row shows the difference of the widths in PbPb and pp data. The shaded band corresponds to systematic uncertainty, and statistical uncertainties are smaller than symbol size.

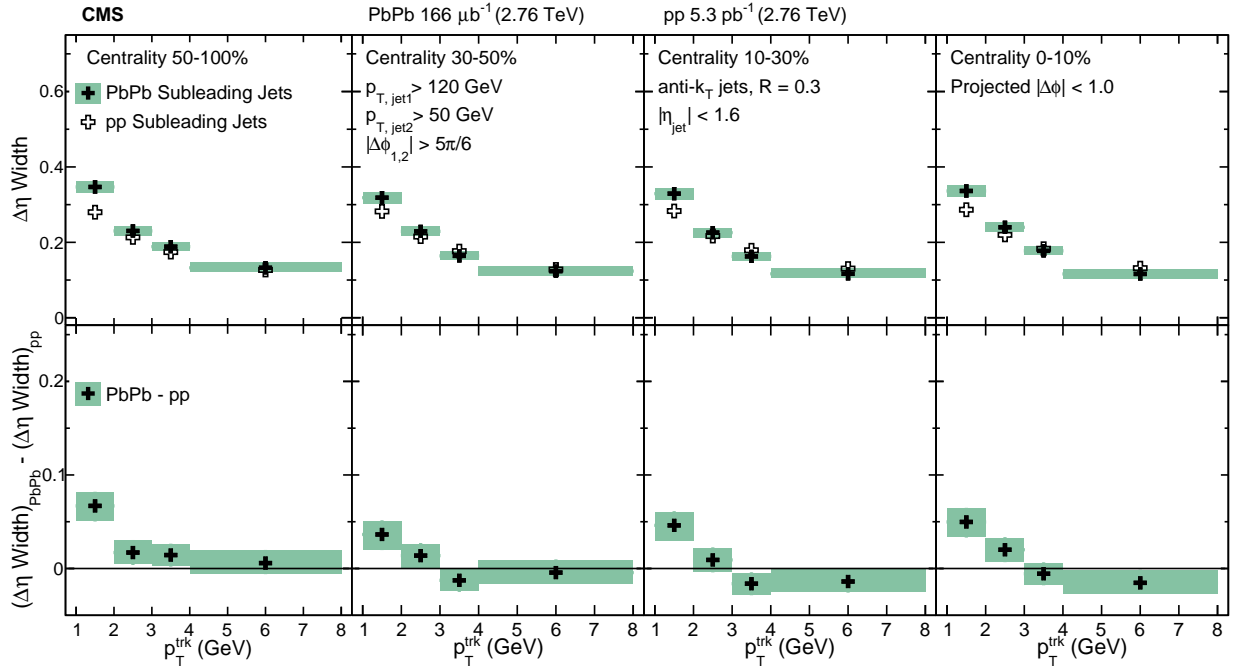


Figure 75. Comparison of the widths in PbPb and pp of the $\Delta\eta$ charged-particle distributions correlated to leading jets with $p_{T,jet2} > 50 \text{ GeV}$, as a function of p_T^{trk} . The bottom row shows the difference of the widths in PbPb and pp data. The shaded band corresponds to systematic uncertainty, and statistical uncertainties are smaller than symbol size.

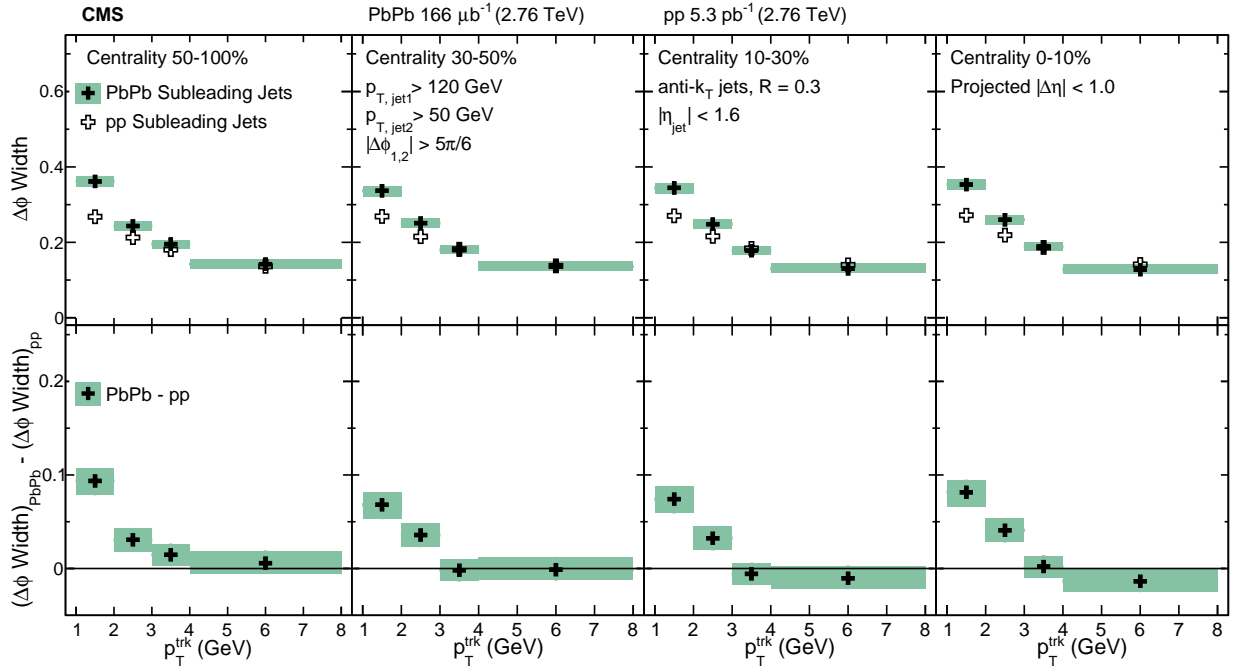


Figure 76. Comparison of the widths in PbPb and pp of the $\Delta\phi$ charged-particle distributions correlated to leading jets with $p_{T,jet2} > 50 \text{ GeV}$, as a function of p_T^{trk} . The bottom row shows the difference of the widths in PbPb and pp data. The shaded band corresponds to systematic uncertainty, and statistical uncertainties are smaller than symbol size.

10.3 Jet shapes at 2.76 TeV and 5.02 TeV

A common observable to characterize and compare the widths of jet peaks is the jet shape $\rho_{\Delta r}$, measuring the fraction of total jet transverse momentum as a function of distance Δr from the jet axis. As discussed in Sec. 4, previous CMS measurements of jet shape [34] have gained particular attention from the theoretical community in efforts to constrain models of jet energy loss. Jet shape measurements to large angles ($\Delta r = 1$, compared to previous measurements to only $\Delta r = 0.3$) may be obtained from correlation studies, extending measurements to the full range of the jet peak and offering the capability of distinguishing between theoretical predictions based on earlier, more narrow, measurements.

In the correlation technique, jet shapes are obtained by weighting correlations by p_T^{trk} , and integrating the resulting (background-subtracted) 2D jet-peak momentum distributions in annuli with radial width $\Delta r = 0.05$, where each has an inner radius of $r_a = \Delta r - \delta r/2$ and an outer radius of $r_b = \Delta r + \delta r/2$. For this measurement, an inclusive high- p_T^{trk} bin is included to capture particles with $20 < p_T^{\text{trk}} < 300$ GeV. The resulting transverse momentum profile of the jet is defined as:

$$P(\Delta r) = \frac{1}{\delta r} \frac{1}{N_{\text{jets}}} \sum_{\text{jets}} \sum_{\text{tracks} \in (r_a, r_b)} p_T^{\text{trk}} \quad (28)$$

This profile is then normalized to unity within $\Delta r = 1$ to produce the jet shape $\rho(\Delta r)$:

$$\rho(\Delta r) = \frac{1}{\delta r} \frac{\sum_{\text{jets}} \sum_{\text{tracks} \in (r_a, r_b)} p_T^{\text{trk}}}{\sum_{\text{jets}} \sum_{\text{tracks}} p_T^{\text{trk}}} \quad (29)$$

The top row of Fig. 77 presents the inclusive jet transverse momentum profile $P(\Delta r)$ in pp and PbPb data at 5.02 TeV, while the middle row shows the jet shape $\rho(\Delta r)$, normalized to unity within $\Delta r = 1$. Here again redistribution of energy from small to large angles from the jet cone is evident in PbPb relative to pp reference, as seen in the dipping then rising trend in the jet shape ratio $\rho(\Delta r)_{\text{PbPb}}/\rho(\Delta r)_{\text{pp}}$ presented in the bottom row.

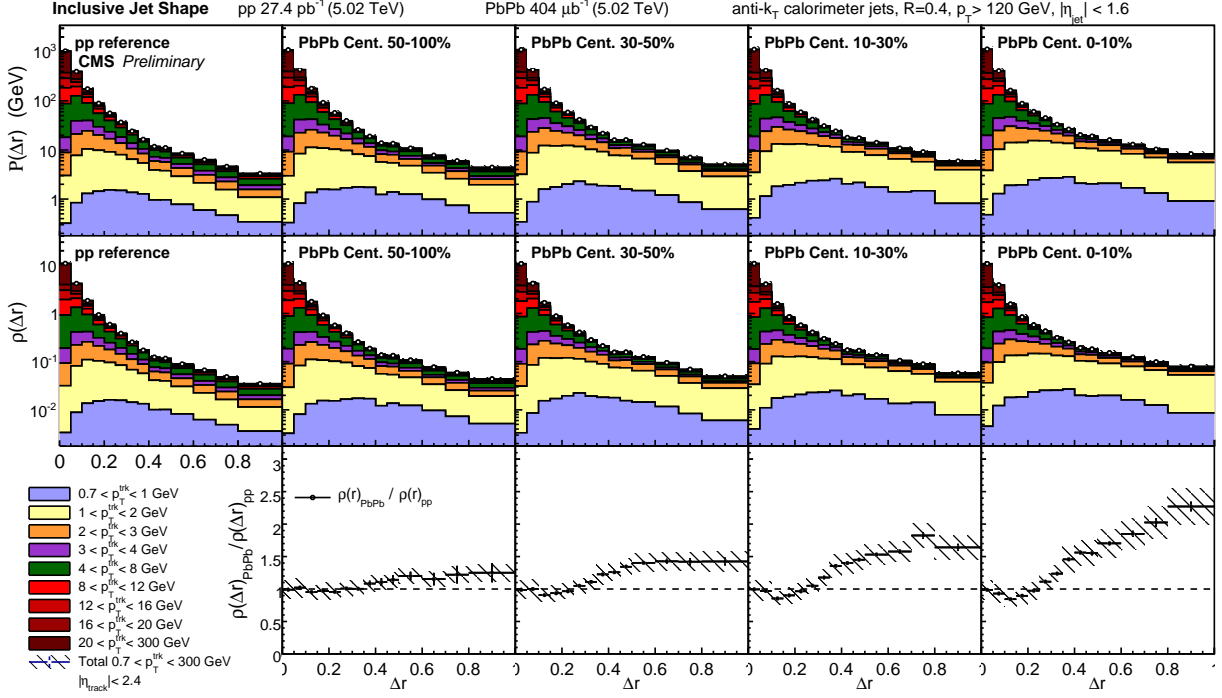


Figure 77. Top row: Transverse momentum profile of inclusive jets $P(\Delta r)$ in pp and PbPb data at 5.02 TeV, shown differentially in p_T^{trk} . Middle row: jet shapes $\rho(\Delta r)$ (normalized to unity over $\Delta r < 1$) in PbPb and pp. Bottom row: jet shape ratio $\rho(\Delta r)_{\text{PbPb}}/\rho(\Delta r)_{\text{pp}}$. Hatched lines on p_T^{trk} -inclusive points show total systematic uncertainties.

In addition to studies of inclusive jet shapes, it is also interesting to consider the jet shapes and jet shape modifications of leading and subleading jets in dijet events. These studies are carried out with the same selection of 2.76 TeV dijet events used for the correlation studies presented in 10.2. In this case, for consistency with a previous CMS study measured the jet shape $\rho(\Delta r)$ within the jet cone radius $\Delta r = 0.3$ [34] at 2.76 TeV, these leading and subleading jet shape measurements at 2.76 TeV are normalized to integrate to unity within the radius $\Delta r < 0.3$. In Fig. 78, the leading jet shape measured with this correlation technique is compared to the published CMS reference and extend this measurement to $\Delta r = 1$, noting that the leading jet shape is consistent within uncertainties with the previous measurement for an inclusive jet selection of all jets with $p_T > 100$ GeV. A new measurement of subleading jet shape in Fig. 79 is then presented. As noted in the correlation width measurements discussed in Sec. 10.2, subleading jets in pp data are broader than leading jets in pp data. Therefore, although the PbPb-to-pp *modifications* are similar for leading and subleading jets, the more steeply falling pp leading jet shape results in a greater *relative*

modification shown in the jet shape ratio $\rho_{\text{PbPb}}(\Delta r)/\rho_{\text{pp}}(\Delta r)$ for leading than for subleading jets. Similarly, when comparing jet shape measurements at 2.76 TeV to those at 5.02 TeV, it is relevant to note that the pp reference is broader at 5.02 TeV than at 2.76 TeV, likely due to the greater fraction of gluon versus quark jets that pass the kinematic selections of the analysis at the higher center-of-mass energy.

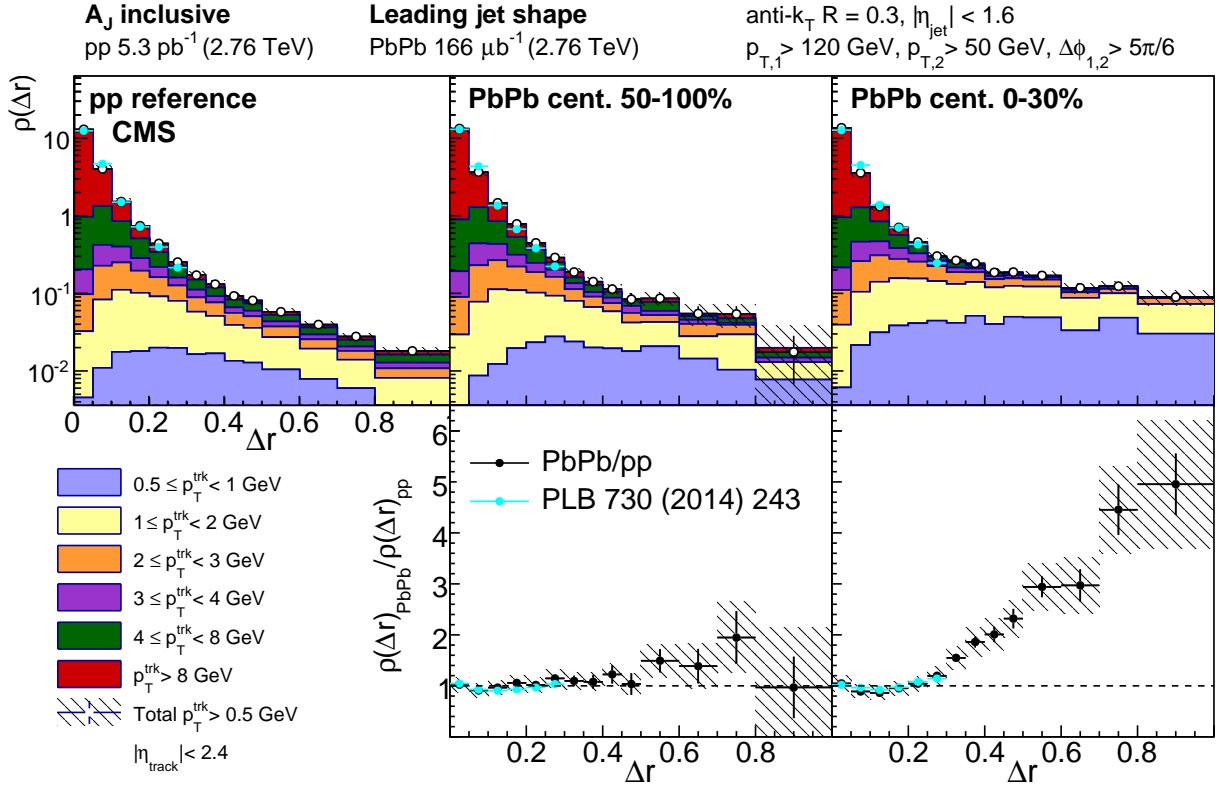


Figure 78. Top row: leading jet shape $\rho(\Delta r)$ for pp reference and central and peripheral PbPb data, shown for all tracks with $p_T^{\text{trk}} > 0.5$ GeV and decomposed by track transverse momentum. Shapes are normalized to unity over the region $r < 0.3$ for consistency with the published reference shown (Ref. [34]). Bottom row: leading jet shape ratio $\rho(\Delta r)_{\text{PbPb}}/\rho(\Delta r)_{\text{pp}}$, again with published reference.

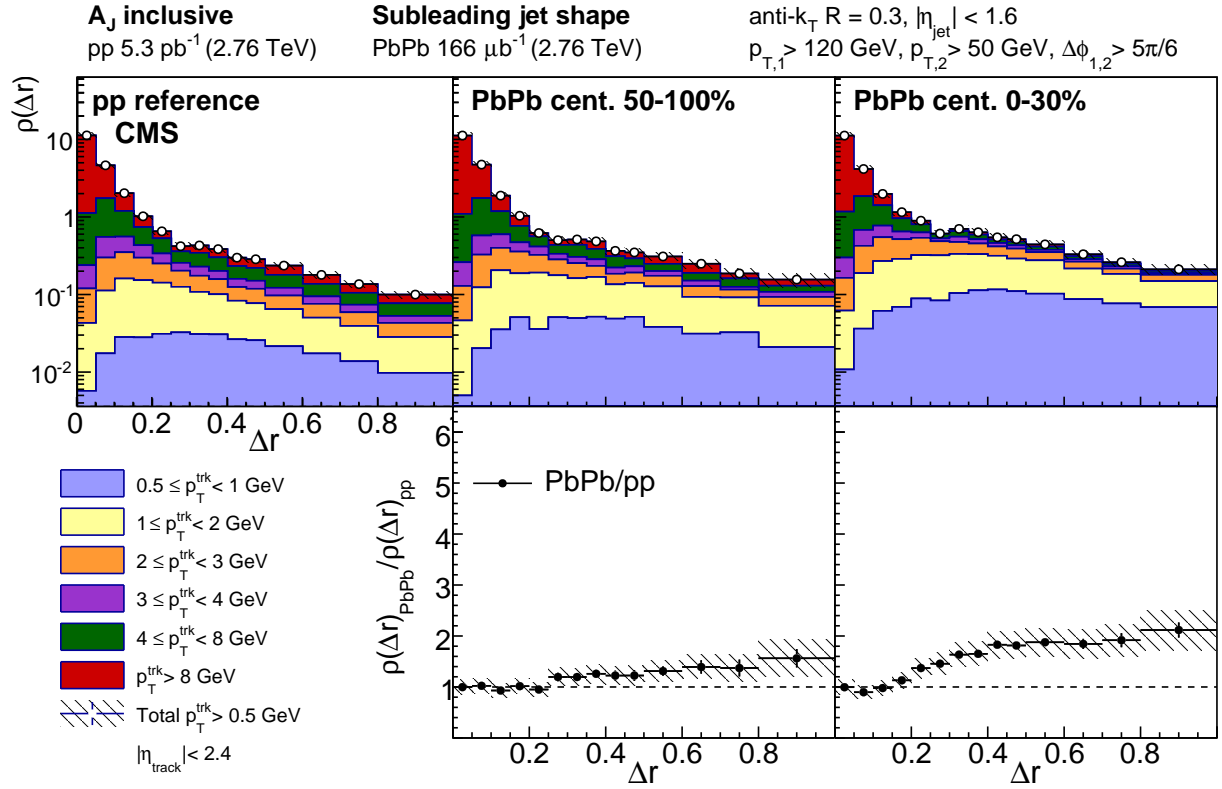


Figure 79. Top row: subleading jet shape $\rho(\Delta r)$ for pp reference and central and peripheral PbPb data, shown for all tracks with $p_T > 0.5$ GeV and decomposed by track transverse momentum, normalized to unity over the region $\Delta r < 0.3$ Bottom row: subleading jet shape ratio $\rho(\Delta r)_{\text{PbPb}}/\rho(\Delta r)_{\text{pp}}$.

10.4 Decomposition of hemisphere momentum balance in dijet events at 2.76 TeV

The dijet results at 2.76 TeV presented in this analysis are complimented by other CMS measurements conducted on the same data using the “missing- p_T ” hemisphere momentum balance method presented in Ref. [39] and discussed in Secs. 3 and 4. In this analysis, a “dijet” axis is constructed by averaging the leading jet and subleading jet axes (these are separated by $\Delta\phi_{1,2} = \pi$ on average, but are not necessarily parallel in each event due to 3-jet events) to construct a dijet axis, dividing the event into leading and subleading hemispheres with respect to this axis, and comparing the hemisphere-wide distributions of p_T^{trk} (projected, in this case, onto the combined dijet axis) to obtain the subleading-to-leading balancing distribution as a function of distance from the dijet axis Δr . The jet track correlation technique may be used to obtain this same measurement (comparing subleading-to-leading distributions on average rather than event-by-event, and making use of the fact that the subleading and leading jet axes are *on average* perfectly back-to-back). When this cross-check is performed *without background subtraction*, the two techniques yield consistent results, despite methodological differences and differences in jet- η cuts. This hemisphere-wide missing- p_T technique is also used to extract differences in total particle yields between the leading and subleading hemispheres, and shows an average excess of 4-5 particles with p_T^{trk} in the subleading hemisphere compared to the leading hemisphere [39]. In the dijet correlation studies presented in this analysis *with background subtraction*, however, only approximately 2 additional particles were found correlated to the subleading jet peak compared to the leading jet peak, as shown in Sec. 10.2. This apparent difference motivates a detailed examination and decomposition of the distribution of p_T^{trk} in dijet events in order to consider contributions to the hemisphere-wide momentum balance from both the leading and subleading jet peaks, and from the long-range correlated underlying event.

For this investigation, the dijet samples of 2.76 TeV PbPb and pp data are each divided based on asymmetry parameter A_J to further illuminate quenching effects and to decompose the contributions to the hemisphere p_T^{trk} balance studied in Ref. [39]: a balanced sample with $A_J < 0.22$, and an “unbalanced” sample with $A_J > 0.22$. Transverse momentum distributions for each sample are constructed in $\Delta\eta - \Delta\phi$ for each sample, and are corrected for pair-acceptance effects. Like all particle density and p_T^{trk} correlations studied in this analysis, these show jet peaks on an underlying

event that shows significant $\Delta\phi$ correlations but is flat in $\Delta\eta$. Correlations are therefore projected into $\Delta\phi$ for further study in order to preserve this underlying event structure. We will begin by presenting measurements of the hemisphere-wide “missing- p_T ” distribution as a function of $\Delta\phi$, and then decompose this distribution into jet peak and underlying event contributions to evaluate the relative contributions from jet peaks and from the underlying event to the overall hemisphere p_T^{trk} balance for balanced and unbalanced dijets.

Figures 80 and 81 present the hemisphere-wide balancing distribution of transverse momentum around the subleading versus the leading jet for balanced and unbalanced dijets respectively. For both selections, a wide excess of soft particles in the subleading versus leading hemisphere in central PbPb collisions relative to pp reference is evident, reflecting the greater quenching of the subleading jet. In the unbalanced selection, as required by momentum conservation, the signal is enhanced in both pp and PbPb data: in pp a large excess of particles with $p_T > 3$ GeV long-range is present on the subleading side, compensating for the lower momentum of the highest- p_T particles in the jet itself. In peripheral PbPb data the distribution is quite similar to pp reference, while in central PbPb data this balancing distribution consists mostly of soft particles $p_T < 3$ GeV, consistent with the findings of a previous CMS study [39]. To better demonstrate these medium modifications, the difference in yield between PbPb and pp collisions is shown in the bottom panels of Fig. 80 and Fig. 81.

To better understand the redistribution of transverse momentum within the QGP, the distributions are then separated into three components as discussed above: the gaussian-like peaks about the leading and subleading jet axes, plus a component accounting for overall subleading-to-leading asymmetry in the $\Delta\phi$ -correlated long-range underlying event (measured in the region $1.5 < |\Delta\eta| < 2.5$). In Fig. 82 and Fig. 83, the jet peak components are shown for balanced and unbalanced jets respectively, presenting subleading results positive and leading results negative (in line with the hemisphere difference measurements in Fig. 81 and Fig. 80). Jet peak distributions after decomposition are projected over the full range $|\Delta\eta| < 2.5$, again for consistency with the hemisphere difference measurements. The top row of each panel first shows the overall distribution of momentum carried by particles with $p_T < 8$ GeV on about the jet peak. The middle two panels then assess modifications to the subleading and leading jets, respectively. Here there is evidence of quenching to both the subleading and the leading jet in central PbPb collisions relative to pp

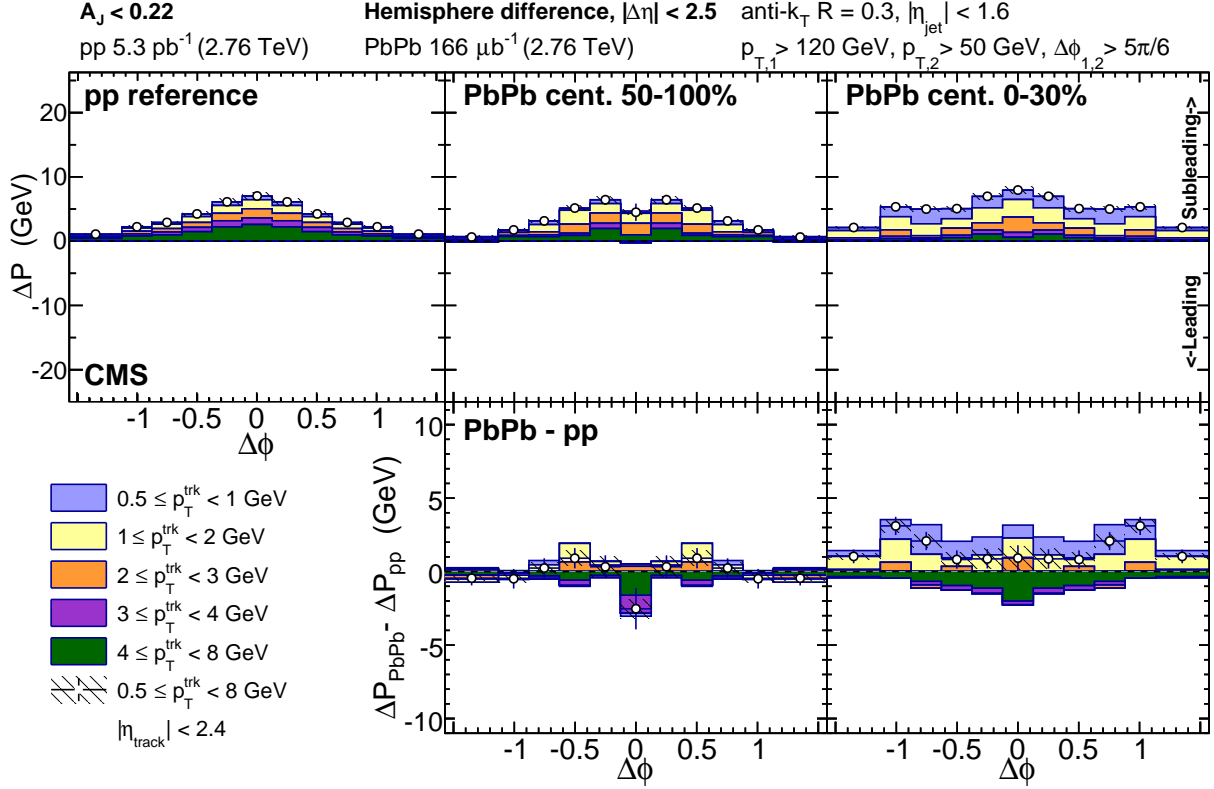


Figure 80. Top row: total hemisphere distribution in $\Delta\phi$ of excess transverse momentum around the subleading relative to the leading jet for balanced dijets with $A_J < 0.22$, shown differentially by track transverse momentum for pp reference, peripheral PbPb, and central PbPb data. Bottom row: PbPb–pp difference in these $\Delta\phi$ momentum distributions.

reference, with an excess of low- p_T^{trk} particles correlated to the jet axis in both the balanced and unbalanced dijet selections, as observed in the charged particle density studies presented in Sec. 10.2. In unbalanced dijets this enhancement of soft- p_T^{trk} particles turns into a depletion at higher- p_T^{trk} , and is greater on the subleading than the leading side. To compare between hemispheres and assess the jet peak contribution to the overall hemisphere momentum balance, the double difference PbPb–pp, subleading–leading is presented in the bottom panel. Here it is evident that the low- p_T^{trk} excess in central PbPb collisions is larger on the subleading than the leading side of the dijet system, but larger subleading-to-leading excess only accounts for only a portion of the total momentum redistribution in unbalanced dijet events.

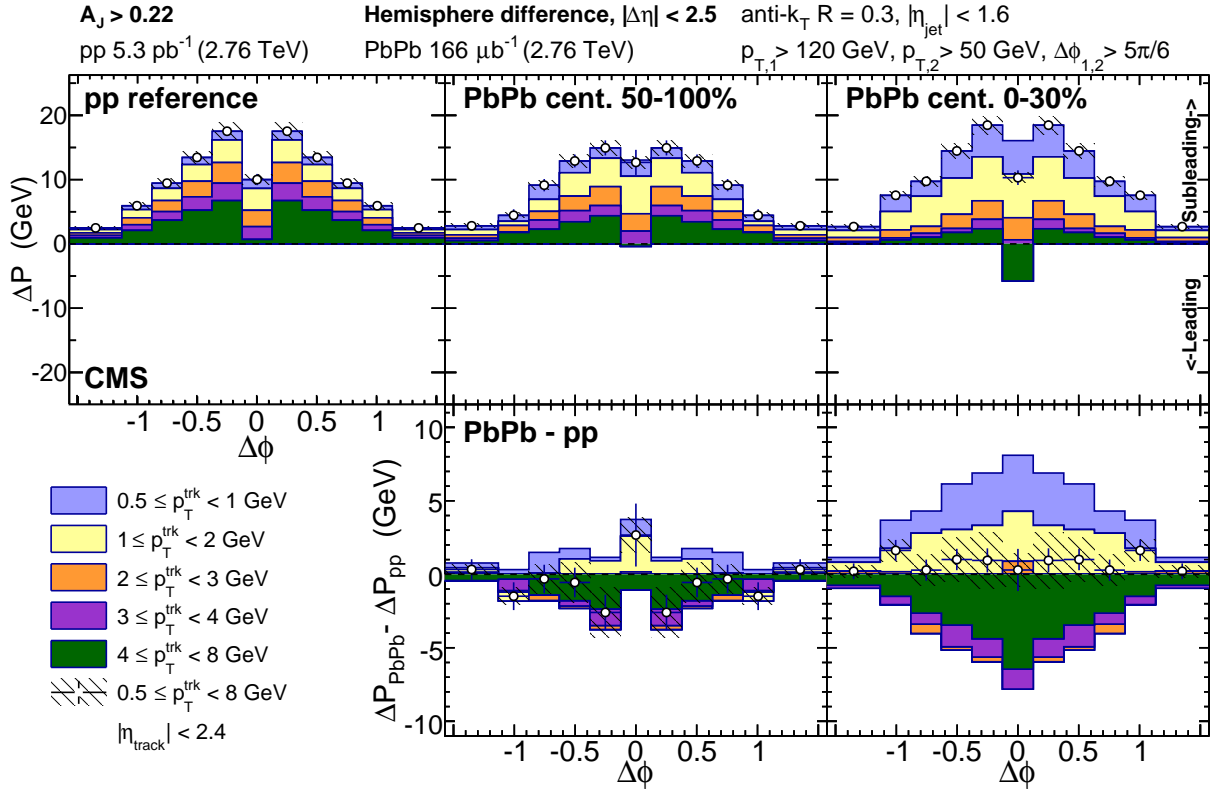


Figure 81. Top row: total hemisphere distribution in $\Delta\phi$ of excess transverse momentum about the subleading relative to the leading jet for balanced dijets with $A_J > 0.22$, shown differentially by track transverse momentum for pp reference, peripheral PbPb, and central PbPb data. Bottom row: PbPb–pp difference in these $\Delta\phi$ momentum distributions.

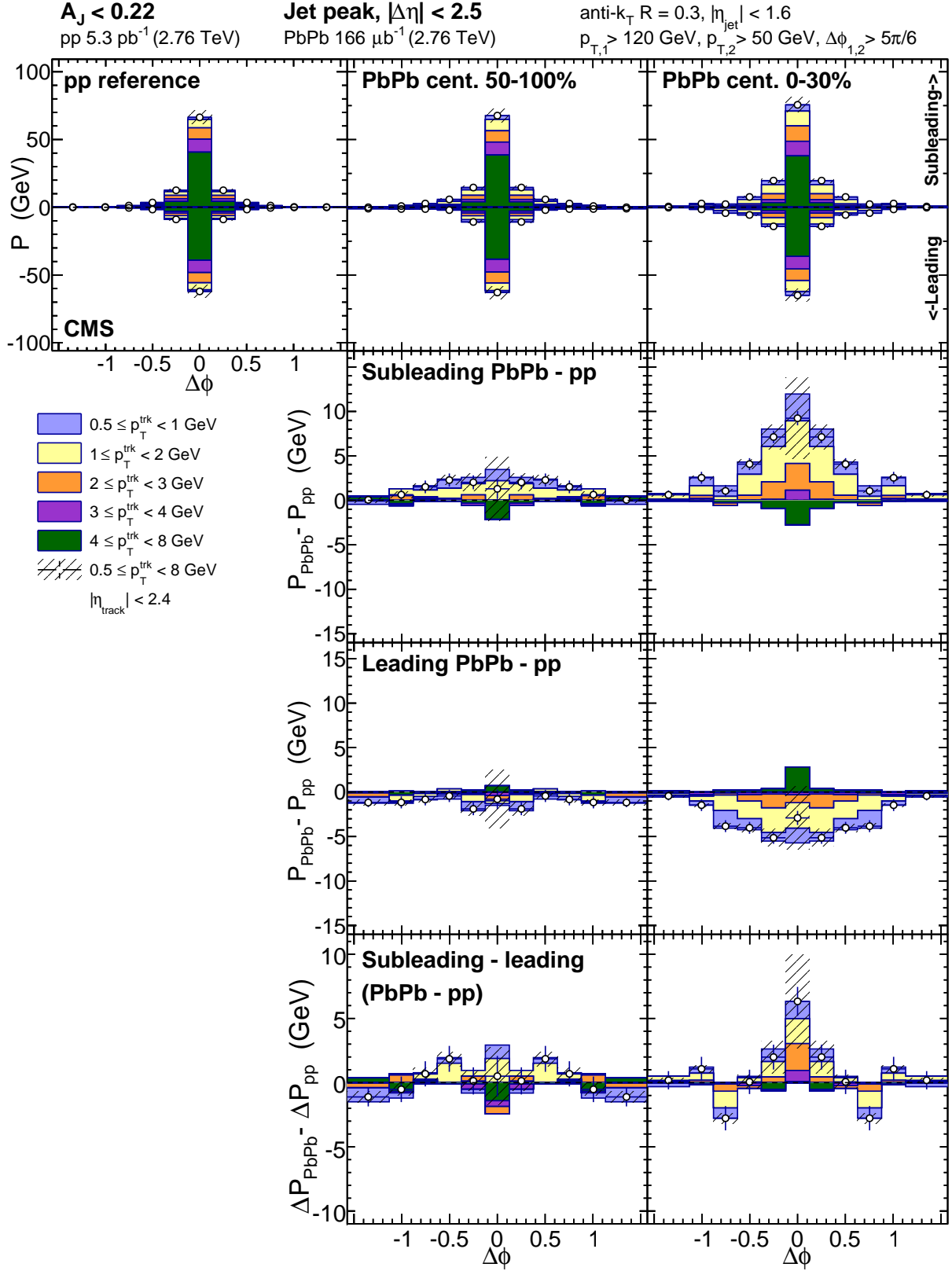


Figure 82. Top row: jet-peak (long-range subtracted) distribution in $\Delta\phi$ of transverse momentum about the subleading (plotted positive) and leading (plotted negative) jets for balanced dijets with $A_J < 0.22$. Middle rows: PbPb–pp momentum distribution differences for subleading and leading jets. Bottom row: PbPb–pp, subleading–leading double difference in these $\Delta\phi$ momentum distributions.

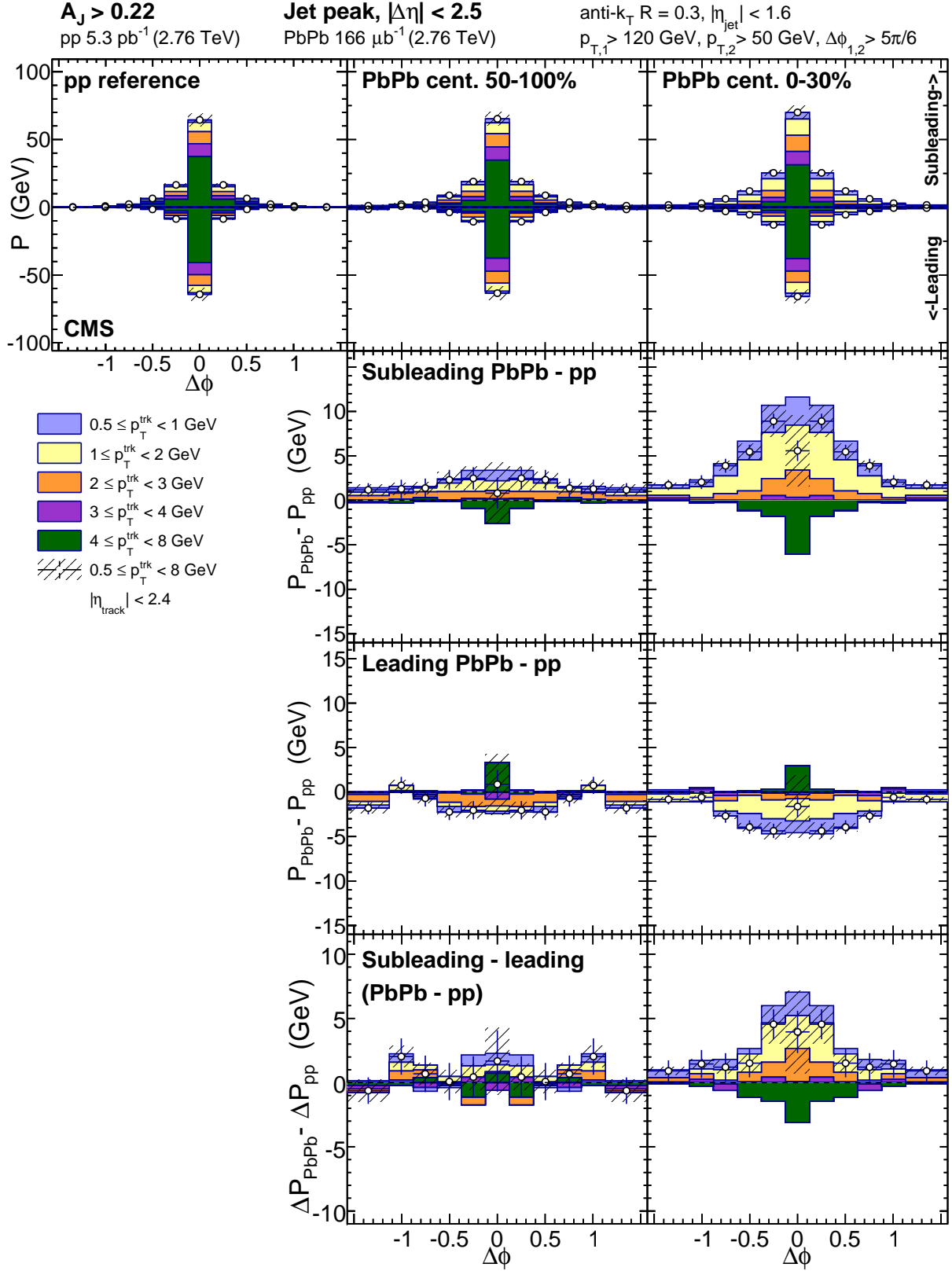


Figure 83. Top row: jet-peak (long-range subtracted) distribution in $\Delta\phi$ of transverse momentum about the subleading (plotted positive) and leading (plotted negative) jets for balanced dijets with $A_J > 0.22$. Middle rows: PbPb–pp momentum distribution differences for subleading and leading jets. Bottom row: PbPb–pp, subleading–leading double difference in these $\Delta\phi$ momentum distributions.

These jet-related studies are complemented by an analysis of the long-range subleading to leading asymmetry, presented in Fig. 84 and Fig. 85 for balanced and unbalanced jets respectively. The long-range correlated background in balanced dijet events is symmetric in pp and peripheral PbPb data, while in central PbPb data there is a small excess of low- p_T^{trk} particles. In unbalanced dijets, however, there is significant asymmetry already in pp reference, with a large correlated excess of particles in all p_T classes less than 8 GeV on the subleading relative to leading side of the underlying event. This asymmetry reflects the presence of other hard-scattering products in the subleading hemisphere dijet event, as required by momentum conservation when selecting asymmetric dijets in vacuum-like collisions. In the presence of the strongly interacting medium, however, this underlying event asymmetry in asymmetric dijet events changes notably. In peripheral PbPb collisions there is already some depletion of momentum carried by high- p_T^{trk} particles, and in central PbPb collisions subleading-to-leading underlying event excesses with $p_T^{\text{trk}} > 2$ GeV vanish nearly completely. To assess the contribution of this long-range asymmetry to the total hemisphere imbalance, the double difference PbPb–pp, subleading–leading is plotted on the bottom panel as for (and on the same scale as) the double difference shown for the jet peaks. To assess the overall hemisphere momentum balance attributed to this long-range asymmetry, the hemisphere integral ($|\Delta\phi| < \pi/2$ and $|\Delta\eta| < 2.5$) is presented in Fig. 86 for balanced versus unbalanced dijets. For unbalanced dijets, the overall asymmetry rises with track- p_T pp reference, but falls with track- p_T for central PbPb data.

Finally, to show the relative contributions to overall hemisphere momentum balance from the leading and subleading jet peaks as well as from the long-range underlying event asymmetry, a summary of hemisphere-integrated excess (PbPb–pp) yield for balanced and unbalanced dijets in central PbPb collisions is shown in Fig. 87 and Fig. 88 for central and peripheral collisions respectively. The top panels of Fig. 87 present total PbPb minus pp differences in transverse momentum associated with the subleading jet (plotted positive) and leading jet (plotted negative). Modifications to the distribution of tracks with $p_T < 3$ GeV are evident for both the leading and subleading jet peaks, with a greater enhancement of low- p_T^{trk} particles associated with the subleading jet. These total jet peak modifications in central PbPb collisions are not significantly different in unbalanced versus balanced dijets. The bottom panels of Fig. 87 present these jet-peak modifications together with the long-range modifications evident in Fig. 86 to show the decomposed

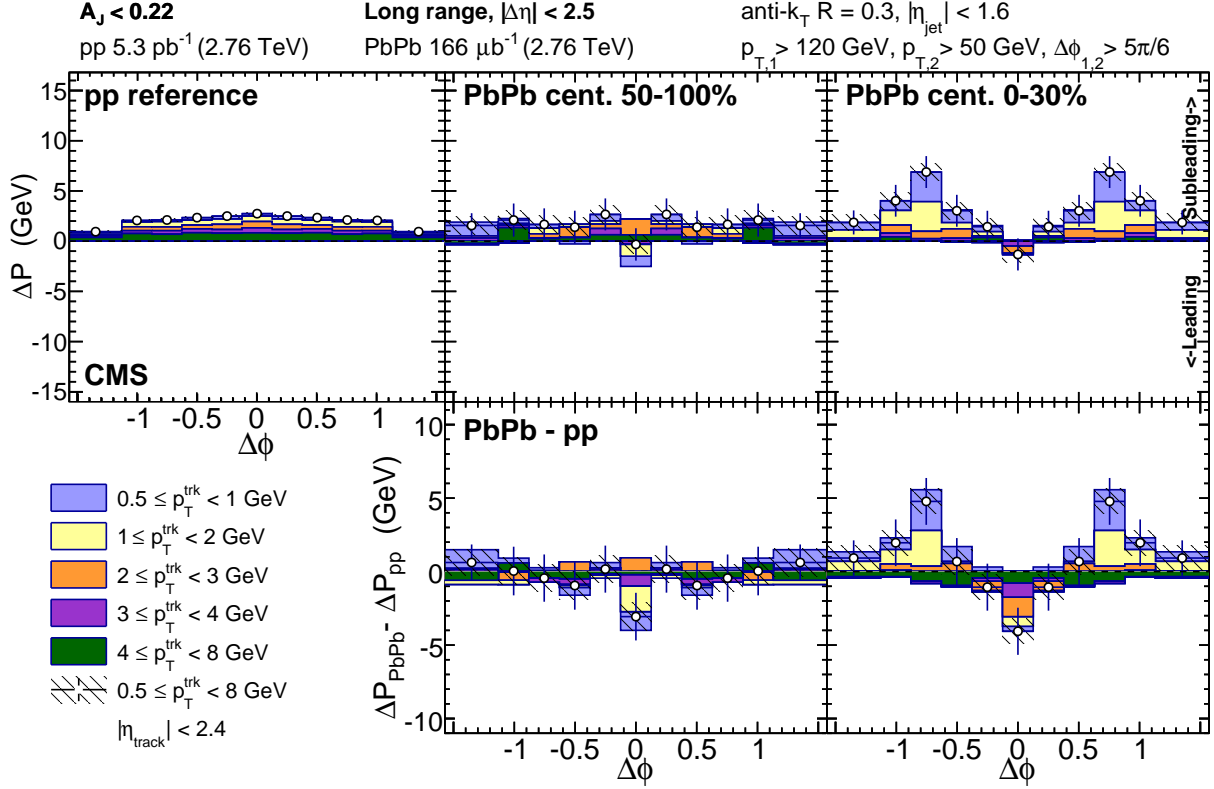


Figure 84. Top row: long-range distribution in $\Delta\phi$ of excess transverse momentum in the subleading relative to leading sides for balanced dijets with $A_J < 0.22$. Bottom row: PbPb–pp difference in these $\Delta\phi$ long-range momentum distributions.

hemisphere-wide differences in associated transverse momentum in each p_T^{trk} range. Unlike the jet peak contributions, the long-range PbPb versus modifications differ outside of uncertainties between balanced and unbalanced dijets: here the depletion of high- p_T^{trk} particles in unbalanced PbPb versus pp dijets corresponds to the reduced contribution from third jets (which are prominently evident in the long-range distribution for pp unbalanced dijet events) in central PbPb unbalanced dijet events. Figure 88 presents the same hemisphere-integrated PbPb minus pp excess information for peripheral collisions for comparison to the central results shown in Fig. 87. Some possible small modifications are already evident in this 50-100% centrality range, but these differences between peripheral PbPb and pp results are in most cases smaller than systematic uncertainties.

The decomposition of integrated jet peak and long-range correlated p_T^{trk} shown in Fig. 87 and Fig. 88 clarify the relationship between the jet peak correlation studies presented in this analysis and the missing- p_T measurements presented in Ref. [39]: as shown through this detailed decomposi-

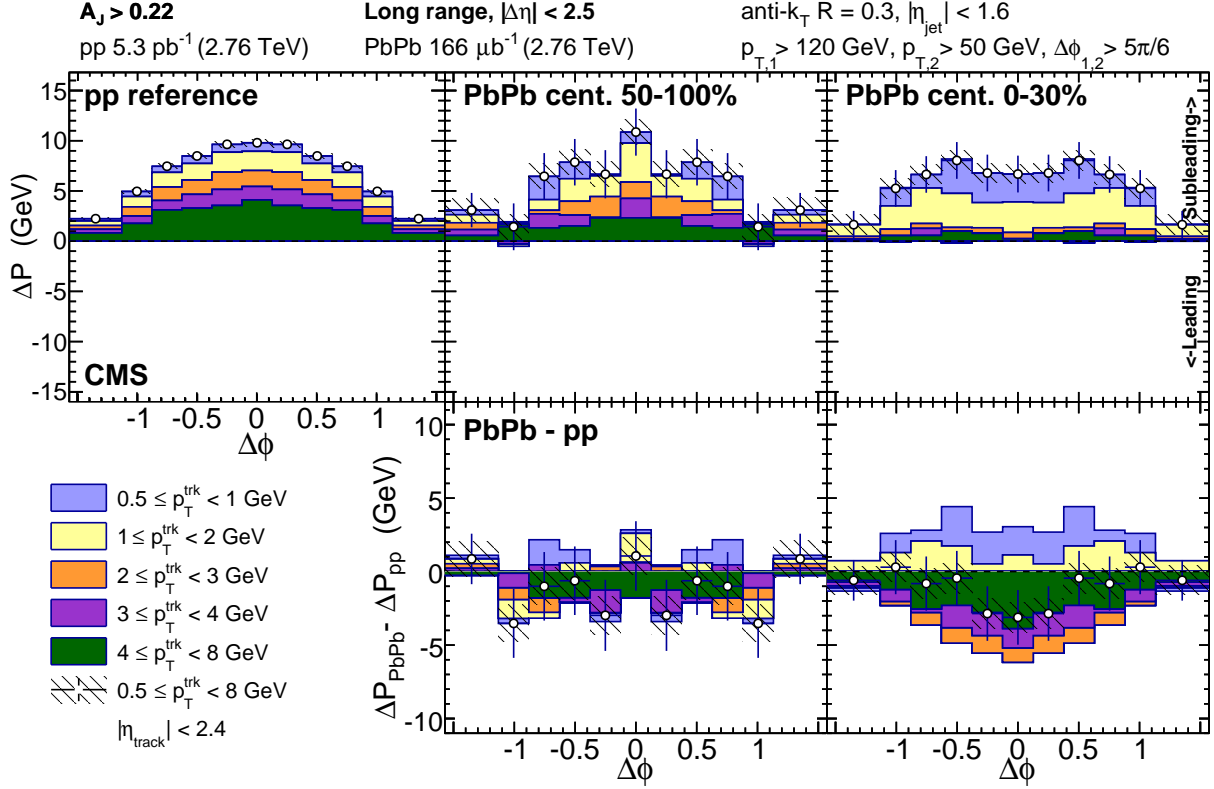


Figure 85. Top row: long-range distribution in $\Delta\phi$ of excess transverse momentum in the subleading relative to leading sides for balanced dijets with $A_J > 0.22$. Bottom row: PbPb–pp difference in these $\Delta\phi$ long-range momentum distributions.

tion, comparing hemisphere distributions as a whole include contributions from the subleading and leading jet peaks studied in correlation studies, but also a contribution from the underlying event. In both PbPb and pp data, the underlying event partially cancels with hemisphere subtraction: contributions from combinatoric background and even flow harmonics (V_2 etc.) will cancel, while contributions from 3rd jets and odd flow harmonics (V_1 , V_3 etc.) will not. As we have seen, in pp the non-cancelling underlying event is dominated by 3rd jets, especially in the unbalanced dijet selection in which their presence is kinematically required. In PbPb (where the contribution from 3rd jet events is smaller), this underlying event has evident contributions from odd flow harmonics as well, reflecting coupling of jets to the event reaction plane.

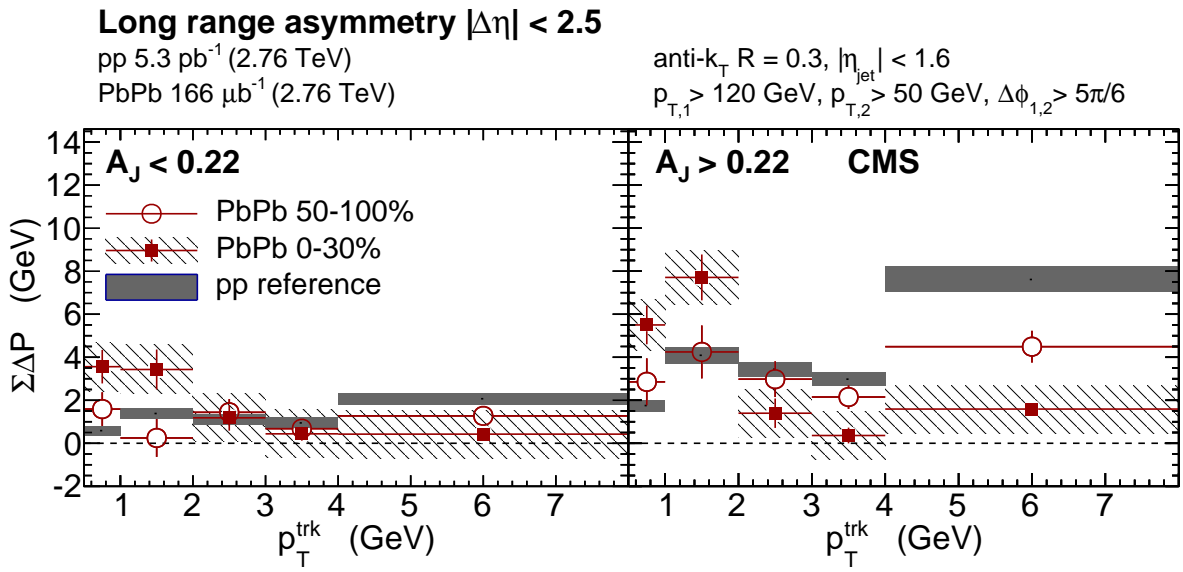


Figure 86. Integrated transverse momentum in the long-range $\Delta\phi$ -correlated distribution as a function of track- p_T integrated over $|\Delta\phi| < \pi/2$ and $|\Delta\phi| < 2.5$ and for pp reference, peripheral PbPb and central PbPb data for balanced compared to unbalanced dijets.

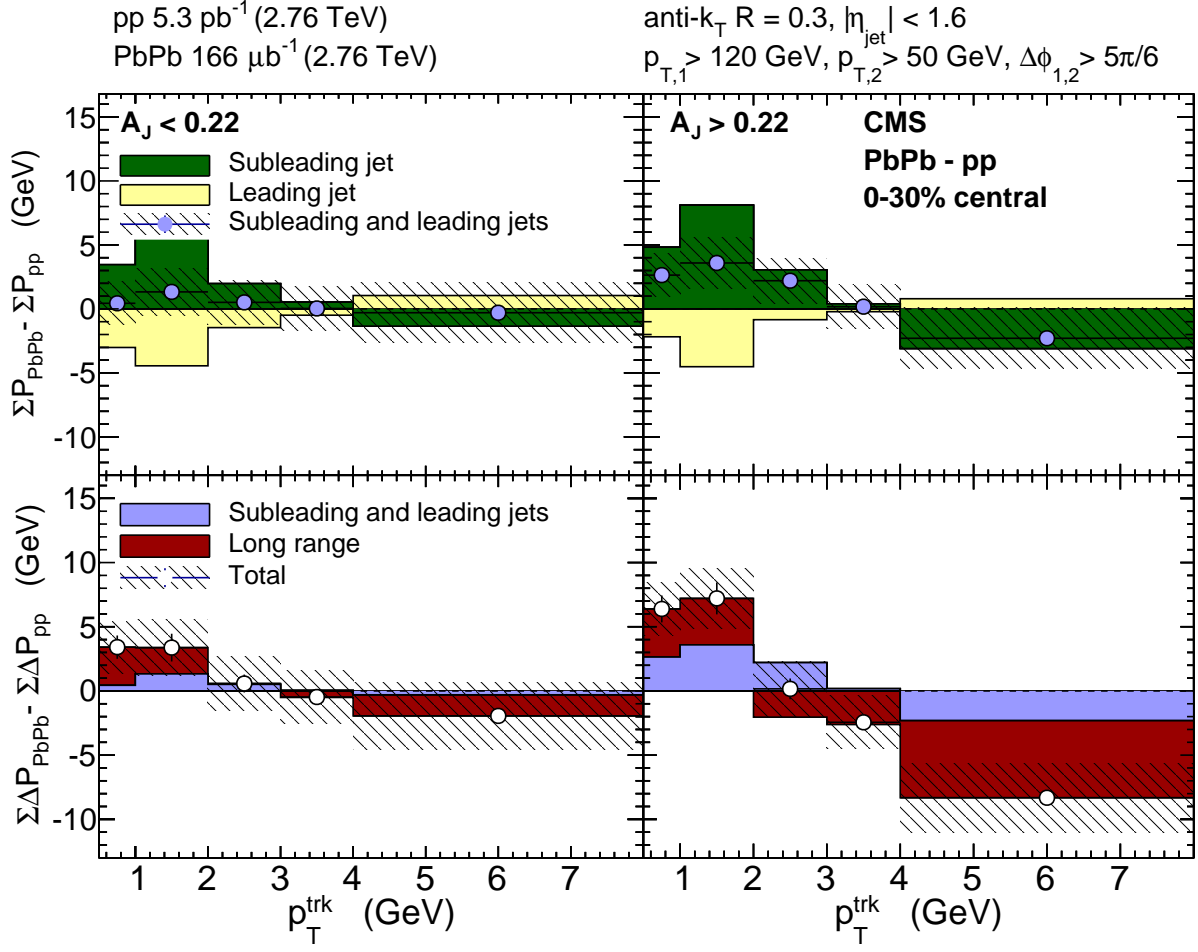


Figure 87. Modifications of jet-hadron correlated transverse momentum in central PbPb collisions with respect to pp reference, integrated $|\Delta\phi| < \pi/2$, $|\Delta\phi| < 2.5$. Top row: subleading and leading jet peak PbPb–pp. Bottom row: relative contributions from jet peaks and long-range asymmetry to the double difference PbPb–pp, subleading–leading in total hemisphere transverse momentum.

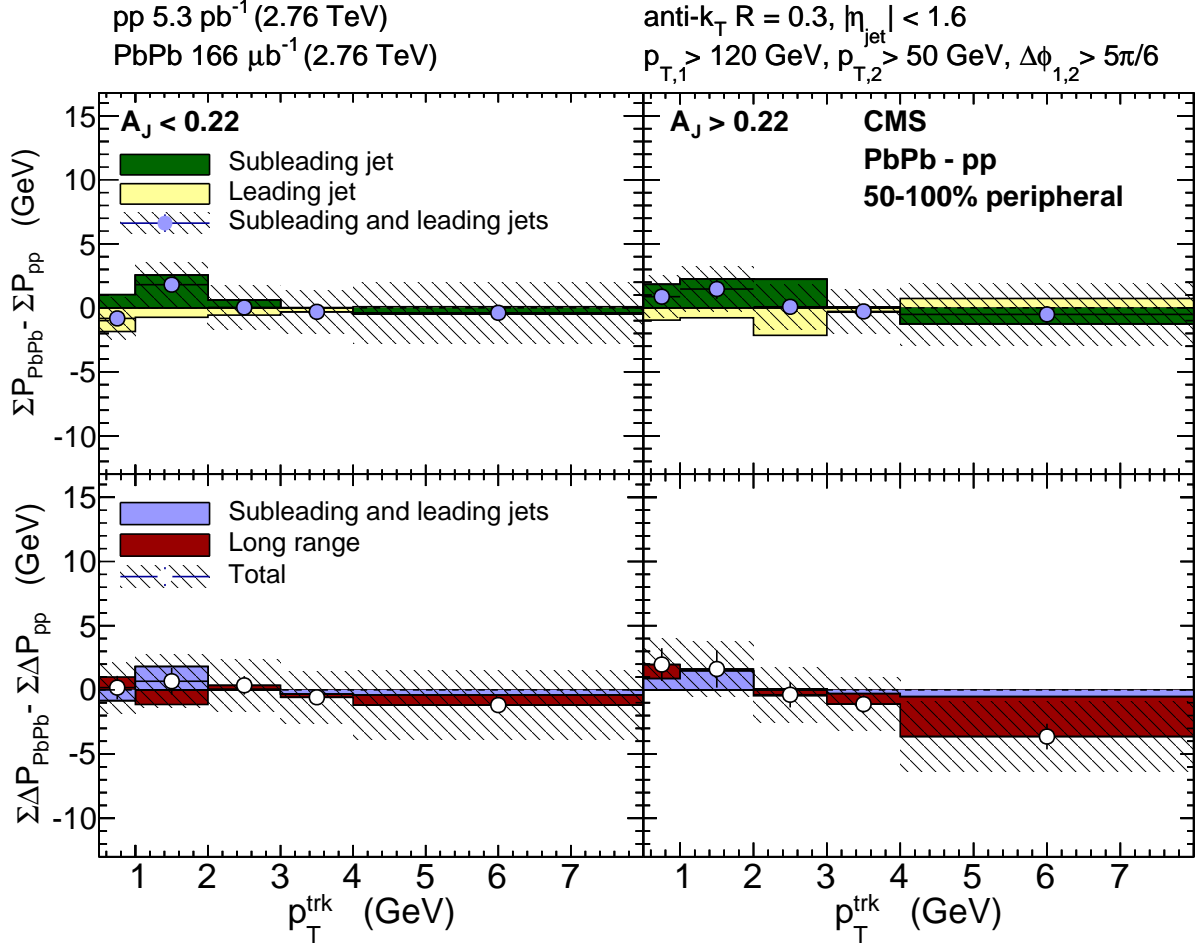


Figure 88. Modifications of jet-hadron correlated transverse momentum in peripheral PbPb collisions with respect to pp reference, integrated $|\Delta\phi| < \pi/2$, $|\Delta\phi| < 2.5$. Top row: subleading and leading jet peak PbPb–pp. Bottom row: relative contributions from jet peaks and long-range asymmetry to the double difference PbPb–pp, subleading–leading in total hemisphere transverse momentum.

10.5 Theory implications of these results

Having extracted a fairly wide range of measurements from jet-track correlations, we may now consider how these measurements may help to constrain the theories of jet quenching summarized Sec. 4. The most direct and immediate comparisons are to jet shape measurements, in which the new results presented here extend previous CMS results, and which have already been directly compared to one theory calculation as shown in Sec. 10.5.1. In other cases direct theory comparisons are not available, but the implications of the following key results of these analysis will be summarized: Sec. 10.5.2 on evidence of quenching to leading and subleading jets, Sec. 10.5.3 on possible interpretations of the distribution of low- p_T excesses in central PbPb collisions, and Sec. 10.5.4 on implications of dijet imbalance studies.

10.5.1 Theory comparisons to extended jet shape measurements

All four models summarized in Sec. 4 compare jet shape predictions to data for $\Delta r < 0.3$, all four can capture the qualitative trend of PbPb/pp modifications data, with all but the hybrid model providing reasonable quantitative agreement. Extending the jet shape measurement to larger angles $\Delta r < 1$ provides the opportunity to discriminate between these different pictures. SCET_G predictions to $\Delta r < 0.5$ at 5 TeV show the continuation of the rising trend noted in previous studies within $\Delta r < 0.3$ at 2.76 TeV [45]. To date, only the coupled jet-fluid model has published jet shape calculations matching data kinematic selections over full the $\Delta r < 1$ range, as shown in Fig 89. These comparisons both show that the model is able to capture the leading and subleading jet shapes with the inclusion of hydrodynamic response, and also illustrate the separate contributions from shower modifications and hydrodynamic response. As these illustrate, shower modifications are larger for subleading than leading jets as expected, while in both cases the modifications at large Δr are driven by hydrodynamic response [51].

10.5.2 Evidence of quenching to leading as well as subleading jets

Across all measurements, there is evidence of quenching not only to subleading jets but also to leading jets, suggesting that for the high- p_T jets studied here leading jets are not substantially surface-biased in the medium. A selection of inclusive jets with $p_T > 120$ GeV behaves very sim-

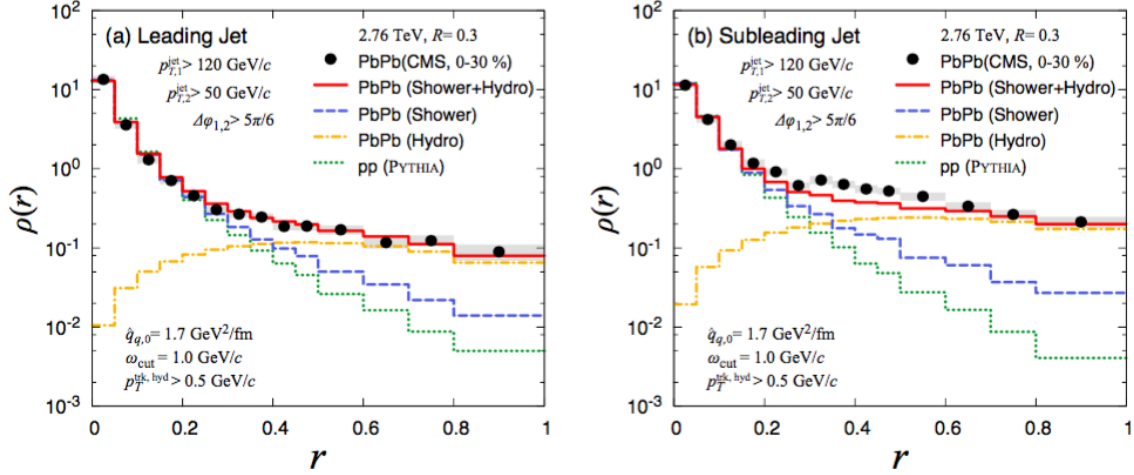


Figure 89. Comparison of leading and subleading jet shape measurements to the jet fluid model from Ref. [51].

ilarly to the leading jets from a dijet sample, and inclusive, leading, and subleading jets exhibit similar signatures of medium-induced energy loss, although the magnitude of this loss is greater (as expected) for subleading jets. This energy loss is evident by slight depletion and narrowing of correlated yields for tracks in the mid- p_T range (approximately $4 < p_T^{\text{trk}} < 16$ GeV). Although measurement uncertainties are too large in this case to make strong claims, this trend of depletion and narrowing is consistent with the expectations from most models of jet energy loss via medium-induced radiation and collisional energy loss. Evidence of quenching is also found in the enhancements of low- p_T tracks correlated to both leading and subleading jets, as discussed in the following section.

10.5.3 Interpretation of the distribution of low- p_T excesses in central PbPb data

As discussed in Sec. 4, soft enhancements in jets passing through the QGP are particularly sensitive to the mechanisms of jet energy loss, including induced “recoil” or “backreactions” in the medium to the propagating probe. In the detailed characterization of these soft enhancements provided by these measurements, we find that excesses of low- p_T particles (with $0.5 < p_T^{\text{trk}} < 3$ GeV) extend to large angles $\Delta\eta = 1$ and $\Delta\phi = 1$ from the jet axis, but also retain a gaussian-like correlation to the jet axis. These modifications also show some possible (not significant with combined uncertainties) dependence on center-of-mass energy, showing greater modifications at

5.02 TeV where gluon jets represent a larger fraction of the total sample. We can consider possible interpretations of these measurements in light of each of the jet quenching models with specific predictions related to soft jet-correlated yields previously summarized in 4.

- **BDMPS-Z as implemented in JEWEL** simulation is able to capture jet profile modifications at $\Delta r \approx 0.3$ only with the inclusion of “recoil partons,” i.e. partons from the medium that interact with the jet that are then kept with the jet through subsequent hadronization [52]. This model (a limiting case in that it assumes no further interaction with the medium for recoil partons) presents a schematic picture of jet-medium interactions that is qualitatively compatible with the peaked excesses observed in central PbPb data. As R_{AA} calculations from JEWEL show substantial dependence on jet reconstruction parameter R up to $R = 1$, it is possible that this approach could also capture modifications to large angles, although quantitative comparison is complicated by challenges in carrying out accurate background subtraction in these Jewel studies [52].
- **Hybrid model** calculations of the angular distribution of missing- p_T clearly illustrate that the “backreaction” of the jet with the medium is needed to capture low- p_T excesses associated with quenched jets in this model. This backreaction is modeled as a plasma wake and mach cone traveling in the same direction as the jet through the medium. Qualitatively, this picture is compatible with the observed trends in low- p_T excesses, although in its current implementation it misses these particles’ quantitative spatial distribution (showing them spread over larger angles than in data) and p_T (resulting in somewhat too many particles with $p_T < 2$ GeV and somewhat too few with p_T in the 2-4 GeV range) [50].
- **The coupled jet-fluid model** implements coupled hydrodynamic medium response in order to fully capture jet shape modifications in PbPb relative to pp for leading and subleading jets over the full $\Delta r < 1$ GeV range. Although calculations are not presented differentially in p_T^{trk} , the hydrodynamic component that drives large-angle modifications is dominated by soft, thermalized particles in the medium that originate from jet-induced excitations in the medium diffuse to large angles from the jet axis. These result in soft excesses extending to large angles from the jet axis as observed in data [51].

- **SCET_G** differs from the previous three models in that it captures low- p_T enhancements not via an explicit medium recoil mechanism but rather through Glauber gluon interactions that mediate interactions between the jet and the medium. These Glauber gluon interactions are used to calculate medium-modified splitting functions that modifications to the parton shower that lead to jet broadening in the medium and result in the characteristic rising trend in the jet shape [45]. Although explicitly p_T differential calculations are not available from SCET_G, it is important to that SCET_G is evidently able to capture large-angle soft modifications without the medium wake or hydrodynamic response needed by other models to describe these trends.

In all, these measurements suggest that medium response or parton shower modifications accounting for the low- p_T excess yields correlated to jets in central PbPb collisions relative to pp reference both extend to large angles from the jet axis (such that measurements with small R capture only part of these modifications). They also suggest that the low- p_T fragmentation products retain some correlation to the jet axis rather than fully thermalizing with the medium, as evidenced by the fact that they appear as peaked excesses in jet-track correlation studies.

10.5.4 Implications of dijet imbalance studies

In studies of momentum balance in unbalanced dijet events (those with $A_J > 0.22$), one key observation is that the sample of pp “dijet” events is in fact dominated by three-jet events as is required by kinematics. In PbPb the unbalanced dijet event is much less dominated by three-jet events, due to both greater contributions from quenched dijets and due to quenching of “third jets” so that these are no longer evident in the event. Subleading-to-leading hemisphere momentum balance studies show greater modification to subleading than leading jets, as expected, but also substantial $\Delta\phi$ asymmetry in the long-range correlated distribution, as modeled on $1.5 < |\Delta\eta| < 2.5$. In balanced dijet events with $A_J < 0.22$, this distribution demonstrates coupling of the jet to the reaction plane via odd v_n flow terms evident in the subleading-to-leading difference in these long range correlated distributions. In unbalanced dijet events this long range distribution is dominated in pp by third-jet and momentum conservation contributions in the mid- p_T range, which is almost completely absent in PbPb data due to the lesser contributions of these third jets.

The A_J -dependence in hemisphere momentum balance is primarily driven by these differences in the long-range correlated underlying event, although subleading jets in asymmetric dijet events do exhibit evidence of greater quenching as expected considering that these events are selected based on greater differences in leading and subleading jet- p_T . In considering theoretical interpretations of momentum balance measurements, such those provided by the hybrid model in Ref. [50], it is important to keep in mind the several different effects that combine to produce the overall hemisphere momentum balance modifications in PbPb compared to pp.

11 CONCLUSIONS

Studies of the quark gluon plasma were carried out via correlations between high- p_T jets and charged hadrons in PbPb and pp data collected at center-of-mass energy 2.76 TeV and 5.02 TeV by the CMS Collaboration. In studies of an inclusive selection of jets with $p_T > 120$ GeV, a comparison of PbPb data to pp data shows a centrality-dependent redistribution of energy from the mid- p_T^{trk} range to soft particles with $p_T^{\text{trk}} < 3$ GeV, with soft excesses in central PbPb data extending to large angles from the jet axis while retaining a gaussian-like distribution. This energy redistribution from hard to soft particles and from small to large angles from the jet axis is evident in charged-particle correlation studies, and also in measurements of the jet shape jet transverse momentum profile. Modifications are found to be slightly (but not significantly) larger at 5.02 TeV than at 2.76 TeV, possibly due to the larger fraction of gluon jets at the higher center-of-mass energy.

In addition to inclusive jet studies, studies of back-to-back dijets with leading jet $p_{T,1} > 120$ GeV, subleading jet $p_{T,2} > 50$ GeV, and azimuthal separation $\Delta\phi_{1,2} > 5\pi/6$ were also carried out. In these studies, evidence of quenching to both leading and subleading jets is observed. Both leading and subleading jet peaks show greater yields of low- p_T particles, and broader jet peaks in central PbPb than pp collisions. Modifications to leading jets are similar to those observed in the inclusive jet sample, while quenching effects are observed to be greater, as expected, for subleading jets. Studies of modifications to jet-correlated hadron yields are also carried out differentially in asymmetry parameter A_J . In this case, slight A_J -dependence is found in modifications to the jet peaks, while larger A_J -dependence is found in the distribution of the subleading-to-leading asymmetry in the long-range-correlated underlying event. In unbalanced pp “dijet” events, asymmetry in this underlying event is dominated by third jets and momentum conservation contributions; in PbPb, the contribution from third jets is nearly non-existent due both to the greater contribution to unbalanced dijet samples from quenched dijets, and to quenching of these additional jets.

Together, these studies provide a detailed characterization of charged hadron distributions and momentum flow from the “jet perspective” in heavy ion events. Characterizing modifications to leading and subleading jet peaks in A_J -inclusive, balanced, and unbalanced dijet events can serve as a bridge between measurements of dijet asymmetry and measurements of jet modification

observables, facilitating the physical interpretation of the interactions that result in modifications to dijet observables. Furthermore, a number of recent developments in theoretical models have suggested that a combination of medium-induced parton shower modifications and possible medium “recoil” or hydrodynamic response are needed to account for observed modifications to fragmentation functions and jet shapes within narrow jet cone radii of $\Delta r = 0.3$ and $\Delta r = 0.4$. These results show modifications extending to much larger angles of at least $\Delta r = 1$ from the jet cone, providing additional constraints on models that aim to capture interactions between a propagating jet and the quark gluon plasma including medium response in low- p_T sector.

REFERENCES

- [1] Vardan Khachatryan et al. Correlations between jets and charged particles in PbPb and pp collisions at $\sqrt{s_{\text{NN}}} = 2.76$ TeV. *JHEP*, 02:156, 2016.
- [2] Vardan Khachatryan et al. Decomposing transverse momentum balance contributions for quenched jets in PbPb collisions at $\sqrt{s_{\text{NN}}} = 2.76$ TeV. *JHEP*, 11:055, 2016.
- [3] Azimuthal correlations of charged hadrons in pbpb collisions at 2.76 tev. 2017.
- [4] O. K. Kalashnikov and V. V. Klimov. Phase transition in the quark-gluon plasma. *Physics Letters B*, 88:328–330, December 1979.
- [5] Edward V. Shuryak. Quantum Chromodynamics and the Theory of Superdense Matter. *Phys. Rept.*, 61:71–158, 1980.
- [6] Siegfried Bethke. World Summary of α_s (2012). 2012. [Nucl. Phys. Proc. Suppl.234,229(2013)].
- [7] J. D. Bjorken. Highly relativistic nucleus-nucleus collisions: The central rapidity region. *Phys. Rev. D*, 27:140–151, Jan 1983.
- [8] Ulrich W. Heinz and Maurice Jacob. Evidence for a new state of matter: An Assessment of the results from the CERN lead beam program. 2000.
- [9] I. Arsene et al. Quark-gluon plasma and color glass condensate at RHIC? The perspective from the BRAHMS experiment. *Nucl. Phys. A*, 757:1, 2005.
- [10] K. Adcox et al. Formation of dense partonic matter in relativistic nucleus nucleus collisions at RHIC: Experimental evaluation by the PHENIX collaboration. *Nucl. Phys. A*, 757:184, 2005.
- [11] B. B. Back et al. The PHOBOS perspective on discoveries at RHIC. *Nucl. Phys. A*, 757:28, 2005.
- [12] John Adams et al. Experimental and theoretical challenges in the search for the quark gluon plasma: The STAR collaboration’s critical assessment of the evidence from RHIC collisions. *Nucl. Phys. A*, 757:102, 2005.

- [13] Miklos Gyulassy. Introduction to qcd thermodynamics and the quark-gluon plasma. *Progress in Particle and Nuclear Physics*, 15:403 – 442, 1985.
- [14] Sourav Sarkar, Helmut Satz, and Bikash Sinha. The physics of the quark-gluon plasma. *Lect. Notes Phys.*, 785:pp.1–369, 2010.
- [15] Helmut Satz. Extreme states of matter in strong interaction physics. An introduction. *Lect. Notes Phys.*, 841:1–239, 2012.
- [16] M. A. Stephanov. QCD phase diagram: An Overview. *PoS*, LAT2006:024, 2006.
- [17] Panagiota Foka and Małgorzata Anna Janik. An overview of experimental results from ultra-relativistic heavy-ion collisions at the cern lhc: Bulk properties and dynamical evolution. *Reviews in Physics*, 1:154 – 171, 2016.
- [18] Amaresh Jaiswal and Victor Roy. Relativistic hydrodynamics in heavy-ion collisions: general aspects and recent developments. *Adv. High Energy Phys.*, 2016:9623034, 2016.
- [19] Ulrich Heinz, Chun Shen, and Huichao Song. The viscosity of quark-gluon plasma at RHIC and the LHC. *AIP Conf. Proc.*, 1441:766–770, 2012.
- [20] Michael L. Miller, Klaus Reygers, Stephen J. Sanders, and Peter Steinberg. Glauber modeling in high energy nuclear collisions. *Ann. Rev. Nucl. Part. Sci.*, 57:205, 2007.
- [21] David G. d’Enterria. Hard scattering cross-sections at LHC in the Glauber approach: From pp to pA and AA collisions. 2003.
- [22] A. Majumder and M. Van Leeuwen. The Theory and Phenomenology of Perturbative QCD Based Jet Quenching. *Prog. Part. Nucl. Phys. A*, 66:41, 2011.
- [23] Sergei A. Voloshin, Arthur M. Poskanzer, and Raimond Snellings. Collective phenomena in non-central nuclear collisions. 2008.
- [24] Serguei Chatrchyan et al. Long-range and short-range dihadron angular correlations in central PbPb collisions at a nucleon-nucleon center of mass energy of 2.76 TeV. *JHEP*, 07:076, 2011.
- [25] Serguei Chatrchyan et al. Multiplicity and transverse momentum dependence of two- and four-particle correlations in pPb and PbPb collisions. *Phys. Lett.*, B724:213–240, 2013.

- [26] J. D. Bjorken. Energy loss of energetic partons in QGP: possible extinction of high p_t jets in hadron-hadron collisions. FERMILAB-PUB-82-059-THY, 1982.
- [27] David d’Enterria. Jet quenching. *Landolt-Boernstein, Springer-Verlag*, Vol. 1-23A:99, 2010.
- [28] Nestor Armesto. Nuclear shadowing. *J. Phys.*, G32:R367–R394, 2006.
- [29] K. Aamodt. Suppression of Charged Particle Production at Large Transverse Momentum in Central PbPb Collisions at $\sqrt{s_{NN}} = 2.76$ TeV. *Phys. Lett. B*, 696:30, 2011.
- [30] Vardan Khachatryan et al. Charged-particle nuclear modification factors in PbPb and pPb collisions at $\sqrt{s_{NN}} = 5.02$ TeV. *JHEP*, 04:039, 2017.
- [31] Georges Aad et al. Measurements of the Nuclear Modification Factor for Jets in Pb+Pb Collisions at $\sqrt{s_{NN}} = 2.76$ TeV with the ATLAS Detector. *Phys. Rev. Lett.*, 114(7):072302, 2015.
- [32] Vardan Khachatryan et al. Measurement of inclusive jet cross-sections in pp and PbPb collisions at $\sqrt{s_{NN}}=2.76$ TeV. *Phys. Rev. C*, 2016.
- [33] Serguei Chatrchyan et al. Measurement of jet fragmentation in PbPb and pp collisions at $\sqrt{s_{NN}} = 2.76$ TeV. *Phys. Rev. C*, 90:024908, 2014.
- [34] Serguei Chatrchyan et al. Modification of jet shapes in PbPb collisions at $\sqrt{s_{NN}} = 2.76$ TeV. *Phys. Lett. B*, 730:243, 2014.
- [35] C. Adler et al. Disappearance of back-to-back high- p_T hadron correlations in central Au+Au collisions at $\sqrt{s_{NN}} = 200$ GeV. *Phys. Rev. Lett.*, 90:082302, 2003.
- [36] K. Aamodt et al. Particle-yield modification in jet-like azimuthal di-hadron correlations in Pb-Pb collisions at $\sqrt{s_{NN}} = 2.76$ TeV. *Phys. Rev. Lett.*, 108:092301, 2012.
- [37] Georges Aad et al. Observation of a Centrality-Dependent Dijet Asymmetry in Lead-Lead Collisions at $\sqrt{s_{NN}} = 2.76$ TeV with the ATLAS Detector at the LHC. *Phys. Rev. Lett.*, 105:252303, 2010.
- [38] Serguei Chatrchyan et al. Observation and studies of jet quenching in PbPb collisions at $\sqrt{s_{NN}} = 2.76$ TeV. *Phys. Rev. C*, 84:024906, 2011.

- [39] Vardan Khachatryan et al. Measurement of transverse momentum relative to dijet systems in PbPb and pp collisions at $\sqrt{s_{\text{NN}}} = 2.76$ TeV. *JHEP*, 01:6, 2016.
- [40] Karen M. Burke et al. Extracting the jet transport coefficient from jet quenching in high-energy heavy-ion collisions. *Phys. Rev.*, C90(1):014909, 2014.
- [41] David d’Enterria. *Jet quenching*, volume 23: Relativistic Heavy Ion Physics of *Springer Materials - The Landolt-Börnstein Database*, chapter 6.4. Springer-Verlag, 2010.
- [42] Shanshan Cao, Tan Luo, Guang-You Qin, and Xin-Nian Wang. Linearized Boltzmann transport model for jet propagation in the quark-gluon plasma: Heavy quark evolution. *Phys. Rev.*, C94(1):014909, 2016.
- [43] Shanshan Cao, Tan Luo, Guang-You Qin, and Xin-Nian Wang. Heavy and light flavor jet quenching at RHIC and LHC energies. 2017.
- [44] Yang-Ting Chien and Ivan Vitev. Jet Shape Resummation Using Soft-Collinear Effective Theory. *JHEP*, 12:061, 2014.
- [45] Yang-Ting Chien and Ivan Vitev. Towards the understanding of jet shapes and cross sections in heavy ion collisions using soft-collinear effective theory. *JHEP*, 05:023, 2016.
- [46] Ira Z. Rothstein and Iain W. Stewart. An Effective Field Theory for Forward Scattering and Factorization Violation. *JHEP*, 08:025, 2016.
- [47] Steven S. Gubser and Andreas Karch. From gauge-string duality to strong interactions: A Pedestrian’s Guide. *Ann. Rev. Nucl. Part. Sci.*, 59:145–168, 2009.
- [48] Steven S. Gubser, Silviu S. Pufu, Fabio D. Rocha, and Amos Yarom. Energy loss in a strongly coupled thermal medium and the gauge-string duality. In Rudolph C. Hwa and Xin-Nian Wang, editors, *Quark-gluon plasma 4*, pages 1–59. 2010.
- [49] Jorge Casalderrey-Solana, Hong Liu, David Mateos, Krishna Rajagopal, and Urs Achim Wiedemann. Gauge/String Duality, Hot QCD and Heavy Ion Collisions. 2011.

- [50] Jorge Casalderrey-Solana, Doga Gulhan, Guilherme Milhano, Daniel Pablos, and Krishna Rajagopal. Angular Structure of Jet Quenching Within a Hybrid Strong/Weak Coupling Model. *JHEP*, 03:135, 2017.
- [51] Yasuki Tachibana, Ning-Bo Chang, and Guang-You Qin. Full jet in quark-gluon plasma with hydrodynamic medium response. *Phys. Rev.*, C95(4):044909, 2017.
- [52] Raghav Kunnawalkam Elayavalli and Korinna Christine Zapp. Medium response in JEWEL and its impact on jet shape observables in heavy ion collisions. *JHEP*, 07:141, 2017.
- [53] Lyndon Evans and Philip Bryant. LHC Machine. *JINST*, 3:S08001, 2008.
- [54] S. Chatrchyan et al. The CMS experiment at the CERN LHC. *JINST*, 3:S08004, 2008.
- [55] Tai Sakuma and Thomas McCauley. Detector and event visualization with sketchup at the cms experiment. *Journal of Physics: Conference Series*, 513(2):022032, 2014.
- [56] Serguei Chatrchyan et al. Description and performance of track and primary-vertex reconstruction with the CMS tracker. *JINST*, 9(10):P10009, 2014.
- [57] Vardan Khachatryan et al. Performance of photon reconstruction and identification with the CMS detector in proton-proton collisions at $\sqrt{s_{\text{NN}}} = 8$ TeV. *JINST*, 10:P08010, 2015.
- [58] Vardan Khachatryan et al. The CMS trigger system. *JINST*, 12:P01020, 2017.
- [59] CMS Collaboration. Momentum flow relative to dijets in pbpb collisions at 2.76 tev. *CMS Analysis Note (Internal)*, AN-14-024, 2014.
- [60] CMS Internal. Study of high- p_t charged particle suppression in pbpb compared to pp collisions at 5.02 tev. 2016.
- [61] Gavin P. Salam. Towards Jetography. *Eur. Phys. J.*, C67:637–686, 2010.
- [62] Matteo Cacciari, Gavin P. Salam, and Gregory Soyez. The anti- k_t jet clustering algorithm. *JHEP*, 04:063, 2008.
- [63] Matteo Cacciari, Gavin P. Salam, and Gregory Soyez. FastJet user manual. *Eur. Phys. J. C*, 72:1896, 2012.

- [64] Olga Kodolova, I. Vardanian, A. Nikitenko, and A. Oulianov. The performance of the jet identification and reconstruction in heavy ions collisions with CMS detector. *Eur. Phys. J. C*, 50:117, 2007.
- [65] Serguei Chatrchyan et al. Studies of jet quenching using isolated-photon+jet correlations in PbPb and pp collisions at $\sqrt{s_{\text{NN}}} = 2.76$ TeV. *Phys. Lett. B*, 718:773, 2013.
- [66] Serguei Chatrchyan et al. Measurement of jet fragmentation into charged particles in pp and PbPb collisions at $\sqrt{s_{\text{NN}}} = 2.76$ TeV. *JHEP*, 10:087, 2012.
- [67] CMS. Identification and Filtering of Uncharacteristic Noise in the CMS Hadron Calorimeter. *JINST*, 5:T03014, 2010.
- [68] Torbjorn Sjöstrand, Stephen Mrenna, and Peter Skands. PYTHIA 6.4 physics and manual. *JHEP*, 05:026, 2006.
- [69] S. Agostinelli et al. GEANT4—a simulation toolkit. *Nucl. Instrum. and Methods A*, 506:250, 2003.
- [70] I. P. Lokhtin and A. M. Snigirev. A model of jet quenching in ultrarelativistic heavy ion collisions and high- p_{T} hadron spectra at RHIC. *Eur. Phys. J. C*, 45:211, 2006.
- [71] Serguei Chatrchyan et al. Azimuthal anisotropy of charge particles at high transverse momenta in pb-pb collisions at $\sqrt{s_{\text{NN}}} = 2.76$ TeV. *Phys. Rev. Lett.*, 109:022301, 2012.
- [72] Serguei Chatrchyan et al. Centrality dependence of dihadron correlations and azimuthal anisotropy harmonics in PbPb collisions at $\sqrt{s_{\text{NN}}} = 2.76$ TeV. *Eur. Phys. J.*, C72:2012, 2012.
- [73] K. Aamodt et al. Harmonic decomposition of two-particle angular correlations in Pb-Pb collisions at $\sqrt{s_{\text{NN}}} = 2.76$ TeV. *Phys. Lett. B*, 708:249, 2012.

APPENDICES

A Jet kinematics

The following sections summarize jet kinematics for inclusive jets and dijets at 2.76 TeV, for inclusive jets at 5.02 TeV, and for dijets in each asymmetry class at 2.76 TeV.

A.1 Jet kinematics at 2.76 TeV

The kinematic observables of jets in pp and PbPb 2.76 TeV events (solid markers) are compared with Monte Carlo (hatched marks). All spectra have been normalized to unity. Comparing the jet spectra observed in PbPb data (pp data) and in PYTHIA+HYDJET (PYTHIA) samples, a reasonable agreement in the overall shape is found.

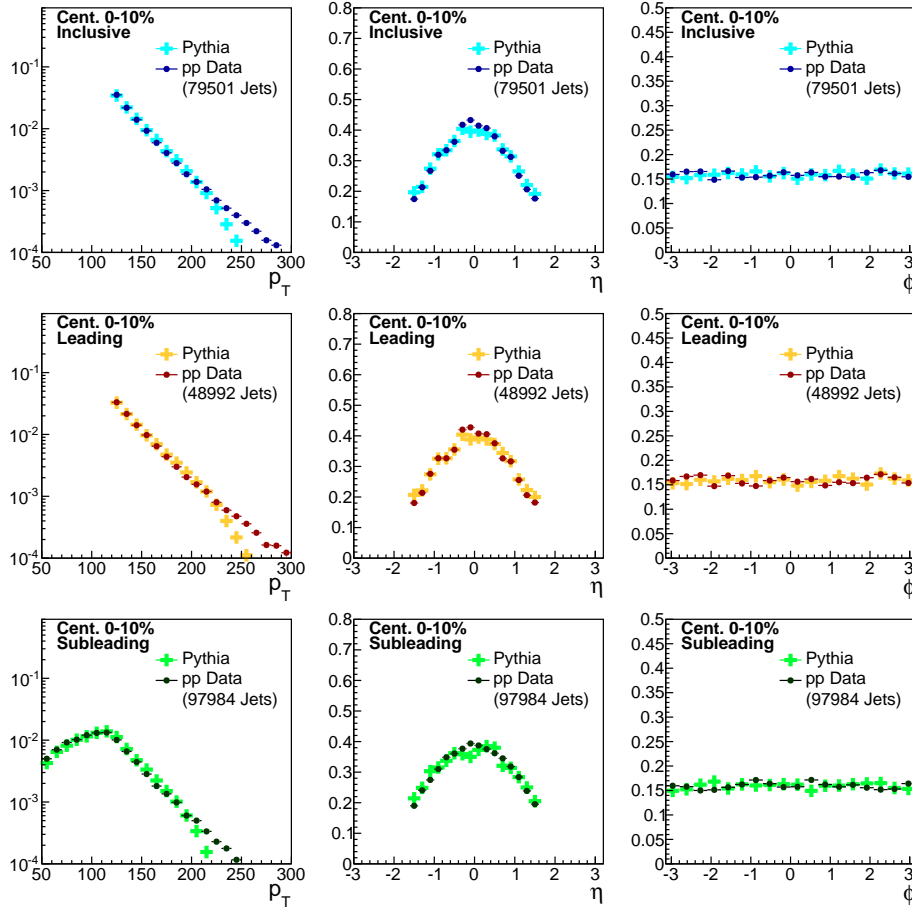


Figure 90. Distribution of transverse momentum, pseudorapidity, and azimuthal distribution of all jet selections for Pythia data compared to PYTHIA simulation.

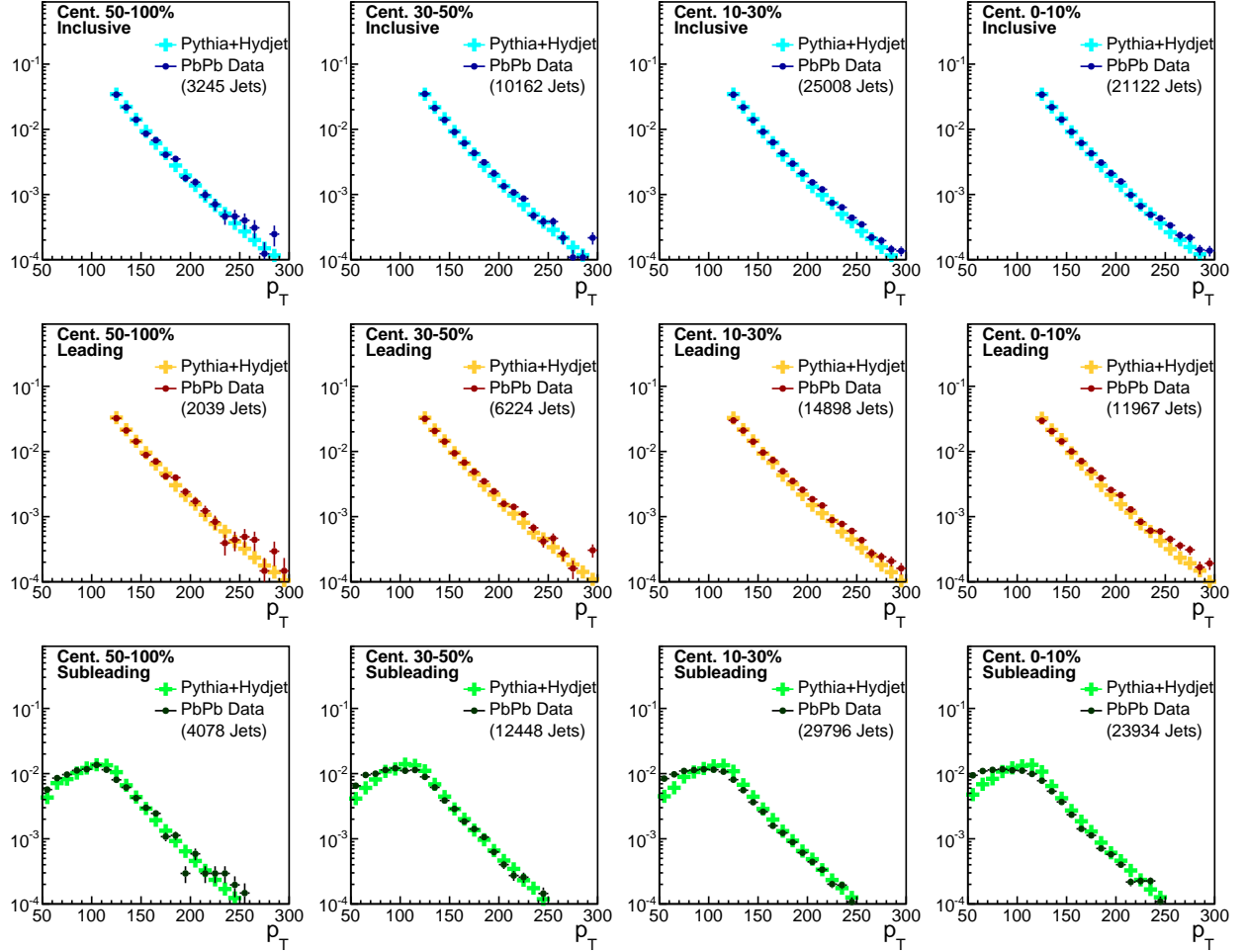


Figure 91. Transverse momentum distribution of all jet selections for PbPb data at 2.76 TeV compared to PYTHIA+HYDJET simulation.

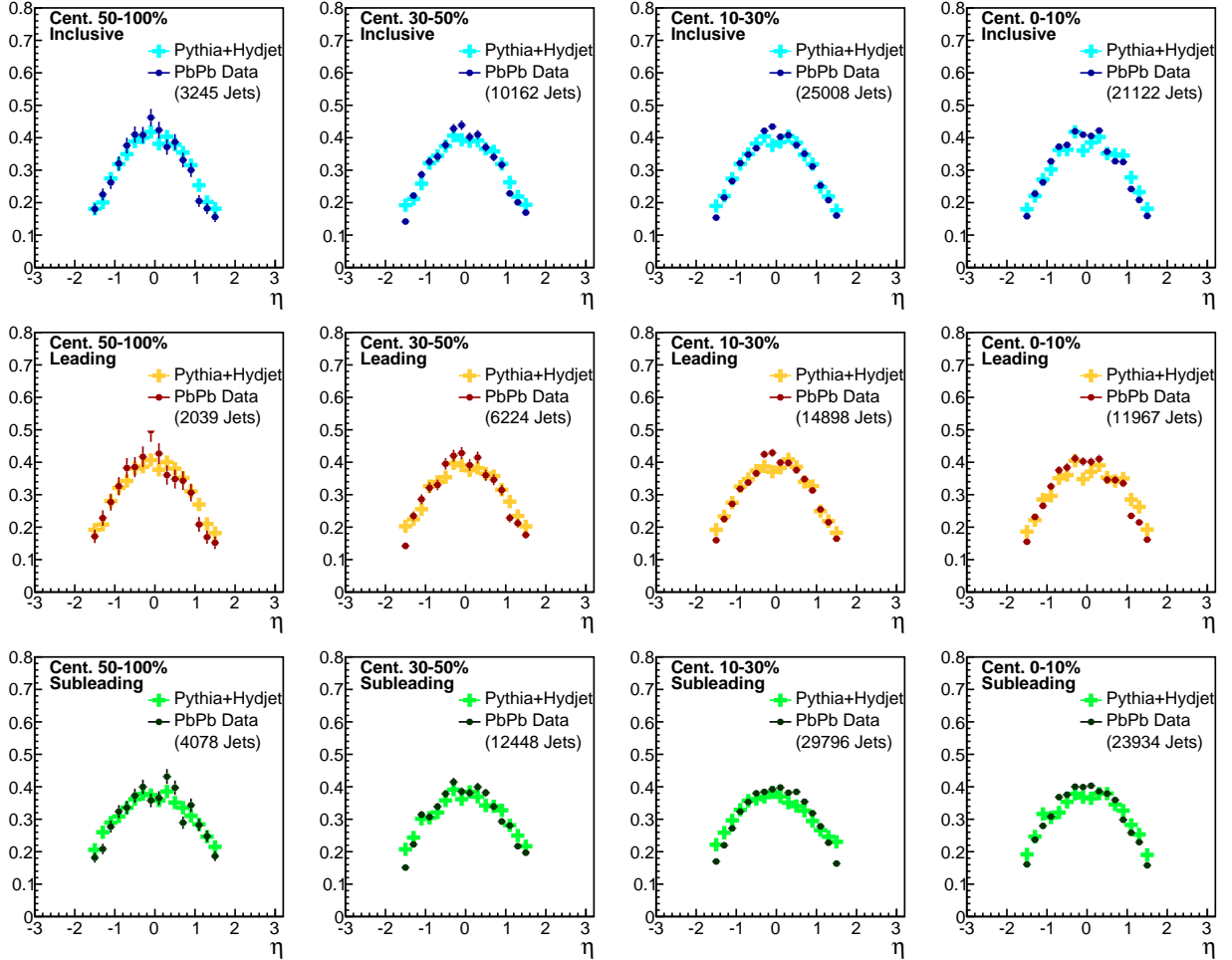


Figure 92. Pseudorapidity distribution of all jet selections for PbPb data at 2.76 TeV compared to PYTHIA+HYDJET simulation.

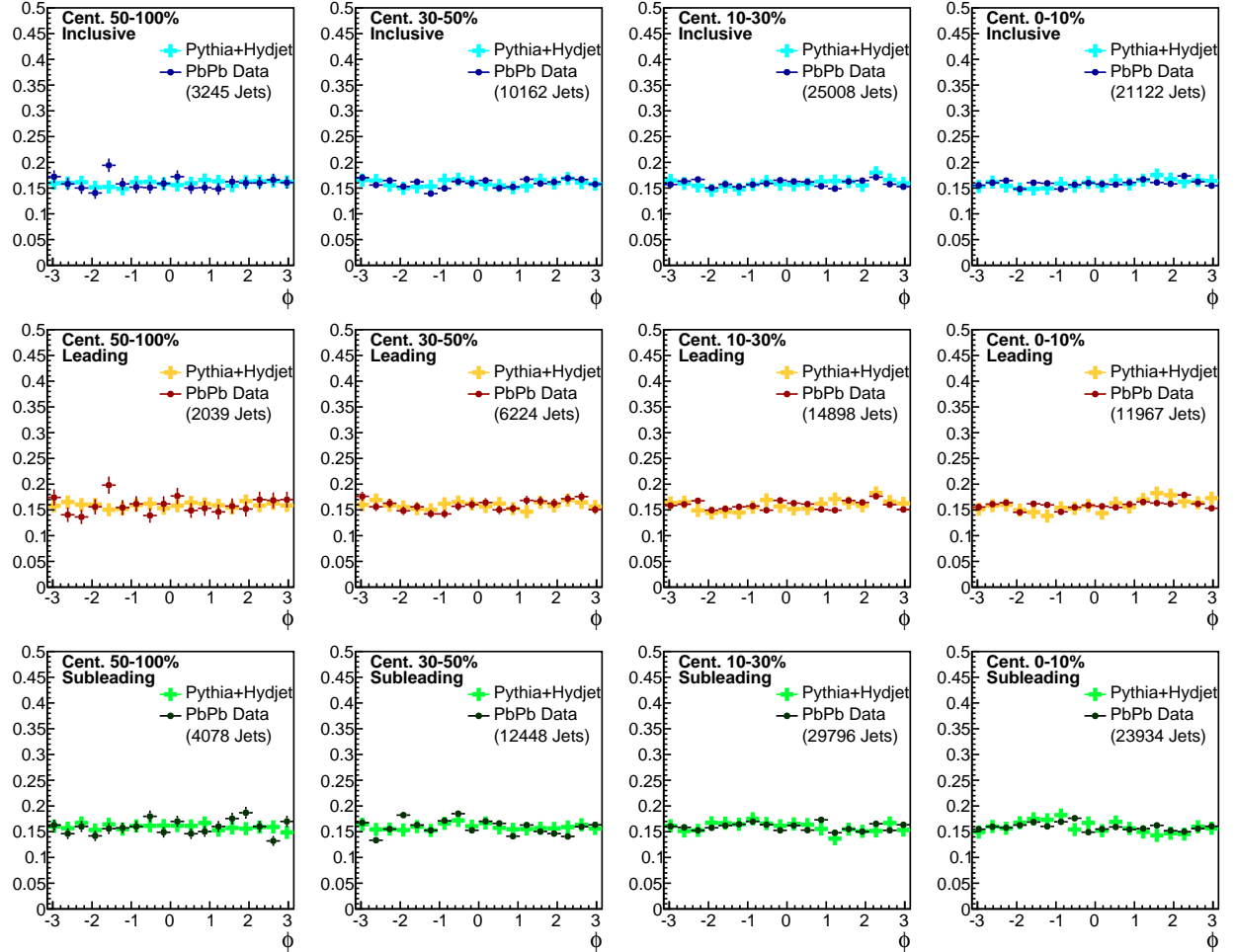


Figure 93. Azimuthal angle distribution of all jet selections for PbPb data at 2.76 TeV compared to PYTHIA+HYDJET simulation for each collision centrality bin.

A.2 Inclusive jet kinematics at 5.02 TeV

Jet p_T , η , and ϕ distributions for 5.02 TeV data, comparing PbPb data to PYTHIA+HYDJET and pp data to PYTHIA simulation.

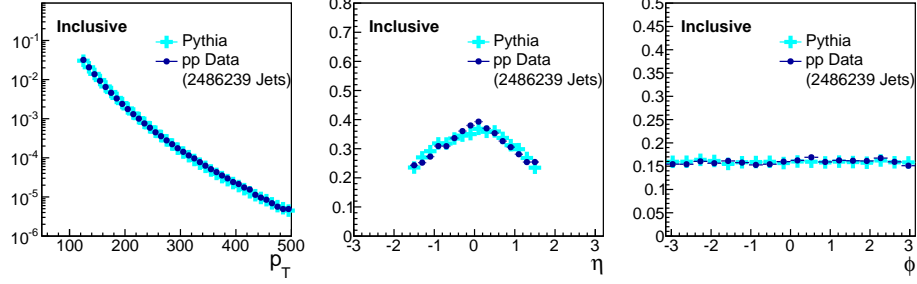


Figure 94. Distribution of pseudorapidity distribution of all jet selections for PbPb data compared to PYTHIA+HYDJET simulation for each collision centrality bin.

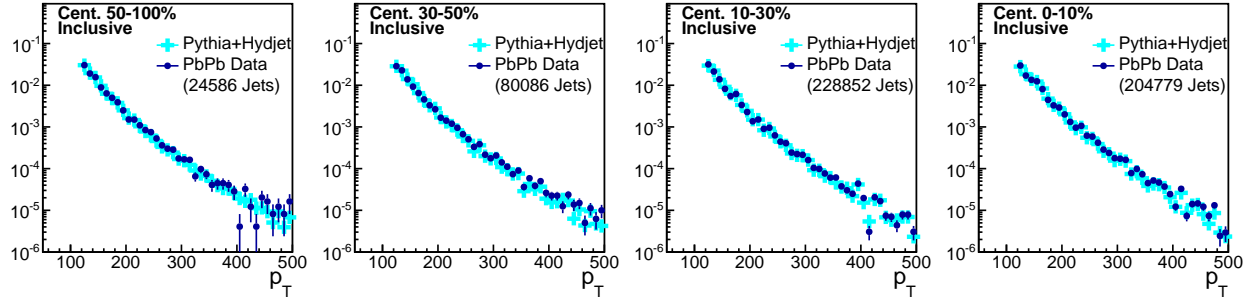


Figure 95. Transverse momentum distribution for PbPb data compared to PYTHIA+HYDJET simulation for each collision centrality bin.

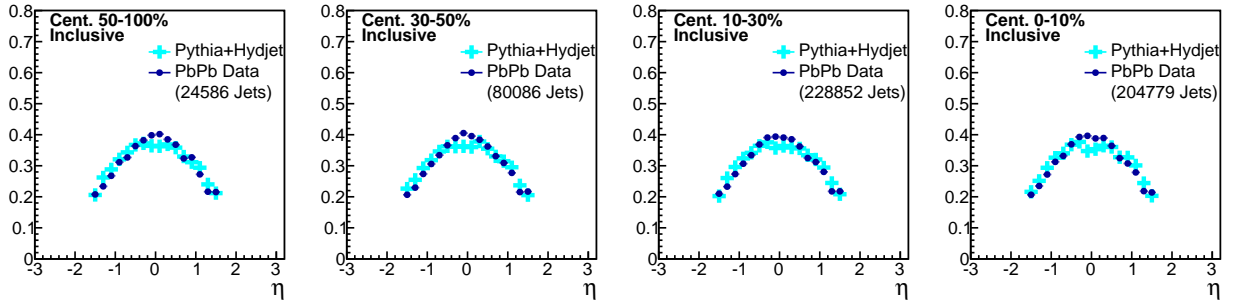


Figure 96. Jet η distribution for PbPb data compared to PYTHIA+HYDJET simulation for each collision centrality bin.

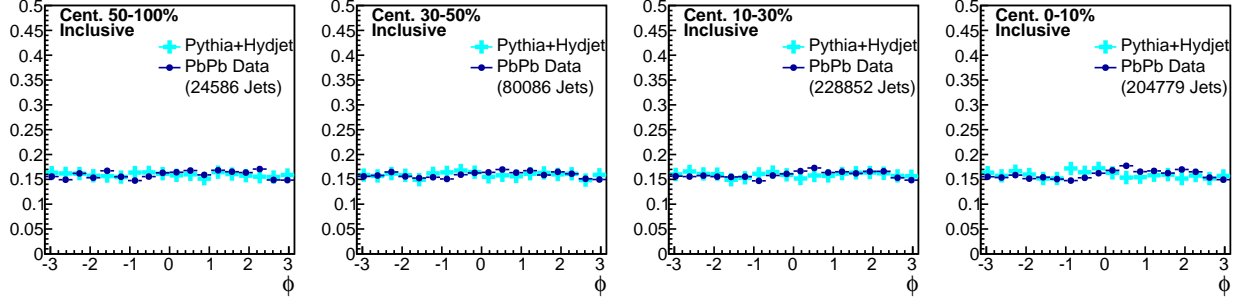


Figure 97. Jet ϕ distribution for PbPb data compared to PYTHIA+HYDJET simulation for each collision centrality bin.

A.3 Dijet kinematics in asymmetry classes at 2.76 TeV

In the figures below, jet transverse momentum, pseudorapidity, and azimuth are shown for our A_J -inclusive sample, compared to each A_J selection in our analysis. Note that A_J -selection primarily affects the subleading jet spectrum, while the leading jet spectrum is nearly unchanged. Jet η and jet ϕ exhibit no significant A_J -dependence for leading or subleading jets. Distributions are shown first for pp, and then for PbPb data at 2.76 TeV.

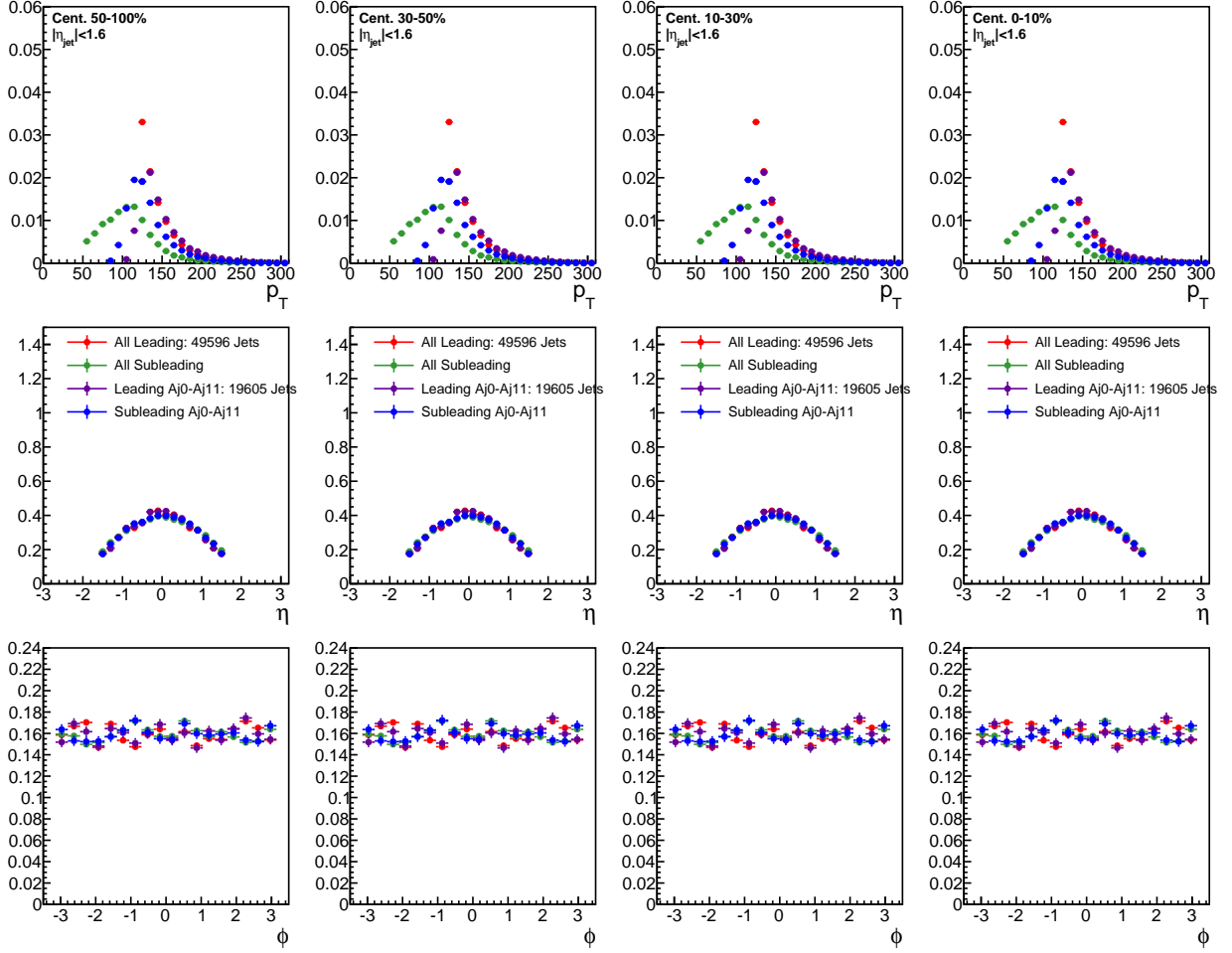


Figure 98. Jet p_T , η , and ϕ for all pp dijets and for pp dijets with A_J : $0 < A_J < 0.11$.

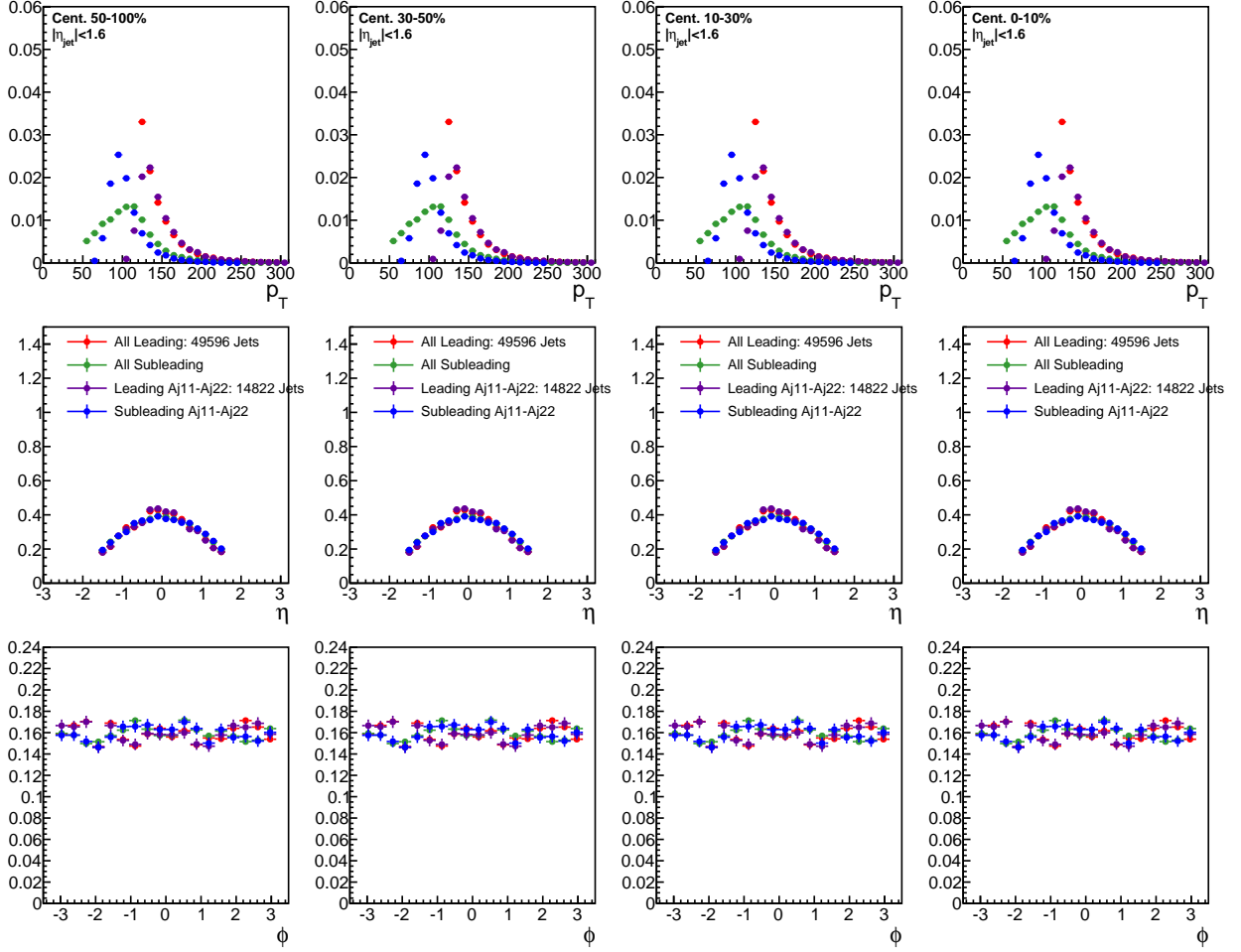


Figure 99. Jet p_T , η , and ϕ for all pp dijets and for pp dijets with A_J : $0.11 < A_J < 0.22$.

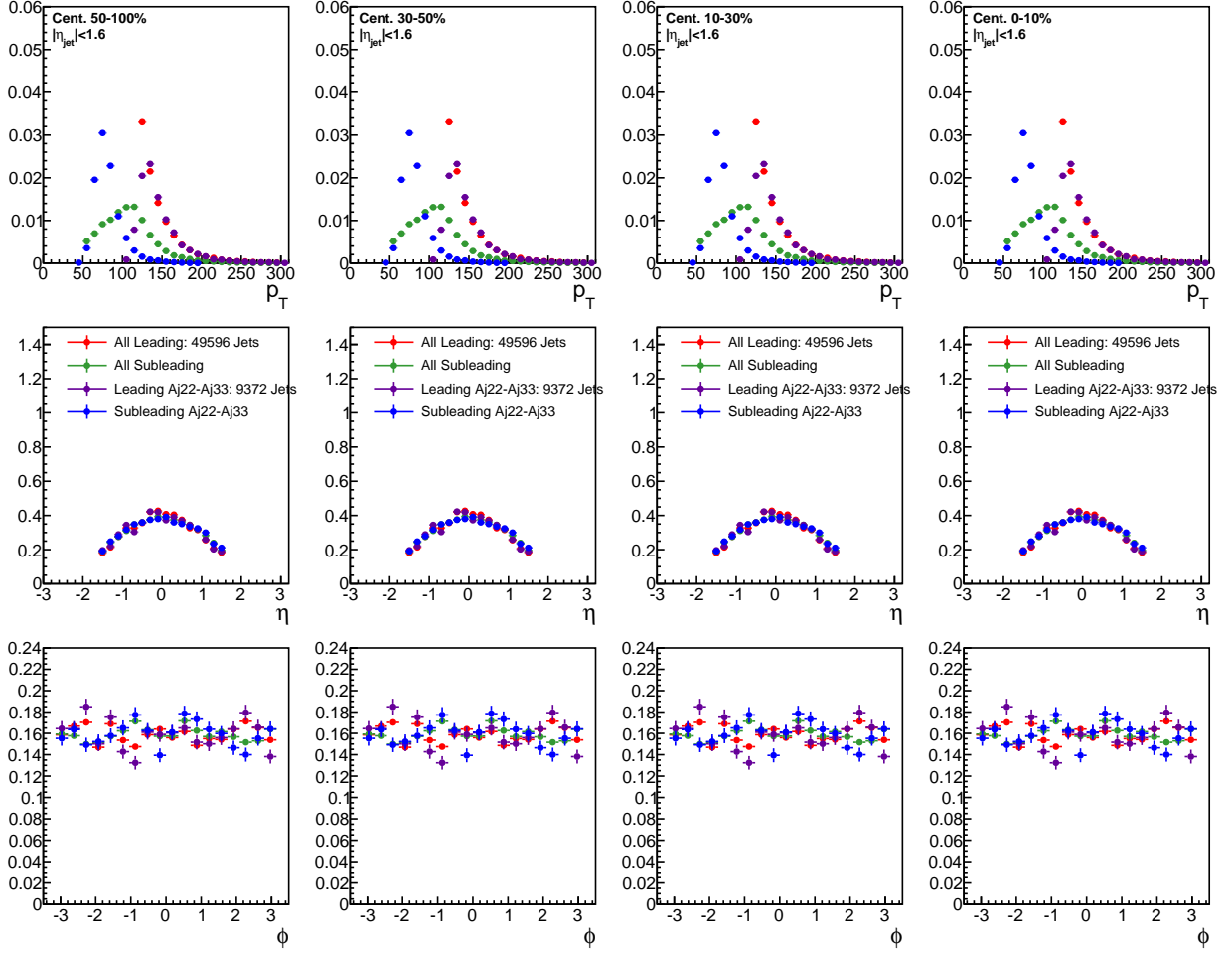


Figure 100. Jet p_T , η , and ϕ for all pp dijets and for pp dijets with A_J : $0.22 < A_J < 0.33$.

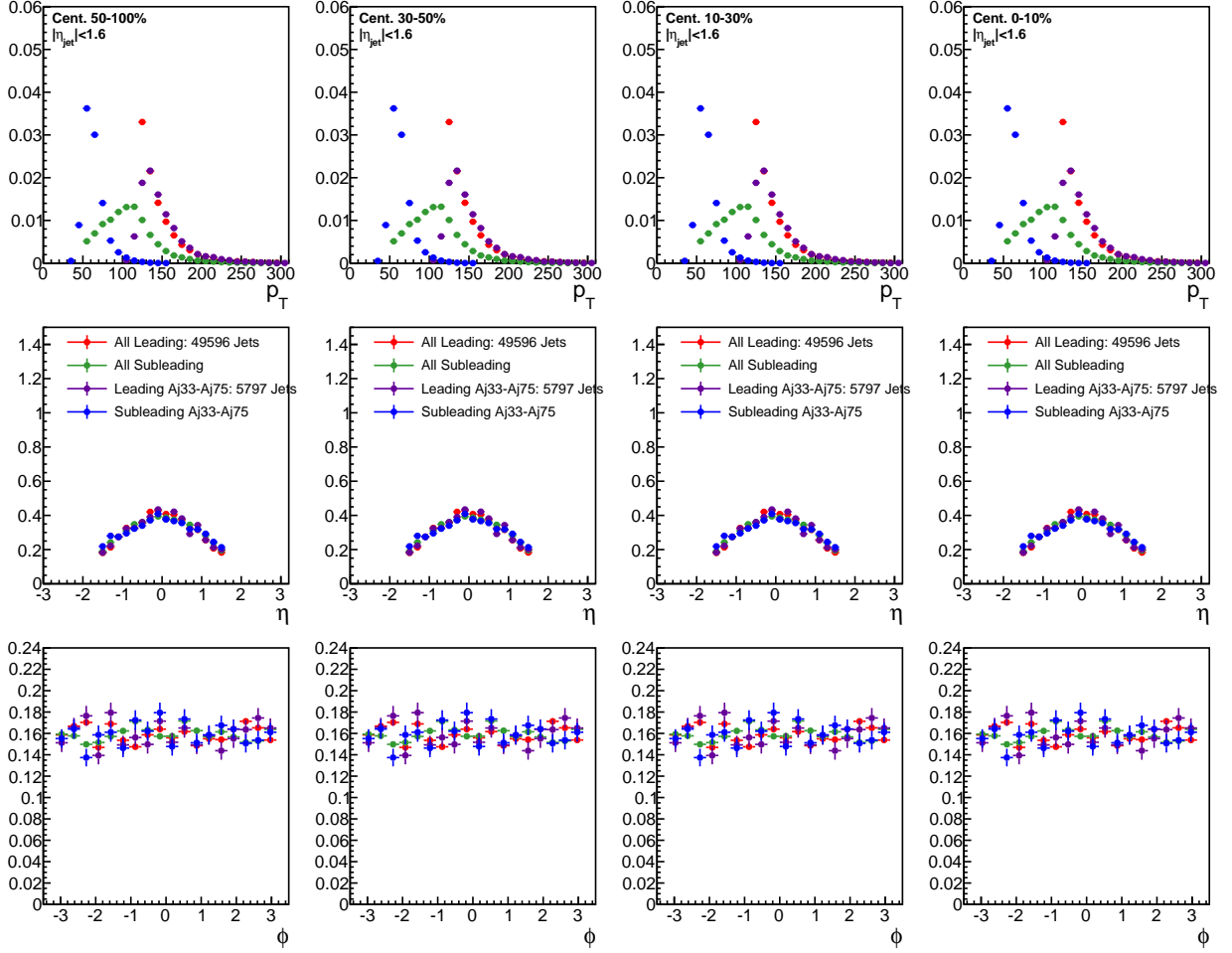


Figure 101. Jet p_T , η , and ϕ for all pp dijets and for pp dijets with A_J : $A_J > 0.33$.

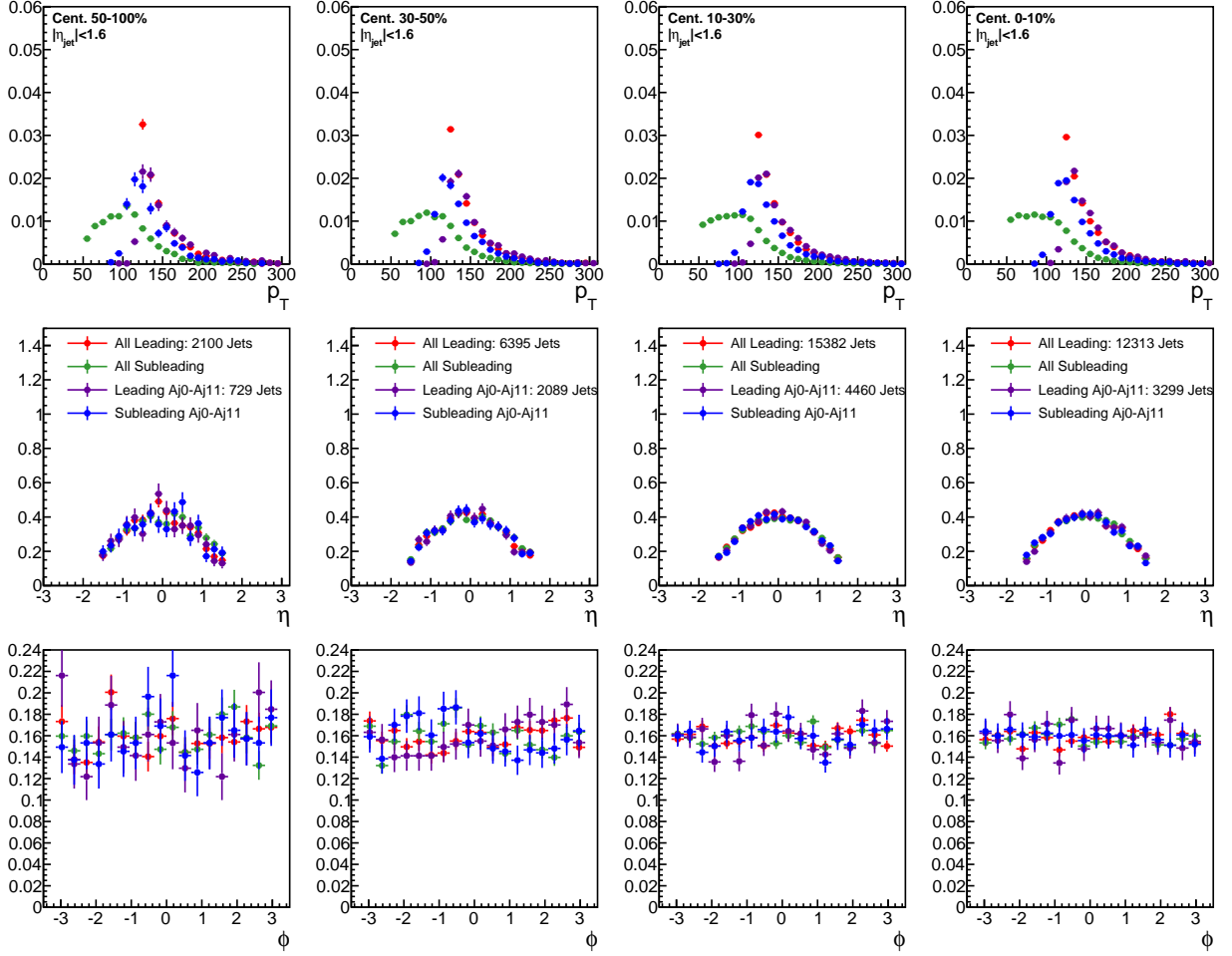


Figure 102. Jet p_T , η , and ϕ for all PbPb dijets and for PbPb dijets with $0 < A_J < 0.11$.

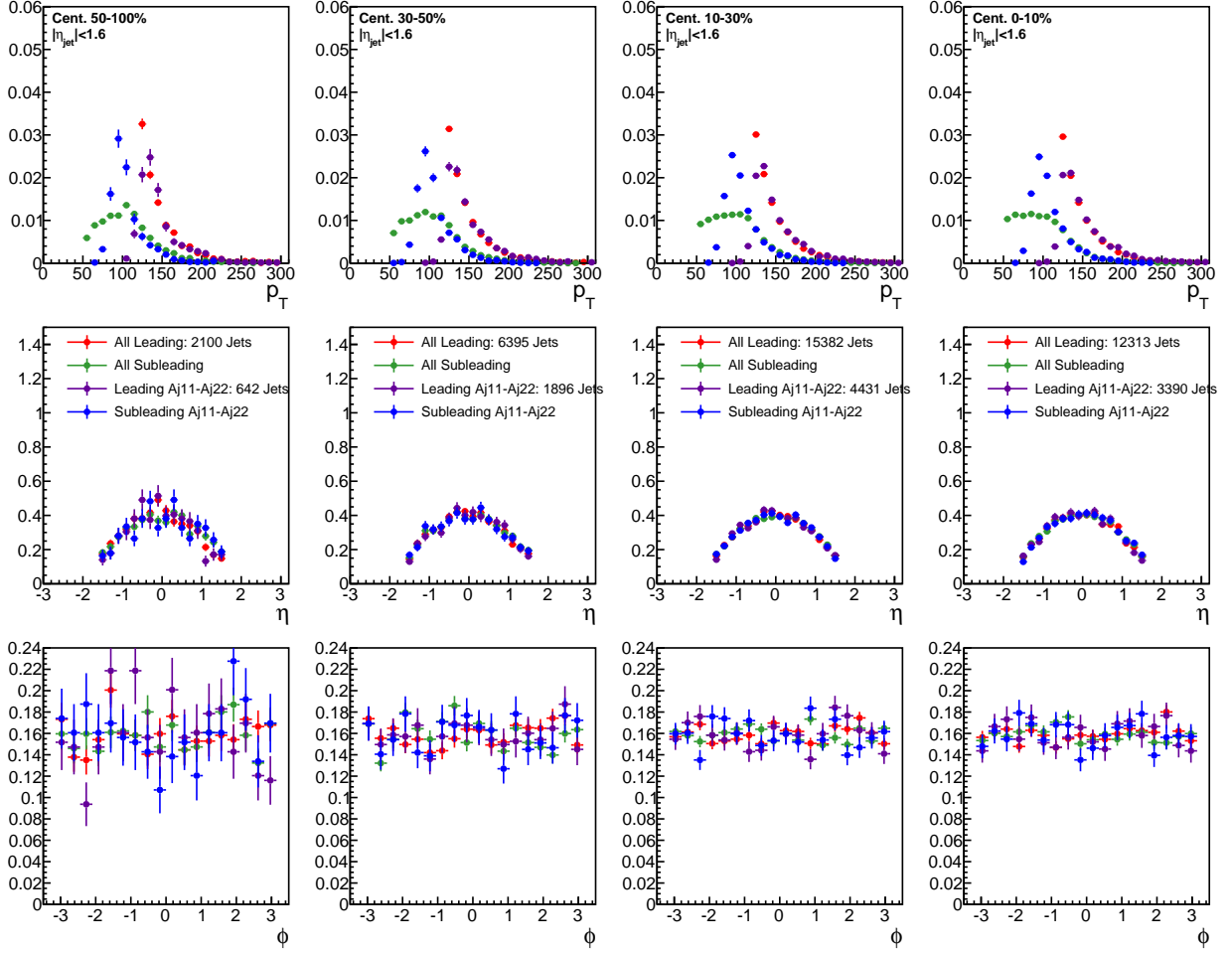


Figure 103. Jet p_T , η , and ϕ for all PbPb dijets and for PbPb dijets with $0.11 < A_J < 0.22$.

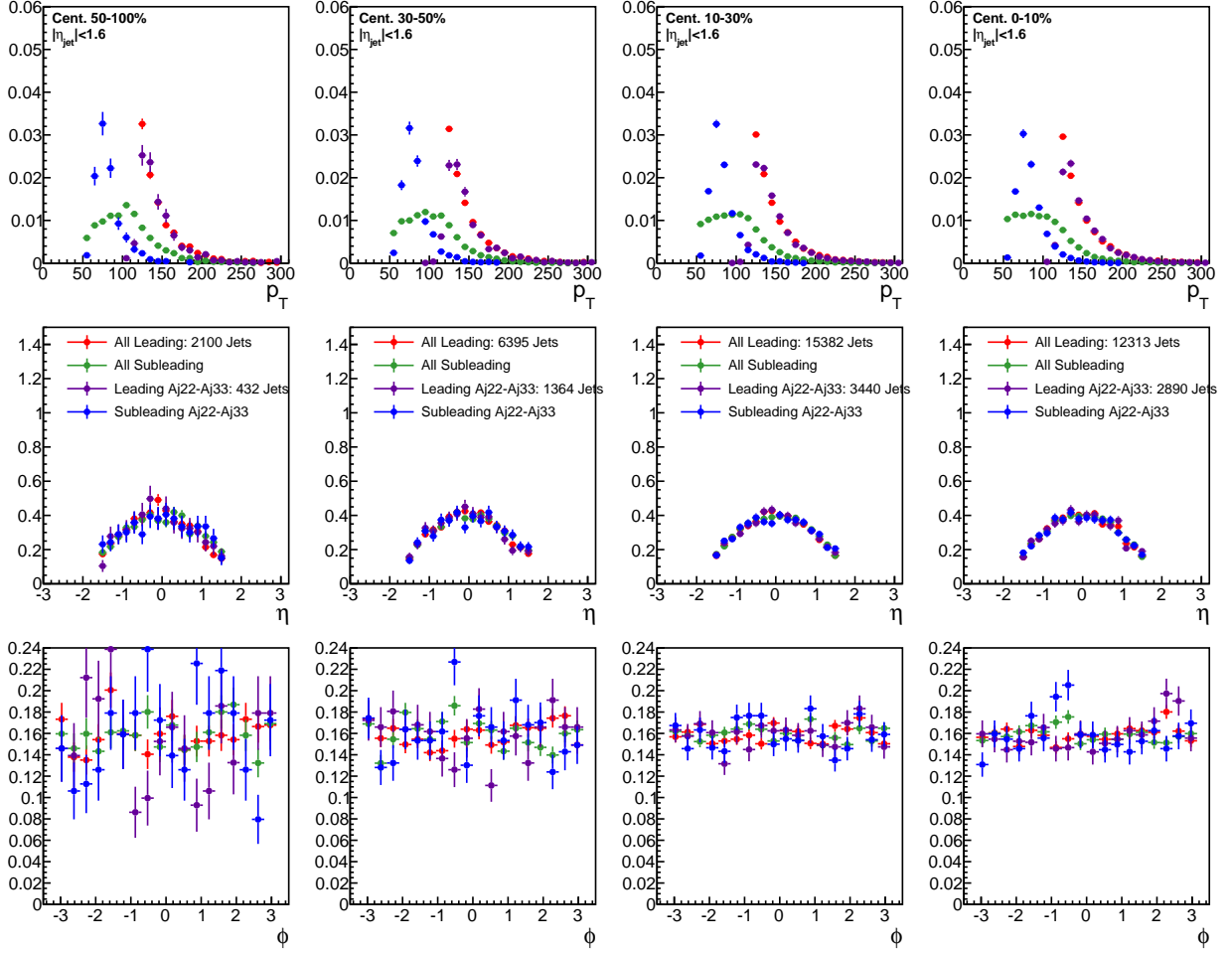


Figure 104. Jet p_T , η , and ϕ for all PbPb dijets and for PbPb dijets with $0.22 < A_J < 0.33$.

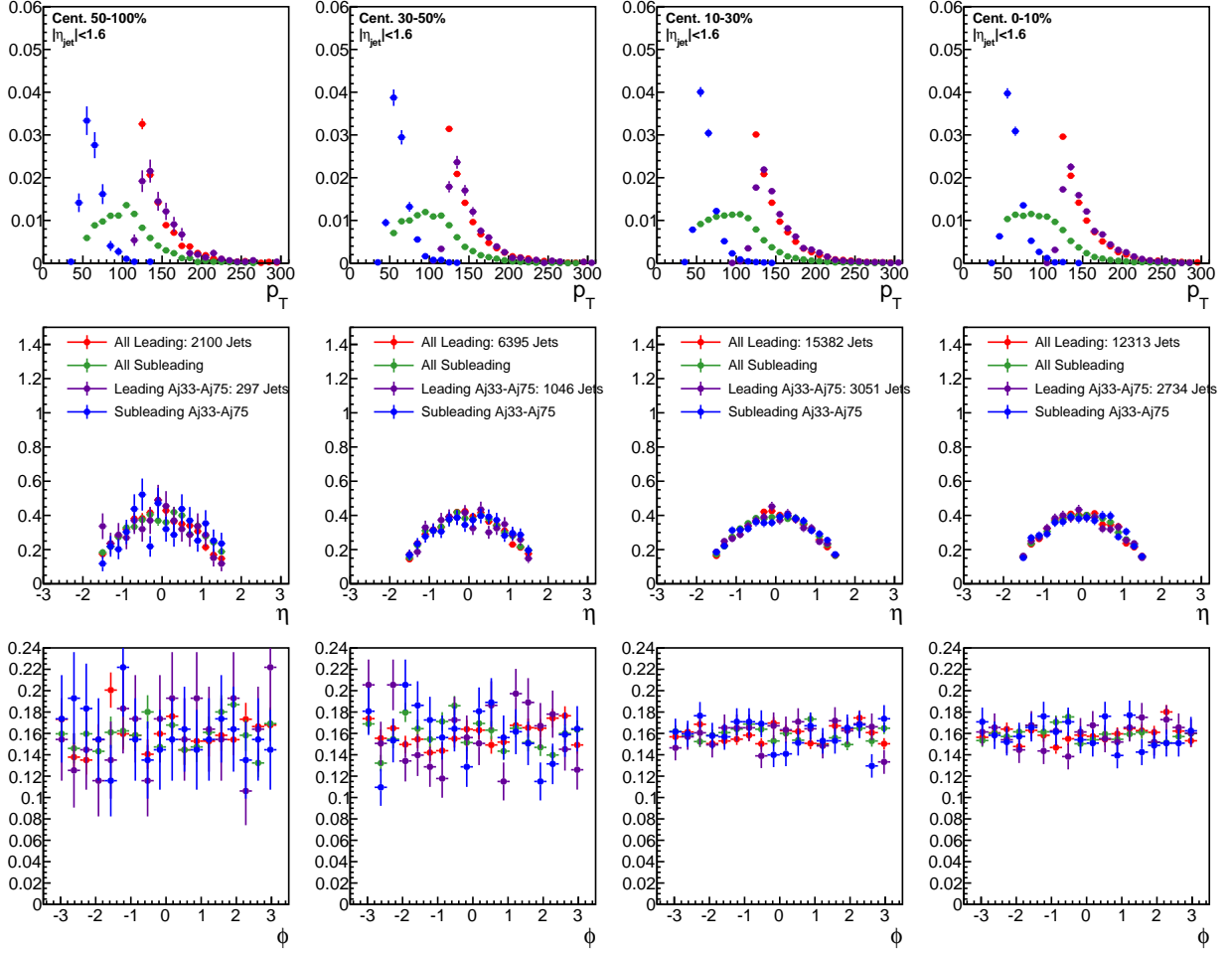


Figure 105. Jet p_T , η , and ϕ for all PbPb dijets and for PbPb dijets with $A_J > 0.33$.

B Background fitting details

Figures 106-109 show the two steps of fits involved in modeling the the background distribution in $\Delta\phi$, as discussed in section 9.3.

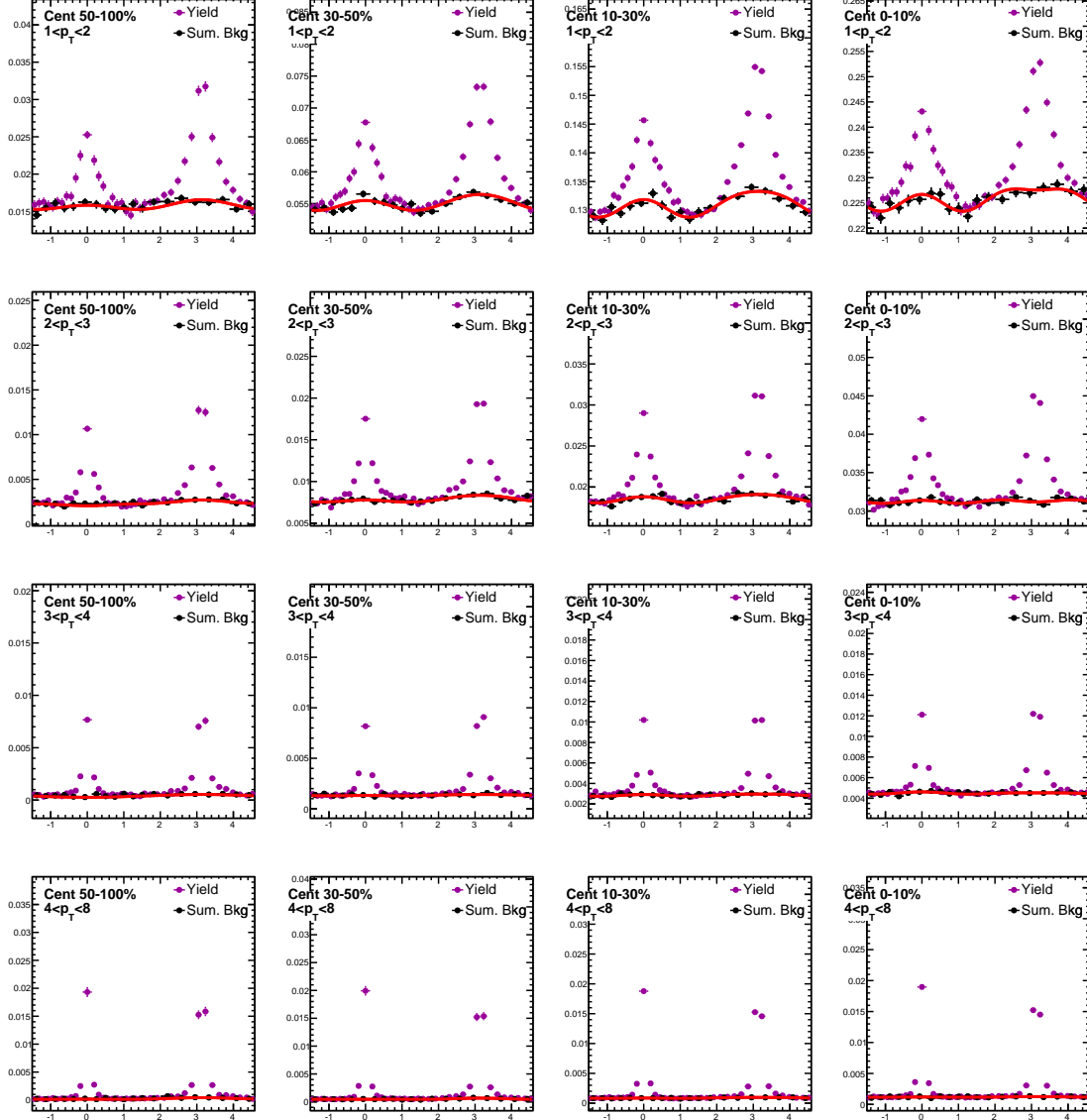


Figure 106. Dijet combined background $\Delta\phi$ distributions, estimated by projection over the region $1.5 < |\Delta\eta| < 3.0$. Here the "near-side" region $-\frac{\pi}{2} < \Delta\phi < \frac{\pi}{2}$ is taken from the leading jet correlation, while the "away-side" $-\frac{\pi}{2} < \Delta\phi < \frac{\pi}{2}$ is taken from the subleading jet correlation. The resulting combined background distribution is fit with the function $B^{dijet}(\Delta\phi) = B_0(1 + 2V_1\text{Cos}(\Delta\phi) + 2V_2\text{Cos}(2\Delta\phi) + 2V_3\text{Cos}(3\Delta\phi))$.

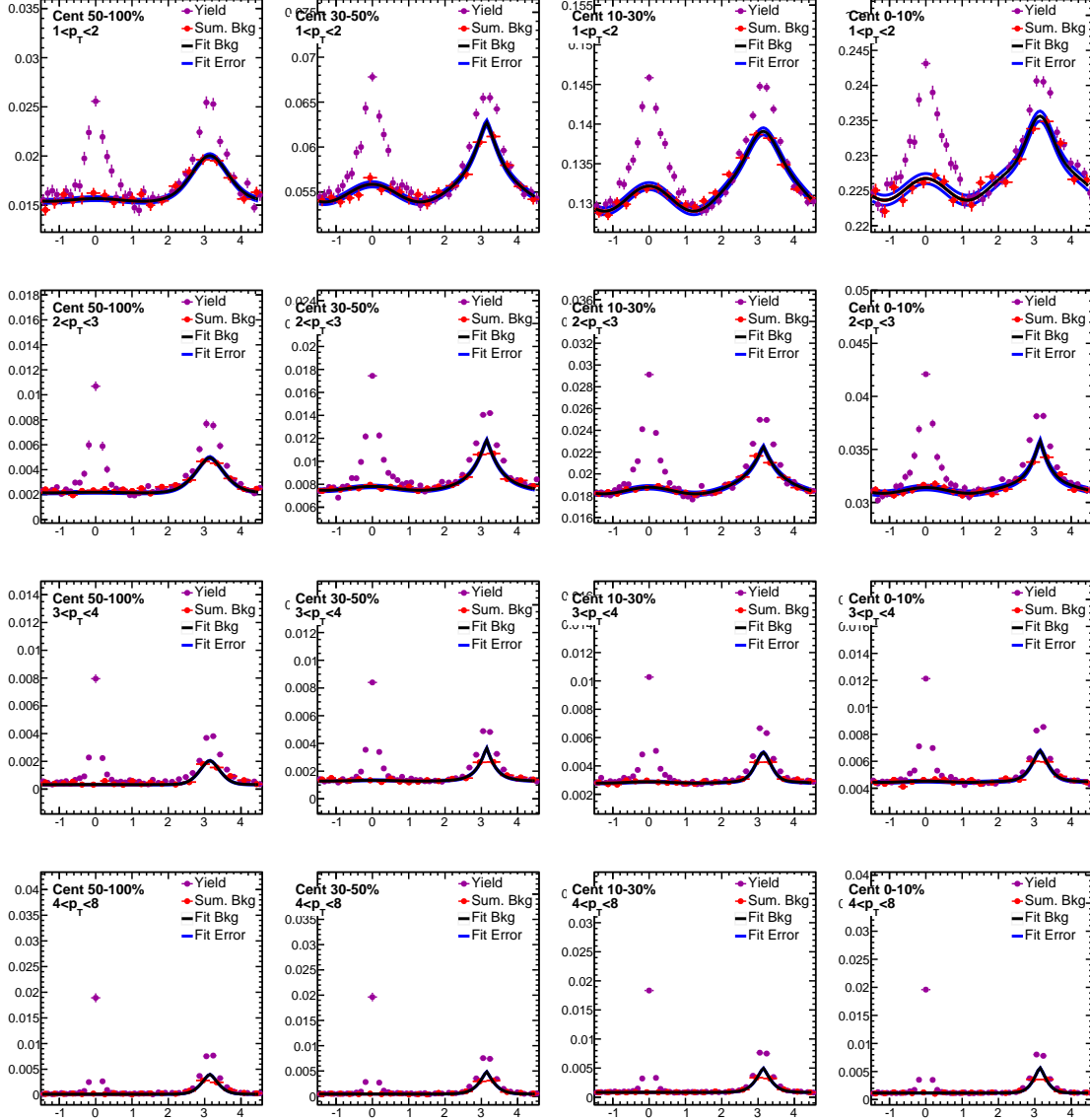


Figure 107. Background leading jet $\Delta\phi$ distributions, estimated by projection over the region $1.5 < |\Delta\eta| < 3.0$, is fit as shown. The 2D background distribution is estimated by propagating the black fit line in $\Delta\eta$, with uncertainty assigned by varying fit parameters by the appropriate fit error as shown in the blue error band.

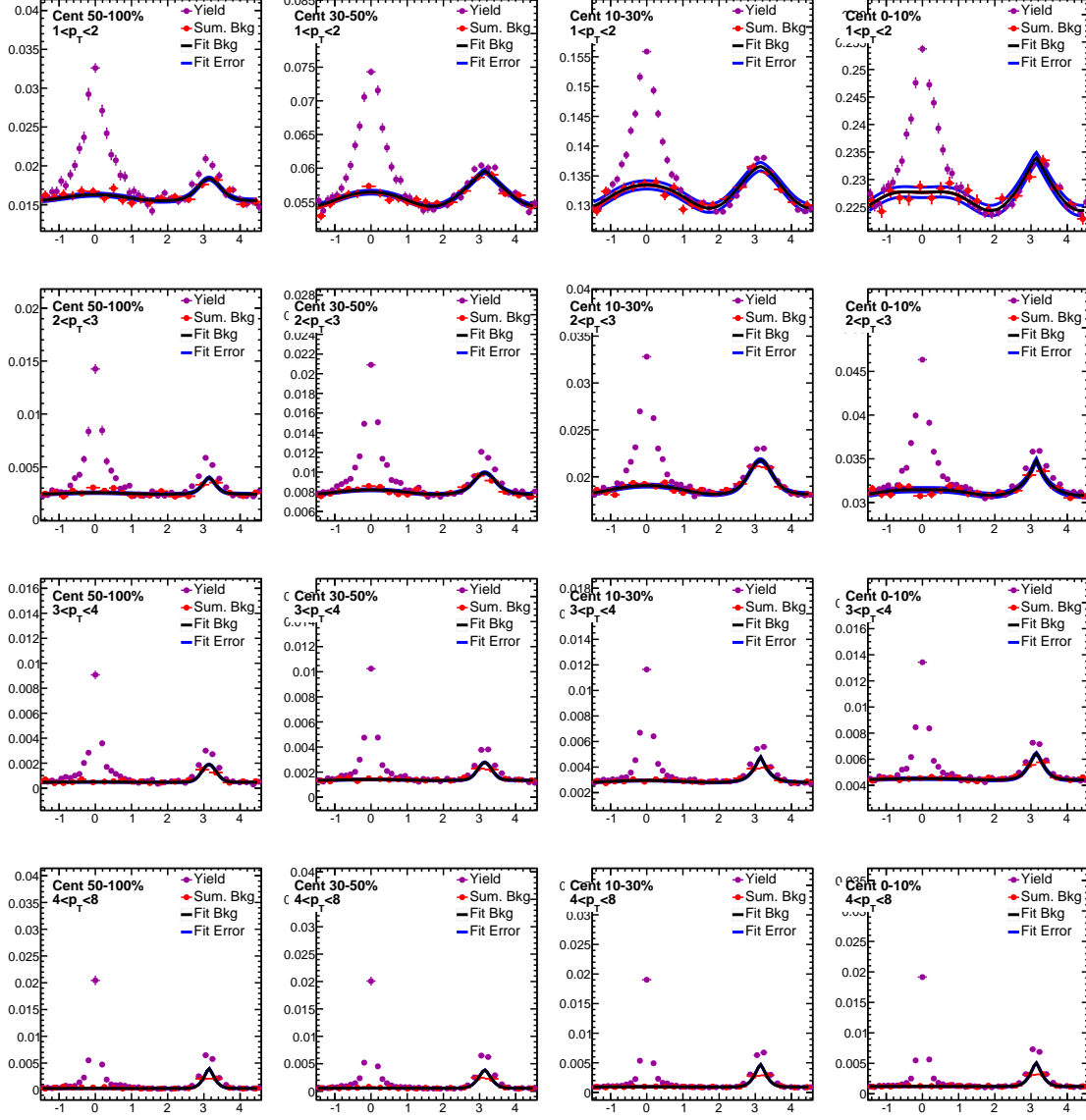


Figure 108. Background subleading jet $\Delta\phi$ distributions, estimated by projection over the region $1.5 < |\Delta\eta| < 3.0$, is fit as shown. The 2D background distribution is estimated by propagating the black fit line in $\Delta\eta$, with uncertainty assigned by varying fit parameters by the appropriate fit error as shown in the blue error band.

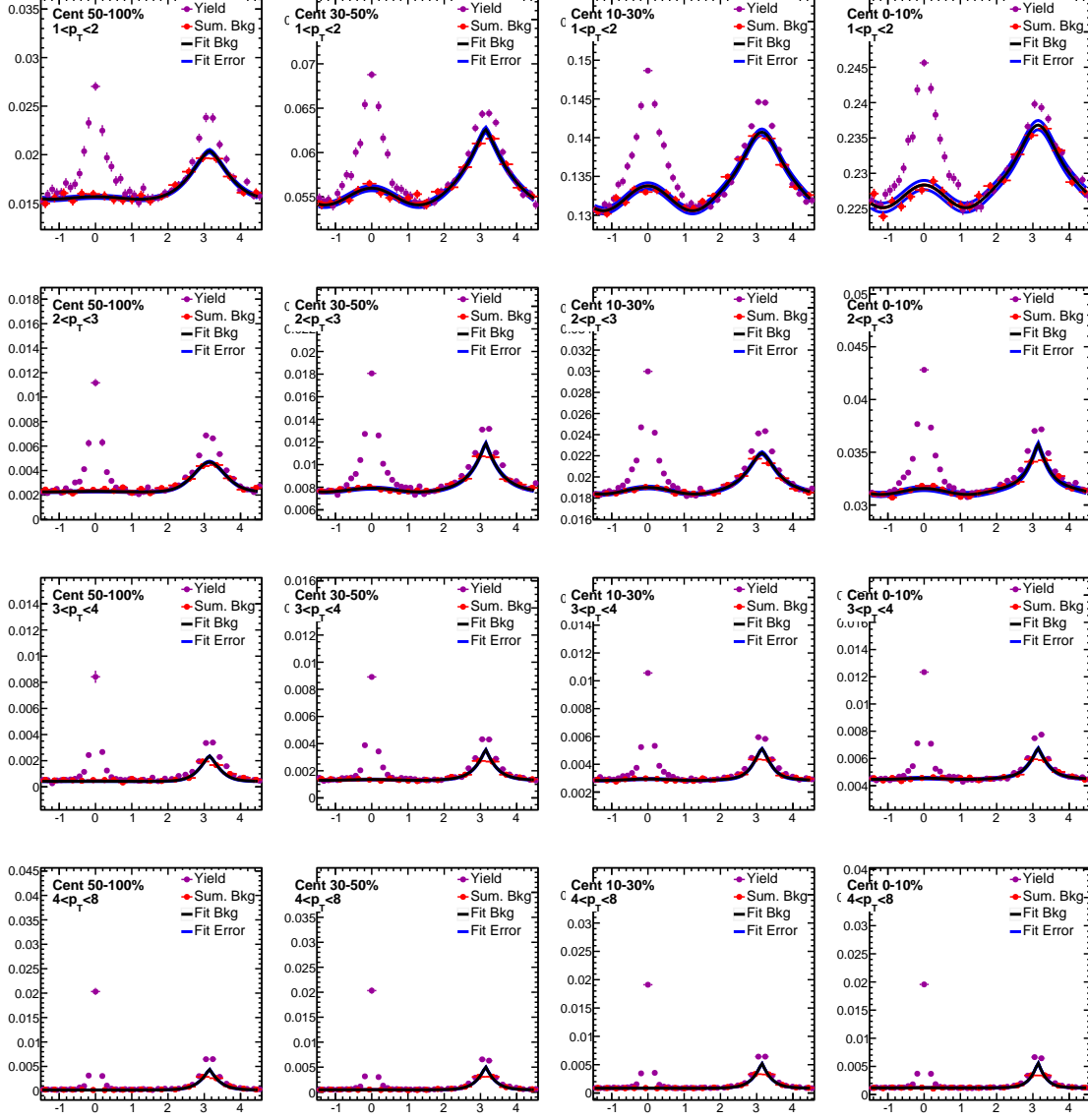


Figure 109. Background inclusive jet $\Delta\phi$ distributions, estimated by projection over the region $1.5 < |\Delta\eta| < 3.0$, is fit as shown. The 2D background distribution is estimated by propagating the black fit line in $\Delta\eta$, with uncertainty assigned by varying fit parameters by the appropriate fit error as shown in the blue error band.

C Pair acceptance and event decomposition systematic uncertainties

Figure 110 illustrates the estimation of pair-acceptance uncertainty, determined by considering the sideband asymmetry in the $\Delta\eta$ distributions of background subtracted yield.

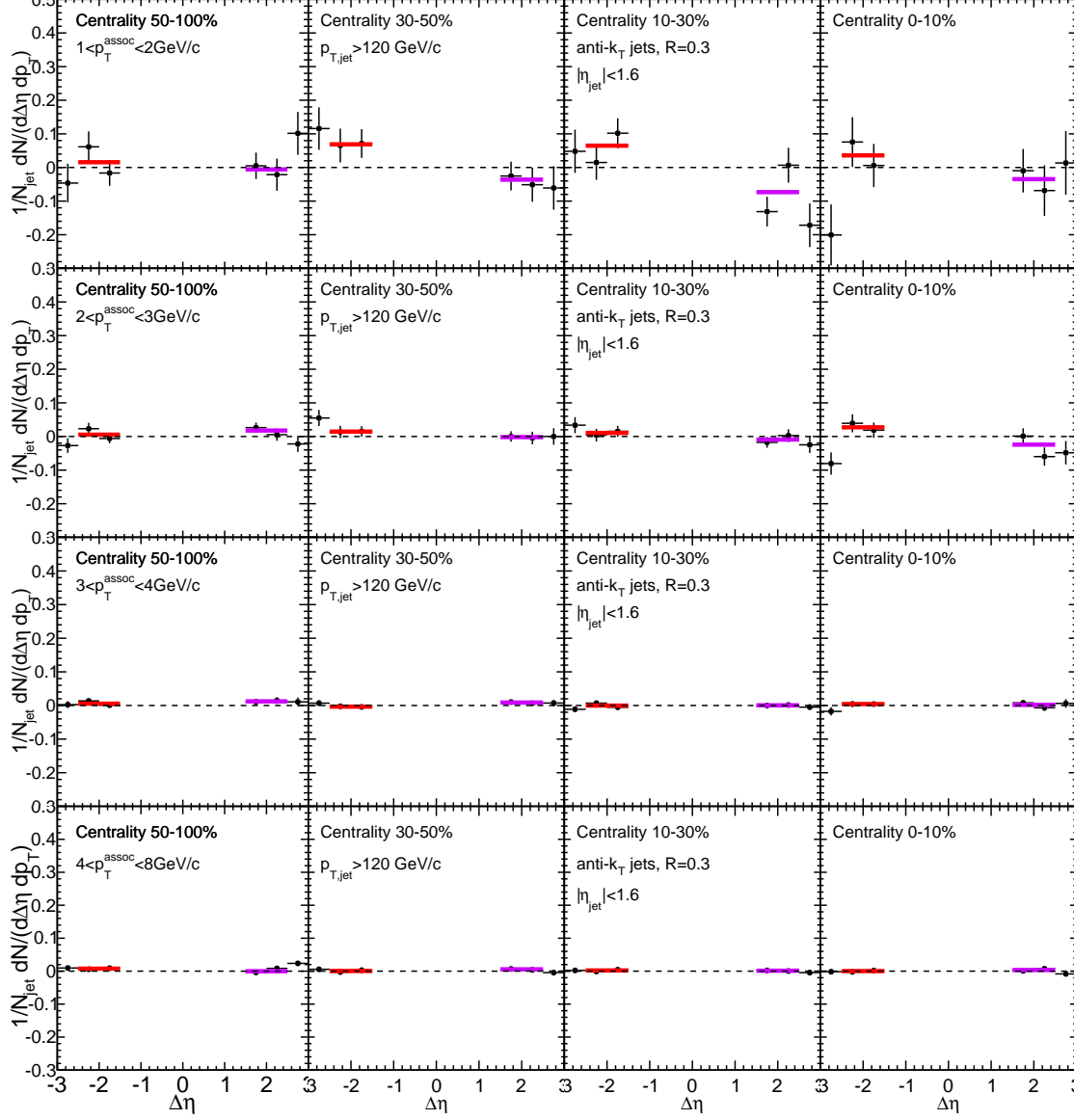


Figure 110. Background-subtracted inclusive jet $\Delta\eta$ distribution is shown for sideband region $1.5 < |\Delta\eta| < 3.0$ only. Each side is fit separately with a horizontal line, and the greater deviation from zero is assigned as systematic uncertainty arising from the pair-acceptance correction.

Figure 111 illustrates the background-subtraction systematic uncertainty estimation: the average content of the two $1.5 < \Delta\eta < 2.0$ bins is assigned as systematic uncertainty for each p_T and centrality bin.

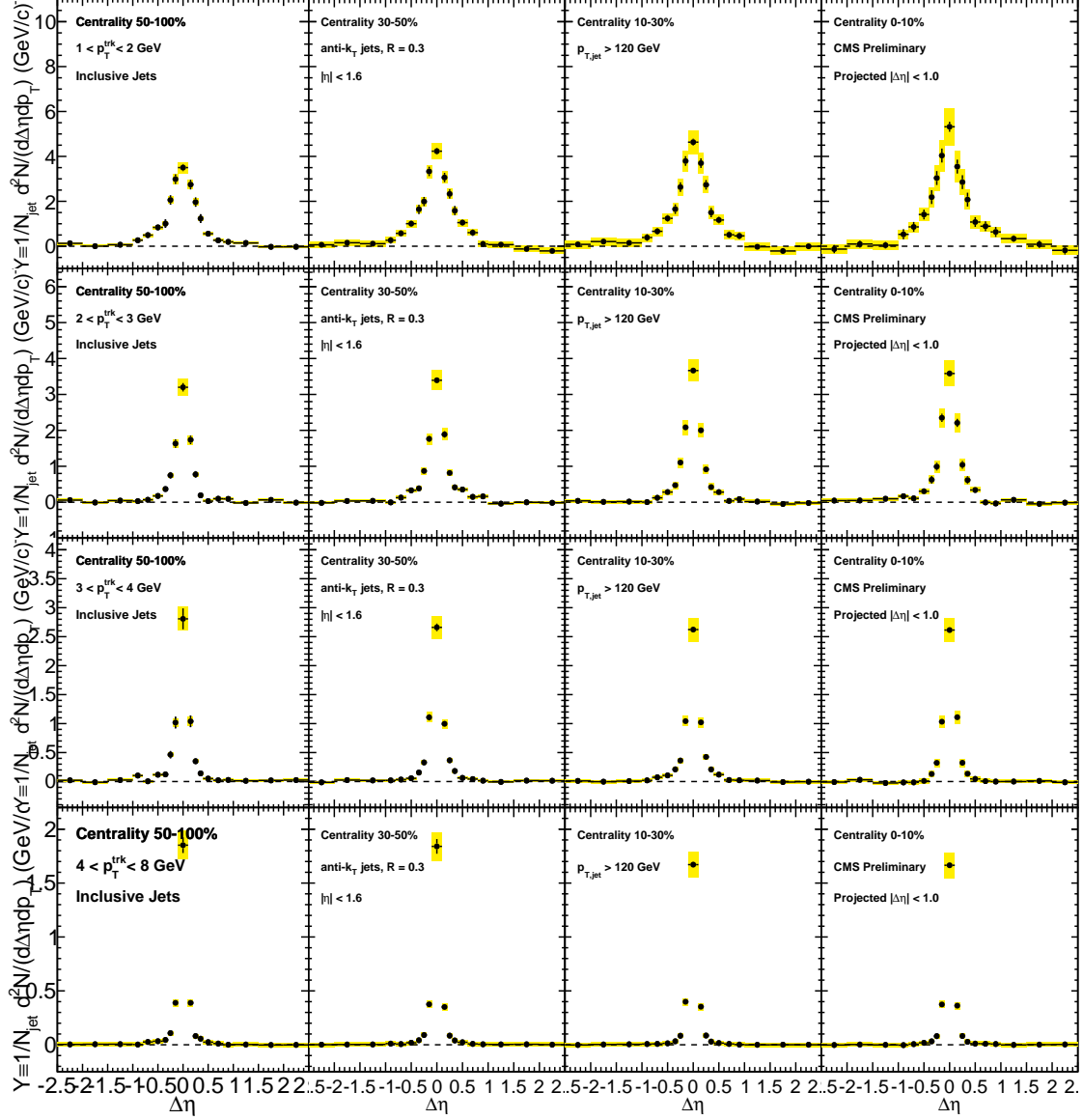


Figure 111. Inclusive jet correlated yield in $\Delta\eta$, shown to axis range $|\Delta\eta| < 2.0$. The deviation of the most peripheral points from zero is assigned as systematic uncertainty as discussed in the Systematic Uncertainty section above.

D Correlation widths and related uncertainty

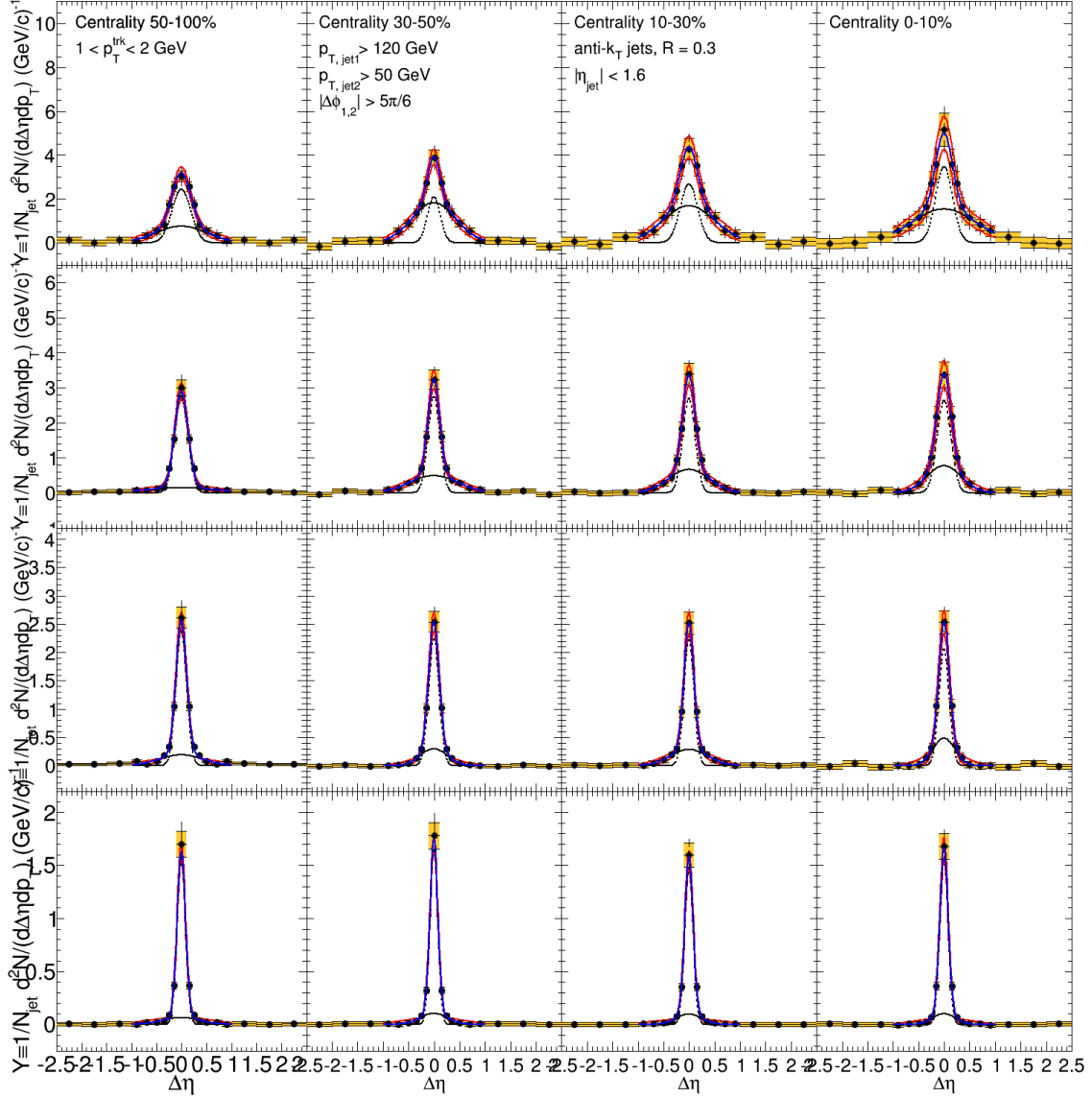


Figure 112. Illustration of the fits used to determine the distribution widths (shown here for leading jet PbPb $\Delta\eta$ correlations). Correlations are fit to a double gaussian (shown in blue, with black dashed lines indicating constituent gaussians), and width is taken as the $\Delta\eta$ value containing 67% of the total yield. Points are varied by their systematic errors and the fits are repeated (shown in red) to obtain the systematic error on the width.

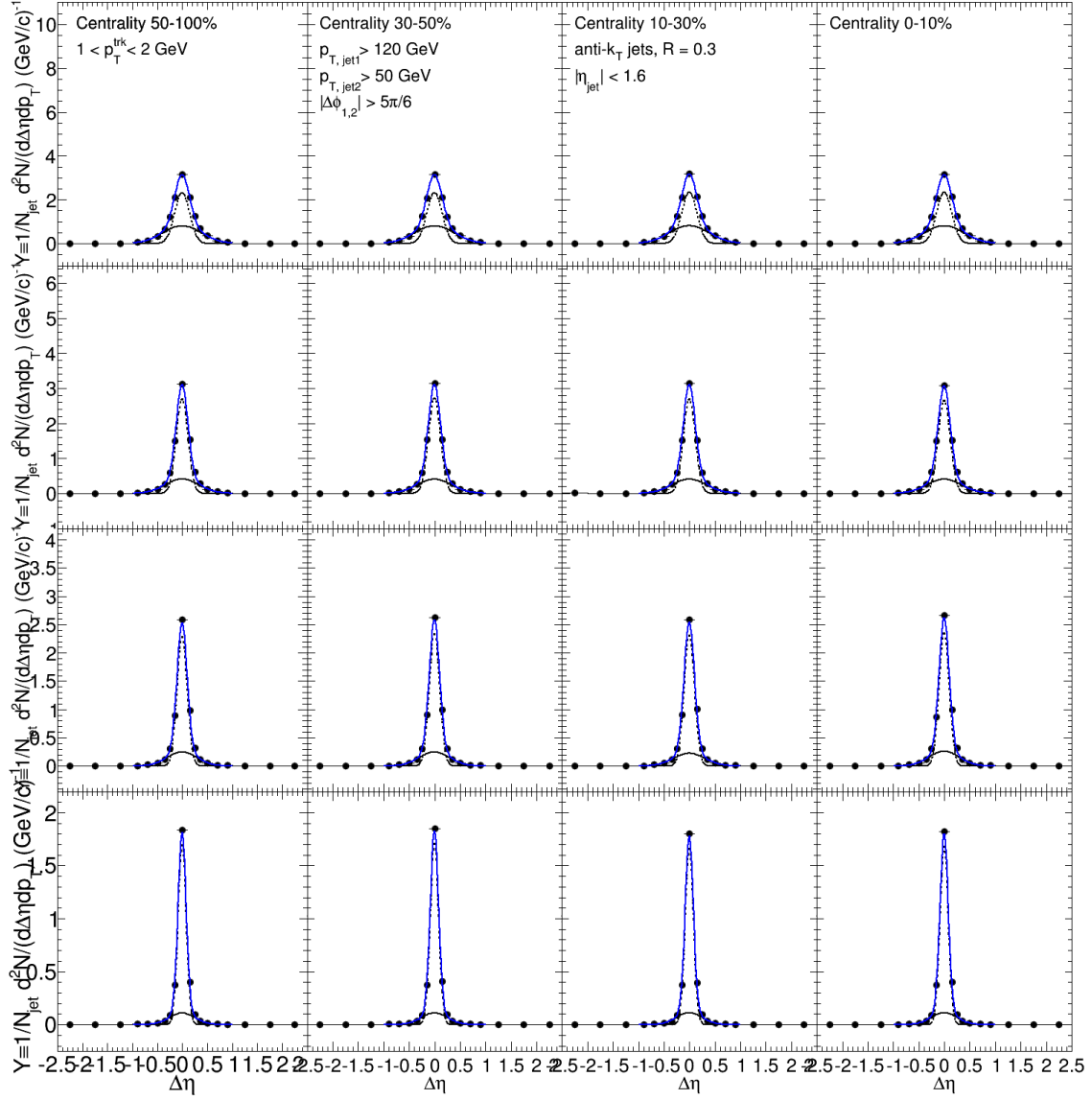


Figure 113. Illustration of the fits used to determine the distribution widths (shown here for leading jet pp $\Delta\eta$ correlations). Correlations are fit to a double gaussian (shown in blue, with black dashed lines indicating constituent gaussians), and width is taken as the $\Delta\eta$ value containing 67% of the total yield.

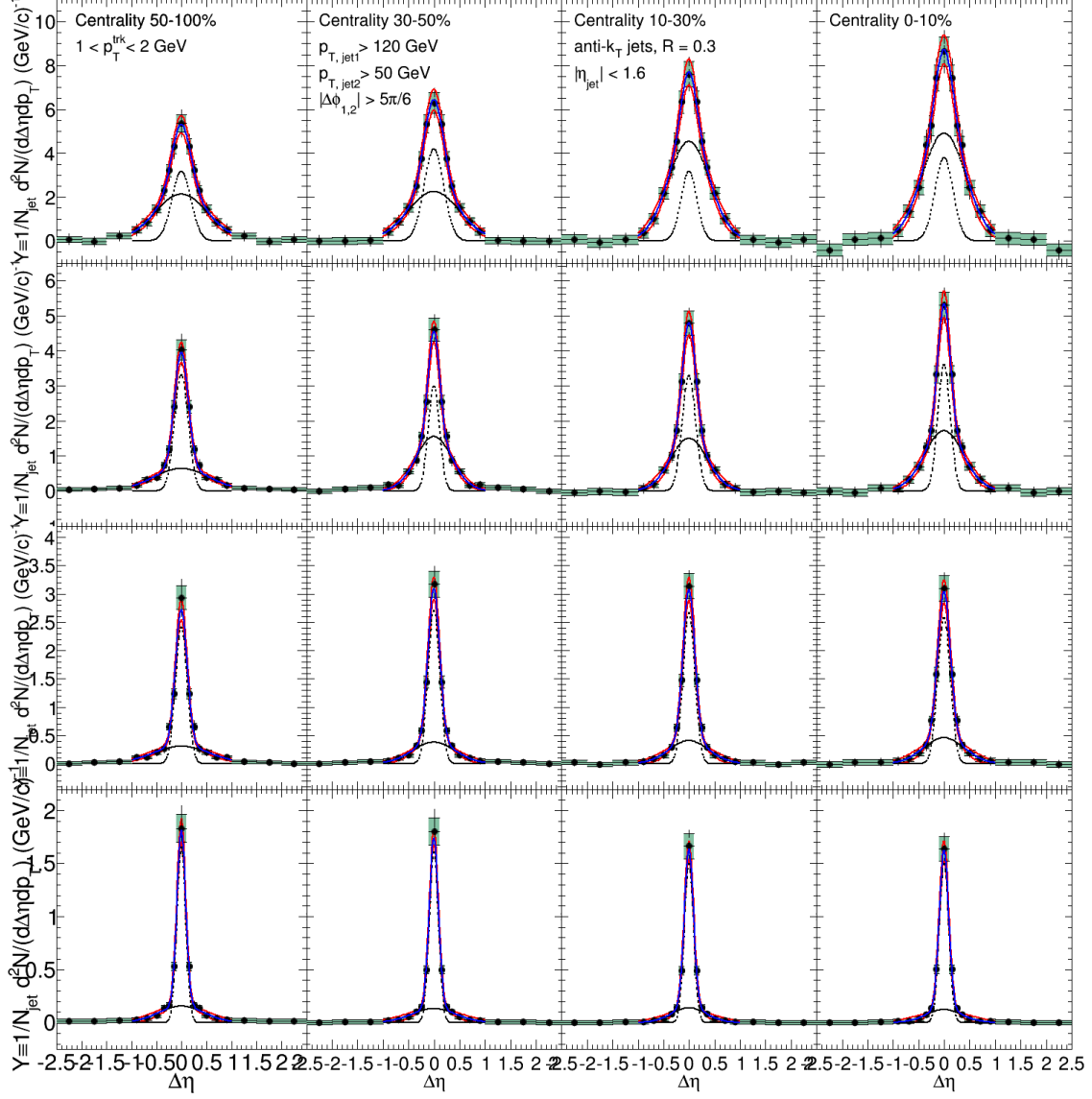


Figure 114. Illustration of the fits used to determine the distribution widths (shown here for subleading jet PbPb $\Delta\eta$ correlations). Correlations are fit to a double gaussian (shown in blue, with black dashed lines indicating constituent gaussians), and width is taken as the $\Delta\eta$ value containing 67% of the total yield. Points are varied by their systematic errors and the fits are repeated (shown in red) to obtain the systematic error on the width.

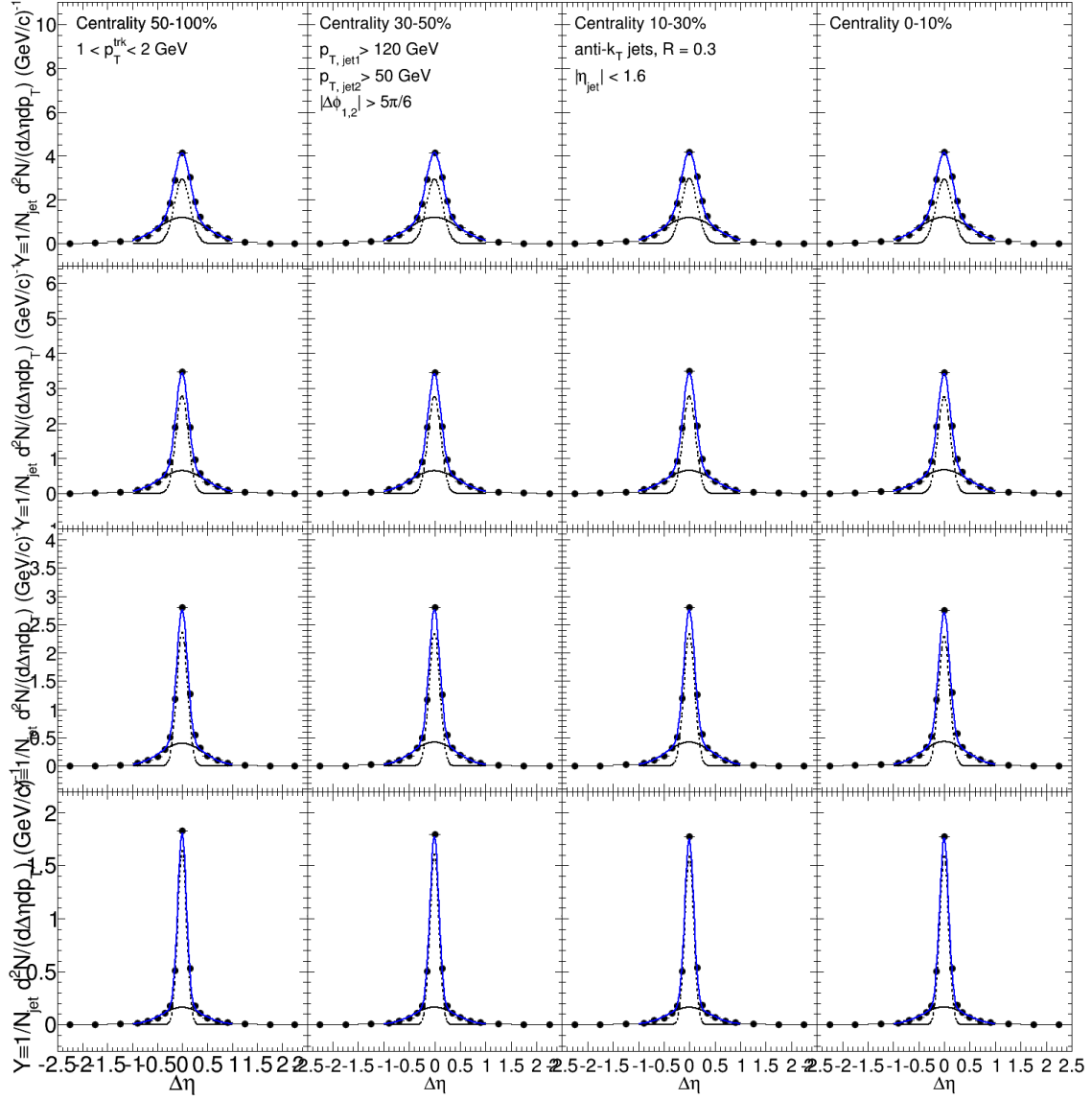
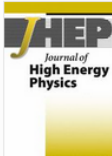


Figure 115. Illustration of the fits used to determine the distribution widths (shown here for subleading jet pp $\Delta\eta$ correlations). Correlations are fit to a double gaussian (shown in blue, with black dashed lines indicating constituent gaussians), and width is taken as the $\Delta\eta$ value containing 67% of the total yield.


E Open access statements for material adapted from previous publications



[Journal of High Energy Physics](#)
November 2016, 2016:55 | [Cite as](#)

Decomposing transverse momentum balance contributions for quenched jets in PbPb collisions at $\sqrt{s_{NN}} = 2.76$ TeV

Authors [Authors and affiliations](#)

The CMS collaboration , V. Khachatryan, A. M. Sirunyan, A. Tumasyan, W. Adam, E. Asilar, T. Bergauer, J. Brandstetter, E. Brondolin, M. Dragicevic, J. Erö, M. Flechl, M. Friedl, R. Frühwirth, V. M. Ghete, [show 2250 more](#)


[Open Access](#) | Regular Article - Experimental Physics
First Online: 09 November 2016

3

1

Citations


Shares



[Journal of High Energy Physics](#)
January 2016, 2016:6 | [Cite as](#)

Measurement of transverse momentum relative to dijet systems in PbPb and pp collisions at $\sqrt{s_{NN}} = 2.76$ TeV

Authors [Authors and affiliations](#)

The CMS collaboration , V. Khachatryan, A. M. Sirunyan, A. Tumasyan, W. Adam, E. Asilar, T. Bergauer, J. Brandstetter, E. Brondolin, M. Dragicevic, J. Erö, M. Flechl, M. Friedl, R. Frühwirth, V. M. Ghete, [show 2288 more](#)

[Open Access](#) | Regular Article - Experimental Physics
First Online: 04 January 2016

8

6

Citations

Shares

First issued by the Director-General – 16.10.2014
Amended by the Director-General – 27.04.2017

Open Access Policy for CERN Publications

CERN is committed to Open Access, as it reflects values that have been enshrined in our Convention for more than sixty years and is becoming increasingly important for the Member States, the European Commission and other institutional partners across the world. For over twenty years, most of CERN's physics publications have been made immediately and openly accessible online, in the form of CERN preprints, before publication in journals. This is generally known as "Green" Open Access.

VITA

NAME: Hallie Causey Trauger

EDUCATION: Ph.D., Physics, University of Illinois at Chicago, 2017
M.Ed., Secondary Science, University of Illinois at Chicago, 2015
M.S., Physics, University of Illinois at Chicago, 2014
B.A., Political Science, University of Chicago, 2010

HONORS: Paul M. Raccah Award for the highest score on the Doctoral Qualifying Exam, University of Illinois at Chicago, 2014
Student Marshal, highest academic honor at the University of Chicago, 2010

TEACHING: 12th Grade Computer Science, Back of the Yards College Preparatory High School, Chicago, IL 2016-2017
9th Grade Physics, Back of the Yards College Preparatory High School, Chicago, IL 2014-2017
Physics 104 (TA leading algebra-based mechanics workshop), University of Illinois at Chicago, 2013-2014
Physics 108 (TA for algebra-based electricity & magnetism discussions and labs), University of Illinois at Chicago, 2012-2013

PUBLICATIONS: Khachatryan, Vardan et al. Decomposing transverse momentum balance contributions for quenched jets in PbPb collisions at $\sqrt{s_{NN}} = 2.76$ TeV. JHEP 1611 (2016) 055.
Khachatryan, Vardan et al. Correlations between jets and charged particles in PbPb and pp collisions at $\sqrt{s_{NN}} = 2.76$ TeV. JHEP 1602 (2016) 156.

PRESENTATIONS: “Jet-track correlation studies in PbPb and pp collisions at 5.02 TeV,” at Quark Matter XVI, Chicago, IL, February 2017.

 “Heavy ion jet results from CMS ” at the 2015 US LHC Users Association Meeting, Batavia, IL, November 2015

 “Heavy ion jet results from CMS and ATLAS” at the 12th Conference on the Intersections of Particle and Nuclear Physics, Vail, CO, May 2015

 “Jet quenching studies in CMS” at the Winter Workshop on Nuclear Dynamics, Keystone, CO, January 2015. J.Phys.Conf.Ser. 636 (2015) no.1, 012012